Numerical investigation of the turbulent boundary layer over dimpled surfaces

Yu Yu Lin

Master of Science Thesis

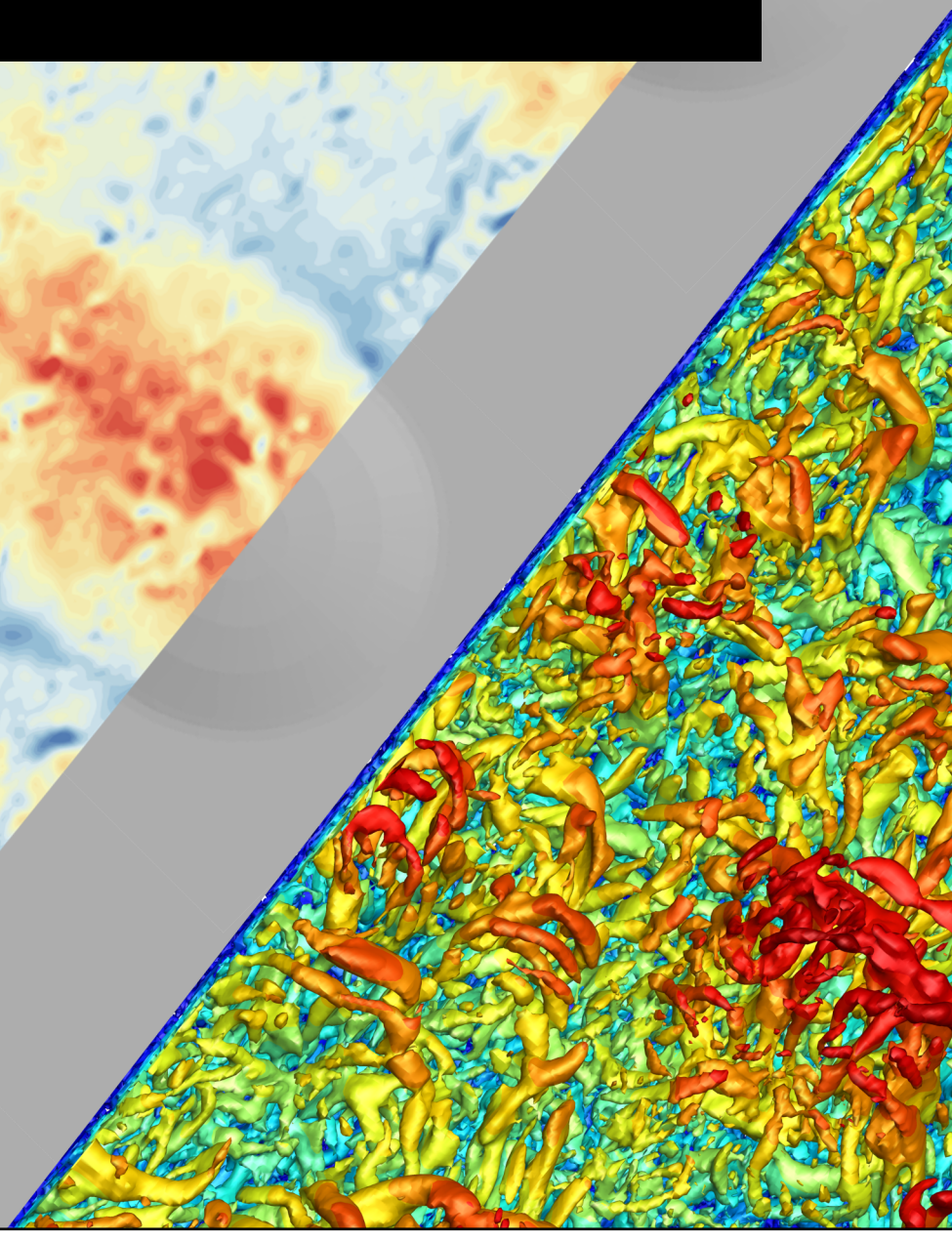

TU Delft Delft University of Technology

Delft Aerospace, the Aerodynamics, Wind Energy,
Flight Performance & Propulsion (AWEP) Department

Numerical investigation of the turbulent boundary layer over dimpled surfaces

Master of Science Thesis

For the degree of Master of Science in Aerospace Engineering at Delft University of Technology

Yu Yu Lin

January 11, 2021

Faculty of Aerospace Engineering · Delft University of Technology

Delft University of Technology
Department of Aerodynamics

The undersigned hereby certify that they have read and recommend to the Faculty of Aerospace Engineering for acceptance a thesis entitled

Numerical investigation of the turbulent boundary layer over dimpled surfaces

by

Yu Yu Lin

in partial fulfillment of the requirements for the degree of

Master of Science Aerospace Engineering

Dated: January 11, 2021

Supervisor(s):

Prof. dr. S. (Stefan) Hickel

Dr. ir. B.W. (Bas) van Oudheusden

Ir. J. (Jordi) Casacuberta Puig

Drs. ir. O.W.G. (Olaf) van Campenhout

Reader(s):

Prof. dr. ing. G. (Georg) Eitelberg

Acknowledgements

This thesis marks the wild journey of a year of research at Delft University of Technology, and it would not have been possible without the help of many people.

Firstly, I would like to express my appreciation to Prof. Steven Hickel and Dr. Bas van Oudheusden for their insightful advice and supervision. Their analytical insight and thorough understanding of the turbulent boundary layer have been of generous support to the foundation for this work.

I am gratefully indebted to Jordi and Olaf for assisting me in setting up the simulation and scope of this project. Olaf's enthusiastic involvement and his in-depth knowledge of experimental works have been a great encouragement. Jordi's deep understanding of the numerical theory and pellucid guidance lights up the path to the success of my work.

Many thanks to my friends in the Netherlands. The whole journey would have been very challenging without them. Together we have overcome many difficulties throughout the time in the Netherlands.

Lastly, I would like to express love to my family for their unquestioning support in every way. This thesis would not have been possible without my family's support and cheers.

Yu-Yu Lin
Zoetermeer, The Netherlands
January 08, 2021

Abstract

Dimples are shallow, indented surfaces that attempt to reduce drag in turbulent boundary layer flows. However, the underlying effect of the dimples on the drag is not entirely understood. This thesis sets out to expand our understanding; a numerical investigation of turbulent boundary layer flow over dimpled surfaces is conducted. This research aims to verify the drag results from recent experimental studies and investigate the possible drag-reducing mechanism of a dimpled plate.

The research considers shallow, rounded-edge dimples with a staggered layout. Implicit large eddy simulation (ILES) is carried out with the cell spacing close to direct numerical simulations (DNS). Simulation outputs conclude that the dimple plate causes a total drag increase of approximately 1% compared to a smooth plate. This value confirms the results of Spalart et al. and recent wind tunnel measurements within the Aerodynamics group. The turbulent coherent structures are further investigated by performing hole-filtering sampling to the quadrant events. Results suggest that the dimple plate induces a more intense turbulent activity in the buffer layer. The increased occurrence contributes to a higher Reynolds shear stress. The development of quadrant events is further analysed using a Variable-Interval Time-Averaging (VITA) technique. It reveals that the averaged quadrant event development between two plates is almost the same. However, a more extended sweep development is found in the wake region. Given such a mild even evolution, the resulting Reynolds shear stress generation remains the same. Lastly, the coherent structure response is linked to the skin friction response through the Fukagata-Iwamoto-Kasagi (FIK) identity. The resulting decomposition using the FIK identity reveals that dimples contribute to higher total drag due to increased Reynolds shear stress. On the other hand, the observed skin friction reduction seems relative to the mean flow convection.

Despite opposing the idea of drag reduction by dimples, this research provides a high-fidelity dataset could provide the foundation for the study of other passive flow devices.

Table of Contents

List of Figures

List of Tables

Glossary

List of Acronyms

CFD	Computational Fluid Dynamics
LES	Large Eddy Simulation
ILES	Implicit Large Eddy Simulation
DNS	Direct Numerical Simulation
NUS	National University of Singapore
DUT	Delft University of Technology
RANS	Reynolds-averaged Navier-Stokes simulation
PIV	Particle Image Velocimetry
TLT	Tornado Like Technology
FIK	Fukagata-Iwamoto-Kasagi identity
TBL	Turbulent Boundary Layer
ZPGBL	Zero Pressure Gradient Boundary Layer
TKE	Turbulent Kinetic Energy
VLSM	Very Large Scale Motion
WENO	Weighted Essentially Non-Oscillatory scheme
SALD	Simplified Adaptive Local Deconvolution scheme
PPE	Pressure Poisson Equation
BiCGstab	Stabilised bi-Conjugate Gradient scheme
CFL	Courant-Friedrichs-Lwey condition

B.C.	Boundary condition
JPDF	Joint Probability Density Function
VITA	Variable-Interval Time-Averaging
RHS	Right Hand Side of the equation
LHS	Left Hand Side of the equation

List of Symbols

δ^*	Boundary layer displacement thickness
δ_0	Inlet boundary layer thickness
$\Delta x, \Delta y, \Delta z$	Streamwise, vertical and spanwise cell spacing
$\Delta x^+, \Delta y^+, \Delta z^+$	Streamwise, vertical and spanwise cell spacing, scaled by inner variables
η	Normalised vertical coordinate
γ	Rescaling factor
$\hat{u}$	Moving average of the velocity
κ	Kármán constant
$\langle u \rangle, \langle v \rangle, \langle w \rangle$	Ensemble-averaged velocity in x, y, z coordinate
μ	Dynamic viscosity
ν	Kinematic viscosity
$\omega_x, \omega_y, \omega_z$	Vorticity in x, y, z coordinate
ρ	Fluid density
$\sigma^2_{\hat{u}}$	Velocity variance of moving-averaged velocity
τ_w	Wall shear stress
θ	Boundary layer momentum thickness
B	Wall law intercept constant
C_d	Drag coefficient
$C_{f,\delta}$	Skin friction from the first FIK term
$C_{f,\overline{I}_{x,z}}$	Skin friction due to FIK spatial developing terms
$C_{f,\overline{u'v'}}$	Skin friction due to Reynolds shear stress
C_f	Skin friction coefficient
C_p	Pressure coefficient
D	Dimple diameter
d	Dimple depth
$D(t)$	Detector function
d/D	Depth ratio
H	Hole-filtering criteria
$I_{x,z}$	Spatial developing term

I_x	Homogeneous spatial developing term
l^+	Viscous length scale
L_X, L_Y, L_Z	Streamwise, vertical and spanwise domain length
L_{rec}	Recycling length
L_{ref}, U_{ref}	Reference length, velocity scale
L_x, Lz	Streamwise and spanwise spacing between dimples
M_{q_i}	Quadrant event mask
N_x, N_y, N_z	Number of the streamwise, vertical and spanwise cells
p	Pressure
$P(u', v')$	Joint Probability Density Function
$Q1, Q3$	Outer interaction and inner interaction event
$Q2, Q4$	Ejection and sweep event
R	Dimple radius
r	Dimple edge curvature radius
Re_δ	Reynolds number based on boundary layer thickness
Re_τ	Reynolds number based on wall shear stress
Re_θ	Reynolds number based on momentum thickness
Re_D	Reynolds number based on dimple diameter
Re_x	Reynolds number based on streamwise location
S	Rate-of-strain tensor
T^+	Wall oscillating period as scaled by inner variables
t_{event}	Triggering time of a quadrant event
T_w	Time interval of a moving window
u', v', w'	Velocity fluctuation in x, y, z coordinate
$u'v'$	Reynolds shear stress
u, v, w	Velocity in x, y, z coordinate
u^+, v^+, w^+	Velocity in x, y, z coordinate, scaled by inner variables
u^*	Friction velocity
U_∞	Freestream velocity
u_ω	Induced velocity field by vortex activity
u_i	Inlet plane velocity
u_s	Source plane velocity
W_m^+	Maximum spanwise wall velocity scaled by inner variables.
x, y, z	Streamwise, vertical and spanwise coordinate
y^+	Vertical coordinate as scaled by inner variables
y_{wd}	Wall distance

Chapter 1

Introduction

In 1977, a group of soviet nuclear scientists is working on the cooling system design at the Kurchatov Nuclear Energy Institute. They apply dimples on heat exchangersto enhance heat transfer. Accidentally, they find a favorable drag reduction on such surface. The result is then published by Kiknadze, Krasnov, et al. (1984). Since the discovery of dimple drag reduction, there has been some research groups that work on dimpled surfaces, trying to characterise the drag reduction effect and its working mechanism. Mainly, the research groups are from the National University of Singapore (NUS) by Mitsudharmadi et al. (2009); Tay et al. (2014) and from Delft University of Technology (DUT) by Vervoort (2009); van Nesselrooij et al. (2016) and van Campenhout et al. (2016). This thesis builds on previous research in DUT and further investigates the drag-reducing mechanism of dimples in turbulent boundary layer flows using a numerical approach. Therefore, this thesis first aims to summarise the state of art in dimple drag reduction, some relevant statistical analysis techniques and aerodynamic theories. Then, this thesis aims to compare current numerical results to literature, investigating the response in the turbulent coherent structures. It is hoped that with high-resolution simulations, a deeper understanding of the flow physics and the drag reducing mechanism can be reached.

1-1 Drag Reduction by Dimples

Among all forms of drags in a cruising transport aircraft, turbulent viscous drag contributes over 50% to the total drag (Abbas et al., 2013). Since skin friction is a primary source of drag, a cornucopia of flow control ideas that try to reduce skin friction has been proposed. These techniques can be roughly grouped into two categories (Gad-el-Hak, 2007): passive and active techniques. Regarding dimpled surfaces, it falls into the passive flow control technique. Dimples are shallow, indented surfaces that attempt to reduce drag in turbulent boundary layer flows. Since the dimple geometry is simple and shallow, they can potentially be manufactured easily. Due to its simplicity and high applicability, many studies have been done on such a simple surface. Early studies found that dimples enhance heat transfer by increasing vortex mixing near the surface. Recently, the research focus has shifted towards its drag

performance: groups in Delft University of Technology and National University of Singapore are actively investigating flows over dimpled surfaces to evaluate dimple drag reduction capability and its working mechanism. Tay (2011) in NUS reported a 2% drag reduction in a channel flow. van Nesselrooij et al. (2016) found a 4% reduction with a staggered dimple layout. Their results also revealed a favourable trend as Reynolds number increases and it's sensitivity to the presence of pressure gradients. However, a recent study by Spalart et al. (2019) contradicted the positive results from previous studies. Both experimental and Direct Numerical Simulations (DNS) were carried out using similar dimple parameters as van Nesselrooij et al. (2016). The results, however, suggested that the effect of dimples on the total drag is neutral to mild negative. Spalart et al. (2019) further argued that the skin-friction reduction is dominated by the increased form drag due to the presence of dimpled surfaces. They concluded that the domination over skin-friction reduction, in general, lead to total drag increase.

Potential convergence issue in Spalart et al. (2019). A 1% to 2% drag increase is found in both experimental and DNS investigations from Spalart et al. (2019). However, the author of this report believes there are some factors that might affect their numerical results, and thus a follow-up study is needed to verify the drag result. In detail, a small domain containing only two dimples with streamwise periodic boundary condition is used in their DNS study, as shown in Fig. 1-1. The influence of such small domain should be further evaluated. From the time history in total drag coefficient, as shown in Fig. 1-2, it seems that there are some oscillations after the initialisation. It could be attributed to the limited domain that leads to such oscillations. Physically, the periodicity allows signals to stay in the computational domain. If the domain is too limited, it is possible that the flow could not reach quasi-equilibrium before being recycled to the inlet. In practice, one need to examine the integral length scale and make sure that the domain length is larger than the integral scale. It is thus unconvincing to conclude there is an overall drag increase, based on the oscillated drag signals. Indeed the difference is subtle, but a detailed analysis is still needed to quantify the overall dimple effect.

1-2 Scope & Objectives

Research objectives. Owing to the lack of detailed and validated numerical studies on dimples and the fact that drag results from scholars are inconsistent currently, there is a need

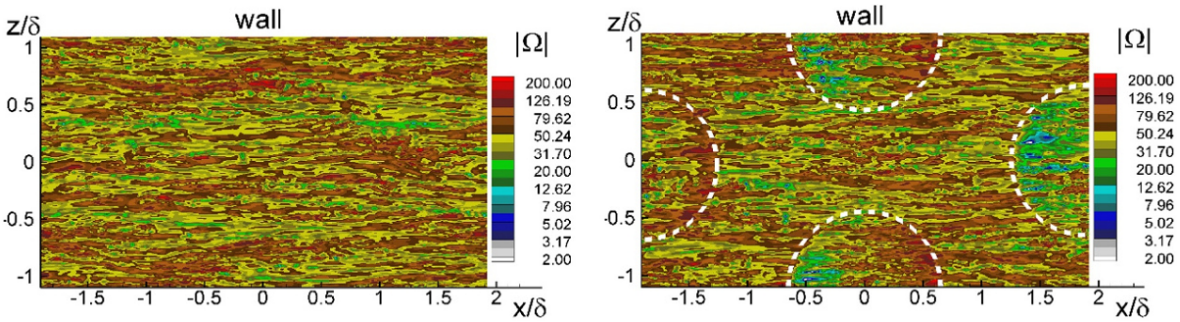

Figure 1-1: Snapshots of vorticity magnitude from Spalart et al. (2019)

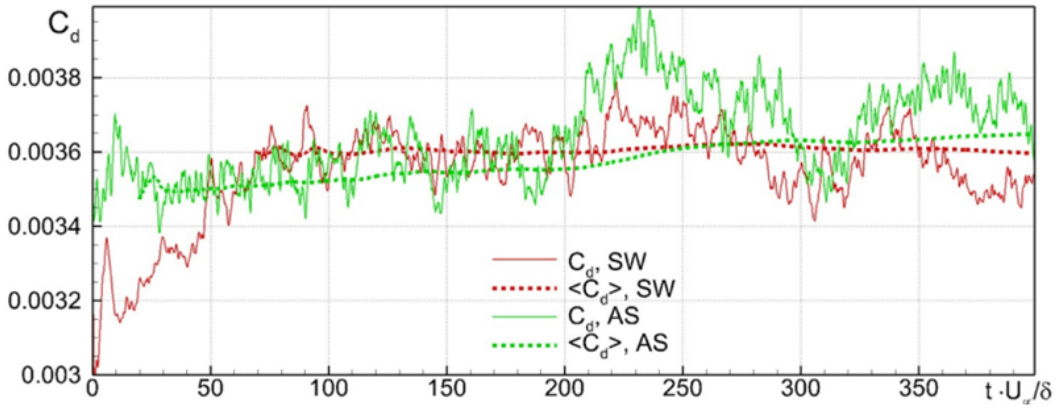

Figure 1-2: Time history of the domain-averaged total drag coefficient from Spalart et al. (2019). Red line is the smooth wall, and green line is the dimpled surface. Dash line represents the running-averaged value.

to perform high resolution, well-validated numerical simulations to study the flow physics of dimples and verify the drag results. The objectives are thus three-folded:

- **Verify the drag result from Spalart et al. (2019).** As stated above, a detailed analysis is needed to verify the overall dimple effect.
- **Investigate the spatial distribution of the responses across dimples.** Most results are obtained experimentally, and thus the drag values are drawn from the direct force measurement. It will be insightful to investigate the spatial distribution of the responses to better understand the flow physics of a drag-reducing dimple.
- **Quantitatively study the impact of dimples on the turbulent boundary layer.** Few researches focus on the statistical analysis of the response. It is thus desirable to apply statistical techniques to quantify the responses and link each term in the Navier-Stokes equation to the variation of the skin friction.

Research questions. Based on above objectives, four questions have been identified:

1. Can the drag result from Spalart et al. (2019) be reproduced?
2. How does a dimple locally affect the mean flow of the turbulent boundary layer? What are the developed flow structures and the corresponding drag in spanwise and streamwise direction?
3. How does a dimple affects the turbulent coherent structures?
4. How does a dimple affects each drag-contributing term?

1-3 Thesis structure

Firstly, Chap. 2 considers the details of dimple drag reduction. An overview of the academic literature regarding dimple drag performance, design parameters, and the working mechanism

will be covered. Next, Chap. 3 discuss the flow problem, dimple parameters and numerical setup. Also, statistical analysis techniques shall be discussed here. Following the methodology, Chap. 4 then presents the results from solver outputs. Validation on the simulated skin friction will first be given. The flow topology and the drag results will then be covered and compared with literature. After presenting the solver outputs, Chap. 5 discusses the analysis from three statistical techniques, which involves in further sampling, averaging and integration on the raw output data. Lastly, Chap. 6 summarises the founding in previous chapters, and the research questions will be addressed. The recommendations for future research shall also be given. Supporting materials, ancillary figures and data are presented in the Appendix and will be referred to when applicable.

Chapter 2

Theory

2-1 Drag reduction of dimpled surfaces

As stated in the previous chapter, no consensus has been reached on the effect of the dimpled surface and its drag-reducing mechanisms. In order to gain more in-depth insight into its physics, a more detailed literature survey is given in this section. Firstly, a review of past research is shown. Following the introductory text, section 2-1-2 presents the state-of-the-art research in dimple design parameters that are relevant to present project. Section 2-1-3 then identifies the flow structures emerged from different dimple geometry and flow conditions. Lastly, the proposed working mechanism for drag reduction will be discussed in section 2-1-4.

2-1-1 Overview

The research into dimpled surfaces was first led by a group of soviet nuclear scientists in 1977. Their goal was to investigate the heat transfer properties of such surface. Besides a heat transfer enhancement, they accidentally found a favorable drag effect. Kiknadze, one of the nuclear scientests in Kurchatov Institute of Atomic Energy, attributed drag reduction to the vortex topology inside the dimpled surface. After the investigation by Kiknadze, Krasnov, et al. (1984), several research institutes have been investigating such dimpled surface. At Delft University of Technology, Vervoort (2009) conducted an experiment and found a drag reduction up to 13% for a shallow dimple. Although their results from the Large Eddy Simulation (LES) did not support the drag-reducing effect, the impact on the flow was identified. The net effect of the total drag depends on the relative dominance between skin-friction reduction and the increased pressure penalty. At National University of Singapore , Mitsudharmadi et al. (2009) studied the flow topology with different dimple depth. They found the impact of dimple only extend to 10% of the dimple diameter above the wall. Also, in the shallow dimpled surface, the flow over the upstream half of a dimple is much more complex than that of the deep dimples, where flow separations were observed. Following the investigation by Mitsudharmadi et al. (2009), Tay (2011) discovered a drag reduction in a channel flow with different dimple coverage ratios. 2% drag reduction was reported with

high coverage ratio and high Reynolds number. In addition, Tay (2011) found that the drag decreases with increased Reynolds number in both coverage ratios. A recent study by Tay, Khoo, et al. (2015) found a drag reduction up to 3% with a shallow dimple. They proposed that the dimpled surfaces introduce a streamwise vorticity component such that the turbulent energy cascade is suppressed, which is analogous to the working principle for the spanwise oscillating wall. Similar to what Tay, Khoo, et al. (2015) found, van Nesselrooij et al. (2016) in DUT conducted an experimental investigation with different dimple patterns and found that only shallow and staggered array of dimples are capable of achieving drag reduction. They observed that the drag reduction is obtained when rows overlap, suggesting the importance of spanwise interaction of the dimples. Recently, Tay and Lim (2018) used tear-drop shaped dimples and found a drag reduction up to 6%. They found that tear-drop shape might be conducive in reducing the form drag, and thus the total drag is reduced.

Even though several studies have found a drag reduction, the results are not consistent. Lashkov et al. (2002) performed experiments with sharp-edged, low coverage ratio dimples and found a drag increase around 20% to 30%. Burgess et al. (2005) reported a drag increase in rectangular channel flow. Lienhart et al. (2008) performed both an experimental and DNS study over an array of dimples and found no skin friction reduction. They indicated that the effect on the skin friction reduction is annulled by the increased form drag. van Campenhout et al. (2016) found no clear drag reduction either. They proposed that the absences of drag reduction could be attributed to the favourable pressure gradient of the wind tunnel inlet ramp. Leontiev et al. (2017) conducted an experimental investigation on different dimple geometries and only the round-edged dimple exhibited drag reduction in low Reynolds number. Recent experimental and DNS study by Spalart et al. (2019) found that shallow dimples lead to 1% to 2% drag increase. Their results suggested that the skin-friction is indeed reduced, but the increased form drag dominates, leading to a total drag increase. The drag results are summarised in Tbl.2-1.

Even though we can compare two studies to investigate the effect of a specific parameter, in general, it is not fair to compare them all together. For two reasons, firstly, earlier research often focused on the heat transfer enhancement, and the thus the preferred dimple geometry for heat transfer problem is often sharp-edged, as shown by Lashkov et al. (2002); Burgess et al. (2005). Tay, Khoo, et al. (2015) indicated that edge sharpness affects the development in the flow structure over dimple, and thus lead to different drag results. In addition to the sharpness effect, another factor that might increase the uncertainty in the comparison study is the flow type. To be more specific, plane boundary layer flows are different from fully-developed channel flows, where a constant boundary layer thickness is presented in the channel. The results from van Nesselrooij et al. (2016) revealed that the drag reduction seems to do with the small-scale turbulent structures. He performed a Reynolds-averaged Navier-Stokes simulation (RANS) with a drag-reducing dimple geometry but found a drag increase. He further argued that the small-scale turbulence structures might be critical in determining the drag reduction effect since RANS is not able to resolve the turbulence variation. The lack of detailed data and the connection of turbulence structures to drag reduction leads the author to believe that there is a need to perform a high fidelity simulation to investigate the turbulence structures and serves as a benchmark for the future research.

Literature	Set up	d/D	Drag	Notes
Lashkov et al. (2002)	Experimental	7%	>20%	Sharp edge
Burgess et al. (2005)	Experimental	10%	>20%	Sharp edge
Vervoort (2009)	Experimental	2.5%	-13%	
Lienhart et al. (2008)	Experimental	5%	0%	Channel flow
Lienhart et al. (2008)	Numerical	5%	4%	Channel flow
Tay (2011)	Experimental	5%	-2%	Channel flow
Isaev et al. (2013)	Numerical	20%	-7%	Laminar
van Nesselrooij et al. (2016)	Experimental	2.5%	-4%	
van Campenhout et al. (2016)	Experimental	2.5%	0%	
Tay and Lim (2018)	Experimental	4%	-5%	Teardrop dimple
Spalart et al. (2019)	Experimental	2.5%	2%	
Spalart et al. (2019)	Numerical	2.5%	2%	

Table 2-1: Overview of the literature that focuses on drag reduction of dimpled surfaces (in chronological order). Literature without specific notes refers to rounded-edge, spherical dimples under the plane turbulent boundary layer flow.

2-1-2 Dimple design and patterns

In this section, the impact of dimple design parameters on the total drag will be investigated. The findings by various literature will be reviewed and consolidated to illustrate the dimple effect. The dimpled surfaces can be specified by the cross-sectional properties of a single dimple, and the pattern of which the dimples are oriented and placed. Besides the shape and distribution, the coverage of dimpled surface to total area is also considered. For a spherical dimple shown in Fig. 2-1, the geometry can be characterized by diameter to depth ratio d/D, the edge curvature radius r.

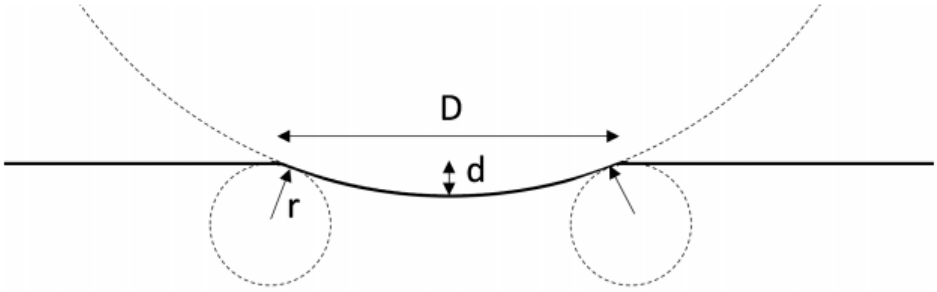

Figure 2-1: Cross-sectional properties of a spherical dimple. (van Nesselrooij et al., 2016)

Depth Ratio

Various scholars have investigated the impact of depth ratio on drag reduction effects. As stated in section 2-1-1, earlier study mainly focused on the heat transfer enhancement, and

thus higher depth ratio was often adapted. The reason for such preference is that the deep dimple often leads to flow separation in the upstream of the dimple, resulting in a formation of vortex structures which increase heat transfer rate on dimples (Turnow et al., 2011; Isaev et al., 2013; Isaev, Schelchkov, et al., 2017). Regarding the effect on drag, Tay, Khoo, et al. (2015) suggested that the flow separation is more likely to happen at lower Reynolds number, and a higher form drag will be expected, leading to a total drag increase. For a high depth ratio dimple, Mitsudharmadi et al. (2009) found that the drag increase seems to remain constant as the depth ratio increase to 12%, shown in Fig. 2-2. At higher depth ratio, an experiment done by Burgess et al. (2005) suggested that for d/D larger than 0.1 (up to 0.3 in their experiment), a substantial drag increase with increasing Reynolds number is obtained. Examining the drag results in Tbl. 2-1, it seems that most drag reduction cases were obtained using shallow dimples. The patent issued by Kiknadze (2013) also claimed that the depth needs to be smaller than 0.1D to have a drag reduction effect. From the above illustration, it can be concluded that in favor of a drag reduction dimple, the depth ratio needs to be small. Higher depth ratio cause flow separation, resulting in higher form drag that overshadows the skin-friction drag reduction effect.

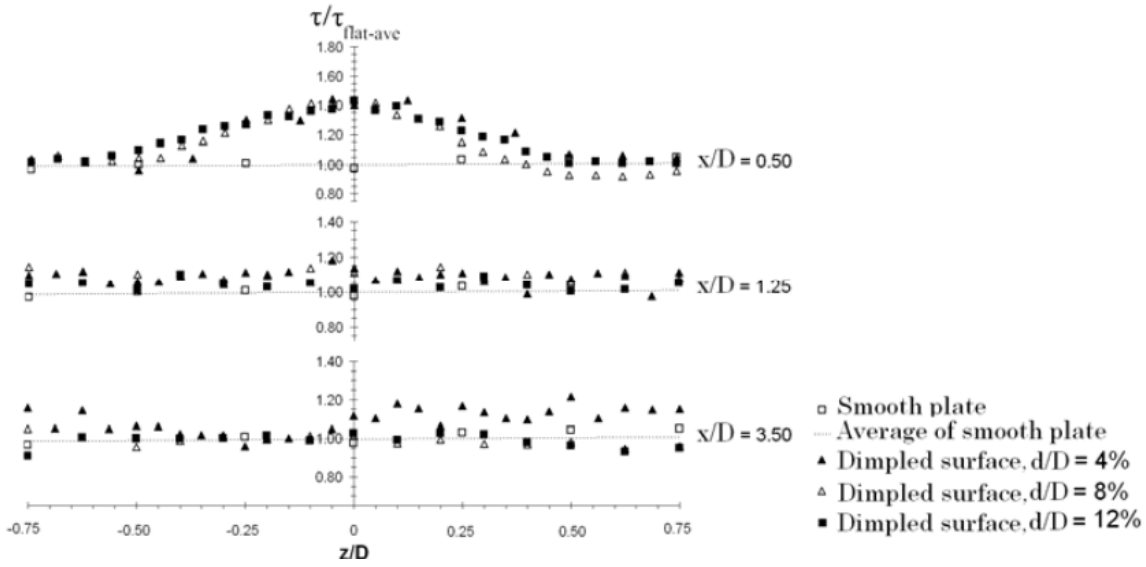

Figure 2-2: Wall shear stress with different depth ratios. (Mitsudharmadi et al., 2009)

Dimple Density

The dimple density can be defined as the ratio of the dimple area to the total plate area. For its impact on dimple performance, Kiknadze (2013) pointed out that coverage ratio should be between 5% to 50% for a drag-reducing dimple, and 10% to 80% for the purpose of heat transfer enhancement. However, the statement by Kiknadze (2013) is not supported by various publications. Physically, a higher coverage ratio is favored, due to the limited extent of influence in the streamwise direction. Both experimental and numerical investigation have confirmed the rapid recovery of the boundary layer profile downstream. Numerically, in a study of the Reynolds number effect, Isaev, Kornev, et al. (2010) performed RANS and found a limited extent downstream. Experimentally, Terekhov et al. (1995) found that the

vortex structure can persist up to 2.5D downstream of a dimple. Mitsudharmadi et al. (2009) performed an oil streak experiment using shallow dimples and found that the effect on the shear stress gradually diminished within 1.25D. Fig. 2-3 shows the oil flow visualization from Mitsudharmadi et al. (2009).

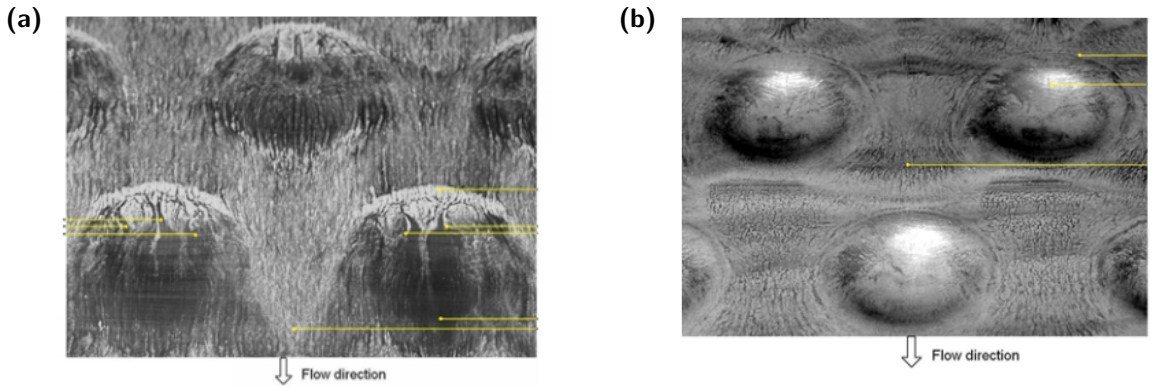

Figure 2-3: Oil flow visualization. (a) d/D = 4% dimples. (b) d/D = 12% dimples. (Mitsudharmadi et al., 2009)

Pattern Layout

In addition to dimple geometry, the arrangement pattern also plays an important role in determining the total drag. In general, two types of patterns can be identified: staggered and aligned, as shown in Fig. 2-4. It has been shown from various literature that staggered pattern is optimal for drag reduction. Tay (2011); Tay, Khoo, et al. (2015) obtained drag reduction using shallow and staggered dimples. The beneficial effect of the staggered pattern was also found by van Nesselrooij et al. (2016). They performed experiments with a staggered pattern and an aligned pattern, which is similar to the staggered case but rotate 90 degrees. They found that the drag reduction was annulled by rotating the dimples into the aligned pattern. The reason for such preference remains unknown. van Nesselrooij et al. (2016) proposed that in a staggered pattern, the arrangement of acceleration and deceleration field leads to regions of alternating spanwise velocity that have a similar effect as the spanwise oscillating wall, generating smaller skin friction. Specifically, the flow is under the influence of the decelerated region between two dimples in the adjacent row, as illustrated in Fig.2.8. In staggered case, the acceleration fields, created by adjacent dimples, are in phase with each other; whereas in the aligned case, the created acceleration fields tend to cancel out, leading to weaker alternating spanwise velocity. In summary, it seems that the staggered pattern is mostly used for drag reduction. No scholars proposed an aligned pattern.

2-1-3 Flow Structures

There have been various studies focused on revealing the flow structure in the dimpled surfaces. Mahmood et al. (2001) found vortical structure pairs shed from the dimples, and thus increase local Nusselt numbers near the downstream dimples. Tran et al. (2011) performed PIV experiments to evaluate the flow structure over the dimple quantitatively. Other

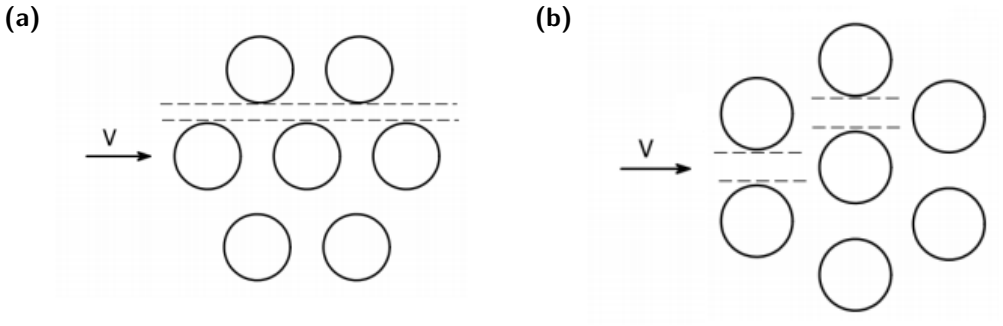

Figure 2-4: (a) Aligned dimples. (b) Staggered dimples. (Veldhuis et al., 2009)

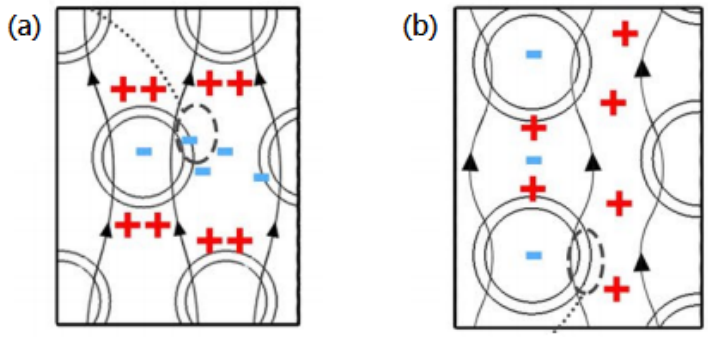

Figure 2-5: high (+) and low (−) velocity regions in staggered (left) and aligned (right) cases. (van Nesselrooij et al., 2016)

researches used qualitative methods like dyes and oil streaks (Mitsudharmadi et al., 2009; Kovalenko et al., 2010). A systematic investigation on flow structure was first done by Kovalenko et al. (2010). They identified four different flow types: the confuser-diffuser structure for small depth ratio at low Reynolds number, single horseshoe vortex for moderate depth ratio, and mono-vortex or two counter-rotating vortices at high Reynolds number and high depth ratio. They further argued that the flow structures are determined by the combination of depth ratio and Reynolds number. Later Tay et al. (2014) performed dye streaks experiment in a hydrodynamic channel flow. They proposed two flow types in addition to the types found by Kovalenko et al. (2010). It seems that no additional flow structures besides these six types have been found in the literature to date. Interestingly, these six flow topologies can be organized into flow development "stages", depends on the flow Reynolds number and dimple depth ratio. The next section will give an overview of the development stages by Tay et al. (2014).

Flow development

The flow development can be sort out from the experiments with different depth ratio and Reynolds number. Starting from low depth ratio at low Reynolds number and changing to high depth ratio and high Reynolds number, Tay et al. (2014) classified the flow structures into six stages:

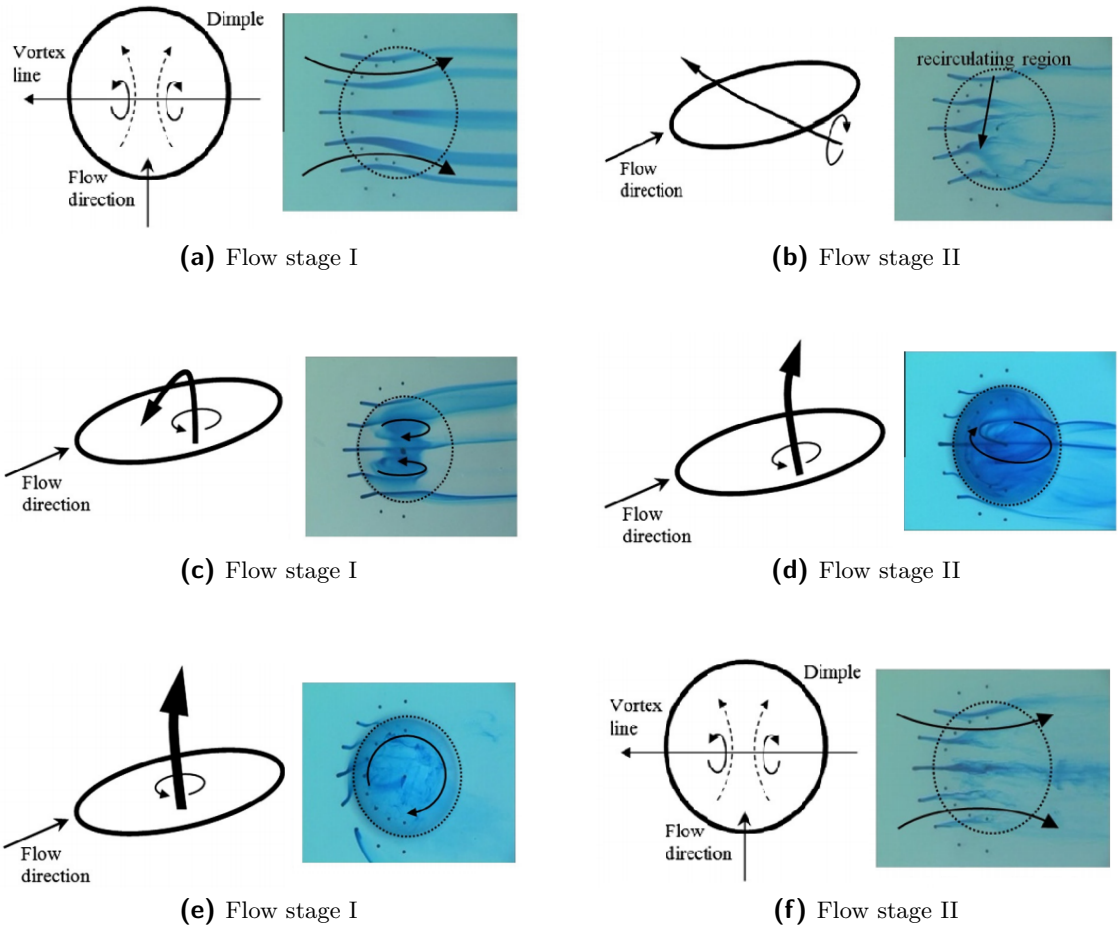

(a) Flow stage I **(b)** Flow stage II

(c) Flow stage I **(d)** Flow stage II

(e) Flow stage I **(f)** Flow stage II

Figure 2-6: Overview of the flow stages. The left panel shows the conceptual model and the right shows the corresponding flow topology. (Tay et al., 2014)

- **Stage I.** The flow is fully attached, and a symmetrical, confuser-diffuser pattern is presented, as illustrated in Fig. 2-6a
- **Stage II.** As Reynolds number increases, the flow becomes separated at the upstream half of the dimple, as indicated in Fig. 2-6b.
- **Stage III.** Two counter-rotating vortices formed inside the dimple. Fig. 2-6c gives an overview of the flow structure.
- **Stage IV.** As Reynolds number further increases, the vortex strength also increases, leading to Instabilities. An asymmetrical vortex formed. Tay called this dominate vortex tornado-like vortex, and found such vortex has a diagonal downstream orientation. Even though the location within the dimple varies, the orientation remains the same. Fig. 2-6d gives an overview of the flow structure.
- **Stage V.** The tornado-like vortex becomes vertical and the tilting angle changes randomly, as shown in Fig. 2-6e

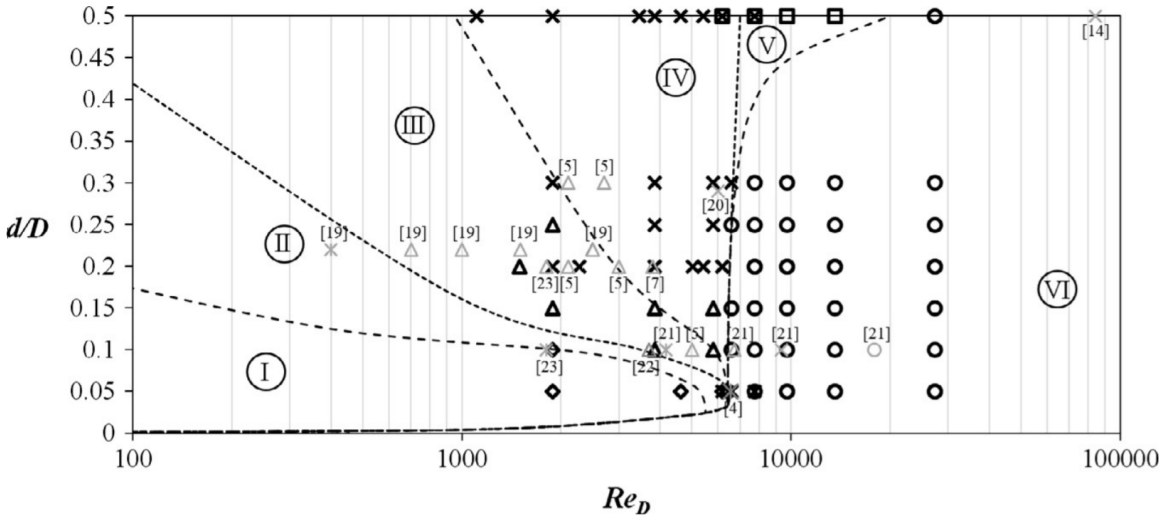

Figure 2-7: Six flow stages on (d/D, Re_D) diagram. (Tay et al., 2014).

- **Stage VI.** The mean flow return to symmetry. No large scale structures are stable. The flow seems built upon the flow pattern of stage I, as shown in Fig. 2-6f

Tay et al. (2014) argued that from their extensive study on different Reynolds numbers and depth ratios, shown in Fig. 2-7, it seems that the flow over dimples generally follows these six stages, as the Reynolds number increases. They also pointed out that for shallower dimples, fewer stages will emerge. For instance, for shallow dimples like d/D = 2.5%, only Stage I and Stage VI are presented.

To sum up, six flow structures have been clearly identified, the question, however, remains under which flow type is capable of achieving drag reduction. Recent studies suggested that flow type I and type VI are the possible candidates for dimple drag reduction, corresponding to (a) and (e) in Fig. 2-8 (Tay, Khoo, et al., 2015; van Nesselrooij et al., 2016; van Campenhout et al., 2016). van Nesselrooij et al. (2016) proposed that the drag reduction might be attributed to the confuser-diffuser pattern, which can be potentially linked to the working mechanism of drag reduction by spanwise wall oscillation.

Impact of Reynolds number on flow structures

The impact of Reynolds number can be summarized in Fig. 2-7. In general, as the Reynolds number increases, the flow topology changes from Stage I to Stage VI. For shallow dimples with $d/D = 5\%$, fully attached laminar flow is observed at low Reynolds number, and a conveger-diffuser flow pattern is presented. At medium Reynolds number, the flow is separated. At high Reynolds number, the flow return to fully attached, turbulent flow. Even though the streakline shows a chaotic pattern, the mean flow remains symmetric about the dimple centerline, and a convergent-divergent flow pattern also appears. The above flow characteristics from low Reynolds number to high Reynolds number refer to flow stages I,II and VI, respectively. In a shallow depth dimple, only these three stages are presented. Fig. 2-8 summarize the flow structures of a dimple with d/D of 5%.

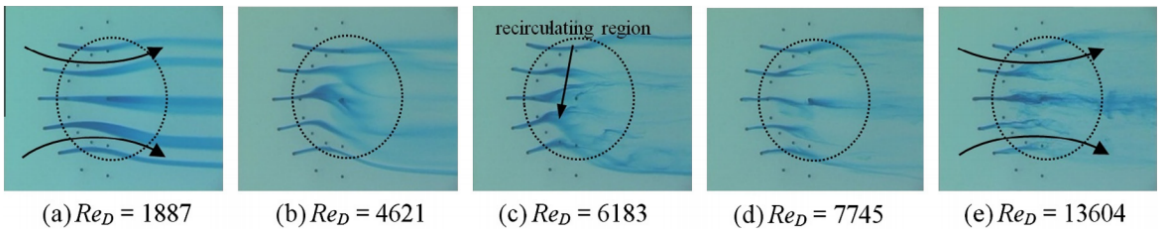

Figure 2-8: Flow over a $d/D = 5\%$ dimple. (Tay et al., 2014)

Impact of depth ratio on flow structures

In general, as the depth ratio increases, the flow tends to separate, leading to vortex formation inside the dimple. We can observe those vortex activity in the flow stage III, IV and V. Specifically, as the depth ratio increases to d/D = 20%, two symmetric counter-rotating vortices are observed in the dimple at low Reynolds number. This symmetry disappears at medium Reynolds number, and one of the vortices becomes more dominant than the other. At higher Reynolds number, the flow returns to symmetry. Fig. 2-9 illustrates the flow over dimples at d/D = 20% (the figure of symmetric counter-rotating vortices are not shown from Tay et al. (2014))

When the depth is further increased to d/D = 50%, a dominate vortex tilting downstream is observed at low Reynolds number. As the Reynolds number increases, the vortex becomes unstable and breaks down. At medium Reynolds number range, the vortex axis becomes vertical. As the Reynolds number further increases, the vortex again appears unstable, but the tiling axis now changes randomly, as shown in Fig. 2-10.

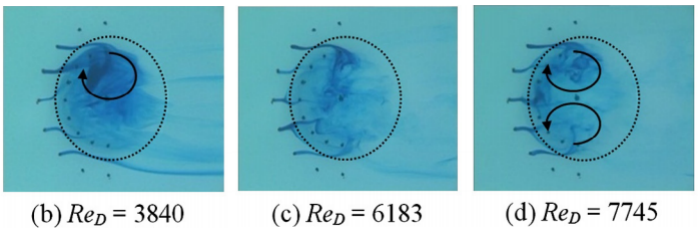

Figure 2-9: Flow over a dimple for $d/D = 20\%$. (Tay et al., 2014)

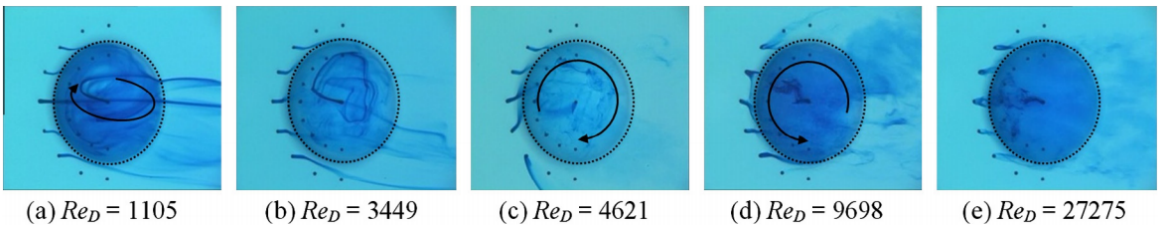

Figure 2-10: Flow over a dimple for $d/D = 50\%$. (Tay et al., 2014)

2-1-4 Proposed Working Mechanism

In this section, four proposed mechanisms shall be discussed. Despite some have less evidence compared to others, they might still give some insights into the physics of flows over dimpled surfaces. Therefore, for the sake of completeness, they are still included. An overview of the proposed mechanisms are shown below:

1. **Tornado Like Technology (TLT).**

   This hypothesis states that self-organizing vortices formed inside the dimple. These vortices counteract the mean flow such that the induced shear opposes the drag, leading to overall drag reduction. This hypothesis is mainly supported by Vida (2004) and Kiknadze, Gachechiladze, et al. (2012). However, The results from Vervoort (2009) opposed this idea. Vervoort (2009) performed LES with different depth ratios and found that even though the vortex indeed reduced shear stress in the upstream half of the dimple, it also entails a higher form drag, leading to an overall drag increase. These vortices were also observed in other literature (Isaev, Leontiev, et al., 2005; Tay et al., 2014) and can be referred to **flow stage III** in Fig. 2-6c. An overview of the vortices and the conceptual diagram are shown in Fig. 2-11.

   As a side note, another proposed mechanism that somehow built upon similar flow topology as TLT has been called **Ball-bearing**. The ball-bearing hypothesis states that the vortices inside the dimples exhibit a similar effect as a ball bearing that reduces the skin friction. However, only one literature supports this mechanism (Wüst, 2004), and the article did not elaborate on how vortex activity can be linked to the working mechanism of ball-bearing. Due to the limited sources and the lack of a tenable mechanism explanation, the author of this report decided not to include this hypothesis as the proposed mechanism.

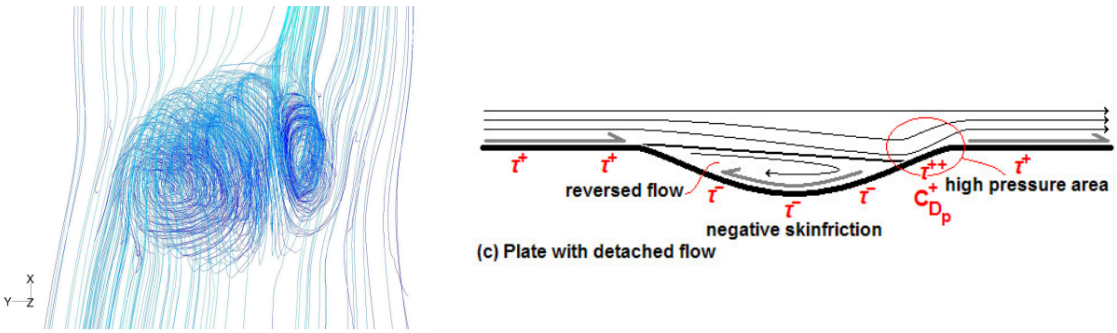

Figure 2-11: Left: path lines from a LES simulation. Right: conceptual diagram for TLT mechanism. (Vervoort, 2009).

2. **Relaminarization.**

   Proposed by Cary Jr. et al. (1980), this theory is based on a balance between the reduction in skin-friction drag and the increase in form drag. When the flow developed over the dimple, regions of favorable and adverse pressure gradients formed. In the favorable pressure gradient region, the flow is re-laminarized and thus reduces the wall shear stress in the subsequent adverse pressure gradient region, resulting in smaller skin

friction. On the other hand, the pressure drag is increased in the dimple. The total drag then depends on the balance between the developed pressure drag and skin-friction drag. Despite the lack of examination in the skin-friction reduction mechanism, it has been confirmed that the total drag reduction for a dimpled surface is determined by the relative dominance between the pressure drag and skin friction drag, as supported by many investigations (Tay, 2011; van Nesselrooij et al., 2016; van Campenhout et al., 2016; Tay and Lim, 2018).

3. **Spanwise shear.**

This hypothesis was first conceived both independently in 2015 by Tay, Khoo, et al. (2015) and also by van Nesselrooij et al. (2016). It suggests that the dimples form spanwise shear over the surface. It is argued that the drag reduction mechanism is analogous to spanwise oscillating walls, where the spanwise periodic forcing interacts with the hairpin vortices and inhibits the turbulent bursting event, leading to a smaller skin-friction drag. In detail, this theory states that the converger-diffuser flow topology, formed in shallow dimples, exhibits a drag-reducing effect. Specifically, the formation of such flow topology reflects a Stokes layer, which is analogous to spanwise oscillating wall cases, altering the turbulent coherent structure. For the experiment evidence,Tay, Khoo, et al. (2015) performed experiments in a turbulent channel flow at moderate Reynolds number and found that the dimple introduces streamwise vorticity into the flow, which generates spanwise flow components in the near-wall region. They further discovered that the energy cascade is suppressed and thus the flow is stabilized. On the other hand, van Nesselrooij et al. (2016) conducted experiments in a wall-bounded turbulent flow and also obtained positive results, with converger-diffuser flow topology presented. In an attempt to explain the origin of such drag reduction, they further performed a RANS simulation to compare the results. The RANS simulation suggested that the small scale turbulence plays a major role in determining the dimple performance since the RANS case exhibited a drag increase while experiments showed a drag reduction (using similar dimple parameters). An overview of the findings from Tay, Khoo, et al. (2015) and van Nesselrooij et al. (2016) are shown in Fig. 2-12.

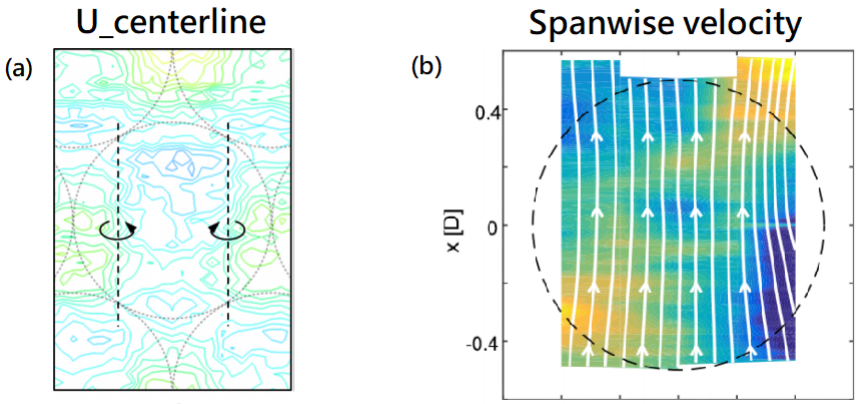

Figure 2-12: (a) Centerline velocity contour and streamwise vorticity. (Tay, Khoo, et al., 2015) (b) converger-diffuser flow patterns. (van Nesselrooij et al., 2016)

To shed lights on the working principle of the spanwise oscillating wall and its connection to flow over dimples, an overview of the working mechanism for the oscillating wall will be given below.

Working mechanism of an oscillating wall.
Choi et al. (1998) found that when applying spanwise wall oscillation, the generated shear layer could be approximated by the laminar solution of the Stokes second problem. The coincidence between the laminar solution and the turbulent spanwise flow components have also been confirmed by Quadrio and Sibilla (2000) and Choi (2002). This similarity suggests two scaling parameters based on the stokes solution. Choi (2002) then conceived two parameters to scale the drag reduction: maximum wall velocity and wall oscillating period. Following the work by Choi (2002), Quadrio and Ricco (2004) performed DNS of a turbulent channel flow with different maximum wall velocity and oscillating period and projected the drag reduction results onto wall velocity-oscillating period diagram. The result is shown in Fig. 2-13. Quadrio and Ricco found that there exists an optimum period of $T^+ \approx 120$. They argued that the optimum period could be attributed to the thickness of the Stokes layer, and thus the time scale that maximizes the interaction between the oscillating wall and the small scale turbulent structures. This time scale conjecture could also explain why the performance drops at extremely large T^+. Particularly, at large T^+, the turbulent structures have enough time to readjust their dynamics between each wall sweep, allowing the turbulence to reach new equilibrium, restoring the unperturbed state. Also for the small T^+, by the time the turbulent eddy interacts with the stoke layers, it has already been advected downstream. Thus, the transient stoke layers do not have enough time to influence the turbulent structures.

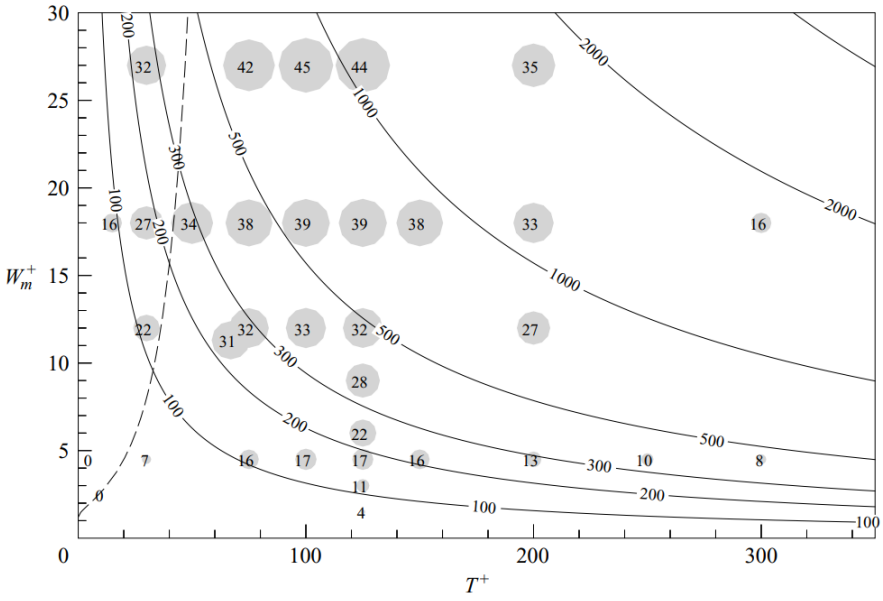

Figure 2-13: Drag reduction in Power saving ratios. X-axis is the non-dimensional oscillating period; and Y-axis is the maximum wall velocity. (Quadrio and Ricco, 2004)

Besides the qualitative explanation by Choi (2002); Quadrio and Ricco (2004), Yakeno et al. (2014) depicted a quantitative picture about how the transient stokes layer affect turbulence structures by performing the so-called FIK identity with Direct Numerical Simulation. They discovered that the Q2 event, which is represented by low-speed fluid moving away from the wall, is suppressed significantly at certain oscillating phases, leading to a smaller Reynolds stress. They concluded that the spanwise wall oscillation reduces the strength of the quasi-streamwise vortices by transient shear layer counteracting the quasi-streamwise vortex. When the shear layer counteracts the quasi-streamwise vortex, the vortex is weakened, and the ejection and sweep events are also inhibited, as shown in Fig. 2-14. Upon the quantitative study, Ricco et al. (2012) computed enstrophy balances and found that the wall oscillation leads to additional enstrophy production. These findings suggested that the small scale turbulence is suppressed.

All in all, the author of this report believes this is by far the most promising hypothesis in explaining dimple drag reduction. The reason is that the theory for the oscillating wall is well-established, and dimple experiments having positive results all showed converger-diffuser flow patterns. Besides the flow topology, another important piece of evidence from the DUT PIV experiments by van Campenhout et al. (2018) suggests a close connection to the theory of spanwise wall oscillation. Specifically, they divided the dimpled surfaces into three regions, as shown in Fig. 2-15. Based on the measured flow characteristics and stoke's solution, they computed the corresponding scaling parameters of the spanwise oscillating wall, and deduced a drag reduction value that closely matched their experimental results, as shown as the red triangle in Fig. 2-15.

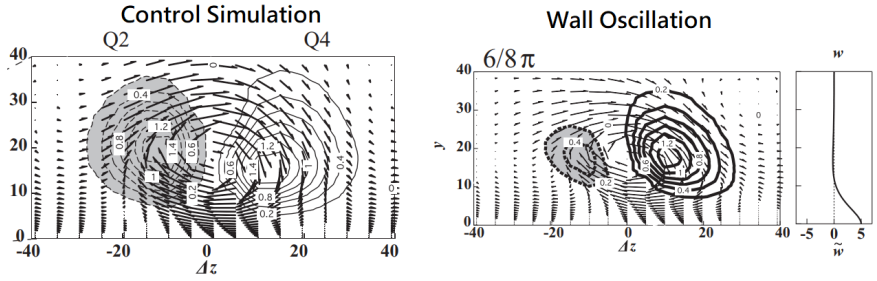

Figure 2-14: The conditionally averaged flow field. Shading represent Q2 and Q4, and quivers indicate conditionally averaged qusai-streamwise vortex. (Yakeno et al., 2014)

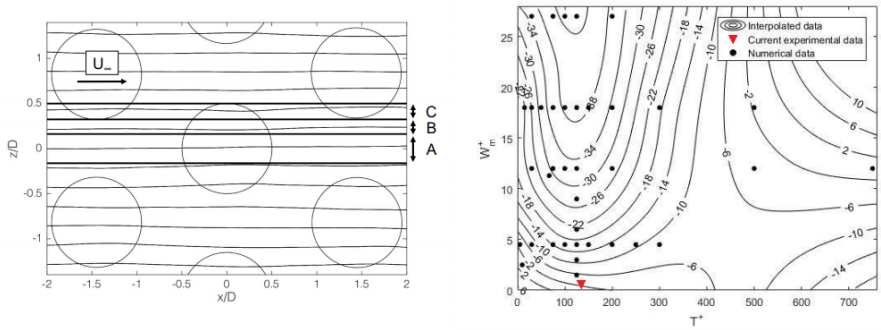

Figure 2-15: Divided dimple regions and predicted drag performance (shown as red triangle) (van Campenhout et al., 2018)

2-2 Turbulent boundary layer flows

2-2-1 Boundary layer fundamental

Inner boundary layer variables

In the near-wall region, the turbulent activity is marginal compared to the upper region and the dynamics are mainly governed by the no-slip wall condition and hence the viscous diffusion. The so-called viscous sublayer thus has a universal behaviour regardless of the condition in the freestream. Specifically, the properties in such layer can be scaled by the friction velocity u^*, which is defined as:

$$u^* = \sqrt{\frac{\tau_w}{\rho}} \tag{2-1}$$

Utilising the friction velocity, inner variables can be derived as:

$$\begin{aligned} u^+ &= u/u^* \\ y^+ &= yu^*/\nu = y/l^+ \end{aligned} \tag{2-2}$$

Where l^+ denotes the viscous length scale. Three distinct regions in the turbulent boundary layer can then be identified:

$$\begin{aligned} 0 \leq y^+ \leq 5 \quad & \text{Viscous sublayer} \quad && u^+ = y^+ \\ 5 \leq y^+ \leq 30 \quad & \text{Buffer layer} && \\ 30 \leq y^+ \leq 350 \quad & \text{Overlap layer} && u^+ = \tfrac{1}{\kappa} \ln y^+ + B \end{aligned} \tag{2-3}$$

As mentioned earlier, the first layer is the viscous sublayer, and the relation is universal. The second layer is the buffer layer, and the turbulence is most active in this layer. The third layer is the overlap layer, where the velocity profile exhibits as a logarithmic function. κ and B depend on the freestream condition like streamwise pressure gradient. For a Zero Pressure Gradient Boundary Layer (ZPGBL), $\kappa \approx 0.41$ and $B \approx 5.0$. An overview of the inner-variable scaled velocity profile is shown in Fig. 2-16. Spalding conceived a single expression which covers these three regions and is an excellent fit until y+ 1000, where the inner-variable scaled profile begins to deviate from the logarithmic curve. The so-called Spalding' s law of the wall is given as:

$$y^+ = u^+ + e^{-\kappa B}\left[e^{\kappa u^+} - 1 - \kappa u^+ - \frac{\left(\kappa u^+\right)^2}{2} - \frac{\left(\kappa u^+\right)^3}{6}\right] \tag{2-4}$$

The deviation above $y + 1000$ is called the wake component and is highly depended on the freestream conditions.

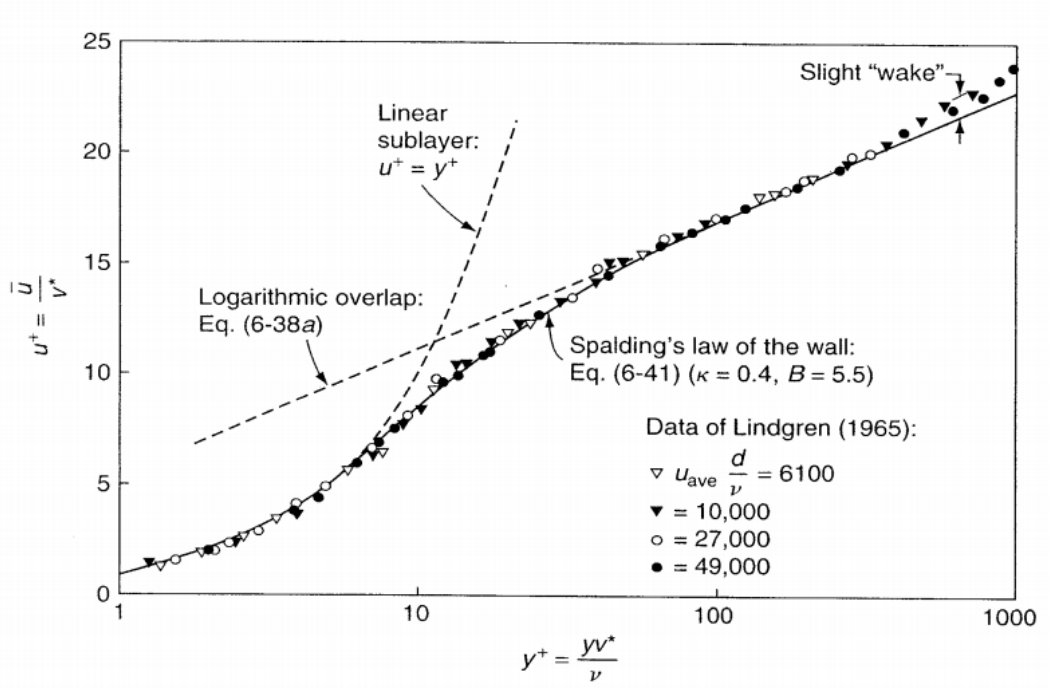

Figure 2-16: Mean velocity profile scaled by inner variables. (White, 2006)

Boundary Layer Profile Properties

Some quantities, which will be used in the later chapter, will be introduced in this section. From the velocity profile, different "thickness" can be defined, based on different physical meanings. The most intuitive one is the boundary layer thickness, defined as the height where the mean velocity equals to $0.99U_\infty$. The displacement thickness δ^* is defined as the total velocity deficit of the boundary layer:

$$\delta^* = \int_0^\infty \left(1 - \frac{u}{U_\infty}\right) dy \tag{2-5}$$

Where U_∞ denotes the freestream velocity, and u is the mean velocity. The displacement thickness can be interpreted as the wall displacement experienced by a fluid parcel in the freestream due to the presence of the boundary layer. With displacement thickness being the deficit of the velocity profile, the underlying deficit of the streamwise momentum can also be deduced through the multiplication between velocity and deficit velocity. This product can be interpreted as the momentum loss carried by the mean flow. Therefore, the integration of the "deficit" flux then gives the so-called momentum thickness θ:

$$\theta = \int_0^\infty \frac{u}{U_\infty}\left(1 - \frac{u}{U_\infty}\right) dy \tag{2-6}$$

Since momentum thickness is a measure of the lost momentum as flow travel downstream, it has a clear connection to the drag production; hence a better indicator of the simulated TBL state. In practice, it is useful to compute the momentum thickness Reynolds number Re_θ and plot the corresponding skin friction to validate the simulated value.

2-2-2 Turbulent coherent structures

Since the 1950s, efforts have been made to reveal the turbulence structures. Even though turbulence exhibits chaotic and fluctuating characteristics, there are certain regions of space and time that possess coherent patterns. Pope (2000) and Nieuwstadt et al. (2016) both give a systematic review of these topics. A synopsis of their publications will be given in the following paragraph.

Low-speed streaks

Flow measurements near the wall indicate regions where the flow velocity is small compared to the surroundings. These so-called "low-speed streaks" were first discovered by Kline et al. (1967). In the water channel experiment by Kline et al. (1967), an array of electrodes were placed in the spanwise direction to generate hydrogen bubbles to visualize the flow field. The results revealed that the structures are confined in the near-wall region, $y^+ < 40$, with long streaks in the streamwise direction. Subsequent studies by Smith and Metzler (1983) further identified the features of the low-speed streaks. They found that at near-wall regions, the spanwise distance between the streaks is between $806\delta_\nu$ and $120\delta_\nu$, and the streamwise length can exceed $10000\delta_\nu$. An overview of the streak structures is shown in Fig. 2-17 from Kline et al. (1967).

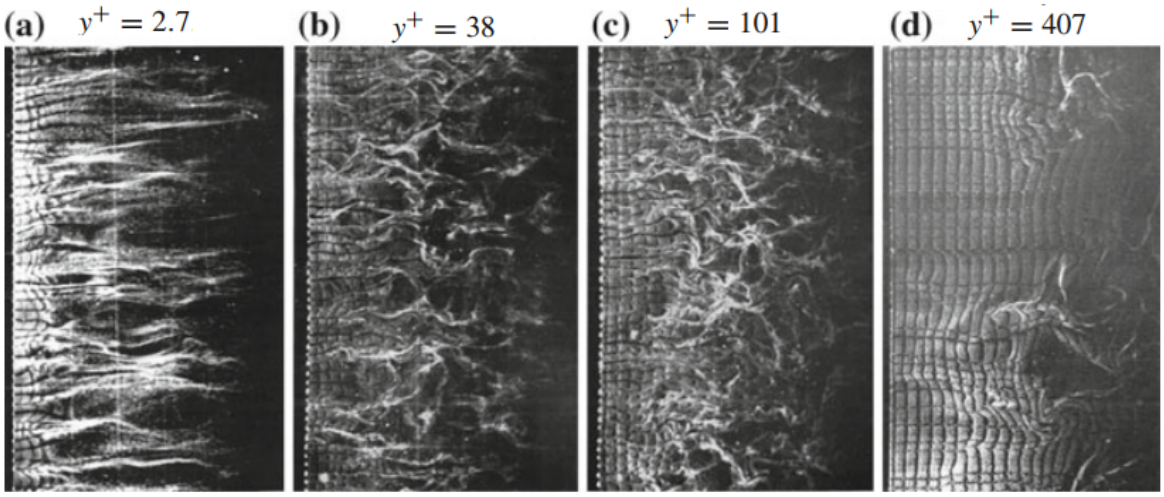

Figure 2-17: Hydrogen bubble visualization of a wall-bounded flow at different wall distance. (Kline et al., 1967).

Hairpin vortices

Hairpin vortices are the horseshoe-like vortices, with two legs pinned at the wall and protruded through boundary layer in both normal and streamwise direction. Hairpin vortices were first identified and modeled by Theodorsen (1952). The presence of hairpin-shaped vortex is closely related to low-speed streaks. Fig. 2-18 gives an overview of the development of hairpin vortices. Since the velocity inside a streak is smaller than the surroundings, mathematically it

leads to lines of vortex sheets at the streak boundaries. The formation of the hairpin vortices can be realized through Fig. 2-18a and Fig. 2-18b. Firstly, the low-speed streak is perturbed by the fluctuating turbulent flow field. The perturbation then becomes unstable through the Kelvin-Helmholtz instability. Then, due to the Kelvin-Helmholtz instability, the vortex sheets roll-up. The instability and roll-up result in concentrated vorticity distribution. Furthermore, such vorticity pattern further influences the vortex structure through self-induced velocity field. As a result, the tips of the vortex moves away from the wall and into a higher flow speed region. At the moment, the vortex structure is stretched along the streamwise direction with 45°-line relative to the wall. The final result is an elongated vortex called hairpin vortex. These vortices have been observed in both numerical studies (Wu et al., 2009) as well as experimental studies (Adrian et al., 2000; Elsinga et al., 2007), as shown in Fig. 2-19a, for instance.

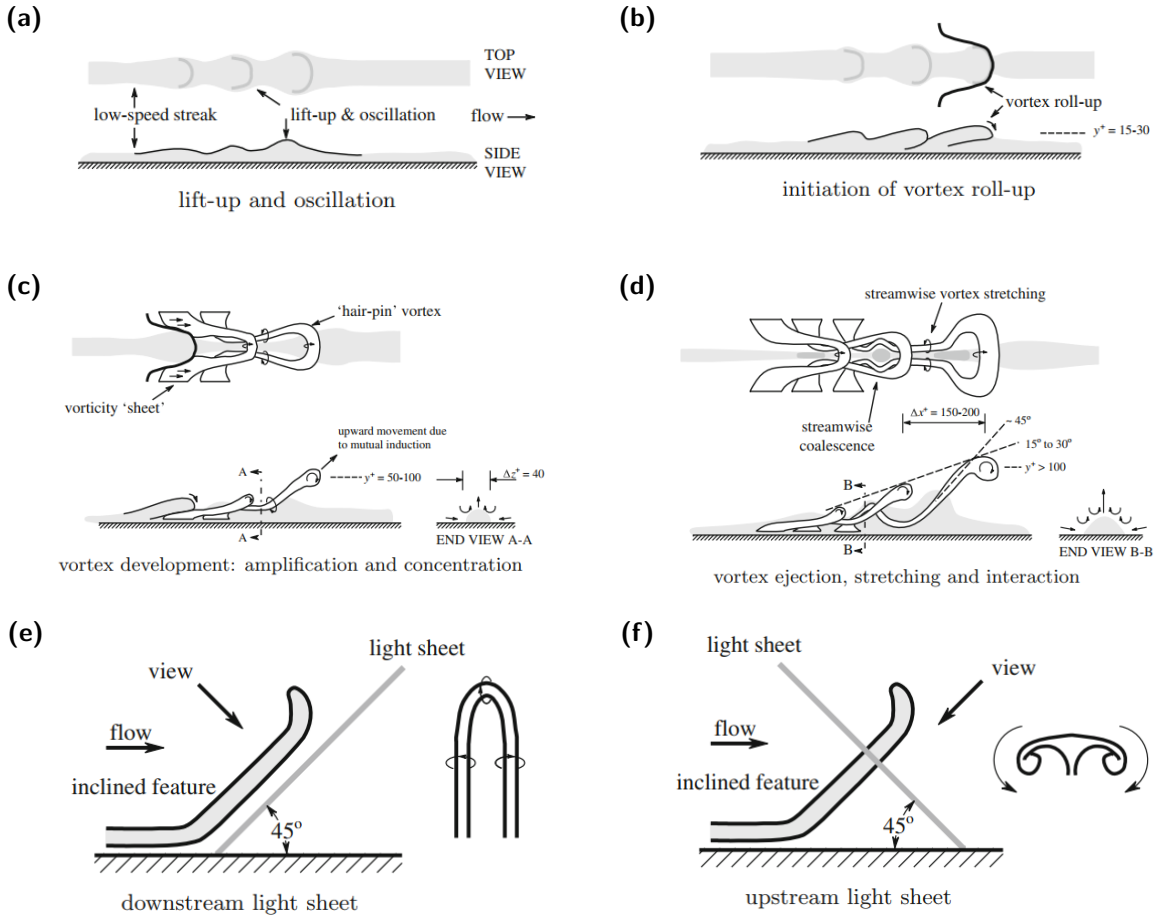

Figure 2-18: The development of Hairpin vortices according to Smith (1984). (Nieuwstadt et al., 2016)

Ejections and sweeps

As stated in the previous section, when the tips of the vortex move into a higher flow speed region, it is stretched. During the stretching process, the vorticity increases. At a certain

moment, the vorticity strength has increased too much that it becomes unstable and the low-speed streak will move rapidly away from the wall, eventually breaking down into finer structures. Kline et al. called such uplifting and the subsequent burst response "ejection event". When ejection occurs, continuity still needs to be satisfied, and thus the near-wall fluid is replaced by high-speed fluid that moves towards the wall. Corino et al. (1969) referred this flow impingement as "sweep event". Physically, the sweep and ejection events lead to turbulent kinetic energy production. Recall that

$$P = -\langle u'v' \rangle \frac{\partial \langle U \rangle}{\partial y} \tag{2-7}$$

where P represents the TKE production term. For the ejection event, the fluid that moves slower than the mean velocity ($u' < 0$) moves away from the wall ($v' > 0$), and thus the production term is positive. Similarly, for the sweep event, fluid that moves faster than the mean velocity ($u' > 0$) impinging the wall ($v' < 0$). The u' and v' components can be further sampled onto u-v plane, as shown in Fig. 2-19b. In quadrant 2 and 4, the uv product is negative and thus contribute to positive production of TKE. Various measurements (Willmarth et al., 1972; Wallace, 2016) have confirmed the importance of ejections and sweeps to production. These investigations suggested that the TKE production near the wall is mainly contributed by the quadrant 2 and 4 events that are relatively violent, occur intermittently and have a short duration, corresponding to the ejections and sweeps.

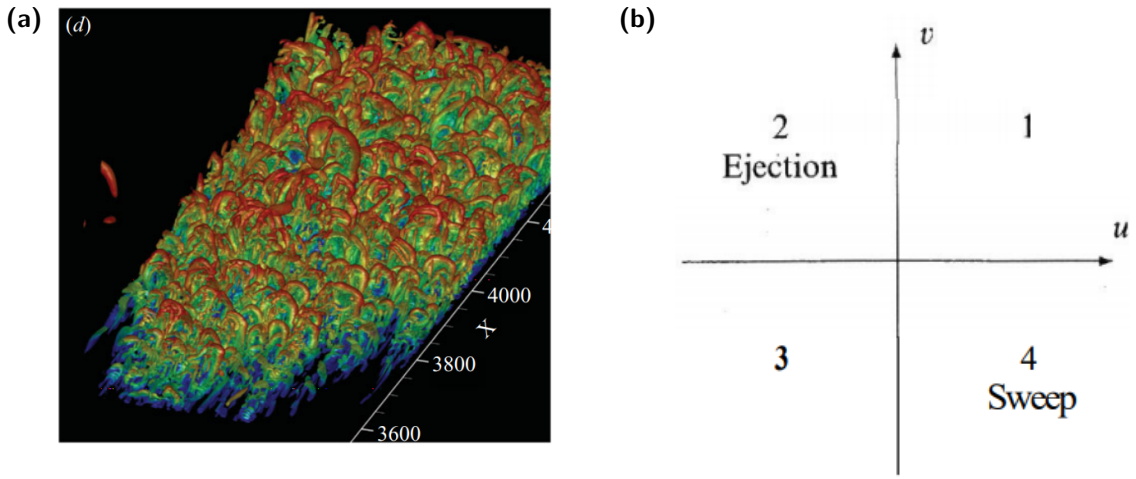

Figure 2-19: (a) Vortex structures from a Direct Numerical Simulations of a zero pressure gradient turbulent boundary layer. (Wu et al., 2009). (b) u-v sample plane, indicating the numbering of the four quadrants. (Pope, 2000).

Quasi-streamwise vortices

Bakewell et al. (1967) found pairs of counter-rotating vortices in $y^+ \leq 10$ region, and they also observed that the vortices are tilted from the streamwise direction. They called these vortices as quasi-streamwise vortices. In a DNS study that attempts to test different methods to detect near-wall vortical structures, Kasagi et al. (1995) found that regions where intense turbulent kinetic energy production occurred lies on both sides of the quasi-streamwise vortices. The

founding suggests that ejection and sweep events are inherently linked to the quasi-streamwise vortices. Fig. 2-20 illustrates the vortices and two events by Piomelli (2001).

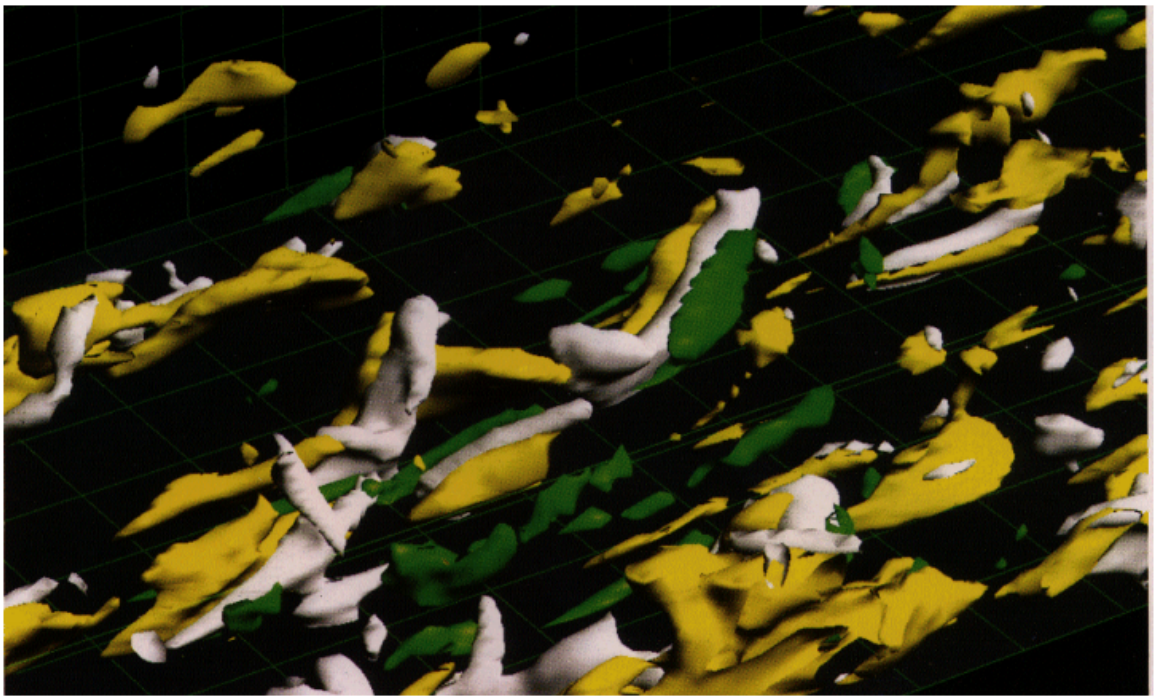

Figure 2-20: Ejections (yellow) and sweeps (green) with qusai-streamwise vortical structures (white). (Piomelli, 2001)

Very Large Scale Motions

The Very Large Scale Motion (VLSM) is a region of meandering positive and negative streamwise velocity fluctuations that spans a very long streamwise extent. This coherent structure is first proposed by Hutchins et al. (2007) and later by Dennis (2015), whom named such structures as "superstructures". These structures can be found in the logarithmic and lower wake region. Fig. 2-21 shows the structure of a VLSM from Hutchins et al. (2007).

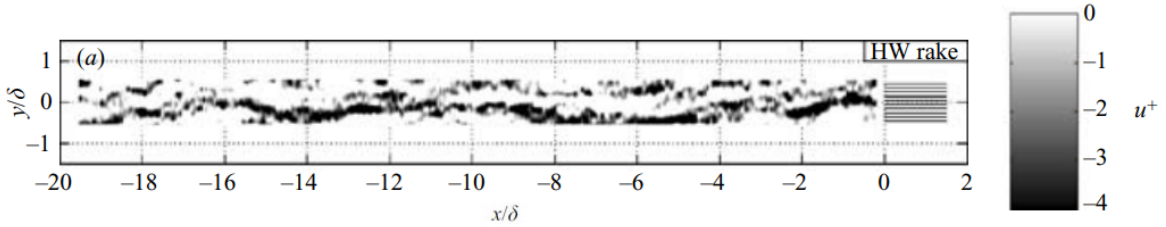

Figure 2-21: Hot wire rake measurement for $Re = 14,380$. Freestream direction is pointed towards positive x-axis. (Hutchins et al., 2007)

2-3 Relevant theory

2-3-1 Biot-Savart law

Biot-Savart law tells us how a volume of vorticity spanned in the space induces the velocity field. The induced velocity $\vec{u_\omega}$ at a point x_p by an arbitrary volume of vorticity $\omega(x, y, z)$ can be expressed as:

$$\vec{u_\omega} = \frac{1}{4\pi} \int_V \frac{\vec{\omega} \times \vec{r}}{|r^3|} \mathrm{dV} \tag{2-8}$$

If the vorticity is concentrated along a curve from point a to point b with a constant circulation Γ, then the induced velocity can be simplified as:

$$\vec{u_\omega} = \frac{\Gamma}{4\pi} \int_a^b \frac{\vec{\mathrm{dl}} \times \vec{r}}{|r^3|} \tag{2-9}$$

From the above expression, it is found that the induced velocity can be qualitatively realised using the right-hand rule, where the right thumb points in the direction of vorticity, and the fingers curling along the orientation of the bounding curve indicates the induced velocity vector. An overview of the induced velocity is shown in Fig. 2-22

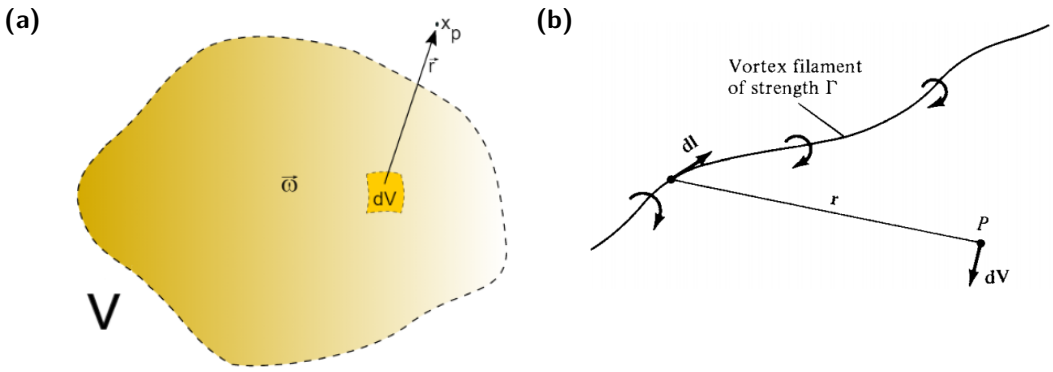

Figure 2-22: Illustration of the Biot-Savart law. (a) An arbitrary volume of vorticity (Ferreira, 2018). (b) An arbitrary vortex filament. (Anderson, 2011)

Chapter 3

Methodology

In this chapter, the realisation of the simulation and data analysis shall be summarised. This chapter's structure is split into three sections: formulation of the flow problem and simulations, relevant numerical methods, and data analysis. Firstly, the parameters of the dimple plate and the mesh settings and boundary conditions will be given along with a short discussion of the flow problem. After characterising simulation settings, a brief introduction to some numerical techniques that penitent to the current project will be covered. Lastly, an overview of the statistical technique is presented.

3-1 Formulation of the flow problem

3-1-1 Governing equations

The target of interest of the current project is in the regime of the low-speed aerodynamics. Hence, the flow problem can be approximated as incompressible flow. In the incompressible regime without any heat-transfer in the system, the governing equations of a Newtonian fluid with dynamic viscosity μ read:

$$\nabla \cdot \boldsymbol{u} = 0 \tag{3-1}$$

$$\rho \frac{\partial \boldsymbol{u}}{\partial t} + \rho(\boldsymbol{u} \cdot \nabla)\boldsymbol{u} = -\nabla p + \mu \nabla^2 \boldsymbol{u} \tag{3-2}$$

Where ρ represents the density field, p represents the pressure field and $\boldsymbol{u}$ denotes the velocity vector field (u, v, w). For the present case, u is taken as streamwise velocity, v is vertical velocity and w stands for spanwise velocity. Present simulations have been performed using TU Delft in-house solver, INCA (Hickel, Egerer, et al., 2014). The Navier-Stokes equations are non-dimensionalized in the solver. The reference scales for the above system of equation are the length scale L_{ref}, velocity scale U_{ref} and the density scale ρ_{ref}. Consequently variables can be expressed in non-dimensional form:

$$p = p^* \rho_{ref} U_{ref}^2 \quad , \quad \rho = \rho^* \rho_{ref} \quad , \quad t = t^* \frac{L_{ref}}{U_{ref}} \quad \text{and} \quad u = u^* U_{ref} \tag{3-3}$$

The non-dimensionalized system of equation then reads:

$$\begin{aligned} \nabla^* \cdot \boldsymbol{u}^* &= 0 \\ \frac{\partial \boldsymbol{u}^*}{\partial t^*} + (\boldsymbol{u}^* \cdot \nabla^*)\, \boldsymbol{u}^* &= -\nabla^* p^* + \frac{1}{Re} \nabla^{*2} \boldsymbol{u}^* \end{aligned} \tag{3-4}$$

Where the superscript $*$ denotes the non-denationalised quantity. For the present case, the reference scales are based on inflow boundary layer thickness and freestream velocity, and are all set to 1. The exact value of the inflow boundary layer thickness, δ_0, and the freestream velocity, U_∞, can then be retrieved from the input freestream Reynolds number. The Reynolds number is set to match the experiment inflow from van Nesselrooij et al. (2016); van Campenhout et al. (2016) and is equals to $16,500$ at the domain inlet. As such, after the inflow adjustment region, the inflow Reynolds number is about $20,000$. With an inlet boundary thickness of $10mm$, the freestream velocity is about $24.7ms^{-1}$. Also, the inflow turbulent intensity I is set to 0.7% to match the experiment value. Tbl. 3-1 summarises the prescribed freestream conditions.

δ_0[mm]	$U_\infty[ms^{-1}]$	$Re_{\delta_{inlet}}$[-]	I[-]
10	24.7	16500	0.7%

Table 3-1: Overview of the freestream conditions.

3-1-2 Simulation set-up

Dimple geometry

An overview of the dimple design parameters can be found in Fig. 3-1. The dimple design follows the configuration from van Nesselrooij et al. (2016); van Campenhout et al. (2016): a staggered arrangement of shallow, round-edged spherical dimples with the depth ratio $d/D = 2.5\%$. For each dimple, the diameter D is $20mm$. The edge-rounding radius r is 0.5. The dimple density on a plate is 33% and the resulting streamwise spacing L_x and spanwise spacing L_z between each dimple is thus $57.18mm$ and $33mm$, respectively. Tbl. 3-1 summarises the design parameters of the staggered dimple plate.

Numerical set-up and grid topology

The computational domain considered in this study is depicted in Fig. 3-2. The length is scaled by the inlet boundary layer thickness δ_0 of $10mm$. The horizontal domain extent is $-12 \leq$

Config.	D[mm]	d/D[-]	**r**[mm]	L_x[mm]	L_z[mm]
Staggered	20	2.5%	0.5	57.18	33

Table 3-2: Overview of the dimple parameters.

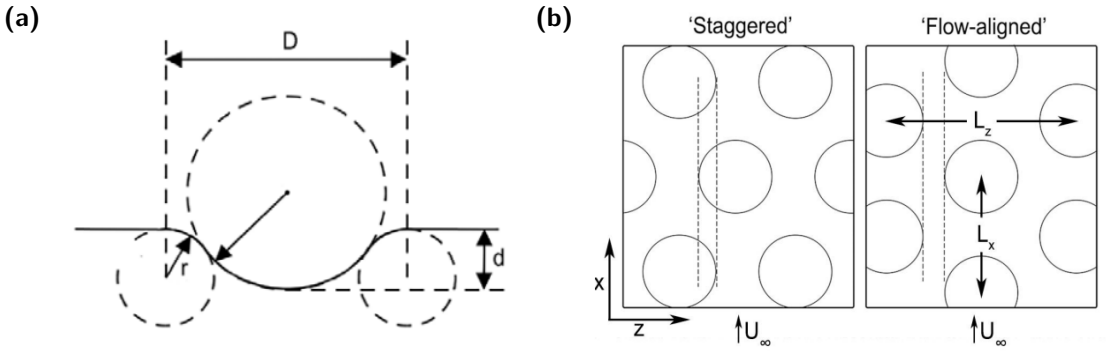

Figure 3-1: Specification of the dimple plate. (a) Dimple parameters (Tay, 2011). (b) Dimple arrangement (van Campenhout et al., 2016).

$x/\delta_0 \leq 34.5$ in the streamwise direction and $-1.65 \leq z/\delta_0 \leq 1.65$ in the spanwise direction. The vertical domain extent is $-0.05 \leq y/\delta_0 \leq 6$. The freestream direction is pointed towards the positive streamwise direction. The recycling-rescaling technique is employed to simulate the turbulent inflow condition. The detail will be presented in the later section. The shaded area, $([-12, 0], [:], [:])$, denotes the inflow recycling module. In the inflow recycling module, the rescaled-recycled profiles are adjusting and developing into a physical turbulent inflow profile. The data collected in this region will thus be discarded.

The inflow is initialised using the DNS data from Spalart (1988), with a momentum thickness

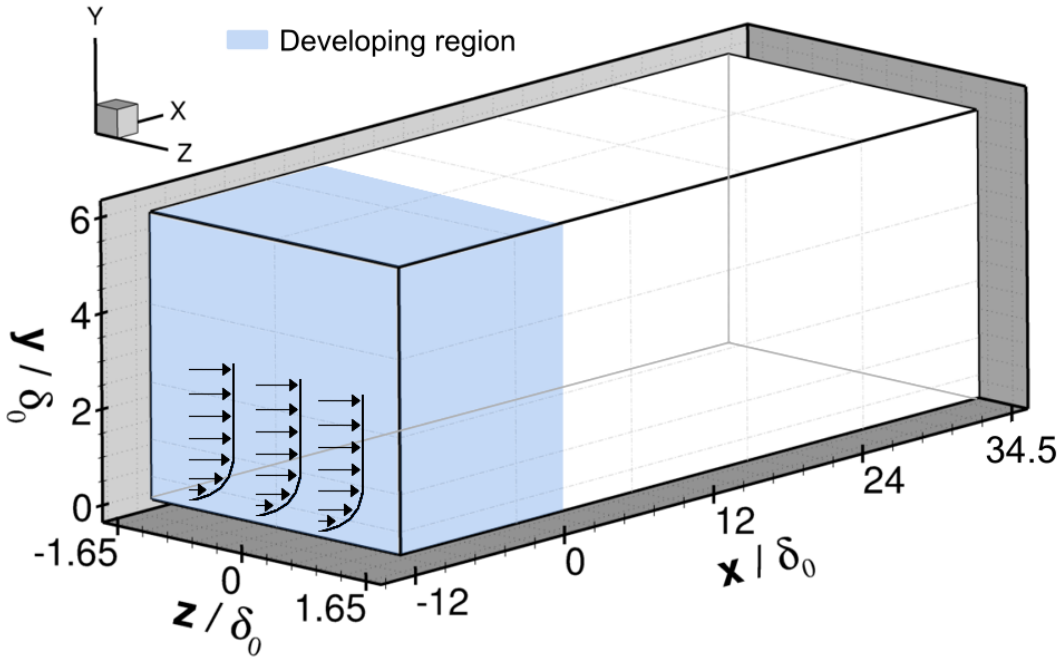

Figure 3-2: Sketch of the computational domain (axes drawn not to scale). The coloured shading denotes the inflow recycling module. The recycled profiles need certain extents to develop before reaching a physical turbulent inflow. The data collected in this region will thus be discarded.

based Reynolds number Re_θ of $1,410$. The total pressure is fixed at the outlet. Spanwise periodicity is imposed in the spanwise direction. No-slip condition is imposed on the lower boundary. No wall model is applied. The decay condition is imposed on the upper boundary. Due to the limited computational resources, current study performs Implicit Large Eddy Simulation (ILES), rather than Direct Numerical Simulation (DNS). The spatial discretisation is based on Weighted Essentially Non-Oscillatory (WENO) schemes with Simplified Adaptive Local deconvolution (SALD) method (Hickel and Adams, 2007). The Pressure Poisson Equation (PPE) is solved by stabilized bi-conjugate gradient (BiCGstab) method (Vorst, 1992). The equation is marched in time using the third order explicit Runge-Kutta scheme (Shu, 1988). The time-step is adapted according to a explicitly specified Courant-Friedrichs-Lwey (CFL) condition. Present simulation sets CFL = 1. Since the computational domain is relatively shallow, a sponge layer is applied near the upper boundary to damp out the perturbation.

For the meshing and plate geometry, a top-view of the dimple pattern and the meshing is shown in Fig. 3-3. The plate is placed such that the smooth region is at the level $y/\delta_0 = 0$. The computational domain is divided into 960 blocks and contains 2.26×10^8 structured cells (including ghost cells). The horizontal grid is uniform, with the streamwise spacing, Δx, being 2x larger than the spanwise spacing, Δz. In the vertical direction, hyperbolic refinement towards the wall is implemented. Below the $y/\delta_0 = 0$, an uniform vertical spacing is adapted to ensure sufficient wall y^+ across the dimple surface. Fig. 3-3(b) shows the top-view and lateral-view of the meshing around the dimple. The computational domain and grid spacings are summarised in Tbl. 3-3. The grid spacing is compared with the guideline values from Bannier et al. (2015), shown in Tbl. 3-4. It can be found that current mesh is refined enough and fall below the range of typical LES set-up.

Output data specification

During the simulation, three types of output data are generated: mean statistics, snapshots and probe data. Mean statistics are collected after the initial transient is washed-out from the domain. The statistics are then collected over two flow-through cycles. The snapshots are also generated for every 50 time steps after the initial transient is washed-out. However, they are collected only for one flow-through cycle due to the limited storage. In total, 241 and 273 snapshots are generated for the smooth plate and dimple plate case, respectively. Two simulation cases together generate almost 20 TB data. Lastly, the probe data is collected for every time steps, but with the limited spatial resolution. Total probe numbers are 675 and 720 for the smooth plate and dimple plate, respectively. Probes are placed around the $3rd$ dimple at three normalised vertical level, $y_{wd}/\delta_0 = 0.01, 0.02, 0.2$. The probe arrangement is shown in Fig. 3-4.

$(N_X,\ N_Z,\ N_Y)$	L_X/δ_0	L_Z/δ_0	L_Y/δ_0	Δx	Δz	Δy_{min}	Δy_{max}
$1824 \times 250 \times 300$	46.5	3.3	6.05	0.0254	0.0132	0.00085	0.057

Table 3-3: Overview of the domain sizes and cell spacing.

	Δx^+	Δz^+	Δy^+_{wall}
LES guideline	$30 \rightarrow 60$	$12 \rightarrow 25$	$0.3 \rightarrow 1$
Present ILES	**17.84**	**8.92**	**0.73**
DNS guideline	$6 \rightarrow 12$	$3 \rightarrow 6$	$0.3 \rightarrow 1$

Table 3-4: Current cell spacing compared with standard LESs and DNSs. Computed at the wall and at $x/\delta_0 = 0$.

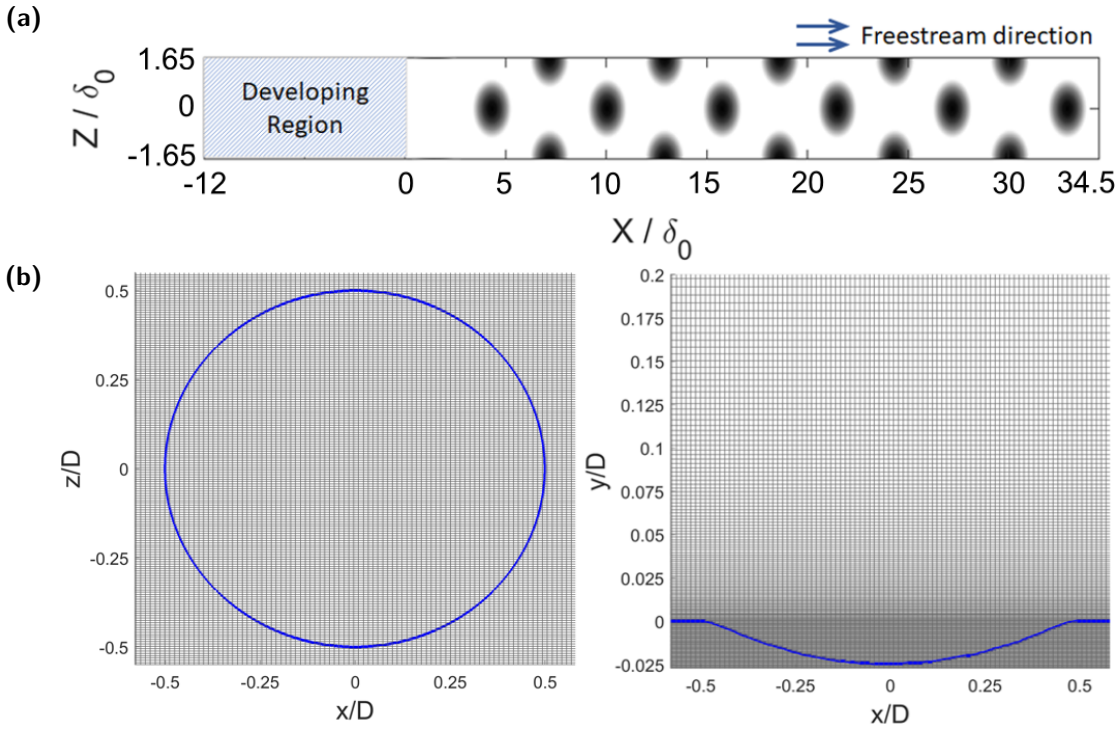

Figure 3-3: Dimple pattern and grid topology. (a) Top-view of the computational domain and the staggered dimple arrangement. (b) Top-view and lateral view of the mesh around a dimple. Blue line marks the dimple geometry.

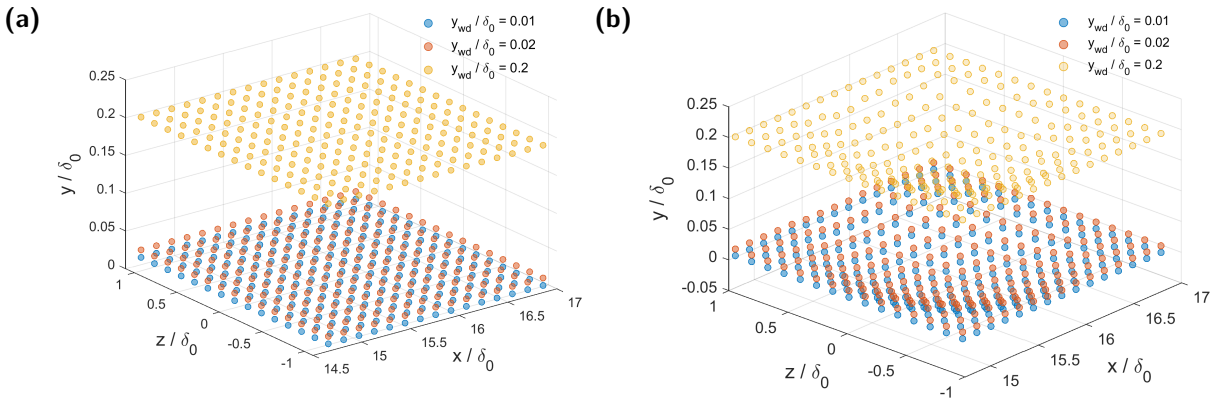

Figure 3-4: Probe placement around the $3rd$ dimple. (a) Smooth plate. (b) Dimple plate.

3-2 Relevant numerical methods

3-2-1 Immersed boundary method

The immersed boundary method is an approach to represent the effect of any arbitrary body in the simulation. This method is developed by Peskin (1972) to simulate the cardiac blood flow. One advantage of using such a method is that the grid generation is straightforward since the body does not have to conform to a Cartesian grid. As the grid does not necessarily conform to the body boundary, the governing equation in the vicinity of the boundary needs to be modified to include boundary conditions. In the present project, the solver uses a so-called cut-cell approach to represent the effect of the body boundary. A brief introduction will be given in the following paragraph.

Firstly, the level-set criteria of the geometry interface are computed at the beginning of the computation for a non-moving body. Mesh cells that are intersected by the immersed boundary are then identified. These cells are marked as cut-cells. An illustration of a cut-cell is shown in Fig. 3-5(a). With the level-set, the aperture, A_i, at each cut-cell face and volume fraction, $\alpha_{i,j,k}$, inside the fluid can be calculated. Next, the cut-cell face fluxes are scaled with the face apertures to maintain the finite-volume formulation. At the interface, $\Gamma_{i,j,k}$, the no-slip B.C. and the Neumann condition for pressure are imposed on the corresponding cell face. The cut-cell method usually generates some cells with a very small volume fraction, which could lead to numerical instability. To address this issue, fluid from small cut-cells whose $\alpha_{i,j,k} < 0.5$ is mixed with the fluid in the neighbouring cells. In two dimensional problem, three neighbouring target cells are mixed with small cut-cell, shown in Fig. 3-5(b). An overview of this cut-cell method can be found in Hu et al. (2006) and Meyer et al. (2010).

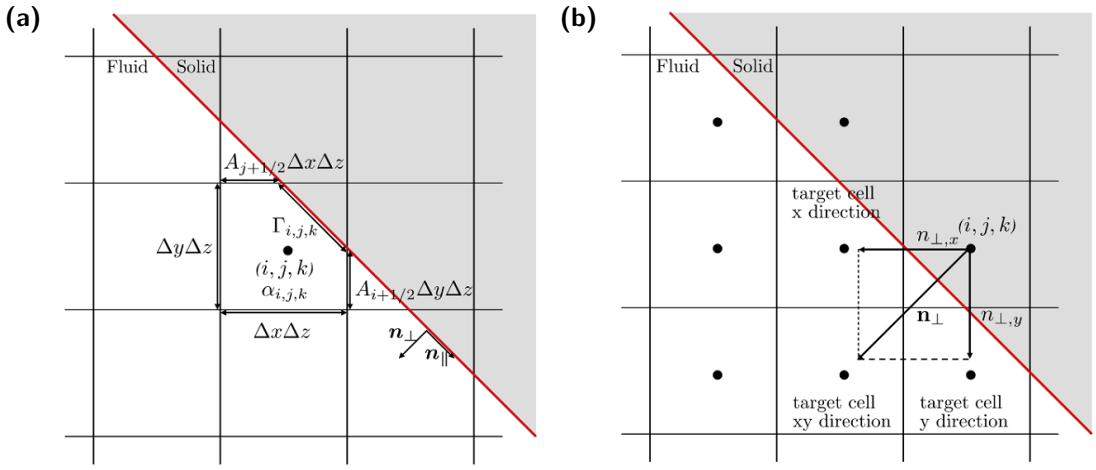

Figure 3-5: (a) Overview of a cut-cell. (b) The target cells to mix the small cut-cell fluid for a 2D problem. (Meyer et al., 2010)

3-2-2 Turbulent inflow generator

The prescription of correct and physical inflow boundary conditions is critical to achieve a realistic flow. For steady RANS, one could specify the mean velocity and the perturbation field. However,for LES and DNS simulations, an instantaneous, physical inflow profile is needed to represent the turbulence in the inflow boundary. Intuitively, one could impose a laminar inflow B.C. and simulate the natural transition to achieve a realistic turbulent inflow. However, the required amount of computational power would be prohibitively large. If we are not interested in transition problem, the best practice is to seek more economical methods. In this thesis project, we will use the rescaling/recycling technique. An overview of this approach shall be given below.

Recycling inflow means the inflow B.C. is computed from a reference turbulent profile. This reference profile could be derived in two ways. One is from a precursor simulation where it provides accurate boundary conditions to the primary simulation. The other way is to extract and rescale the turbulent profiles on an arbitrary downstream plane on the fly. This method is first proposed by Lund et al. (1998) and has been implemented with various algorithms. In this survey, we present the implementation in the INCA solver. In this case, the turbulent profile at the source station is decomposed into mean and fluctuating parts. Then, the scaling is applied directly to the entire profile. Specifically, the flow field is first decomposed into mean and fluctuating parts:

$$u_i(x, y, z, t) = U_i(x, y) + u^{'}(x, y, z, t) \tag{3-5}$$

where the mean flow is assumed to be homogenoues in spanwise direction. Then, a rescaling factor γ is computed based on the ratio of friction velocity in the inflow and source plane

$$\gamma = \frac{u_{\tau,i}}{u_{\tau,s}} \tag{3-6}$$

where the subscript i is the inlet plane; s is the source plane. The fluctuating parts is then rescaled according to γ. The final inflow profile will be the mean flow from the specified inlet inflow profile superimposed with the rescaled fluctuation profile. For the present case, the mean flow is the DNS data from Spalart (1988), with a momentum thickness based Reynolds number Re_θ of $1,410$. This method essentially represents a "modified Spalart method" in a sense that it does not apply a coordinate transformation (Lund et al., 1998). Moreover, recycling inflow method implies a "pseudo-periodic" approach: the recycling information will feed to inflow plane, but the info in the outflow plane will not affect inflow conditions. In practice, the rescaled profile might not reach physical turbulence in the first place, and a developing region is needed to allow the flow to adjust and reach quasi-equilibrium. The adaption length then depends on the external condition, initial conditions and discretisation method. Therefore, a sensitivity test is needed to determine a proper adaption length to model a realistic turbulent inflow B.C. This analysis will be given in the Chap. 4-1-2.

3-3 Data analysis methods

3-3-1 Quadrant Analysis

In this section, the quadrant analysis and its extended method will be reviewed. Quadrant analysis decomposes the Reynolds stress $\overline{u'v'}$ into four quadrants according to the signs of the streamwise and wall-normal velocity, and provides quantitative information on the TKE production. This analysis was first conducted by Wallace et al. (1972). They performed hot-film measurements of an oil channel flow and classified the products of measured $\overline{u'v'}$ into four groups: Q1$(+u', +v')$, Q2$(-u', +v')$, Q3$(-u', -v')$, and Q4$(+u', -v')$. Clearly, Q2 and Q4 correspond to the ejection and sweep events that stated in Section. 2-2-2. Wallace et al. (1972) further sampled the data to compute the relative contribution of each quadrant to the Reynolds stress at different y^+, as shown in Fig. 3-6. At a fixed wall-normal location, the sum of the contributions of all quadrant is unity. At the near-wall region, Q4 contributes more to the shear stress than Q2 does, while away from the wall, the contribution is reversed.

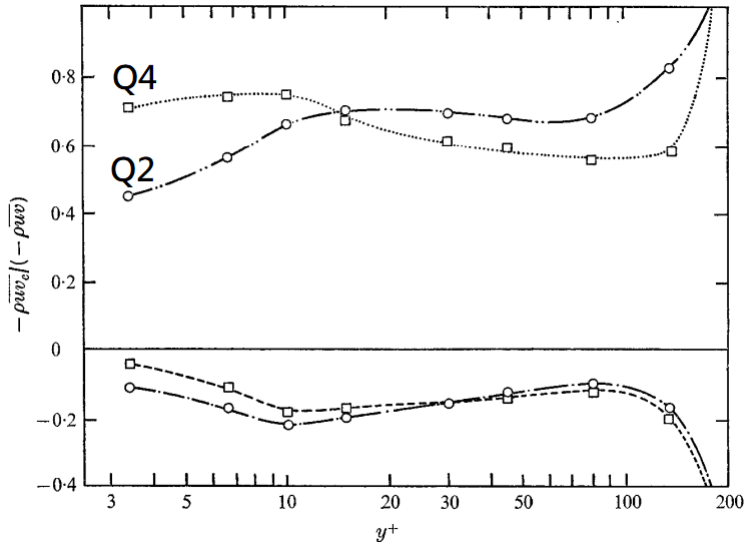

Figure 3-6: Relative contribution of each quadrant to the Reynolds stress.(Wallace et al., 1972)

The Reynolds shear stress $\overline{u'v'}$ can also be expressed by the integration of Joint Probability Density Function (JPDF) of the velocity fluctuations

$$\overline{u'v'} = \int_{-\infty}^{\infty} u'v'P(u', v')du'dv' \tag{3-7}$$

where $P(u', v')$ represents the JPDF of u' and v'. Wallace et al. (1972) used the channel flow data from Brodkey et al. (1974) to compute the JPDF at a various wall-normal location. They found that Q2 and Q4 mainly contribute to the Reynolds shear stress, as the major axis of the JPDF is tilted along Q2 and Q4 direction. Besides JPDF, the weighted JPDF (that is, the integrand $u'v'P(u', v')$) can also be computed, and it gives the locations of the peak values, which tells us the values of (u', v') that contribute most to the Reynolds stress at certain wall-normal location. An illustration of JPDF and weighted JPDF (covariance integrand) are shown in Fig. 3-7 for reference.

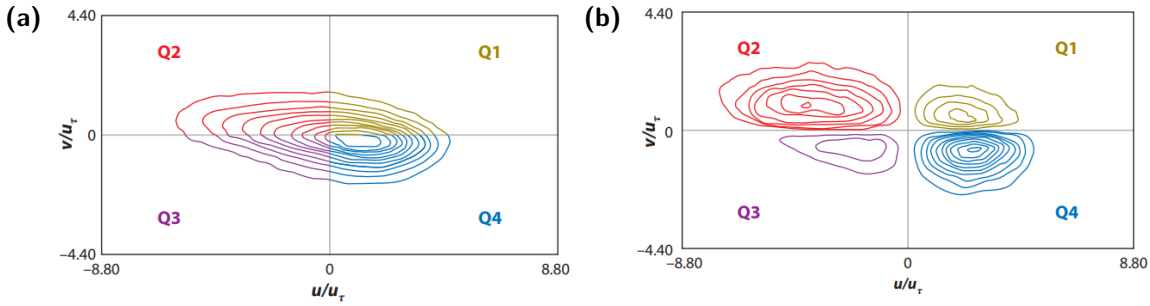

Figure 3-7: (a) Joint Probability Distribution Function (JPDF) at $y^+ = 45$. (b) Weighted JPDF at $y^+ = 45$. (Wallace et al., 1977)

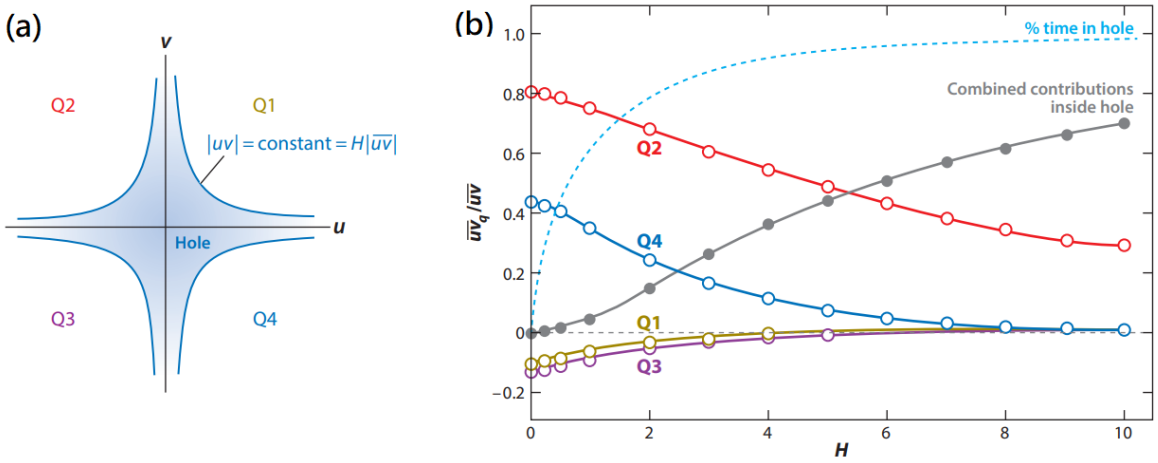

Figure 3-8: Quadrant analysis with hole filtering of Willmarth et al. (1972). Diagrams from Wallace (2016).

In an attempt to investigate intense burst events, Willmarth et al. (1972) conceived a conditional sampling method to filter the quadrant. They filtered out the signal by a hyperbola criterion H in each quadrant. That is, only the data points that their $u'v'$ product are outside of what they called the hole, $|u'v'| \geq H\left|\overline{u'v'}\right|$, are kept. Fig. 3-8 gives an example of extended quadrant analysis from Wallace (2016). With the hole filtering technique, the percentage of time of the events with certain strength can be computed. Fig. 3-8(b) shows the Reynolds shear stress at $y^+ = 30$ for a channel flow with $Re_\tau \approx 1820$, as a function of the filter threshold, H. For H = 5, Q1 and Q3 contribute almost none to the Reynolds stress. Approximately 50% of the Q2 data lie outside of the hole, but these intense events only occur $\approx 10\%$ of the sampling time.

3-3-2 Variable-Interval Time-Averaging (VITA) analysis

In order to study the turbulent boundary layer coherent structures, Blackwelder et al. (1976) proposed a conditional sampling technique to detect and extract the statistically averaged evolution of both ejection and sweep events. The algorithm first defines a small moving window, T_w, and the window will sweep over the streamwise velocity time-series. Within

each moving window T_w, the window time-averaged variance of the signal is computed. If the variance of the velocity signal in certain window is larger than a threshold, a turbulent ejection/sweep event is then detected.

Specifically, the algorithm first compute the moving average of the velocity signal:

$$\hat{u}(t, T_w) = \frac{1}{T_w} \int_{t-\frac{1}{2}T_w}^{t+\frac{1}{2}T_w} u(t')\ dt' \tag{3-8}$$

where T_w is the windowing time and the $\hat{u}$ is a function of both window length and time. Having derived the window-mean velocity, the window-mean variance can be defined as:

$$\sigma_{\hat{u}}^2\ (t, T_w) = \hat{u}^2(t, T_w) - \left[\hat{u}(t, T_w)\right]^2 \tag{3-9}$$

now we have the variance within each moving window $\sigma_{\hat{u}}^2$. The next step is to compare with a threshold value to detect the ejection/sweep event. Blackwelder et al. (1976) used the variance of the entire time-series signal as the threshold parameter. They argued that this approach avoid mis-detecting the coherent structure signal with large scale flow tendency. The variance of the entire velocity signal reads:

$$\sigma_u^2\ (t) = \lim_{t\to\infty} \frac{1}{t} \int_0^t u^2(t')\ dt' \tag{3-10}$$

If the window variance $\sigma_{\hat{u}}^2$ is greater than the variance of the entire signal $k \cdot \sigma_u^2$, where k is a threshold coefficient, then a sweep/ejection is detected. To differentiate each sweep and ejection event, a detector function $D(t)$ was defined as:

$$D(t) = \begin{cases} 1 & \text{if} \quad \sigma_{\hat{u}}^2(t, T_w) > k\sigma_u^2(t) \ \wedge \ \frac{\partial u}{\partial t} > 0 \quad \text{(sweep event)} \\ 0 & \text{if} \quad \sigma_{\hat{u}}^2(t, T_w) < k\sigma_u^2(t) \quad \text{(no event)} \\ -1 & \text{if} \quad \sigma_{\hat{u}}^2(t, T_w) > k\sigma_u^2(t) \ \wedge \ \frac{\partial u}{\partial t} < 0 \quad \text{(ejection event)} \end{cases} \tag{3-11}$$

The threshold coefficient k was set to 1.2 and the windowing time was set to 10 in viscous wall unit (Blackwelder et al., 1976). After identifying a number of events, an ensemble average of the VITA event is derived. To compute the ensemble average, a point of detection is determined at the maximum value of $\left|\frac{\partial u}{\partial t}\right|$. Then, an averaging window $[-3T_w, 3T_w]$ is used to compute the ensemble. Additional criterion is added with the detection algorithm and that is to ignore multiple events inside one moving window. This approach is to avoid aliasing from the packets of turbulent coherent structures (Adrian et al., 2000).

In practice, VITA algorithm have been implemented with various event detection method. In addition to streamwise velocity signal, Morrison et al. (1988) used the temperature signals to pinpoint the events. Bogard et al. (1986) added additional gradient criterion $\frac{\partial u}{\partial t}$ to extract the strong event. In this study, we use a different detection method that in combination with the quadrant-hole filtering strength H. The approach will be discussed in Chap. 5-3-1. An overview of the VITA technique from Blackwelder et al. (1976) is summarized in Fig. 3-9.

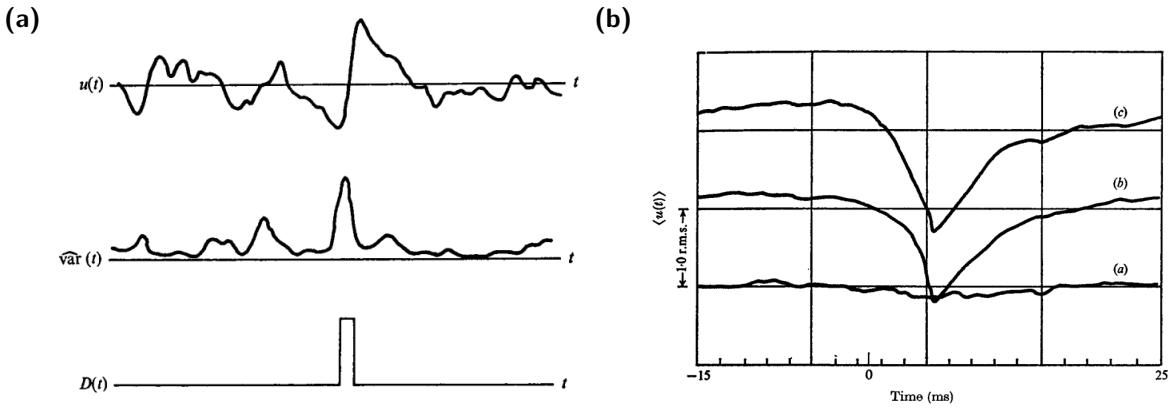

Figure 3-9: Overview of the VITA analysis. (a) Schematic diagram of the detection algorithm. (b) Conditional averaged development of a pseudo-turbulence. A is the level detection only. B is the detection with $u < u_{r.m.s}$. C is the detection with $u < u_{r.m.s}$ and $\frac{\partial u}{\partial t} < 0$

3-3-3 Fukagata-Iwamoto-Kasagi (FIK) identity

In an attempt to quantitatively investigate the effect of flow control technique, Fukagata et al. (2002) derived an expression that relates the Reynolds shear stress to the skin friction drag in channel and plane boundary layer flows. The so-called FIK identity relates the skin friction drag to four components: laminar, turbulent, heterogeneous and transient components, and the turbulent term comes from a weighted integral of the Reynolds shear stress distribution. In this subsection, a derivation of a plane boundary layer with zero pressure gradient will be shown. Following the derivation for plane boundary layer case, the extended FIK identity will be briefly discussed.

To begin with, the incompressible steady RANS equation in streamwise direction (x-direction) with homogenenity in spanwise direction reads:

$$-\overline{\frac{\partial p}{\partial x}} = \frac{\partial}{\partial y}\left[\overline{u'v'} - \frac{1}{Re_\delta}\frac{\partial \overline{u}}{\partial y}\right] + \overline{I_x} \tag{3-12}$$

note that all variables with asterisk superscript represent dimensional variables, whereas the others are non-dimensionalised by freestream U_∞ and boundary layer thickness δ. The Reynolds number Re_δ is defined as $Re_\delta = \frac{U_\infty \delta}{\nu^*}$, and the pressure term is normalised by

the density. The third term on the RHS of the equation denotes the inhomogeneous terms, including convection and diffusion terms, which are given as:

$$\overline{I_x} = \frac{\partial \overline{(uu)}}{\partial x} + \frac{\partial \overline{(uv)}}{\partial y} - \frac{1}{Re_\delta}\frac{\partial^2 \overline{u}}{\partial x^2} \tag{3-13}$$

for a plane boundary layer flow with zero pressure gradient, the first term on the LHS in Eqn. 3-12 vanishes. Further assuming constant freestream velocity and $\frac{\partial \overline{u}}{\partial y} = 0$ at $y = 1$ (represents the boundary layer height), Eqn. 3-12 can be simplified into the following form:

$$0 = \frac{\partial}{\partial y}\left[\overline{u'v'} - \frac{1}{Re_\delta}\frac{\partial \overline{u}}{\partial y}\right] + \frac{\partial \overline{(uu)}}{\partial x} + \frac{\partial \overline{(uv)}}{\partial y} - \frac{1}{Re_\delta}\frac{\partial^2 \overline{u}}{\partial x^2} \tag{3-14}$$

the final expression can be derived by applying triple integration with regard to y, and it is written as

$$C_f = \frac{4(1-\delta_d)}{Re_\delta} + 4\int_0^1 (1-y)(-\overline{u'v'})dy - 2\int_0^1 (1-y)^2\left(\frac{\partial \overline{(uu)}}{\partial x} + \frac{\partial \overline{(uv)}}{\partial y}\right)dy \tag{3-15}$$

where δ_d is the dimensionless displacement thickness. For laminar plane boundary layer flows, the first term on RHS is about $2.6/Re_\delta$ and the third term can be obtained as $0.7/Re_\delta$ by utilizing the similarity solution of Howarth (1938). The summation of these two terms lead to $C_f \approx 3.3/Re_\delta (= 0.66/Re_x^{0.5})$, which is the Blasius solution. The second term then represents the weighted integral of the Reynolds shear stress within the boundary layer (integrate from 0 to 1).

Even though Fukagata et al. (2002) derived a concise expression to illustrate the Reynolds stress contribution to the skin friction, the formulation only holds for idealized geometry. In order to apply FIK analysis to the riblet geometry, Bannier et al. (2015) developed an extend FIK expression that can be utilized for complex surfaces. The idea is that the assumption for homogeneity and integration limit is relaxed. To be more specific, the spanwise direction is no longer homogeneous, and thus the second integration needs to be carried out over the two-dimensional transverse cross-sections $\Sigma(x)$. Also, the integral upper limit y_{top} can be chosen arbitrarily, whereas the original formulation integrates over the entire boundary layer. In this thesis work, the original FIK formulation is re-derived with normalized wall coordinate, and spanwise terms are also retained. The details will be presented in Chap. 5-4.

Chapter 4

Results

Quantities directly derived from the solver are presented in this chapter. Mostly these are raw data with minimum post-processing. Considering the order of interest in this study, the author decides to separate the content between solver outputs and the statistical analysis, where a series of conditional sampling, ensemble averaging and spatial differentiation will be performed. The reason is that these post-processing procedures might introduce additional uncertainties. The goal of this chapter is to validate the drag results from Spalart et al. (2019) and compare the flow topology, boundary layer profile obtained by Tay et al. (2014); Tay, Khoo, et al. (2015) and van Nesselrooij et al. (2016); van Campenhout et al. (2016). The content in this chapter will be structured as follows. Firstly, a validation in Chap. 4-1 is given to stress out the consistency of the present numerical approach. Following the validation, the mean flow topology and its averaged boundary layer profile will be presented in Chap. 4-2 and Chap. 4-3, respectively. Lastly, the averaged drag performance will be discussed and compared with the literature in Chap. 4-4.

4-1 Validation

4-1-1 Wall y^+ and skin friction

Firstly, the wall y^+ in both smooth plate and dimple plate will be examined. To sufficiently resolve the near-wall layer, it is preferable to have the wall $y^+ < 1$.

Fig. 4-1 shows the top-view of the wall y^+ and its spanwise averaged quality. It can be found that the smooth plate has an averaged y^+ of 0.73, at the inflow (excluding turbulent generator region) station. For the dimple plate, the averaged quantity shows a series of oscillations, but its magnitude is still below 1, with a maximum of 0.77 at $x/\delta_0 = 5$. Further examining the top-view y^+ of the dimple plate, it is found that the downstream half of the dimple shows a large y^+, which is due to a large shear in the rear-end of the dimple. Locally the resulting peak value in the first dimple is about 0.95. Since its value is close to 1, the first dimple will not be included in the later analysis. Mostly the observation and analysis will be made based

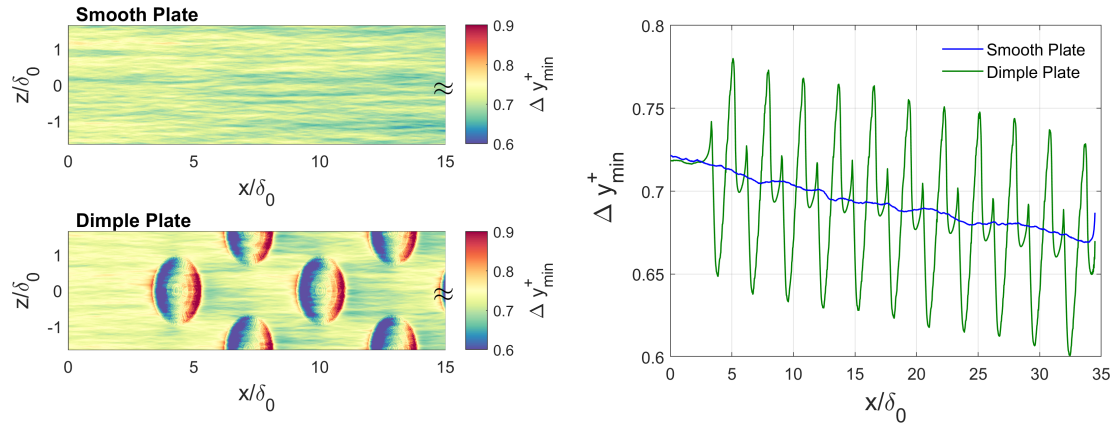

(a) Top-view of the wall y^+. **(b)** Spanwise averaged wall y^+.

Figure 4-1: Wall y^+ of the smooth plate and dimple plate. In the Top-View plot, only half of the streamwise domain is shown for simplicity.

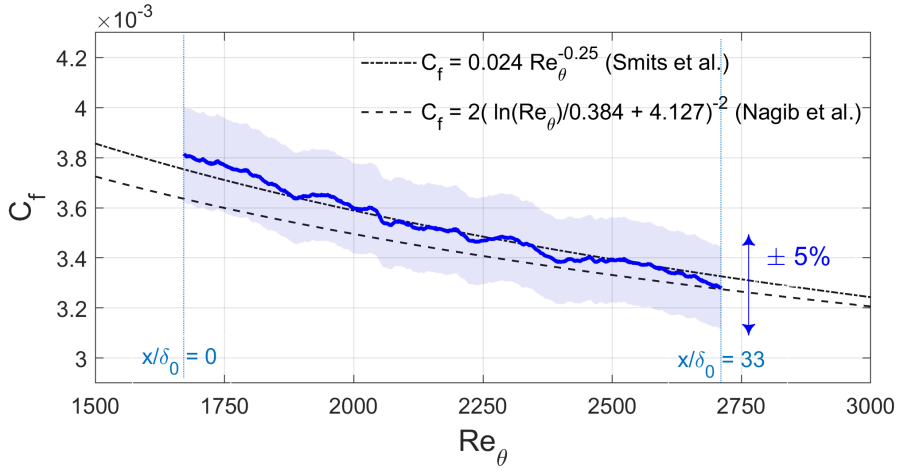

Figure 4-2: Streamwise development of the skin friction coefficient as a function of Re_θ. Asterisk line: the correlation by Nagib et al. (2007), $C_f = 2(\ln(Re_\theta)/0.384 + 4.127)^{-2}$. Triangle line: the correlation given by Smits et al. (1983), $C_f = 0.024 Re_\theta^{-0.25}$. The shading area represents a $\pm 5\%$ variation bound. Dot lines indicate the corrsponding streamwise location.

on the $2nd$ dimple to the $5th$ dimple. The horizontal cell spacing in wall units can also be characterized. The result are compared with the guideline values from Bannier et al. (2015) in Tbl. 3-3. It can be concluded that present implicit LES has a proper grid spacing to resolve the turbulent boundary layer. Next, Fig. 4-2 summarizes the simulated skin friction development. The blue line represents the spanwise averaged C_f. It can be concluded that the current numerical approach demonstrates the ability for deriving accurate skin friction and its spatial development. The result suggests that both the slope and single station value are in close agreement with the empirical formulation. Compared with the correlation given by Smits et al. (1983) and Nagib et al. (2007), the deviation across the streamwise domain is within 1%.

	Δx^+	Δz^+	Δy^+_{wall}
Ref.x0	216.98	108.49	0.73
Ref.x1	108.49	54.24	0.73
Ref.x2	54.24	27.12	0.73
Ref.x5 (present LES)	**17.84**	**8.92**	**0.73**

Table 4-1: Cell spacing at the wall for different levels of refinement.

4-1-2 Sensitivity analysis

In this section, the grid convergence will be discussed along with the sensitivity on the inflow recycling length. Fig. 4-3 shows the mean streamwise velocity profile in wall units at the inflow station, $x/\delta_0 = 0$. The "Refinement xn" refers to different levels of refinement in the horizontal direction. The corresponding cell spacing is listed in Tbl. 4-1. It can be found that the grid is indeed converged, as the resulting profiles are almost identical when the refinement level is above $Ref.x2$. In the near-wall region, values all collapse on the theoretical relation $u^+ = y^+$. Away from the wall, the logarithmic law of the wall, $u^+ = (1/\kappa)\log y^+ + B$, is also recovered, with $\kappa = 0.41$ and $B = 5.1$. The agreement between $Refx5$ simulated profile with those relations again validates the employed CFD method. For the coarse grids like $Refx0$ and $Refx1$, the retrieved B value is about 7.1 and 9.5. These large B could be due to the significant cell aspect ratio. The presence of streamwise pressure gradient due to the poor-resolved flow field could also hamper the development of ZPGBL, leading to a larger B. Next, different inflow recycling lengths are implemented to investigate their impact on the solution. Due to limited resources, the sensitivity runs are performed with $Ref.x1$ grid. Fig. 4-4 illustrates the mean fluctuation and mean flow profile in wall units. It can be observed that the influence on the mean flow is rather subtle. Longer recycling length gives larger skin friction. The deviation from the logarithmic profile is due to limited mesh cell spacing. On the other hand, the fluctuation profile shows a larger variation. In general, more considerable variations are found in the wake region, where the smaller recycling length gives a weaker profile. The fluctuation result suggests as $L_{rec} > 9$, the profile is relatively converged.

4-2 Mean flow topology

After validating the skin friction and grid convergence, comparison and validation of the mean flow topology with the literature is performed. To begin with, Fig. 4-5 show the mean spanwise velocity at the $2nd$ dimple. It is found that the mean flow exhibits an identical mean flow structure. The streaklines and shadings of the mean spanwise velocity reveal a conffuser-diffuer flow topology, which is in agreement with the results from Tay, Khoo, et al. (2015); van Nesselrooij et al. (2016) and Spalart et al. (2019). The order of the spanwise velocity also matches the results from the literature and is of 3% of the freestream velocity. The Reynolds number based on the dimple diameter is about $34,200$, which is smaller than van Nesselrooij et al. (2016), where $Re_D = 40,000$. Still, the resulting flow topology falls into

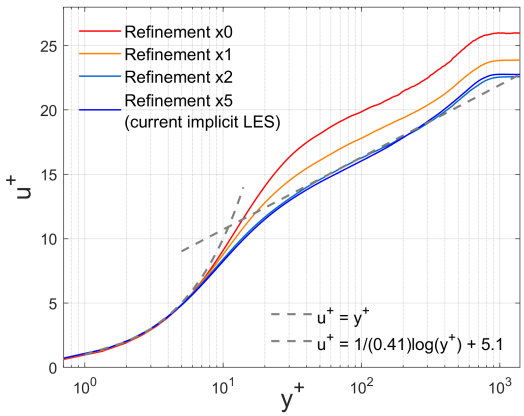

Figure 4-3: Mean streamwise velocity profile in wall units at the inflow station, $x/\delta_0 = 0$, with different levels of grid refinement.

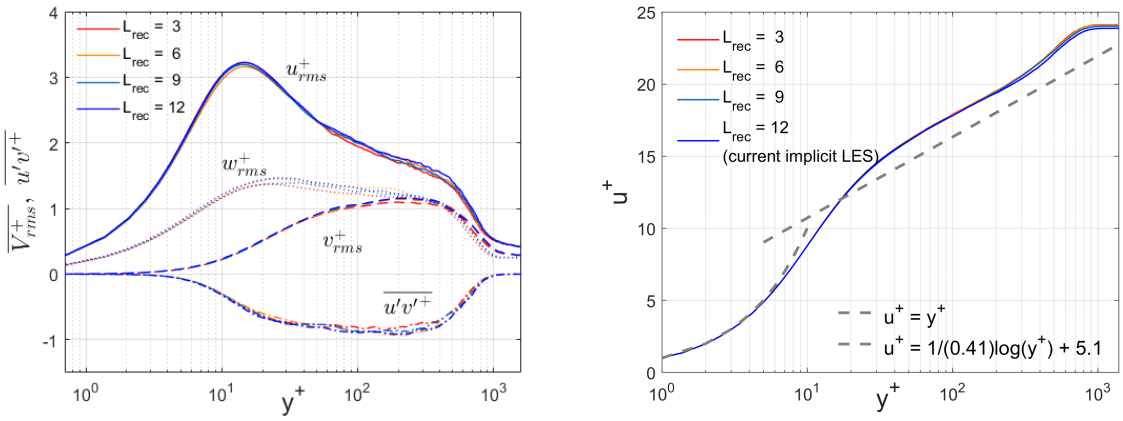

(a) Mean fluctuation profiles.

(b) Mean streamwise velocity profile.

Figure 4-4: Sensitivity of the recycling length L_{rec}.

the **type VI** flow structures according to Tay et al. (2014) and exhibits a turbulent flow with conffuser-diffuser mean flow topology. Even though an identical flow topology is observed, current results suggest that the developed spanwise velocity structure in the downstream half of the dimple is stronger than the upstream half, as revealed in the colour shading in Fig. 4-5a. As for the streamwise velocity in Fig. 4-5b, a larger velocity in the dimple centre is obtained, which is not surprising. Due to the fact that the boundary layer is continuous and follows the geometry variations, the presence of dimples shifts TBL to a lower position at the dimple centre. This means locally at the dimple centre, we are actually in a higher TBL-normalized position, and hence a larger mean streamwise velocity will be expected. Unlike mean spanwise velocity, no upstream-downstream asymmetry is found.

Fig. 4-6 shows the X-Y cross-section at the center plane $z/\delta_0 = 0$. of a smooth plate and dimple plate. To visualize the symmetrical conffuser-diffuser flow pattern, the cross-section plane for spanwise velocity is slightly shifted to $z/\delta_0 = -0.2$. The first row to the third row depicts

the mean streamwise velocity, vertical velocity and spanwise velocity, respectively. Quivers represent the (u, v) velocity vectors. The results are in agreement with the stereoscopic PIV data from van Campenhout et al. (2016). It can be found that as the flow approaches the depression, the flow is decelerated. Still, there is no flow reversal or separation in the resulting mean flow. To eliminate the possibilities of statistical sampling issue, instantaneous shear $\frac{\partial u}{\partial y}$ is also examined, and no flow separation is found. The instantaneous snapshots are sampled over one flow-through cycle, so it should be quite representative of the resolved flow field. For simplicity, the instantaneous shear plots are listed in Appendix. B-1 for reference. Further examining the vertical extent of such topology, as shown in Fig. 4-6, it can be observed that the region of influence extends up to $0.2D$ above the wall for the spanwise velocity; $0.4D$ for the vertical velocity. Notes that the X-Y cross-section is selected at the $2nd$ dimple in this case.

To further quantify the vertical extent of the dimple influence over downstream dimples, several X-Z sections are cropped at upstream half and downstream half of the dimple, and over the $2nd$ to $5th$ dimples. Since the streamwise velocity only shows a symmetrical distribution, for simplicity only the mean vertical velocity and mean spanwise velocity are shown. The mean streamwise velocity slices are included in Appendix. B-2 for reference. Fig. 4-7 and Fig. 4-8 show mean vertical and spanwise velocity in the upstream half (the first row) and downstream half (the second row) of the $2nd$ to the $5th$ dimples. In the mean vertical velocity, the developed flow structure is symmetrical, with the opposite direction. The upward motion in the downstream half extends deeper into the TBL, yet the difference is quite small. For mean spanwise velocity, a convergent flow and a divergent flow in the upstream and downstream is observed respectively. These flow structures are just the conffuser-diffuer flow pattern observed form the top-view figures.

Interestingly, in the upstream half of the dimple, a shallow near-wall layer is formed with a spanwise velocity opposite to the rest of the convergent layer. This residual layer has not been found in the literature. One possible explanation might be flow separation, but no flow

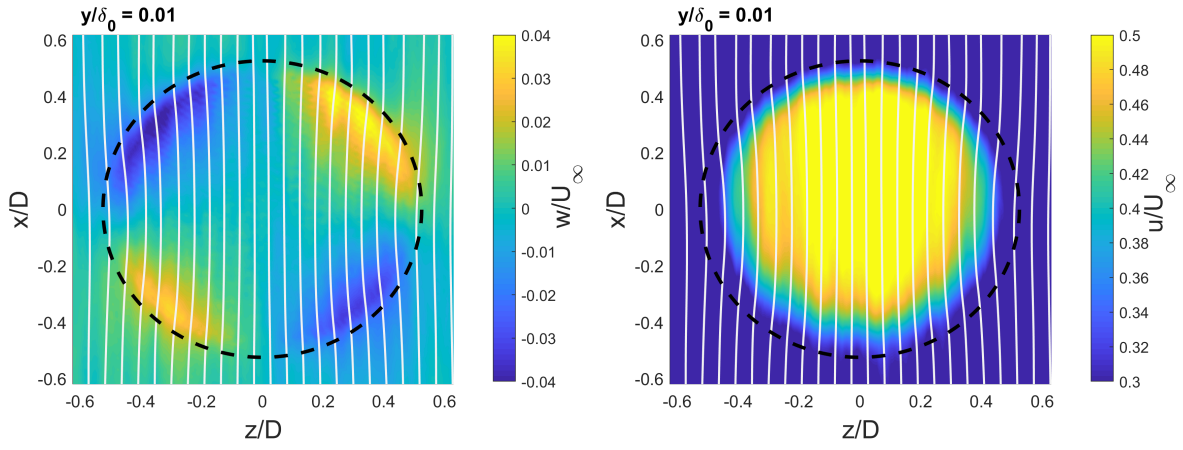

(a) Mean spanwise velocity **(b)** Mean streamwise velocity

Figure 4-5: Mean flow field at $y/\delta_0 = 0.01$ of a dimple plate. The X-Z cross section shown is from the $2nd$ dimple. The grey contour lines show (u, w) velocity vectors in both plots. The freestream is pointed towards positive x-axis.

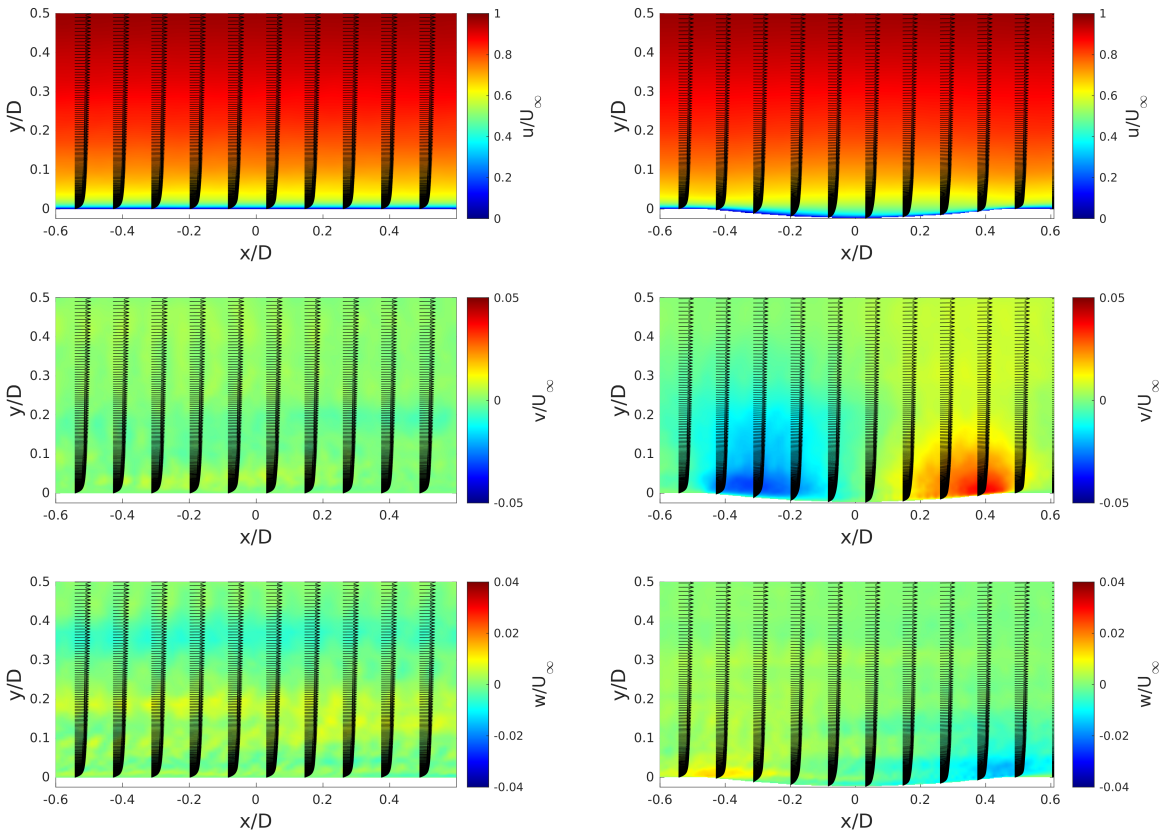

Figure 4-6: X-Y cross section at $z/\delta_0 = 0$ center plane of a smooth plate (left column) and a dimple plate (right colimn). Quiver indicates the (u, v) vector. First row: mean streamwise velocity. Second row: mean vertical velocity. Third row: mean spanwise velocity.

separation is observed either in the instantaneous or mean flow. A separate analysis will be given in the Chap. 5-1 to address the formation of such a near-wall spanwise velocity layer. Regarding the development across downstream dimples, it can be inferred that dimples have a constant depth of influence. This constant extension suggests the effect of the dimple on the flow is mainly scaled by the dimple diameter (and thus Re_D), not the downstream location (Re_x).

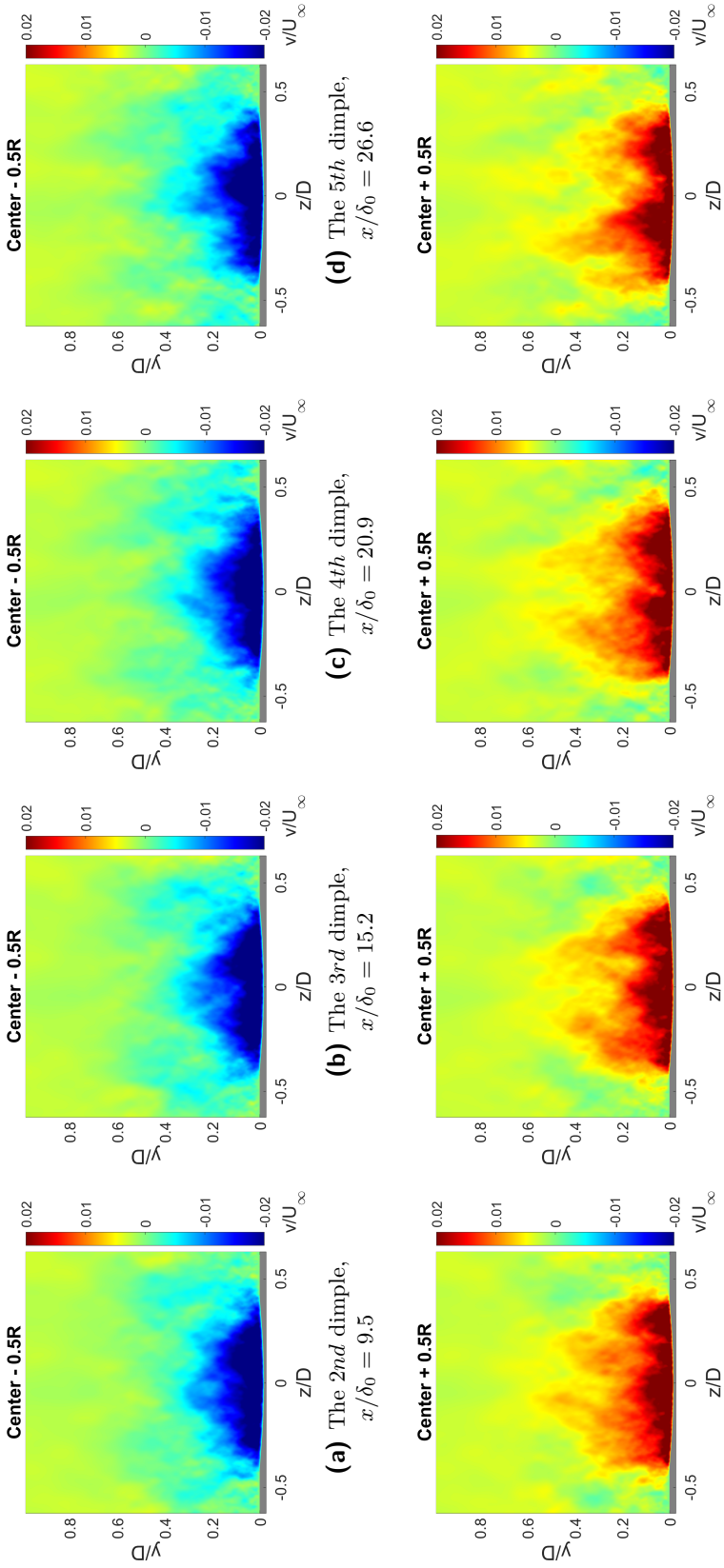

(a) The $2nd$ dimple, $x/\delta_0 = 9.5$

(b) The $3rd$ dimple, $x/\delta_0 = 15.2$

(c) The $4th$ dimple, $x/\delta_0 = 20.9$

(d) The $5th$ dimple, $x/\delta_0 = 26.6$

(e) The $2nd$ dimple, $x/\delta_0 = 10.5$

(f) The $3rd$ dimple, $x/\delta_0 = 16.2$

(g) The $4th$ dimple, $x/\delta_0 = 21.9$

(h) The $5th$ dimple, $x/\delta_0 = 27.6$

Figure 4-7: Mean vertical velocity cross section of the dimple plate at the upstream and downstream Y-Z plane, over the $2nd$ to the $5th$ downstream dimples.

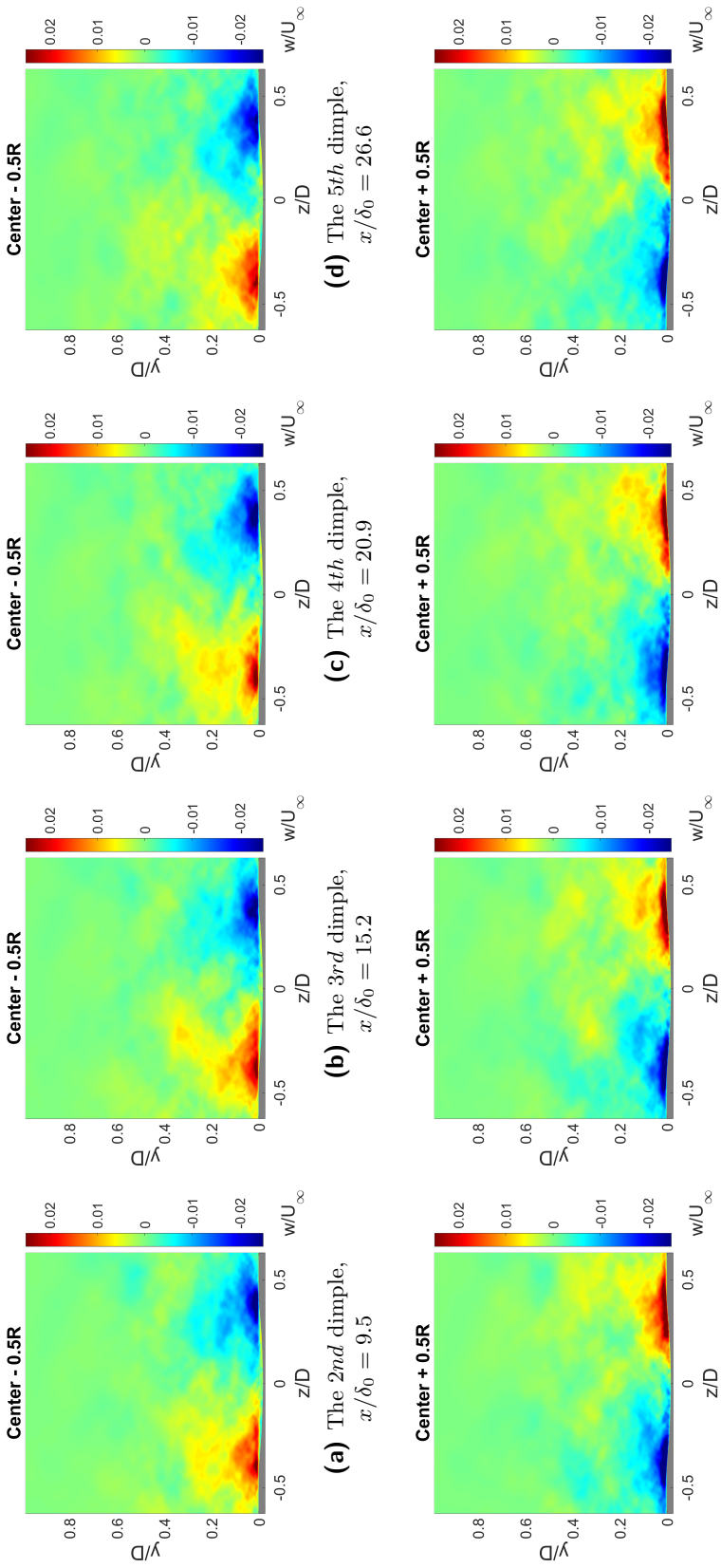

(a) The $2nd$ dimple, $x/\delta_0 = 9.5$

(b) The $3rd$ dimple, $x/\delta_0 = 15.2$

(c) The $4th$ dimple, $x/\delta_0 = 20.9$

(d) The $5th$ dimple, $x/\delta_0 = 26.6$

(e) The $2nd$ dimple, $x/\delta_0 = 10.5$

(f) The $3rd$ dimple, $x/\delta_0 = 16.2$

(g) The $4th$ dimple, $x/\delta_0 = 21.9$

(h) The $5th$ dimple, $x/\delta_0 = 27.6$

Figure 4-8: Mean spanwise velocity cross section of the dimple plate at the upstream and downstream Y-Z plane, over the $2nd$ to the $5th$ downstream dimples.

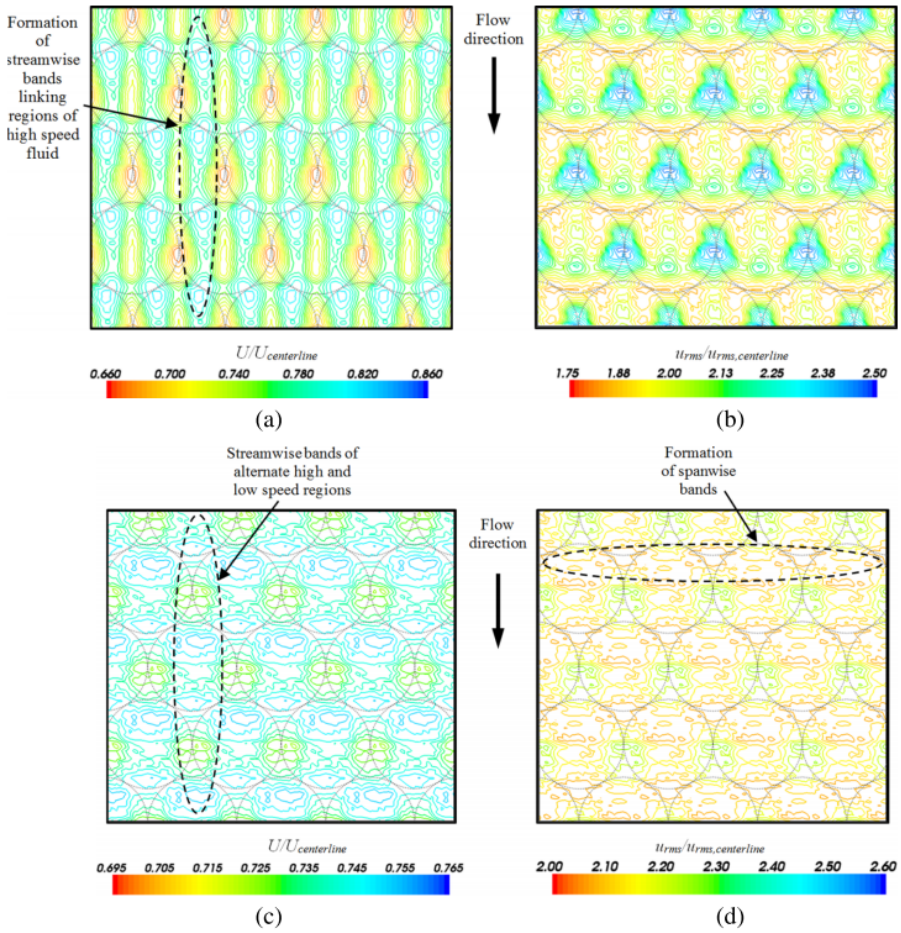

Figure 4-9: The formation of high speed band at $Re = 15000$ at $y/h = 0.05$, where h is the channel height. (a) Normalized streamwise velocity with dimple depth ratio $d/D = 5\%$. (b) Normalized streamwise velocity rms with dimple depth ratio $d/D = 5\%$. (c) Normalized streamwise velocity with dimple depth ratio $d/D = 1.5\%$. (d) Normalized streamwise velocity rms with dimple depth ratio $d/D = 1.5\%$. (Tay, Khoo, et al., 2015)

After inspecting the vertical distribution of the mean flows across downstream dimples, the mean flow development across downstream dimples in X-Z plane is investigated. Fig. 4-10, Fig. 4-11 and Fig. 4-12 show the top view of the mean streamwise, vertical and spanwise velocity distribution respectively. Four vertical levels are cropped to investigate the development in different wall layer. One inside the dimple depression, $y/\delta_0 = -0.03$, one at the near-wall layer, $y/\delta_0 = 0.002$, and the rest two levels are at buffer layer and wake region, $y/\delta_0 = 0.05, 0.1$. Firstly, the mean vertical velocity distribution is quite uniform; four levels show similar behaviour: downward motion in the upstream half; and upward motion in the downstream half.

For the mean streamwise velocity, it is found that in the buffer layer and wake region, a streamwise band linking regions of high-speed fluid is formed inside each dimple. The strength of such band varies across downstream dimples, but the pattern inside the dimple remains similar. These streamwise bands have also been reported by Tay, Khoo, et al. (2015), seen in

the Fig. 4-9. The difference between current results and Tay, Khoo, et al. (2015) is that they used a dimple plate with a higher density, so the high-velocity region forms a continuous band across the dimples. Current set up has a dimple density of 33%, so it allows the high-velocity band to separate from each other, leaving a low-speed region downstream the dimple.

Inspecting the spanwise velocity in Fig. 4-12, in general dimple forms a conffuser-diffuser flow structure, and thus the spanwise velocity shows a quadruple pattern. Nevertheless, inside the dimple, the spanwise velocity distributed as a dipole, forming a diffuser flow pattern. This discontinuity is also observed in the Y-Z section plots in Fig. 4-8. The top-view plots suggest the near-wall spanwise velocity layer exist in the entire upstream half region, and in every dimple. At the near-wall level, $y/\delta_0 = 0.002$, a clear quadruple pattern is formed, which refers to the coffuser-diffuer flow structure. The developed flow field at this level is limited inside the dimple and has a constant strength of approximately 3% of the streamwise velocity magnitude. The top-view plot suggests the flow structure has a similar strength across downstream dimples, and exhibit a streamwise asymmetry, which has been seen in Fig. 4-5a. Move to higher levels, an interesting pattern emerged. The developed quadruple pattern inside each dimple now extends downstream. It even connects to the adjacent quadruple structure formed by nearby dimples, resulting in a continuous sequence of oscillating spanwise velocity in the streamwise direction. This meandering pattern is strongest in the buffer layer. At the wake region, the pattern can still be observed but is weaker than in the buffer layer. Such extended oscillating sequence and its vertical decaying provide powerful evidence that the drag reduction mechanism has a connection to the spanwise wall oscillation. As proposed by van Nesselrooij et al. (2016), in a Lagrangian perspective, fluid parcel travelling downstream of a dimple plate undergoes series of spanwise oscillations, which is analogous to applying a spanwise wall oscillation to achieve drag reduction. The current result suggests the developed spanwise oscillation not only exists locally inside the dimple; it forms a continuous sequence of oscillation at the buffer layer.

After examining the mean flow field, the mean fluctuation is also plotted to investigate the distribution inside the dimple and its responses under the dimple plate. The top-view of the mean streamwise, vertical and spanwise fluctuations are shown in Fig. 4-13, Fig. 4-14 and Fig. 4-15, respectively. Four similar levels are selected. It can be found that the distribution inside the dimple is opposite between streamwise fluctuation and vertical/spanwise fluctuation. In streamwise fluctuation, the upstream half of the dimple has a higher fluctuation level; whereas in vertical and spanwise fluctuation, the fluctuation is stronger in the downstream half. At $y/\delta_0 = 0.1$, the vertical and spanwise fluctuation inside the dimple is convected downstream, and thus the maximum strength is shifted towards the downstream edge of the dimple. Overall, the fluctuation across downstream dimples have a similar distribution. A small decrease in the magnitude of a downstream dimple could be due to the boundary layer growth.

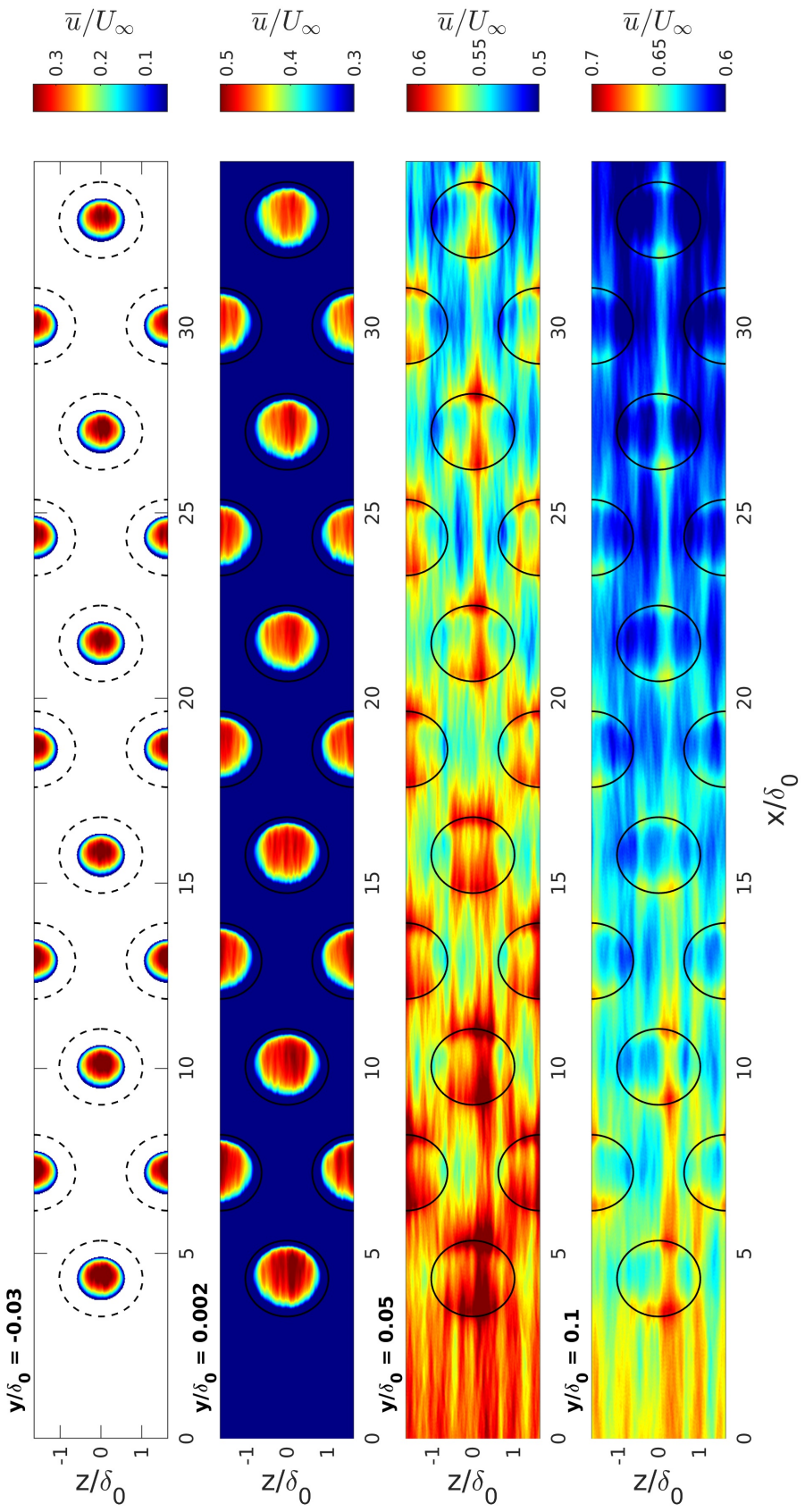

Figure 4-10: Top-view of the mean streamwise velocity at $y/\delta_0 = -0.03, 0.002, 0.05, 0.1$. Black contour lines indicate dimples. Dashed line means the periphery of dimples is above current level.

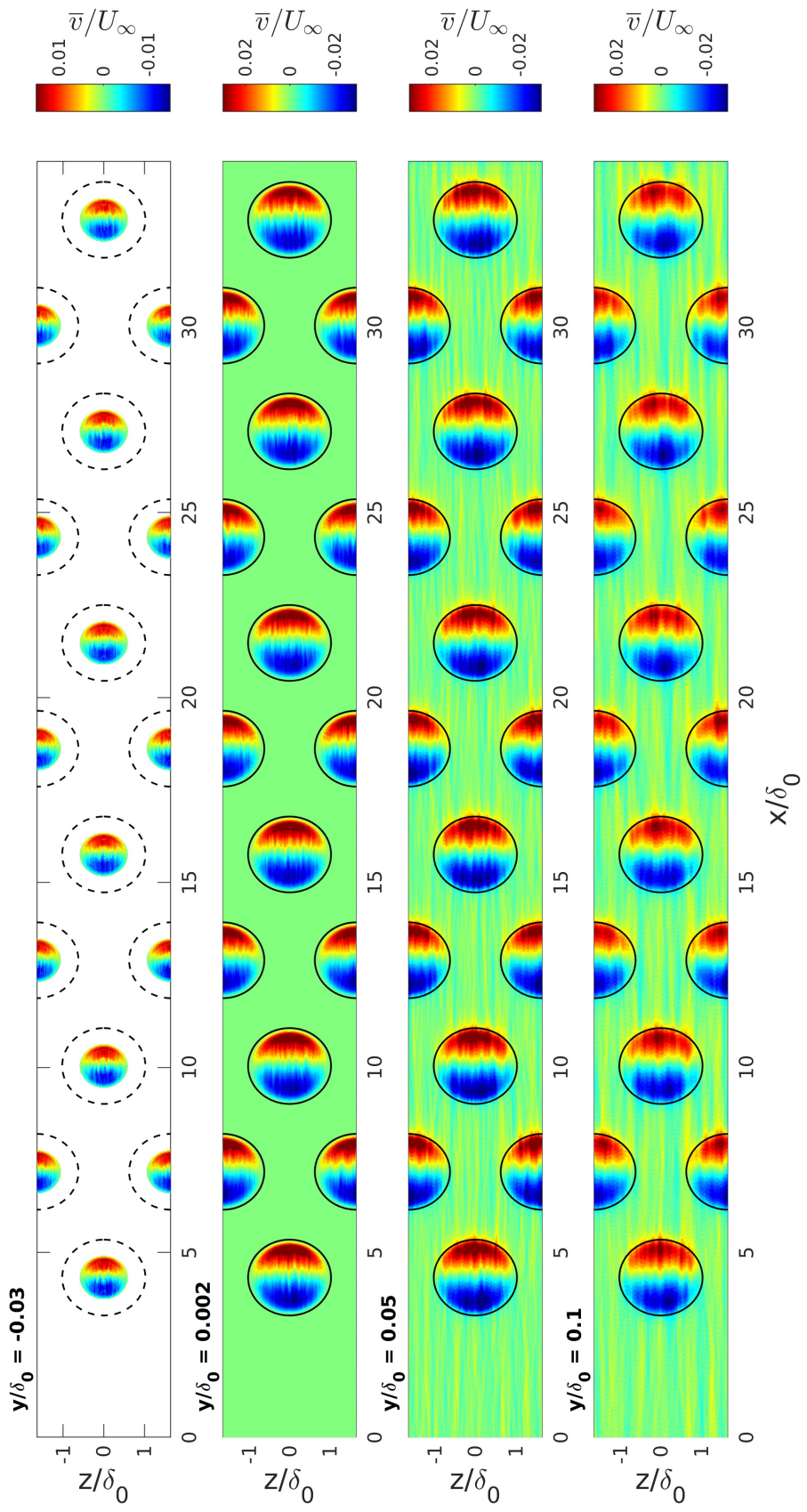

Figure 4-11: Top-view of the mean vertical velocity at $y/\delta_0 = -0.03, 0.002, 0.05, 0.1$. Black contour lines indicate dimples. Dashed line means the periphery of dimples is above current level.

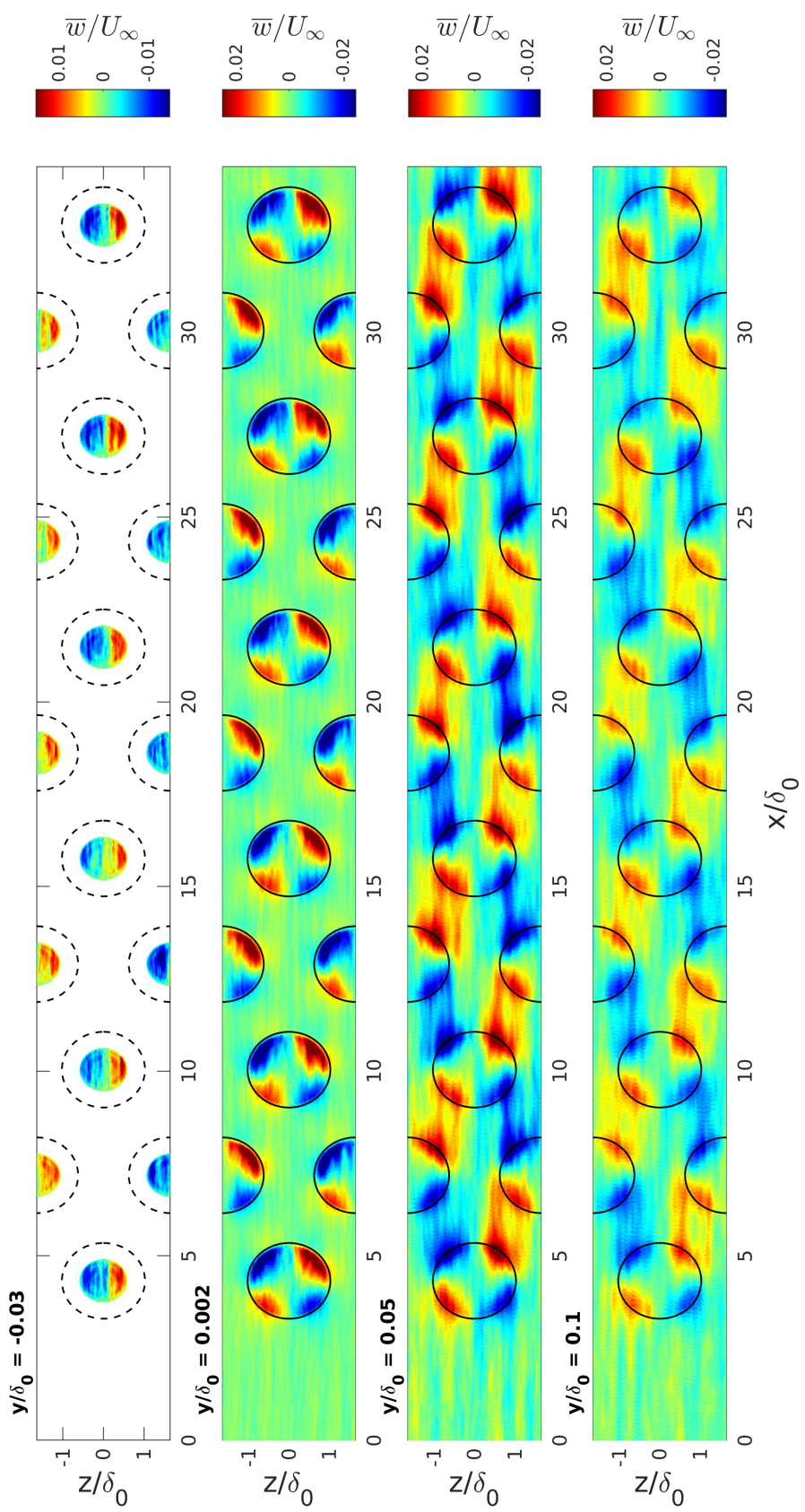

Figure 4-12: Top-view of the mean spanwise velocity at $y/\delta_0 = -0.03, 0.002, 0.05, 0.1$. Black contour lines indicate dimples. Dashed line means the periphery of dimples is above current level.

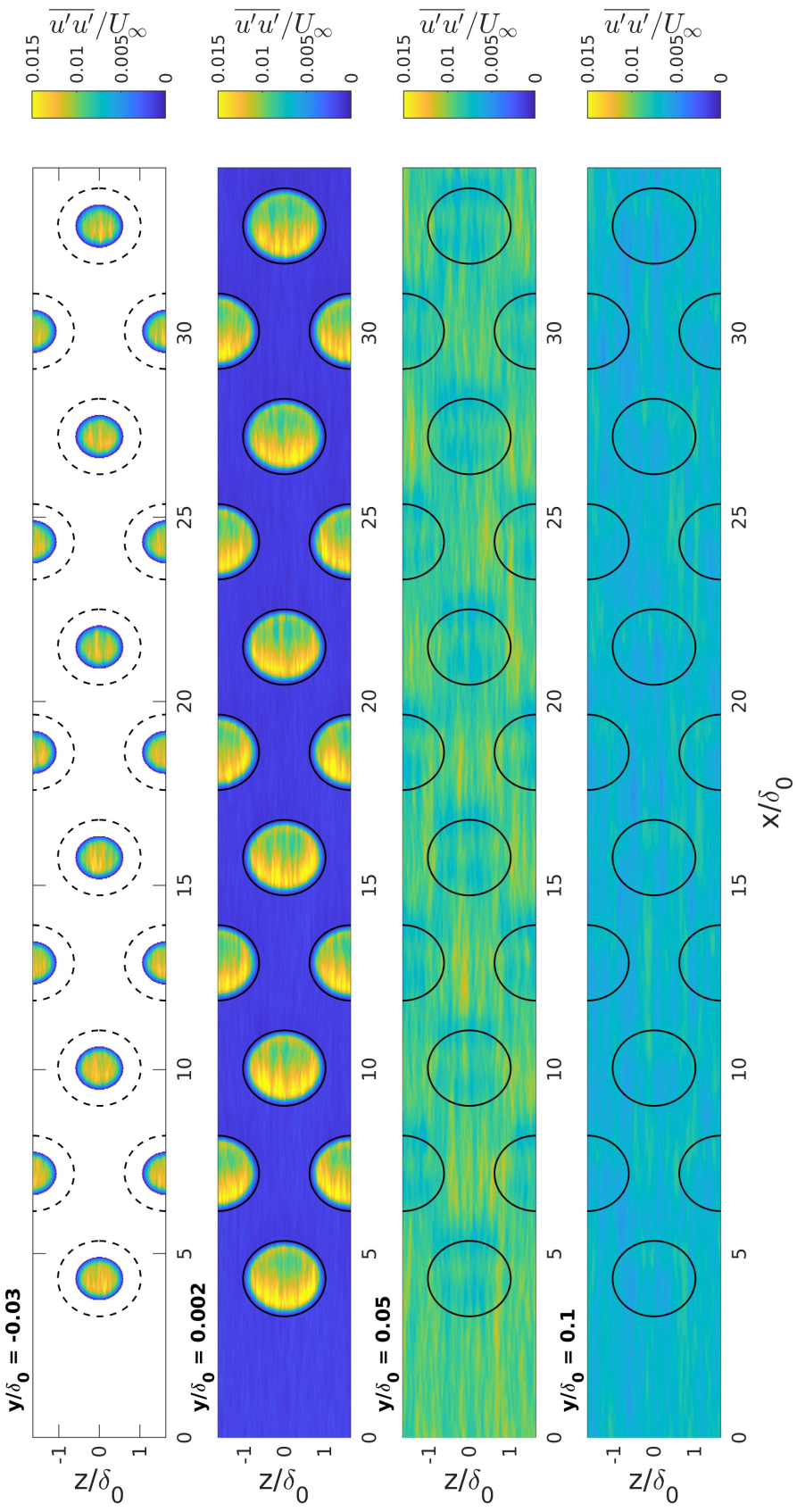

Figure 4-13: Top-view of the man streamwise fluctuation at $y/\delta_0 = -0.03, 0.002, 0.05, 0.1$. Black contour lines indicate dimples. Dashed line means the periphery of dimples is above current level.

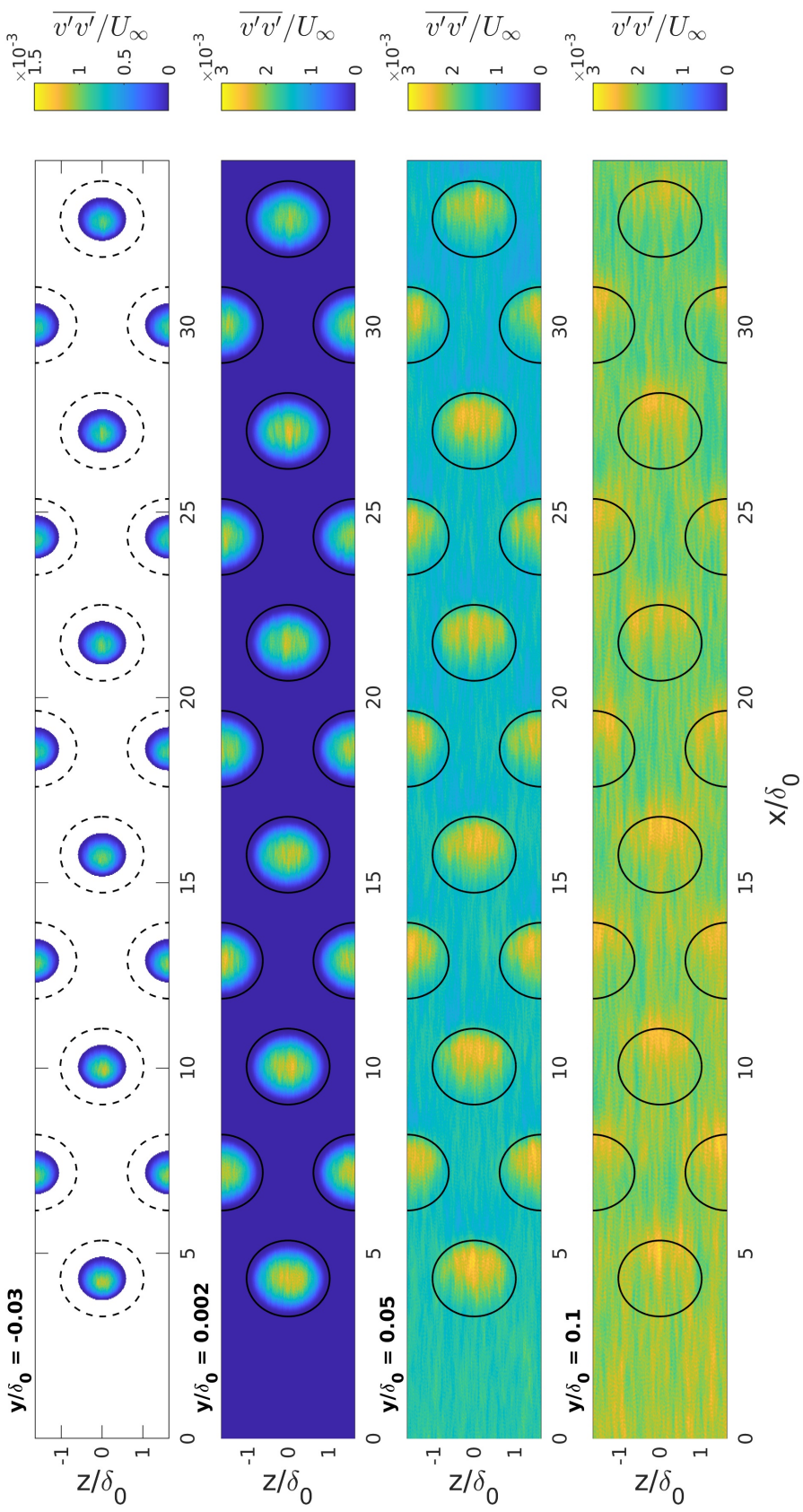

Figure 4-14: Top-view of the mean vertical fluctuation at $y/\delta_0 = -0.03, 0.002, 0.05, 0.1$. Black contour lines indicate dimples. Dashed line means the periphery of dimples is above current level.

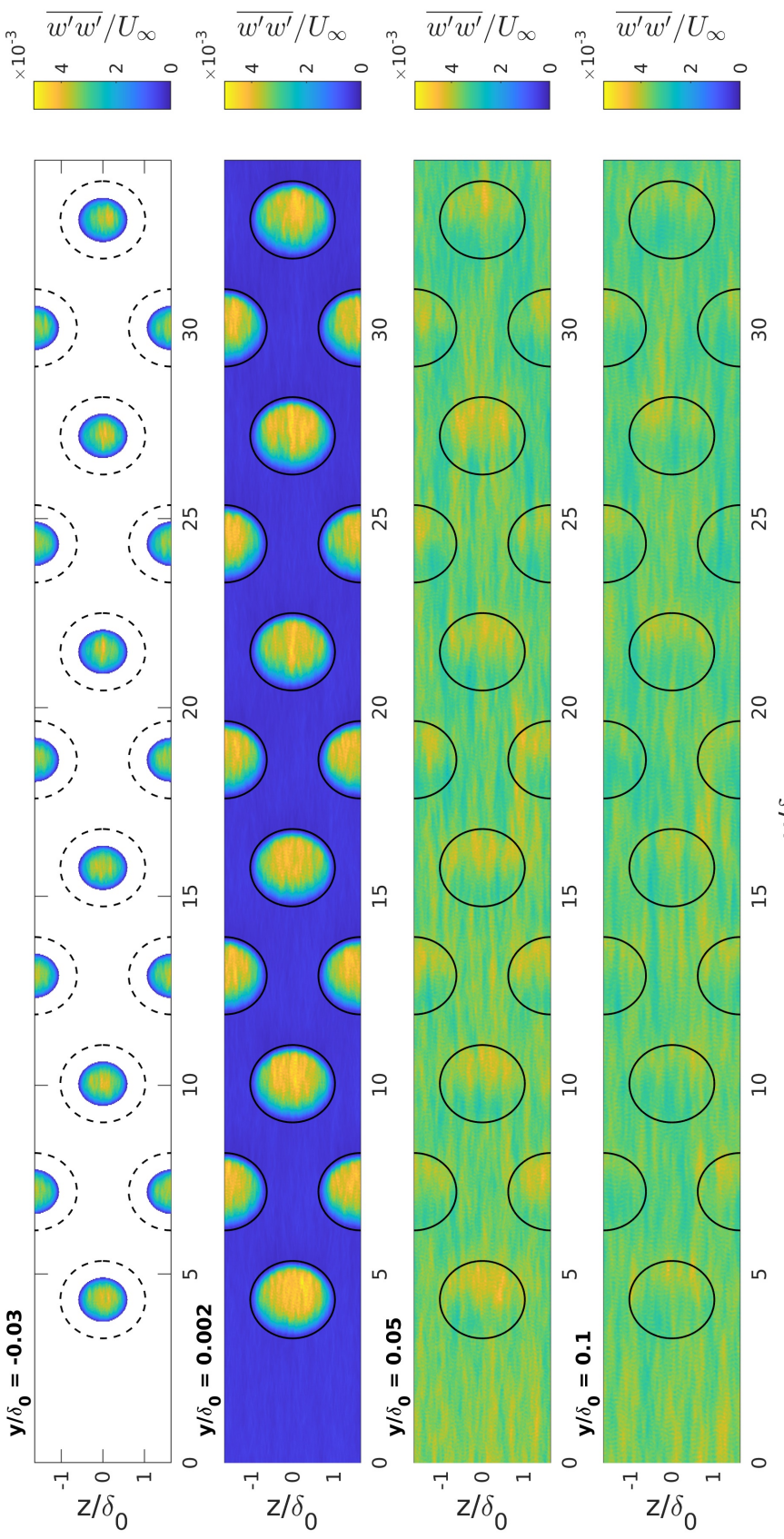

Figure 4-15: Top-view of the mean spanwise velocity at $y/\delta_0 = -0.03, 0.002, 0.05, 0.1$. Black contour lines indicate dimples. Dashed line means the periphery of dimples is above current level.

The mean fluctuation fields from the dimple plate are then compared with the smooth plate. The comparison is achieved by cropping sections at similar normalised vertical position. The numerical solver has the output variable called "wall distance", which could help us retrieve the data with minimum post-processing introduced uncertainty. The variable y_{wd} than refers to the vertical coordinate that follows the local surface. Four vertical levels will be investigated to reveal the impact of dimples on the fluctuation. Fig. 4-16 shows the top-view of the response in mean streamwise fluctuation at $y_{wd} = 0.0025, 0.05, 0.10$ and 0.15. It can be observed that the near-wall layer, $y_{wd} = 0.0025$ has the strongest response. The fluctuation in the upstream half of the dimple becomes stronger; whereas in the downstream the activity is weakened. Observing the responses at different levels, it is further found that patterns remain the same, but at a higher level, the responses are convected downstream. The responses are almost diminished at $y_{wd} = 0.15$, which suggests the influence is mainly below the wake region.

The vertical fluctuation in Fig. 4-17 shows a different response: there is almost no upstream/-downstream asymmetry. At the near-wall layer at $y_{wd} = 0.0025$, dimple increases the vertical fluctuation level in the centre, but reduces around the edge and immediately downstream of it. The higher intensity in the dimple center is not because of the TBL shifting effect. Current plot crops the sections, which have similar distance away from the local surface so that the TBL shifting effect can be ruled out. At buffer layer, $y_{wd} = 0.05$, again the responses are convected downstream, which leaves a large area of lower vertical fluctuation intensity immediately downstream of a dimple. This leads to a lower intensity in the upstream half of the dimple. Moving to higher levels, the responses are weakened and further convected downstream.

Lastly, the mean spanwise fluctuation is shown Fig. 4-18. Compared with other fluctuations, it can be found that the responses in the spanwise fluctuation are the most significant. At the near-wall layer, $y_{wd} = 0.0025$, strong responses are observed inside the dimple. The responses inside the dimple are not symmetrical. In the upstream half of the dimple, a remarkable intensity decrease is found near the dimple edge; whereas the rest area shows an increase. The downstream half, on the other hand, is characterized by a significantly increased intensity. Notably, the responses in the mean spanwise fluctuation at higher vertical levels almost trap inside the dimple, and do not being convected downstream. The downstream-shifting effect can still be seen at $y_{wd} = 0.15$, but the magnitude is relatively small compared to responses in streamwise and vertical fluctuation.

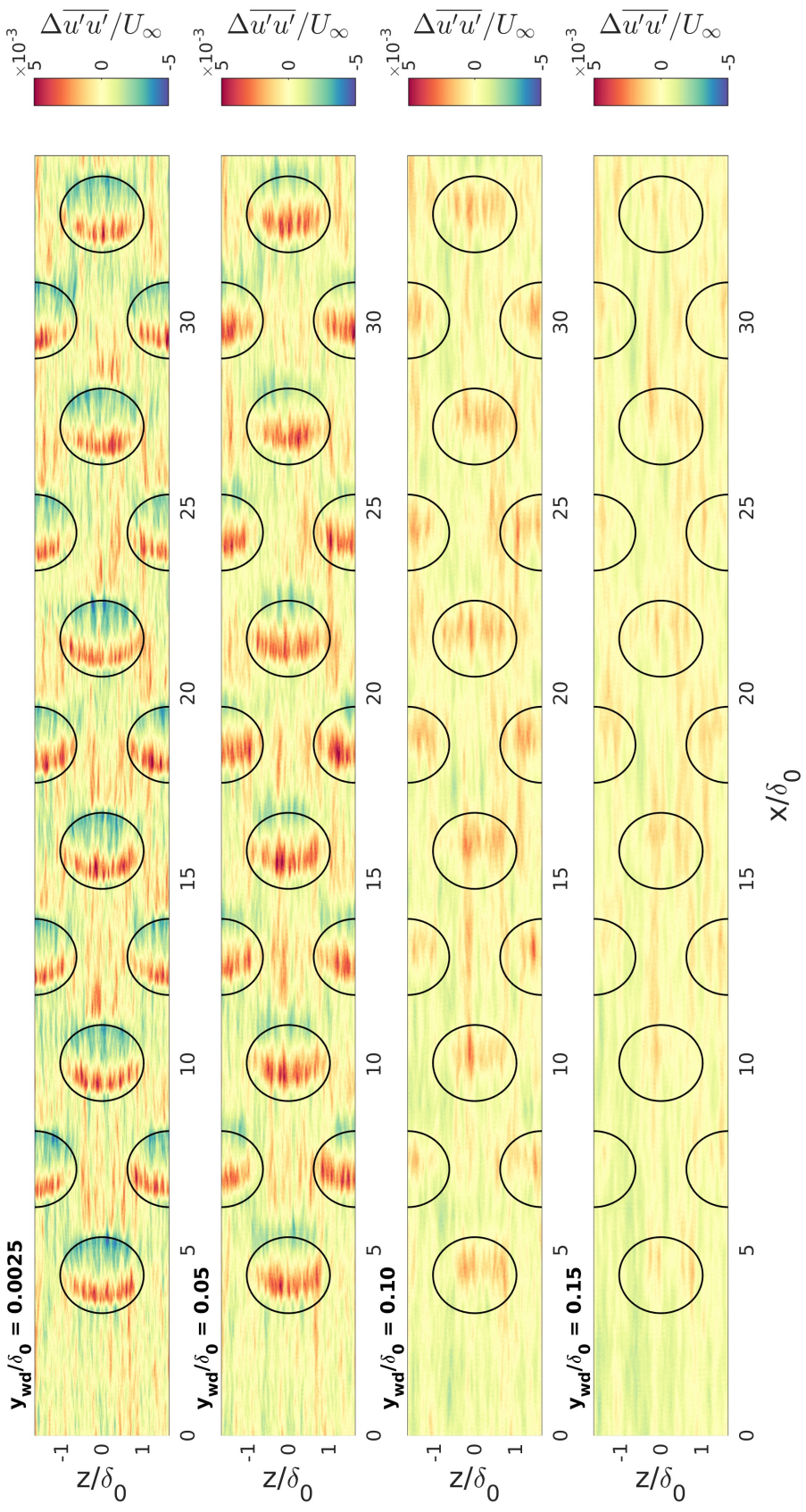

Figure 4-16: Mean streamwise fluctuation difference (dimple plate - smooth plate) at $y_{wd}/\delta_0 = 0.0025, 0.05, 0.1, 0.15$. Black contour lines indicate dimples.

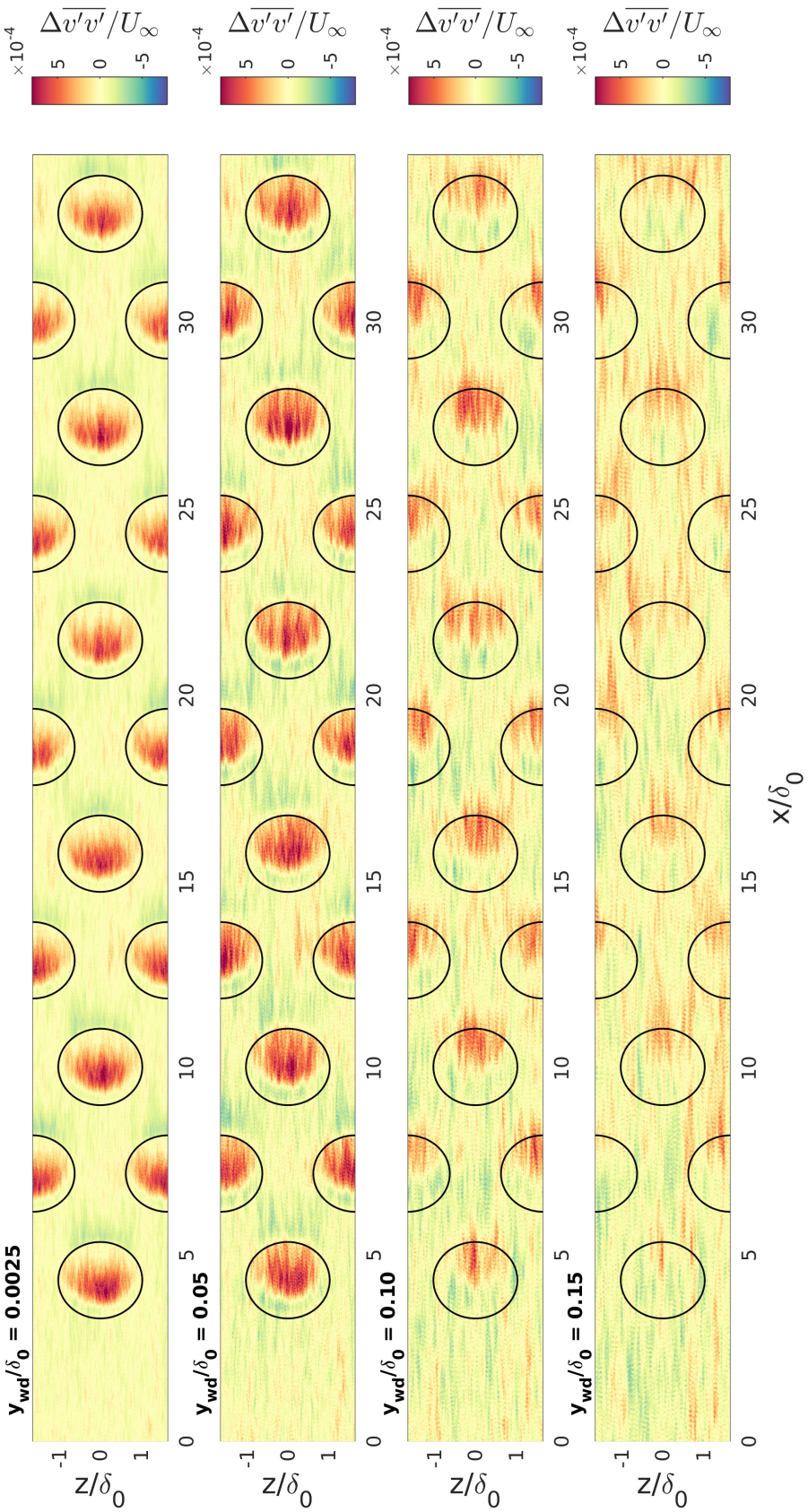

Figure 4-17: Mean vertical fluctuation difference (dimple plate - smooth plate) at $y_{wd}/\delta_0 = 0.0025, 0.05, 0.1, 0.15$. Black contour lines indicate dimples.

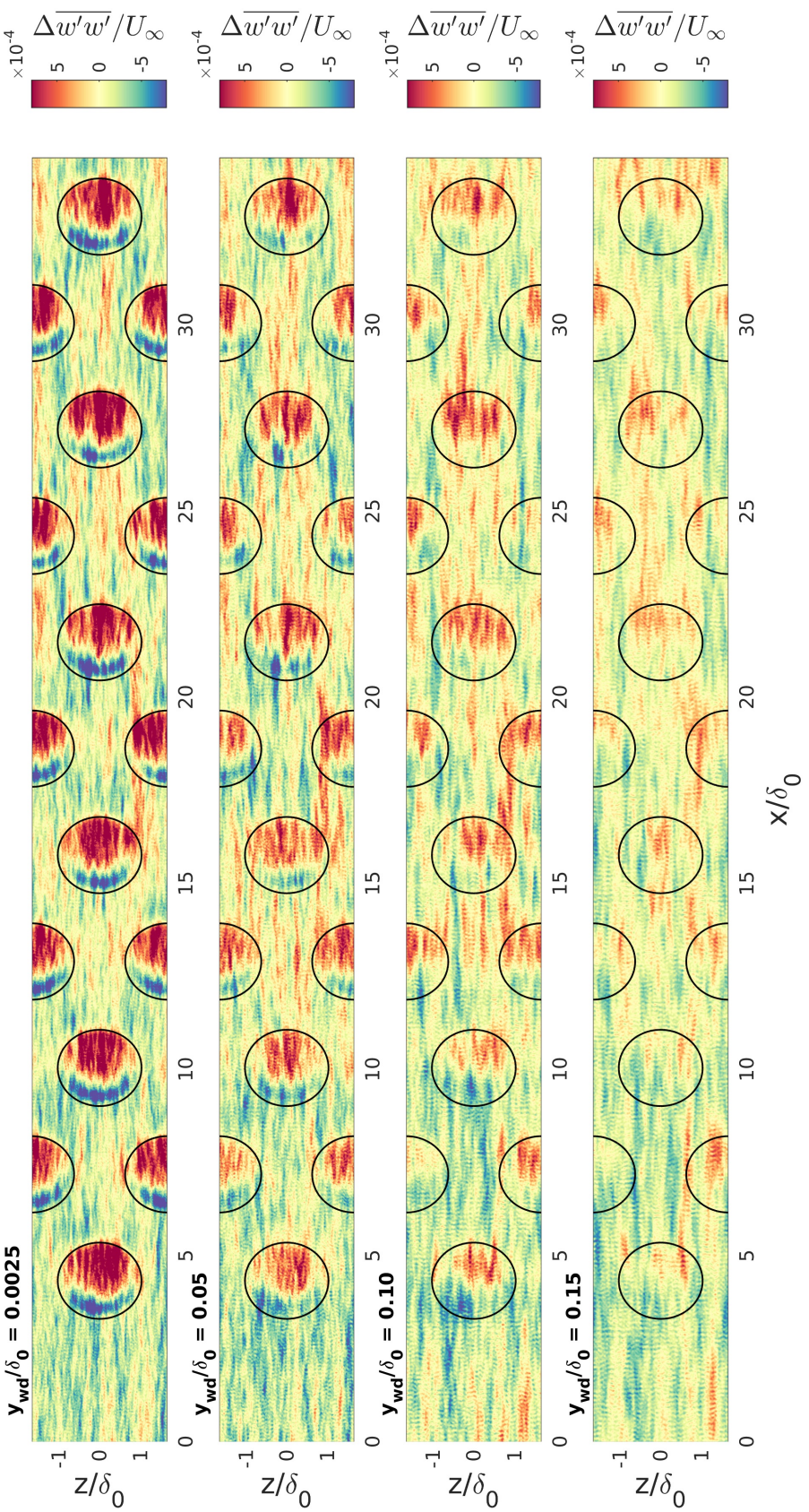

Figure 4-18: Mean spanwise fluctuation difference (dimple plate - smooth plate) at $y_{wd}/\delta_0 = 0.0025, 0.05, 0.1, 0.15$. Black contour lines indicate dimples.

4-3 Mean boundary layer profiles

In the previous section, the mean flow and mean fluctuations are investigated at a few levels and cross-sections in some streamwise locations. In this section, an averaged vertical profile inside the dimple will be presented. Each boundary layer profile inside the dimple is shifted according to its distance from the surface. Since the grid in the y-direction is stretched, spline interpolation is carried out to average the boundary layer profile. Fig. 4-19 shows the averaged boundary layer profiles over the $2nd$ to the $5th$ dimple. All the quantities are scaled in wall units. The black line indicates the mean streamwise velocity, and its value is indicated in the right y-axis. The fluctuations are the coloured lines with its value indicated in the left y-axis. The solid line represents smooth plates; whereas the dashed line represents the dimple plate. Firstly, it can be found from the black lines that dimples result in smaller skin friction, as indicated by the larger value in $\overline{u^+}$. The larger $\overline{u^+}$ value is observed across all downstream dimples. It is found that dimple shifts the logarithmic layer upwards, leading to smaller skin friction. For the mean fluctuations, dimple increases the intensity, meaning that the TBL has a higher turbulent activity. The increased intensity are observed in every fluctuation components and every dimple. The buffer layer shows a larger response; whereas the viscous sub-layer only shows a minimal intensity increase. The influences are mainly in the lower layer of the TBL. In the wake region and above, the influence is insignificant, and the intensity return to its normal level. Overall, a higher turbulence intensity is found in the lower layer. This finding is consistent with the results from van Nesselrooij et al. (2016), where a small increase in the lower layer is found in one of their dimple setups. The figure from van Nesselrooij et al. (2016) is listed in Fig. 4-20 for comparison.

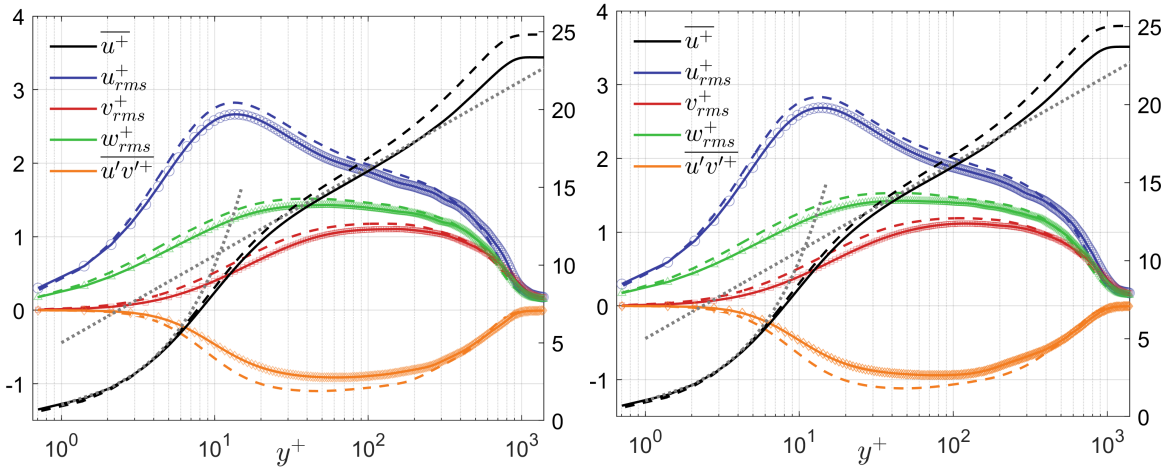

(a) Averaged over the $2nd$ center dimple region, $x/\delta_0 = [9.0, 10.1]$

(b) Averaged over the $3rd$ center dimple region, $x/\delta_0 = [14.7, 16.8]$

Figure 4-19: Mean boundary layer profiles scaled in wall units. Right y-axis: $\overline{u^+}$. Left y-axis: $\overline{u'v'^+}$ (orange), u^+_{rms} (blue), v^+_{rms} (red), w^+_{rms} (green). Solid lines: smooth plate. Dashed lines: dimple plate. The grey lines indicate the theoretical values with viscous sublayer being $u^+ = y^+$ and logarithmic region $u^+ = (1/\kappa)\log(y^+) + B$ with $\kappa = 0.41$ and $B = 5.1$.

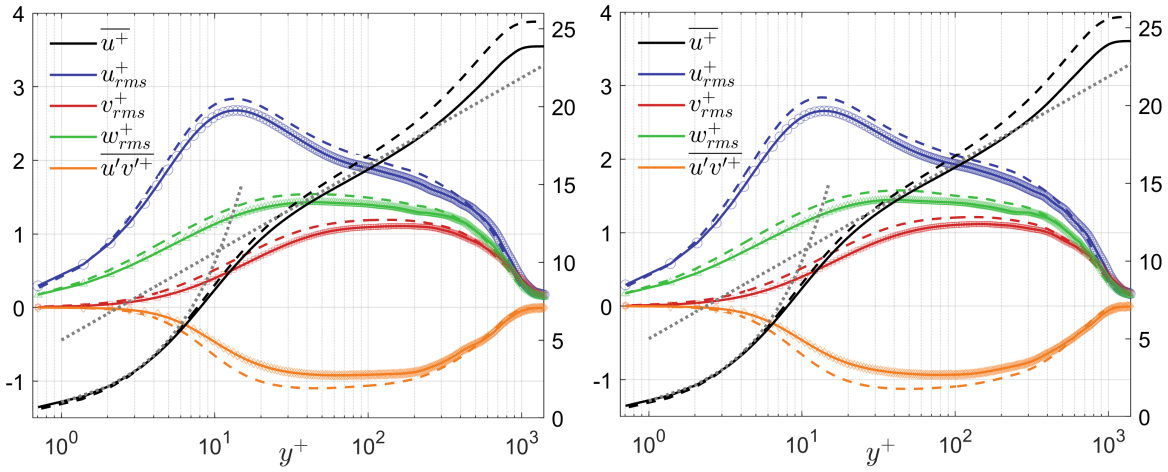

(c) Averaged over the $4th$ center dimple region, $x/\delta_0 = [20.4, 22.5]$

(d) Averaged over the $5th$ center dimple region, $x/\delta_0 = [26.1, 27.2]$

Figure 4-19: Mean boundary layer profiles scaled in wall units. (contd.)

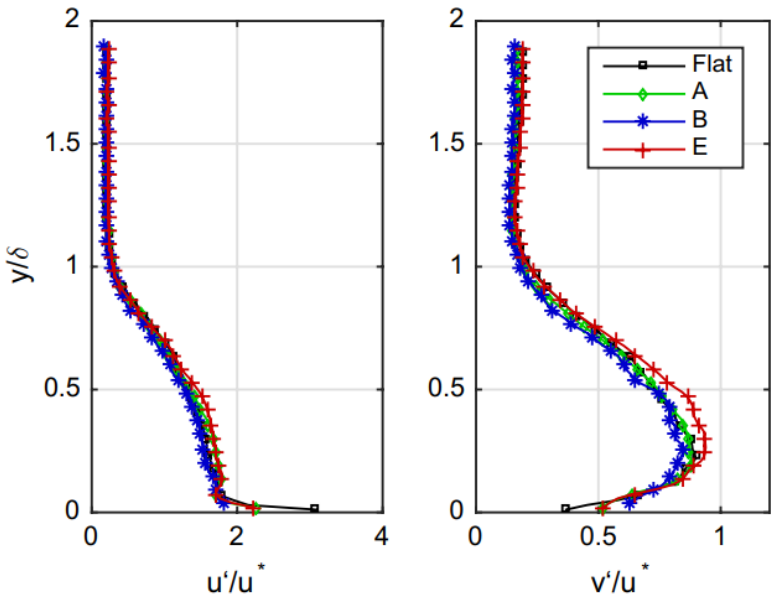

Figure 4-20: Fluctuation profiles at $Re_D = 40,000$. A, B and E refers to different dimple set up. A has a depth ratio $d/D = 2.5\%$ with a staggered layout. B has a depth ratio d/D of 2.5% with an aligned dimple arrangement. E has a similar set up as A, but with d/D of 5.0% (van Nesselrooij et al., 2016)

4-4 Drag results

The drag coefficient is derived from the solver output shear and pressure values. The output module is modified to output the statistics of shear components in streamwise direction only, instead of the Euclidean norm of the whole shear tensor. In detail, the stress τ can be

expressed as:

$$\tau = 2\mu\ \mathbf{S} \tag{4-1}$$

where $\mathbf{S}$ is the rate-of-strain tensor:

$$\mathbf{S} = \frac{1}{2}\begin{bmatrix} 2\frac{\partial u}{\partial x} & \frac{\partial u}{\partial y}+\frac{\partial v}{\partial x} & \frac{\partial u}{\partial z}+\frac{\partial w}{\partial x} \\ \frac{\partial v}{\partial x}+\frac{\partial u}{\partial y} & 2\frac{\partial v}{\partial y} & \frac{\partial v}{\partial z}+\frac{\partial w}{\partial y} \\ \frac{\partial w}{\partial x}+\frac{\partial u}{\partial z} & \frac{\partial w}{\partial y}+\frac{\partial v}{\partial z} & 2\frac{\partial w}{\partial z} \end{bmatrix} \tag{4-2}$$

To extract the shear stress in streamwise direction, only $S_{1,2}$ and $S_{1,3}$ are retained. Fig. 4-21 portrays the top-view of the skin friction, form drag and the resulting total drag. For comparison, the smooth plate skin friction coefficient is also included in the plot.

Firstly, for the pressure coefficient, it can be found that the upstream/downstream half of the dimple has a negative/positive drag contribution, respectively. At the leading edge and trailing edge, there is an opposite contribution, and this is due to the edge rounding of the dimple surface. Overall, the pressure coefficient distribution is developed due to the higher pressure formed inside the dimple. Compared to the RANS simulation from van Nesselrooij (2015), a sharper pressure drag distribution is obtained. Also, the magnitude inside the dimple is larger than van Nesselrooij (2015). This is reasonable since current simulation has a much higher resolution than the RANS set up. Nevertheless, several concentric patterns are observed inside every dimple. This is possibly due to the low plate geometry resolution. With a high-resolution grid, the triangulation is not refined enough to form a smooth surface inside the dimple, and some bumping is formed along the triangulation interface. These bumping in a certain region are thus resolved by the solver. Although these bumpings are resolved, they are found only in the surface variables, and are not found in the near-wall layer and above, the author believes the influence on the drag performance and turbulent coherent structure is marginal. The biggest concern will be if these bumping could locally trigger flow separations in the upstream half of the dimple. However, the instantaneous shear plots in Appendix. B-1 rejects such possibility. Also, the concentric pattern is symmetrical inside the dimple. This suggests that the impact on the average pressure and friction coefficients will be small. Still, to address this issue, new plate geometry has been implemented with much-refined triangulation. The simulation is still ongoing.

Moving on to the skin friction, current high-resolution implicit LES reveals small skin friction in the upstream half of the dimple, and an opposite increased skin friction in the downstream half. The concentric pattern can also be found in the skin friction, but it is relatively insignificant compared to the pattern in pressure coefficient. Away from the dimple region, influence extends to almost every plate area. In the dimple wake region, smaller skin friction is observed; whereas in the inflow region, the skin friction is increased. Compared with the smooth plate skin friction, these upstream/downstream variations are not due to the spatial development of TBL. It must come from the influence of dimples. The extends can be as long as $1.5D$, which is larger than what Mitsudharmadi et al. (2009) have reported as $0.2D$.

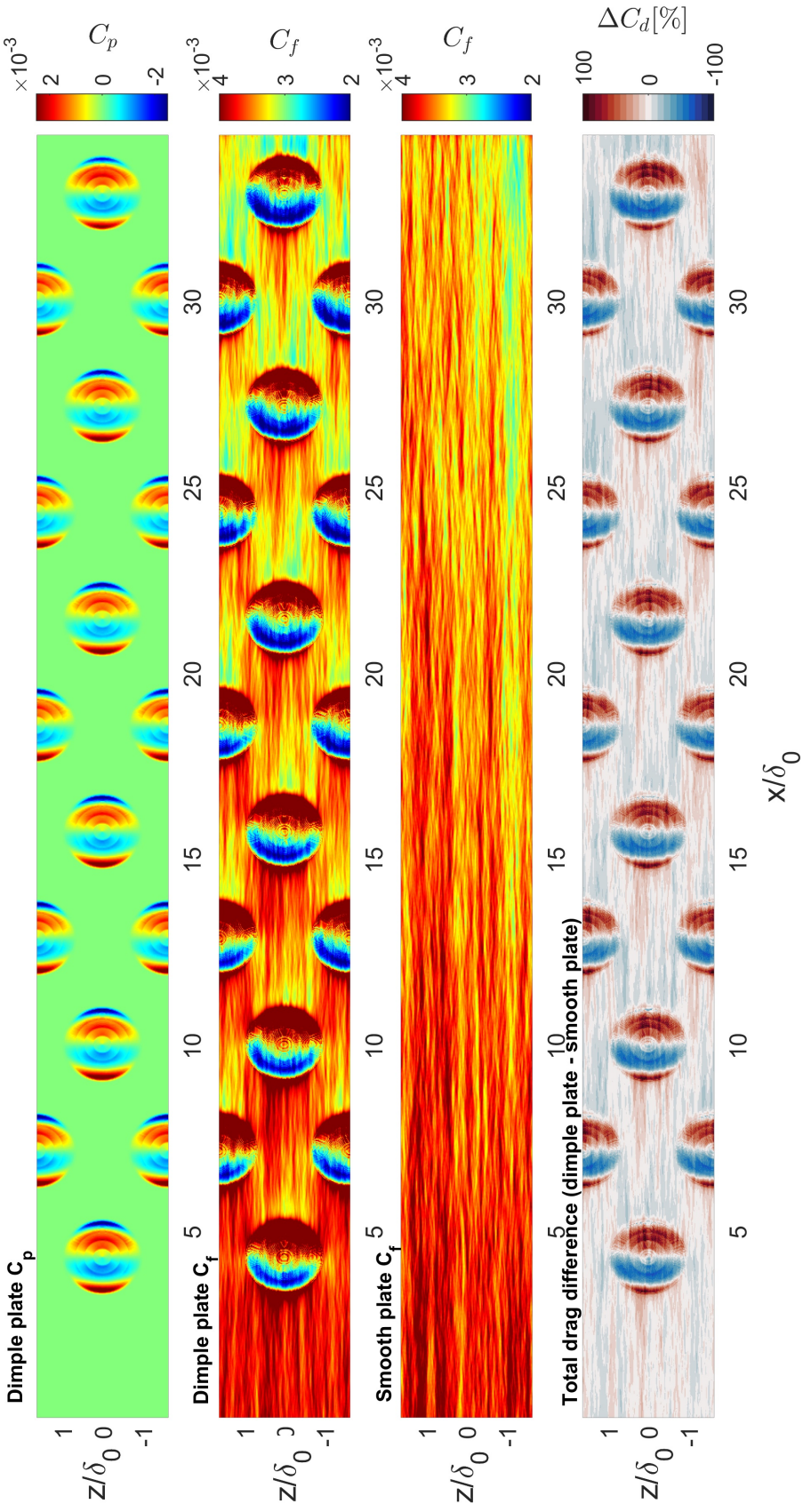

Figure 4-21: Top-view of the mean pressure coefficient, skin friction and total drag difference (dimple plate - smooth plate).

Lastly, a relative difference between the two plates is computed. Since the grids in the horizontal plane are uniform and have the same resolution, the skin friction from the smooth plate is directly subtracted from dimple plate without any interpolation. The result suggests that dimples reduce the total drag in the upstream half of it, but increase in the downstream half. The magnitude variation can be as significant as 70% of the local smooth plate C_f. Away from the dimples, the influence can be clearly seen, but the magnitude is relatively small, within the order of 5%.

Next, spanwise averaged drag is computed to investigate the spatial development of the total drag under the dimple plate. However, the observation made from the top-view plot reveals that the response of surface forces inside the dimple is mostly symmetrical, like an odd extension of a function. It is thus very subtle to infer how the gross effect of dimple on the total drag will be by merely plotting spanwise averaged quantities. Therefore, besides spanwise averaged drag, the streamwise averaged drag is also computed by integrating from the inflow position $x/\delta_0 = 0.$ to any arbitrary downstream location x and dividing the enclosed plate area. Fig. 4-22 shows the spanwise averaged total drag and its streamwise averaged development. It is found that the total drag undergoes a series of oscillations. As the flow travels through a dimple, the drag firstly increases and then followed by a significant drop. As it travels to the downstream half of the dimple, a similar response occurs but with reversed sequence and sign. Inspecting the streamwise averaged total drag, dimple starts having a total drag reduction; but as the flow travels downstream, the gross effect becomes the opposite. Compared two total drag plots, it seems that the total drag reduction at the start could be due to the influence from upstream half of the dimple. Notably, the skin friction at the inflow station shows a small deviation between two plates. The inflow C_f has a 0.6% difference. This could be due to the slightly different meshing, influence from the recycling module. This issue will be further discussed in Chap. 6-1. Therefore, considering the uncertainty of the inflow value, the effect of a complete dimple seems to be neutral to a small total drag increase.

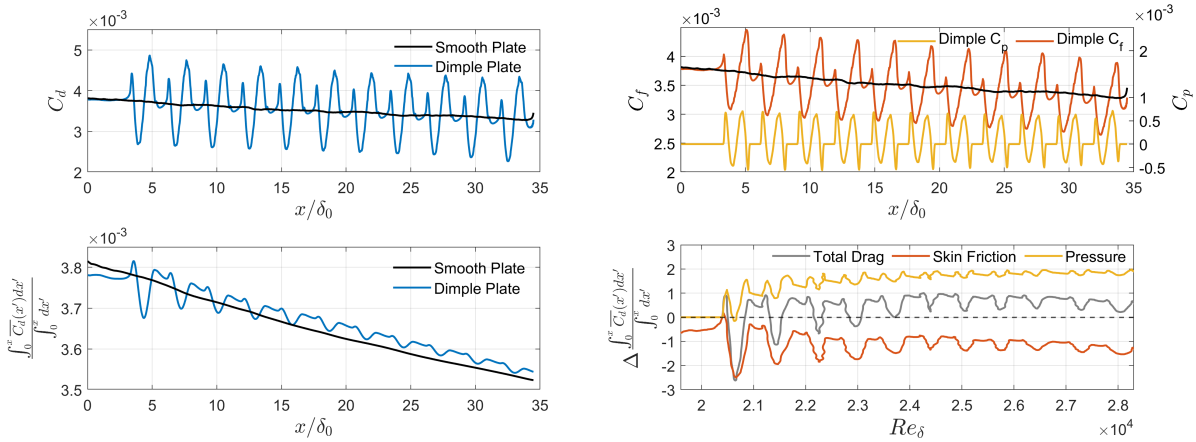

(a) Spanwise averged total drag and its integrated value.

(b) Total drag decomposition and its integrated value.

Figure 4-22: Spanwise averaged Drag of the smooth plate and dimple plate. In the total drag decomposition plot, the left y-axis is the skin friction coefficient; and the right axis is the pressure coefficient.

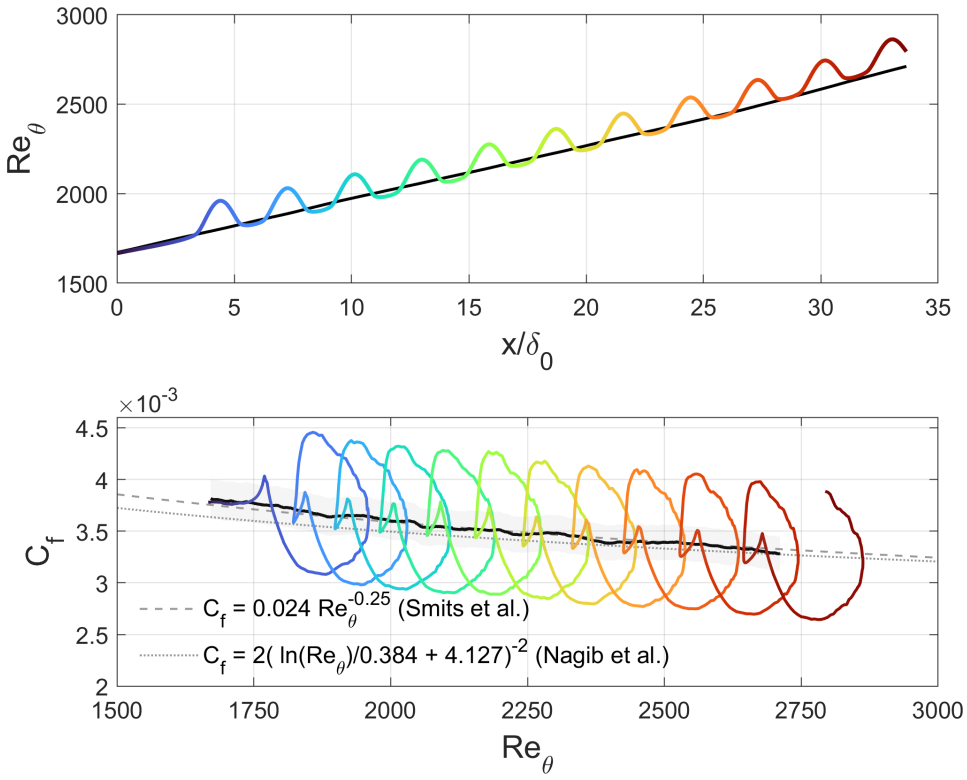

Figure 4-23: Development of the spanwise averaged Re_θ and skin friction versus Re_θ plot. Black line is the smooth plate. Coloured line is the dimple plate. The colour gradient indicates the trajectory along the streamwise direction.

Further decomposing the total drag into skin friction and pressure components in Fig. 4-22b, unlike the total drag, the skin friction variation of the dimple plate is more symmetrical inside each dimple: the leading edge peak strength is comparable to the trailing edge peak. Notes that the y-axis is different for two coefficients. For the pressure coefficient, it shows a similar variation and has the same amplitude as the skin friction. In addition to total drag decomposition, the difference of the integrated total drag between two plates is also computed. The x-axis is the Reynolds number based on the boundary layer thickness, Re_δ. The resulting trend reveals that dimples on average lead to a small total drag increase, in the order of 1%. The above calculation involves the averaged total drag over the whole plate.

The skin friction is further compared with the smooth plate on the Re_θ axis, shown in Fig. 4-23. The coloured-gradient-line indicates the trajectory of the dimple plate. Interestingly, the momentum thickness oscillates across a dimple, leading to a circular path on the Cf-Re_θ diagram. However, at similar Re_θ value, the corresponding skin friction of the dimple plate is different from the smooth plate, suggesting the underlying TBL is not a typical canonical TBL. This can also be confirmed from the $u^+ - y^+$ plot in Fig. 4-19, where the logarithmic region exhibits a larger slope.

To investigate the impact of individual dimple, a circular averaging region is applied in each dimple, and the resulting total drag contribution is shown in Fig. 4-24. Overall, the variation

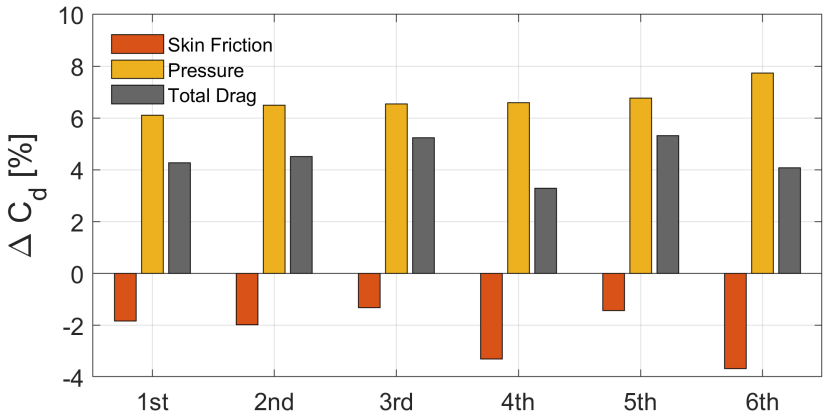

Figure 4-24: Spanwise averaged drag of the smooth plate and dimple plate. In the total drag decomposition plot, the left y-axis is the skin friction coefficient; and the right axis is the pressure coefficient.

across dimples seems relatively large in the skin friction component. This could be due to the spanwise low-speed streak in two plates. During the simulation initialisation, a random seed is picked by the solver to generate the perturbed initial field. It is thus possible that different initial field leads to distinct spanwise structures, and eventually lead to slightly different skin friction distribution. Nevertheless, on average, $\approx 4\%$ total drag increase inside the dimple is obtained, with a 2.8% skin reduction and 6.2% form drag increase. The magnitude of the skin friction reduction is about half of the increased form drag.

All in all, present drag result seems supporting the finding from Spalart et al. (2019) in Fig. 1-2. The order of total drag increase is also in agreement with Spalart et al. (2019). Compared with other researches, shown in Fig. 4-26, present ILES does not found a total drag reduction. All the newly conducted studies yield similar order of the drag increase. According to the results from van Nesselrooij et al. (2016), shown in Fig. 4-25, with a Reynolds number based on dimple diameter Re_D of $34,000$, the simulated total drag reduction would be around 3%! While it could be possible that somewhere goes wrong in the calculation of surface shear, recent measurement conducted by van Campenhout et al. in DUT also obtained a 1% drag increase, which is in line with the recent results from Spalart and van Campenhout. With this regard, it is unlikely that current simulation has a potential systematic bias in drag calculation. In addition, to re-examine previous work in DUT, van Campenhout et al. also did a few validation measurements with regard to the plate set up from Tay, Khoo, et al. (2015) and found drag increases instead. These results contradict previous drag measurement. They argued that those drag reduction measurement could be due to the pressure distortion near the tunnel leading edge and trailing edge, and also the correction of channel width for the channel flow measurement. In detail, they reproduced the set up from van Nesselrooij et al. (2016) and investigate the data processing strategy. With the old strategy, they found an overall drag reduction of 0.5%. However, having corrected the trailing edge pressure, a steady 1% drag increase is retrieved. Similarly, for the Channel flow set up from Tay, Khoo, et al. (2015), they found that after correcting the increased channel width due to the dimple depression, the measured drag reduction is annulled, and about 6% drag increase is recovered. Given those drag increase facts, an investigation of dimple working mechanism is still favoured.

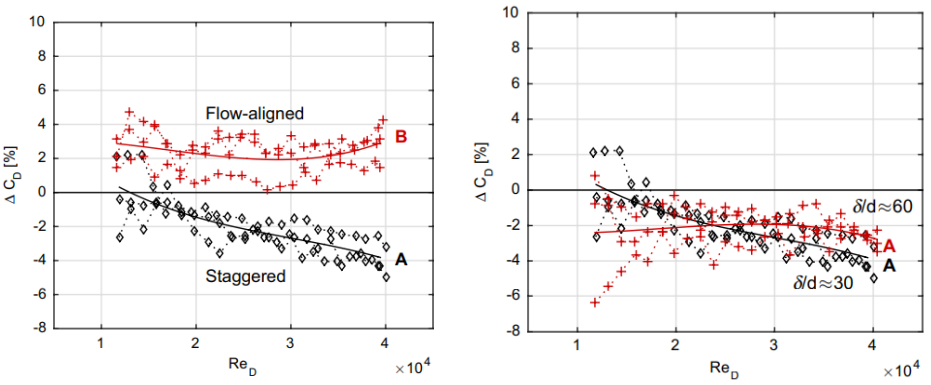

(a) Effect of dimple pattern.

(b) Effect of boundary layer thickness.

Figure 4-25: Drag measurement with DUT16 dimple configuration. (van Nesselrooij et al., 2016; van Campenhout et al., 2016)

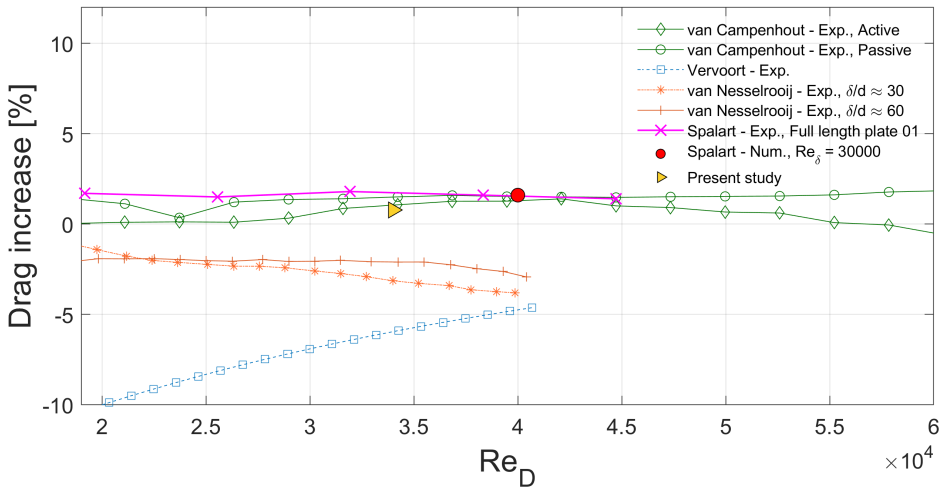

Figure 4-26: Synthesised drag results from van Nesselrooij et al. (2016); van Campenhout et al. (2016) and Spalart et al. (2019). Figure is taken and redrawn from van Campenhout et al. (2016).

From the mean flow top-view in Fig. 4-12, a significant spanwise oscillation is found in the buffer layer, which could still hint a drag reduction mechanism that is analogous to spanwise wall oscillation. The spanwise wall oscillation still stands a chance in explaining the 3% skin friction reduction found in the present simulation. Lastly, regarding the convergence issue in Spalart et al. (2019), unfortunately, present simulations do not output the time series of the averaged forces exerted on the plate. Such quantity is indeed stored in the immersed boundary module in the solver, but the output flag are not switched on. Currently, a new set of simulations are being carried out to address the issue of plate geometry resolution and outputting the time series of averaged forces.

4-5 Summary

In this chapter, mostly the results directly drawn from solver output are considered. The involved post-processing is mainly in the calculation of mean quantities. No conditional sampling, ensemble averaging, and spatial gradient are performed. Those variables include mean flow statistics, raw snapshot slices and surface forces.

Firstly, the simulation is validated with skin friction correlations. The results show remarkable agreement with those formulas. Furthermore, the averaged mean profile also shows a consistent trend as the theoretical values. The sensitivity tests are carried out to assess the grid convergence.

Moving on to the mean flow topology and its boundary layer profiles, a conffuser-diffuser flow structure is identified. Also, the flow shows no separation. These findings are in line with the literature. The developed spanwise velocity has a vertical extends of $0.2D$ and the developed vertical velocity layer is deeper, about $0.4D$. Those layers do not scale with downstream location, which suggests the flow structure is only a function of Re_D, not Re_x. Still, given such consistency, a distinct near-wall spanwise velocity layer is observed. This residual layer is found only in the upstream half of the dimple, and its vertical extent is limited inside the dimple. This near-wall residual layer results in a diffuse flow inside the dimple. Inspecting the spatial development of the mean flow field, a striking spanwise oscillation sequence is spotted. Interestingly, given the fact that the mean flow field shows the most response in the near-wall layer, such spanwise oscillation sequence is only found above the buffer layer. For the mean boundary layer profile, the mean flow profile has a higher u^+, meaning lower skin friction. The fluctuation profiles, on the other hand, show a small increase mainly in the buffer layer. The influence on the fluctuation diminishes farther away from the wall. In the wake region, the difference between the two plates is almost indiscernible in every fluctuation profile.

Lastly, the total drag is retrieved from the solver shear tensor. Only the $\tau_{1,2}$ and $\tau_{1,3}$ are used to compute the skin friction. The top-view of the skin friction suggests that dimple leads to lower skin friction in the upstream half of it, and higher skin friction in the downstream half. Averaged in the spanwise direction, dimple leads to oscillating total drag distribution. With the averaged integrated total drag and its decomposition, $\approx 1\%$ total drag increase is found. Further averaging over each dimple, the pressure drag increase is about 6.2%, with a skin friction reduction of 2.8%. This drag results seem to be contradicting previous drag measurement from DUT (van Nesselrooij et al., 2016; van Campenhout et al., 2016) and NUS (Tay, Khoo, et al., 2015; Tay and Lim, 2018). However, recent validation measurement from DUT might support drag increase result, as the re-installation and measurement of previous work from van Nesselrooij et al. (2016); Tay, Khoo, et al. (2015) reveals a drag increasing result. Explanations are also given, linking to the possible data bias in pressure correction. Nevertheless, the skin friction effect might be originated from the spanwise oscillation seen from the top-view of the mean spanwise flow. A detail investigation is still favourable. Therefore, in the following chapter, three different statistical analysis method will be employed to evaluate the response in the turbulent coherent structure, and explore the possible working mechanism of the skin friction reduction.

Chapter 5

Analysis

In this chapter, three different statistical analysis techniques will be employed to investigate the turbulent coherent structure. The content is organized as follows. Firstly, Chap. 5-1 examines the formation of the near-wall velocity layer observed inside the upstream half of the dimple. Chap. 5-2 then starts sampling the collected snapshot data to evaluate the occurrence of quadrant events and their contribution to the Reynolds shear stress. After revealing the statistical status of the coherent structure, Chap. 5-3 steps forward to evaluate the development of intense quadrant events. In Chap. 5-4, a relation between the responses in mean flow, coherent structure and skin friction will be developed qualitatively. Lastly, a discussion on the underlying uncertainties of the above mentioned statistical techniques will be given.

5-1 The formation of near-wall spanwise velocity layer

In the chapter 4-2, a near-wall spanwise velocity layer is observed in the upstream half of a dimple. This near-wall layer has not been reported either from the experimental study by van Nesselrooij et al. (2016); Tay et al. (2014) or numerical investigation by Lienhart et al. (2008); Spalart et al. (2019). Therefore, in this section, further analysis will be carried out to study the mean flow field, and try to explain the origin of such layer.

Fig. 5-4 shows a Zoom-in Y-Z cross-section of the mean spanwise velocity. The left column indicates the upstream half cross-section at $x = xc - 0.75R,\ 0.5R,\ 0.25R$ (xc represents the dimple center); the right column indicates the downstream half. It is found that the layer mainly occurs inside the dimple, and it only exists in the upstream half of the dimple. Also, the strength of such a layer is increased as we approach the dimple centre. This residual layer could be realized by mass conservation. As the flow impinging the dimpled surface, the flow suddenly experiences a depression. Due to mass conservation, locally the flow has to decelerate and expand, leading to a diffuser flow pattern. Since this mechanism is due to the geometry of the plate, and only the near-wall region experience large geometry variation, it could explain why such a pattern only exists in the near-wall layer. However, that is only half the story.

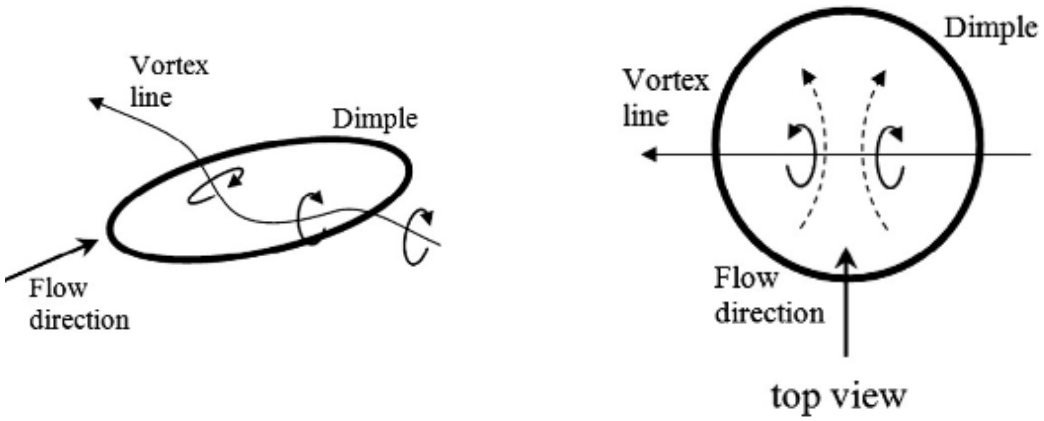

(a) Top-view of the vortex line.

(b) Top-view of the vortex line and induced flow field.

Figure 5-1: The formation of confuser-diffuser flow pattern. (Tay et al., 2014)

The above hypothesis can not explain why the flow in the downstream half does not exhibit a near-wall confuser flow: as the flow leaves the dimple, it should experience a geometry contraction, and hence the flow accelerates, leading to a confuser flow. Nevertheless, the downstream cross-section suggests a diffuser flow pattern, and no near-wall layer is observed. Also, the mass conservation hypothesis can not explain why the upstream layer is stronger as the fluid parcel move towards the dimple centre: the geometry variation is milder as the parcel reaches the centre, so ideally such layer should also be weaker. Therefore, an additional theory must be introduced to explain the origin of the near-wall spanwise velocity layer.

The vortex dynamics provides a different perspective to the simulated flow field by examining the vortex-induced flow field. Utilising Biot-Savart law, the simulated flow field can be decomposed into components induced by vortices. Tay et al. (2014) also uses Biot-Savart law to explain the formation of confuser-diffuser flow structures. They argued that because the vortex line must follow the dimpled surface, the principle vortex line, which is pointed towards positive z-axis, will be tilted in such a way that the induced flow field forms a confuser-diffuser flow pattern. Fig. 5-1 shows the overview of a vortex line and the induced velocity field. Since the near-wall spanwise velocity layer is observed below the confuser-diffuser structure, it must be relative to the interaction between vortex lines and dimple surface. Fig. 5-2 gives an overview of the vorticity components in wall coordinate $y_{wd} = 0.01$ and $y_{wd} = 0.02$.

For the streamwise vorticity, it forms a quadruple around the dimple edge. Interestingly, the strength between the upstream half and downstream half is different: the downstream half ω_x is stronger. The quadruple pattern is tilted towards downstream at a higher level. Considering a positive streamwise vortex that forms at the edge of the upstream half dimple, the induced velocity field is a clockwise circulation. Inside the dimple, it generates a spanwise velocity component that enters the Y-Z plane, which translates to a confuser flow structure. Similarly, the negative streamwise vortex forms a counter-clockwise circulation and induces a diffuser flow structure inside the dimple. Combining two components and observing the quadruple ω_x in Fig. 5-2a, it can be concluded that the streamwise vorticity forms a confuser-diffuser

flow structure across the dimple.

Moving forward to the vertical vorticity ω_y, the vorticity has a dipole-like distribution. In contrast to streamwise vorticity, the vertical vorticity does not tilt downstream. Considering a positive vertical vorticity core and a negative vorticity core at the negative and positive spanwise poles respectively, the wall-normal vorticities induce flows on the x-z plane. Positive ω_y forms a counter-clockwise flow around the negative spanwise pole; negative ω_y forms a clockwise flow around the positive spanwise pole. Overall, this pattern forms a difuser-confuser flow structure. Therefore, the induced flow field by ω_y *opposes* the confuser-diffuser flow formed by ω_x.

After inspecting the induced velocity field by each vorticity components, a hypothesis could be proposed, in which the formation of near-wall spanwise velocity layer could be explained. The flow over the dimpled surface is developed due to the mass conservation and vortices induced velocity field. Firstly, as the flow crosses the dimple, locally the depression creates an expansion in space, and thus to satisfy the mass conservation law, a diffuser-confuser structure is formed. Then considering the induced velocity field, the streamwise vorticity creates a

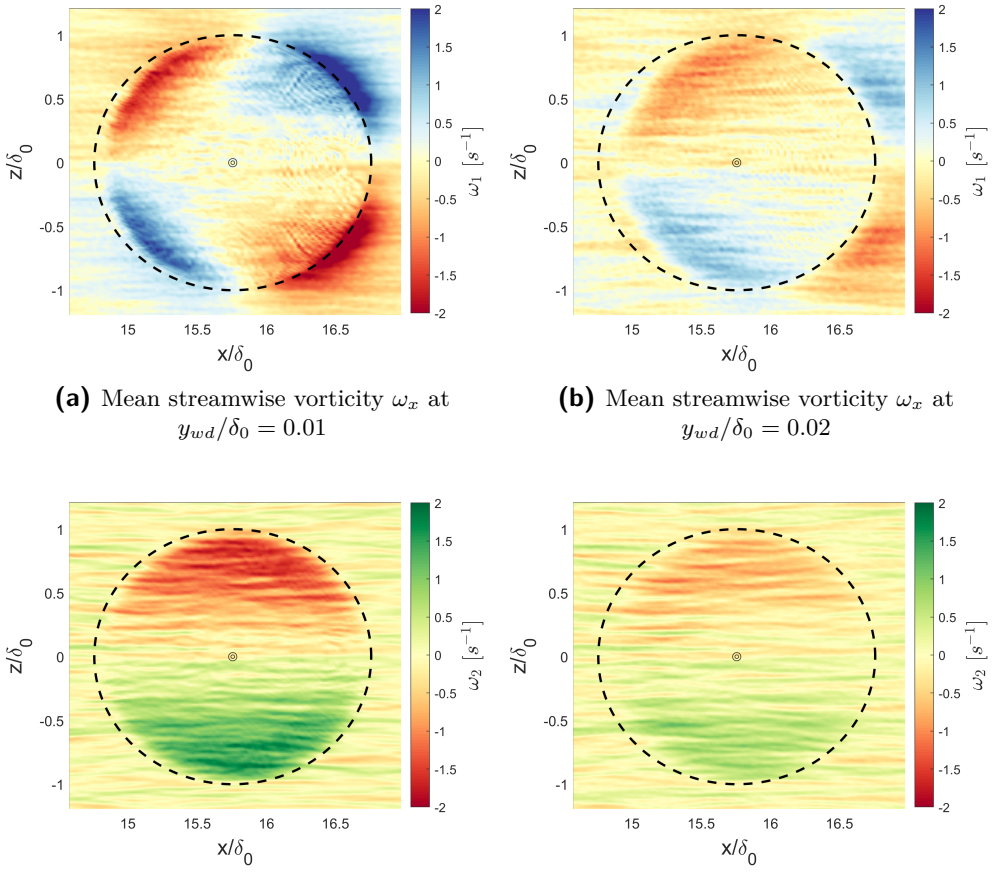

(a) Mean streamwise vorticity ω_x at $y_{wd}/\delta_0 = 0.01$

(b) Mean streamwise vorticity ω_x at $y_{wd}/\delta_0 = 0.02$

(c) Mean vertical vorticity ω_y at $y_{wd}/\delta_0 = 0.01$

(d) Mean vertical vorticity ω_y at $y_{wd}/\delta_0 = 0.02$

Figure 5-2: Mean vorticity components over the $3rd$ dimple.

confuser-diffuser structure. Since the upstream half streamwise vorticity is relatively weak, such induced confuser-diffuser flow is annulled by the induced field from the vertical vorticity. The cancellation still leads to a flow field that forms a confuser-diffuser flow structures but leaves a shallow, near-wall spanwise velocity layer in the upstream half of the dimple due to mass conservation. The vortex line visualisation in Fig. 5-3 supports this hypothesis. Fig. 5-3a and Fig. 5-3b visualises the L2-norm of the vorticity vector over the $3rd$ dimple. Firstly, the vector directions are consistent with the results from Tay et al. (2014), meaning that such visualisation could indicate the formation of confuser-diffuser flow structures. The shading suggests that the upstream half is weaker than the downstream half, hinting a less developed confuser-diffuser flow in the upstream half of the dimple. Fig. 5-3c and Fig. 5-3d depicts the L2-norm of the vorticity vector but without the principle component ω_z. The arrow length and shading suggest a relatively weak component in the upstream half of the dimple. It means the L2-norm difference in the upstream half is indeed due to ω_x and ω_y, and the formation of confuser-diffuser flow structure is weaker in the upstream half, leading to a shallow, near-wall spanwise velocity layer.

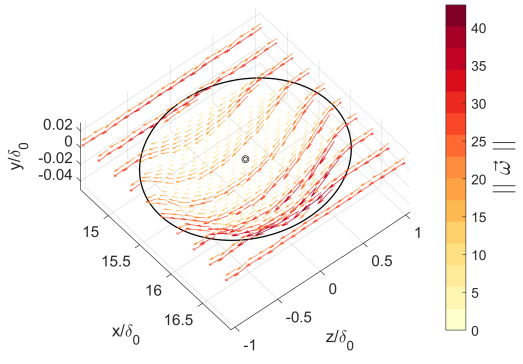

(a) Top-down view of the L2-norm $\|\vec{\omega}\|$

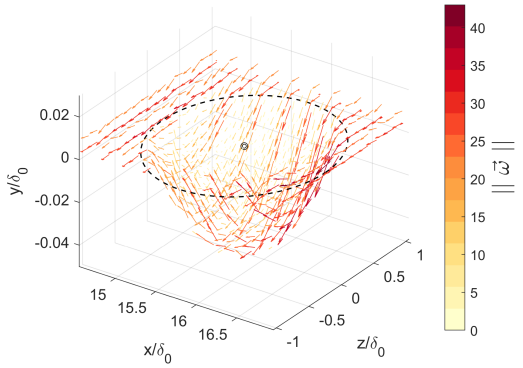

(b) 3D view of the L2-norm $\|\vec{\omega}\|$

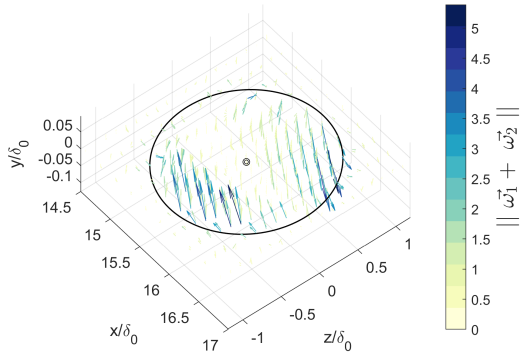

(c) Top-down view of the L2-norm $\|\vec{\omega_x} + \vec{\omega_y}\|$

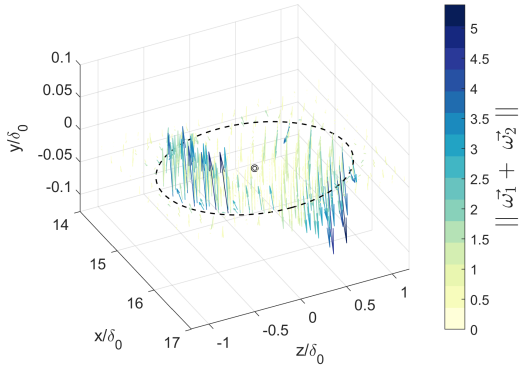

(d) 3D view of the L2-norm $\|\vec{\omega_x} + \vec{\omega_y}\|$

Figure 5-3: L2-norm of the vorticity vector over the $3rd$ dimple. The freestream direction is pointed towards positive x-axis.

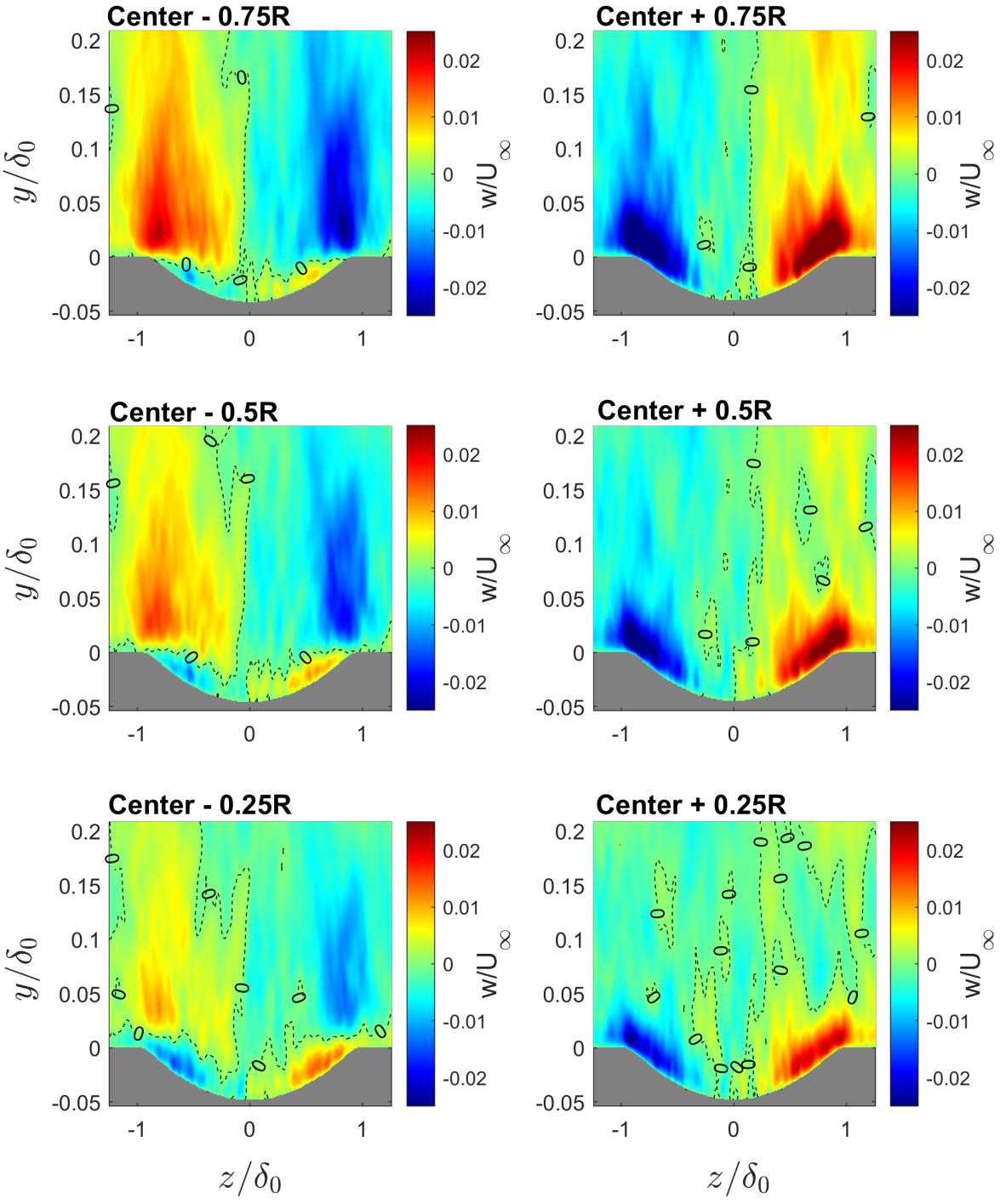

Figure 5-4: Zoomed-in Y-Z cross section of the spanwise velocity. Left column: upstream half cross sections. Right column: downstream half cross sections.

5-2 Quadrant Analysis

Results from the raw scatter data, shown in Appendix. B-5, suggest the impact of dimples on the turbulent boundary layer is barely discernible by visual inspection, compared to other drag-reducing techniques. To further investigate the responses, the raw data is normalised and divided into into 200 × 200 bins. By dividing a continuous variables into discrete categories, it becomes possible to qualitatively describe how dimple affect turbulent boundary layer statistics.

5-2-1 Joint Probability Density Function (JPDF)

The Joint Probability Density Function (JPDF) is calculated by dividing the quadrant incidence in each bin with the binned area. The binned snapshots consist of velocity fluctuations in a rectangle box of $1.05D$ around the dimple and is sampled over one flow-through cycle, resulting in $\approx 2,900,000$ data pairs in each vertical level. The raw data is normalised by its fluctuation level. Such normalisation gives a systematic measure of the turbulent boundary layer internal dynamics between the smooth plate and dimple plate. Fig. 5-6, 5-7 gives an overview of the resulting smooth plate JPDF and the responses under the dimple plate over the $3rd$ dimple at $y/\delta_0 = 0.01,\ 0.02,\ 0.15$ and 0.2. The responses over the $4th$ dimple are in general very similar to the $3rd$. Therefore, for simplicity, we will only show the plots from the $3rd$ dimple, and the results from the $4th$ dimple are summarised in Appendix. B-6. A separate discussion on the response across dimples will be given in the later section.

To begin with, the smooth plate JPDF will be examined. In the buffer layer, $y/\delta_0 = 0.01, \text{and} 0.02$, the main axis is tilted along the Q2-Q4 axis. The tilting is a typical characteristic for anisotropic turbulence. The occurrence of ejection and sweep in the buffer layer is higher than in the wake region. At $y/\delta_0 = 0.02$, Q2 and Q4 account for 68% of the sampled event; whereas at $y/\delta_0 = 0.2$ the occurrence drops to $\approx$ 66%. In the wake region, the data point inside each quadrant spreads more evenly, hinting a more isotropic state of the TBL. It also means a more uniformed velocity distribution and fewer strong events in the population. In contrast to distributions in the wake region, the buffer layer shows a long-tailed

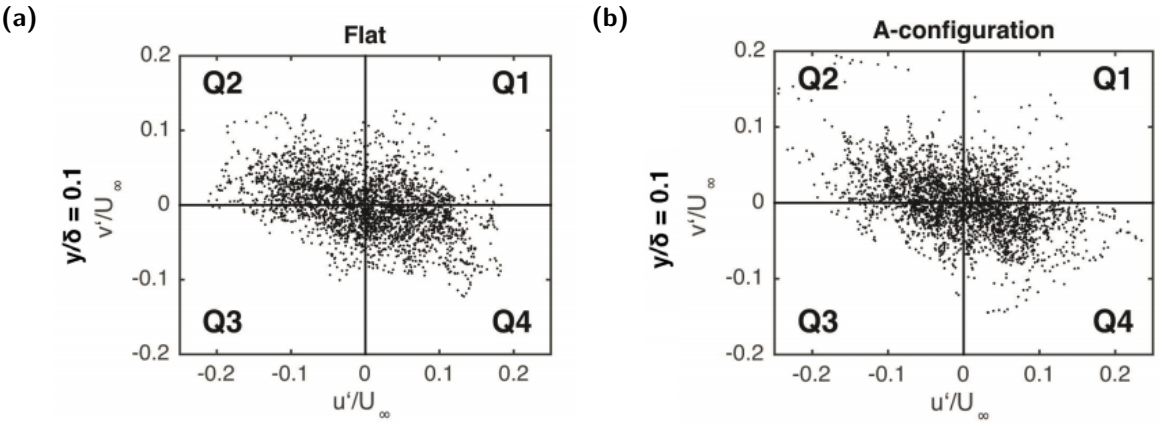

Figure 5-5: Quadrant scatters of a (a) smooth plate and (b) dimple plate at $y/\delta = 0.1$ (lower) with $Re_D = 40000$ (van Campenhout et al., 2016).

distribution. The tails data mainly come from the vertical fluctuations, seen from the longer y-axis extend in the Fig. 5-6a and Fig. 5-6b. Compared with the experimental result from van Campenhout et al. (2016) shown in Fig. 5-5, a consistent result is obtained: the tail distributions are also presented in their scatters, while the sweep and ejection occurrence in the current numerical study gives a higher value than van Campenhout et al. (2016). On average, current sampling gives 66% occurrence while van Campenhout et al. (2016) obtained 64.8%. Such small deviations might be due to the sampling uncertainly or different Re_D. Current Re_D is about $34,000$, whereas the Re_D from van Campenhout et al. (2016) is $40,000$.

After validating the result of a smooth plate, the quadrant scatters of the dimple plate will be studied. Fig. 5-7 depicts the JPDF differences between dimple plate and smooth plate. At $y/\delta_0 = 0.01$ (Fig. 5-7a), quadrant scatters move away from the x-axis. Along the x-axes, the JPDF difference is negative, suggesting the dimple plate induces a stronger vertical fluctuation in the buffer layer. As for the streamwise fluctuation, no dominant patterns are emerged. The responses in the buffer layer decay at a higher level. At $y/\delta_0 = 0.02$, the above motioned

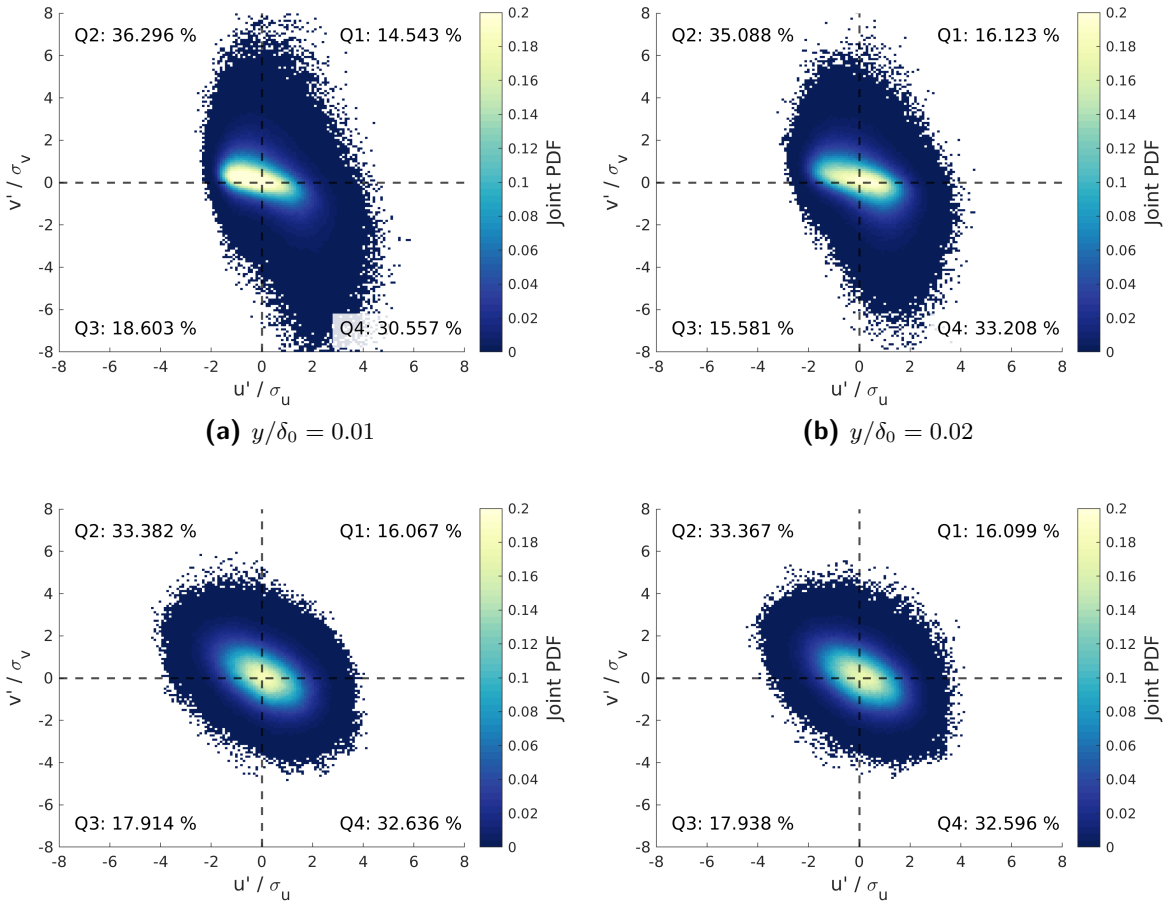

(a) $y/\delta_0 = 0.01$ **(b)** $y/\delta_0 = 0.02$

(c) $y/\delta_0 = 0.15$ **(d)** $y/\delta_0 = 0.20$

Figure 5-6: Quadrant Joint Probability Density Function (JPDF) of a smooth plate at four levels over the $3rd$ dimple. The results are drawn from sampling the raw data into 200×200 bins.

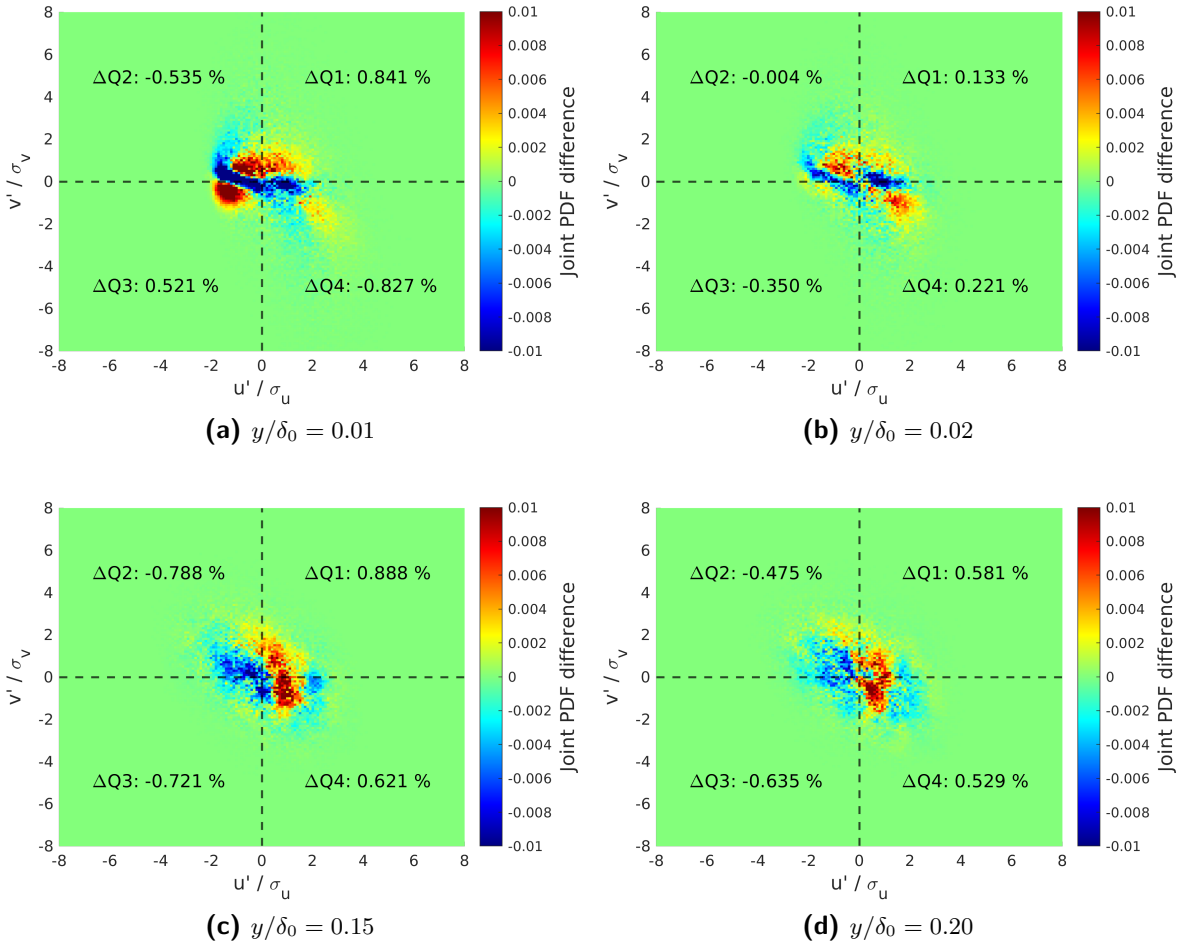

(a) $y/\delta_0 = 0.01$ **(b)** $y/\delta_0 = 0.02$

(c) $y/\delta_0 = 0.15$ **(d)** $y/\delta_0 = 0.20$

Figure 5-7: J-PDF differences (Dimple plate - Smooth plate) at four levels over the $3rd$ dimple.

responses are also found but with smaller magnitude. In the wake region (Fig. 5-7c, 5-7d), the vertical fluctuation responses is no longer found. Instead, a clear shift of the streamwise fluctuation is observed. The scatters move towards the positive x-axis, meaning that dimple increases the occurrence of positive u', which leads to an increased incidence in Q1 and Q4 events.

Overall, although tendencies in increasing the occurrence in stronger v' in the buffer layer and positive u' in the wake region are found, the responses the corresponding quadrants are relatively small. This suggests that the impact of a dimple on the occurrence is minimal, and is of the order of $O(1\%)$. Still, an overall trend can be observed. Dimples increase the occurrence in Q1 and Q4 events.

5-2-2 Weighted Joint Probability Density Function (Weighted JPDF)

In the previous analysis, the raw data scatters are re-sampled into discrete bins, and the corresponding joint probability is calculated. The occurrence in each bin can thus be quantified.

However, JPDF only tells how likely are those events going to happen, but it does not give us the distribution of the corresponding Reynolds shear stress. To extract such information, the JPDF are multiplied by the bin coordinates $u'v' \cdot P(u', v')$. This weighted JPDF is a measure of the contribution from each bin to the Reynolds shear stress. Fig. 5-8 illustrates the contribution of each $u'v'$ pairs to the Reynolds shear stress of a smooth plate. Since stress is the product between JPDF and corresponding coordinates, the weighted JPDF is zero along x and y-axis by definition. Therefore, the scatter is split into quadruples. By the colour shadings, larger contributions are associated with ejection and sweep event. Comparing JPDF with weighted JPDF, it can be realised that the most probable pairs of $u'v'$ do not coincide with the pairs that generate the largest contribution to the Reynolds shear stress. The largest contribution lays on the out-skirt of the maximum JPDF. Therefore, it is found that the intense, energetic events which occur less frequently are the main source of Reynolds shear stress. This phenomenon is especially dominant in the buffer layer sweep event, where a long tail spreading into large v' is observed.

Regarding the responses, it is found that in all four levels, the ejection and sweep motions are

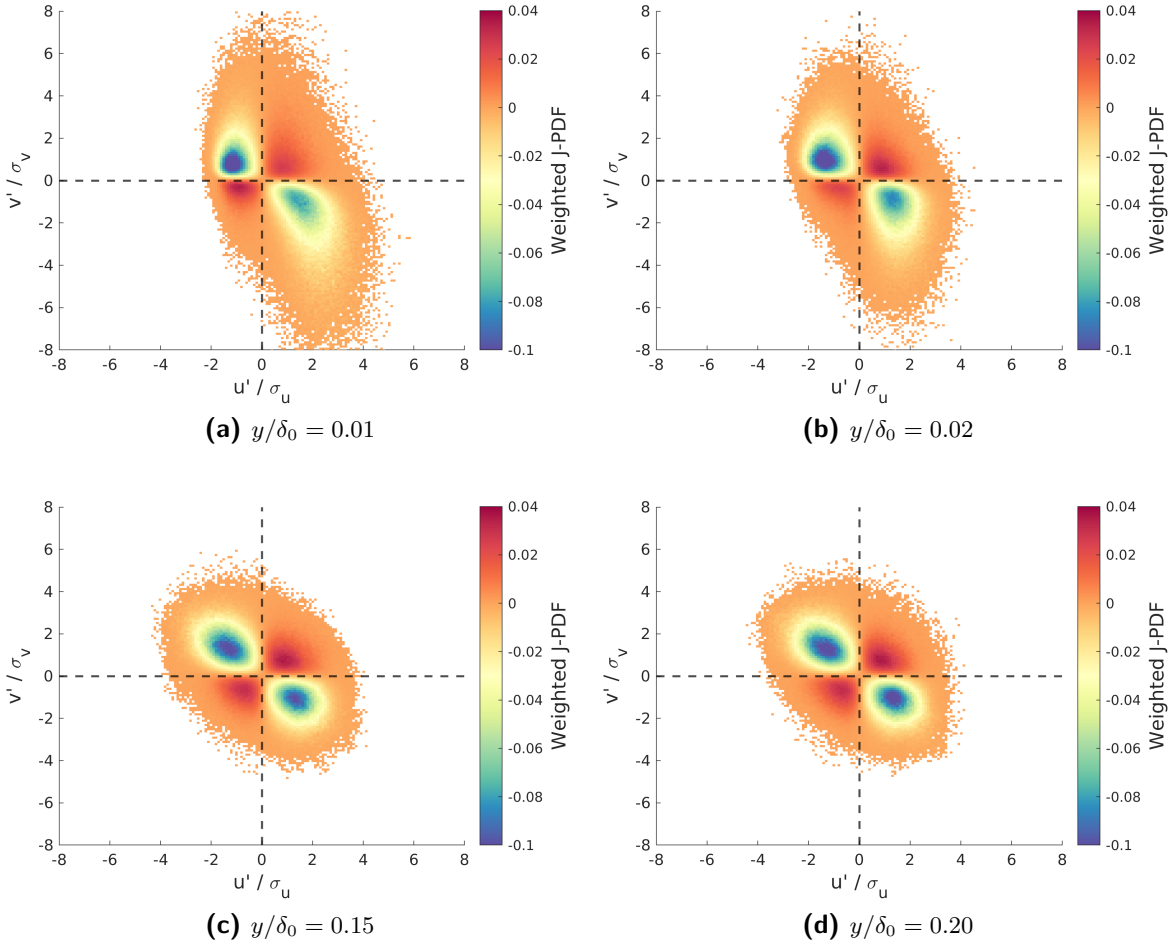

Figure 5-8: Weighted Joint Probability Density Function of a smooth plate at four levels over the $3rd$ dimple. The results are drawn from sampling the raw data into 200×200 bins.

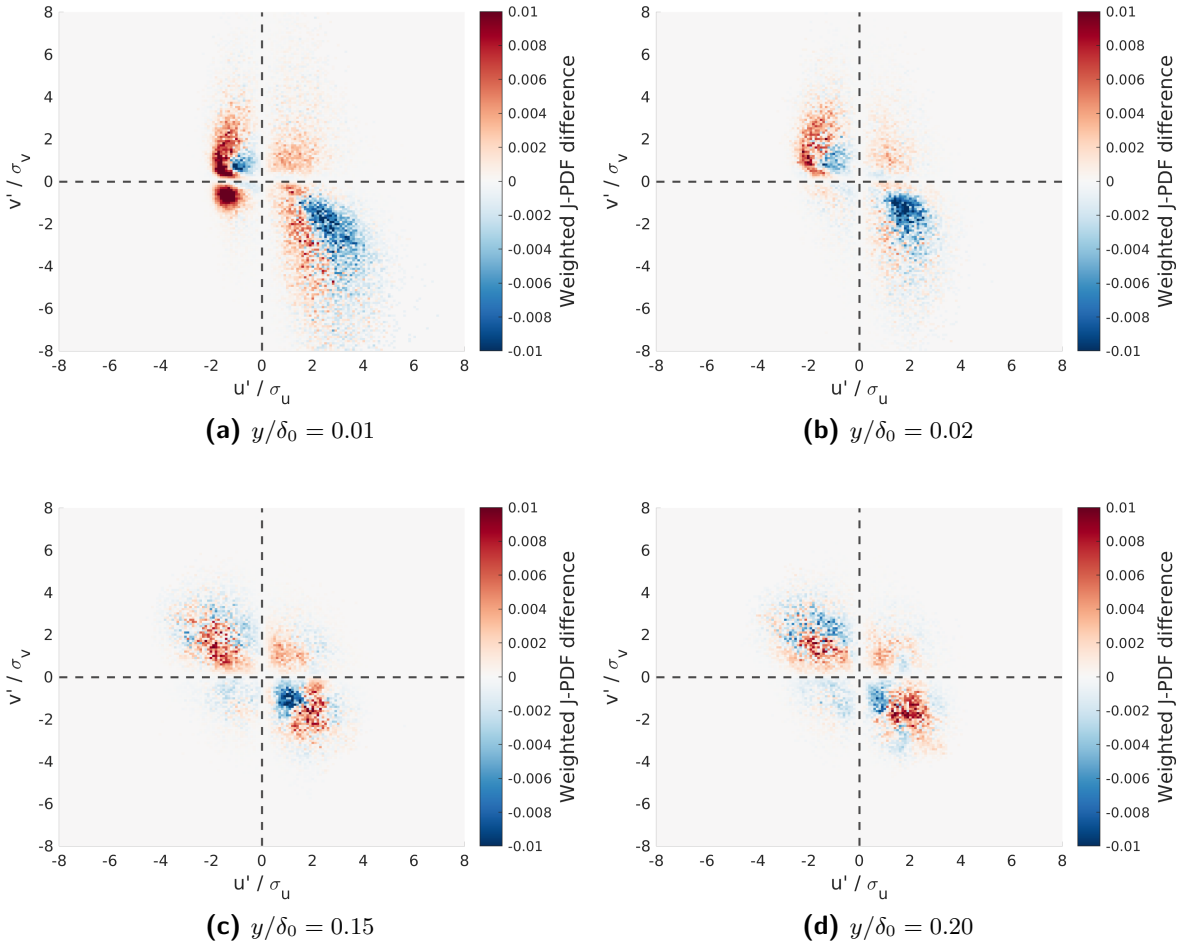

Figure 5-9: Weighted JPDF differences (Dimple plate - Smooth plate) at four levels over the $3rd$ dimple.

the most responsive quadrant compared to inward interaction and outward interaction. It is partially due to the fact that ejection and sweep have prevailing occurrences, so it becomes more sensitive to a unit change of $u'v'$ coordinate. A distinct pattern between the buffer layer and wake region is found. In the buffer layer, the weighted scatters move towards negative x-axis for the sweep and ejection event. Notes that the Reynolds shear stress in both quadrants are negative. Therefore, the extrema are actually moving towards positive x-axis. It means the principal contributors to the Reynolds tress in the ejection quadrant are the weaker ones. In contrast, the more intense sweep events are now the main source of the Reynolds stress inside the sweep quadrant. Also, a long tail in the sweep event is observed, meaning the response in the sweep motion extends to the intense event. In the wake region, the responses are relatively mild and are confined in the weaker event. The weighted scatters in the ejection motion move towards positive y-axis, hinting the contributor now shifts to a stronger event. On the contrary, the primary stress source in the sweep quadrant becomes the weaker event. To sum up, the JPDF and weighted JPDF give a qualitative description of the internal structures of the turbulent coherent structure and its contribution to the Reynolds

shear stress. Moving a step forward, the following section performs conditional sampling based on the hole-filtering technique to evaluate the contribution from each quadrant event.

5-2-3 Hole-filtering sampling

Weighted JPDF tells us how each fluctuation bin contributes to Reynolds stress. However, it did not quantitatively reveal how different event strength contributes to Reynolds stress. Physically, the shear stress can be interpreted as the streamwise momentum transferred by the vertical fluctuations. Therefore, it is the product of u' and v' that defines such a stress-generating event. To investigate response in different strength, a conditional sampling technique based on the magnitude of $u'v'$ is applied. This so-called hole-filtering technique

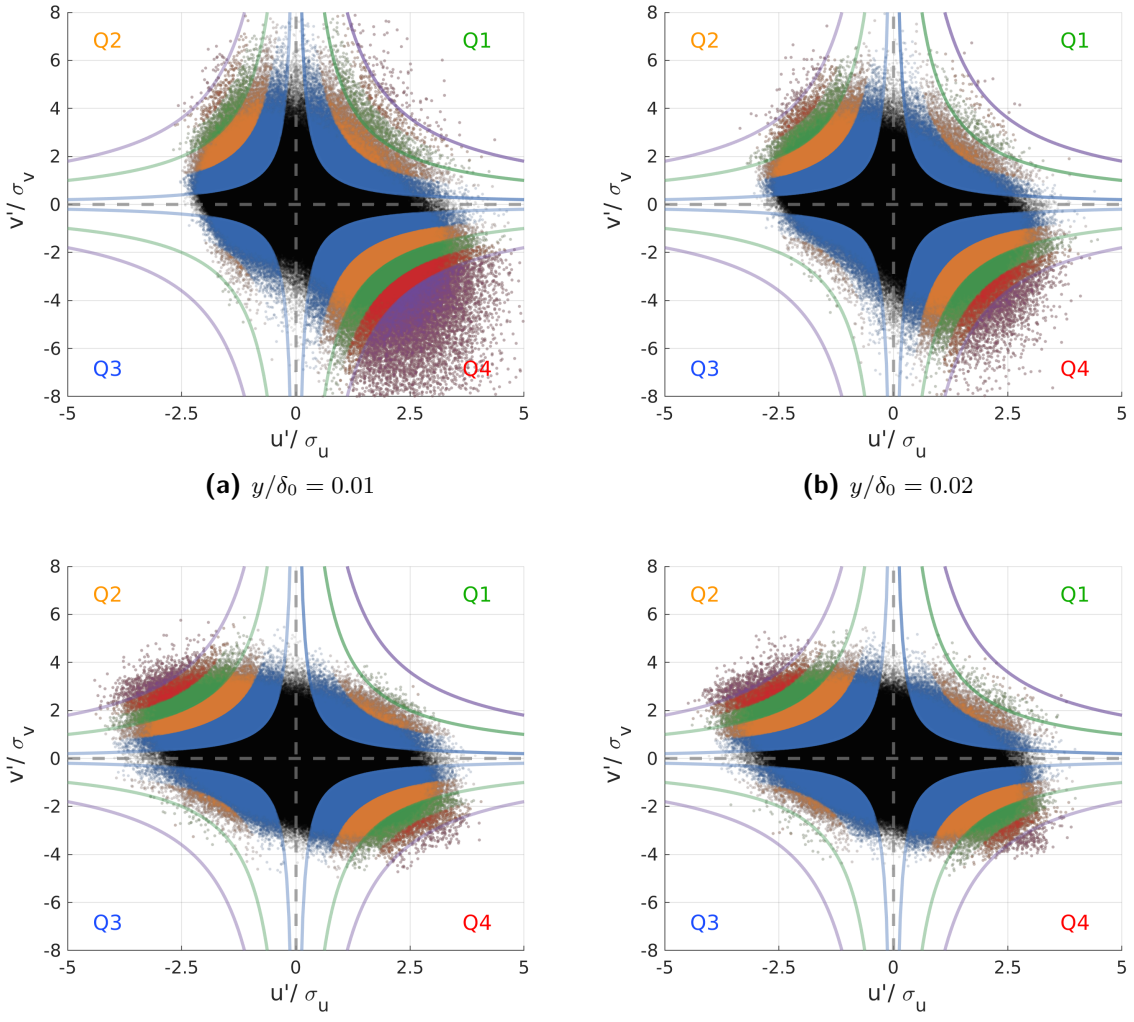

(a) $y/\delta_0 = 0.01$ **(b)** $y/\delta_0 = 0.02$

(c) $y/\delta_0 = 0.15$ **(d)** $y/\delta_0 = 0.20$

Figure 5-10: Normalized fluctuation scatter of a smooth plate and its hole-filtering Criteria $\mathbb{H}$. Coloured scatters indicate the data in each criteria. The line plots illustrate the Criteria $H = 1, 3$ and 5.

has already been discussed in Chapter. 3-3-1, so here we will quickly go through how the the algorithm is implemented. Firstly, the raw $u'v'$ pairs are categorised into four quadrants. In each quadrant, a hyperbolic curve family is defined. This curve family is the hole-filtering criteria $\mathbb{H}$. The last step is to collect the scatter pairs $u'v'$ that corresponds to each hyperbolic curve strength H.

Fig. 5-10 portrays the hole-filtered scatters of a smooth plate. The coloured shading indicates the scatters that fall inside a hole-filtering strength bin. For visualisation, three hyperbolic strength $H = 1, 3, 5$ are overlaid in each subplot. The black scatters are the event that has strength $H < 1$. In general, patterns between the buffer layer and the wake region are different. In the buffer layer, sweep events are more active compared to ejection events. The sweep event extends to $H > 6$; whereas the ejection can only be found for $H < 4$. In contrast to the buffer layer, ejection events in the wake region are the principle quadrant that has intense events. Also, the strength difference between each quadrant is smaller in the wake region. This results in a more symmetrical occurrence distribution, as have seen in Fig. 5-6.

Above scatter plot only gives a qualitative observation of the characteristics of the smooth plate. To study the responses under the dimple plate, data inside each quadrant and strength bin is further sampled. In each sampled bin, the stress contribution is normalised by the total stress. The normalisation results in a decomposition of each quadrant in each strength and its partition to the total Reynolds shear stress. Fig. 5-11 depicts the overall partitions to total Reynolds shear stress in each quadrant in the buffer layer and the wake region. To begin with, the general behaviour of each quadrant of a smooth plate is shown. The partitions between the buffer layer and the wake region is again remarkable. In the buffer layer, the principal contributor to the shear stress is the sweep event (Red line), seen from the higher percentage to total shear stress at $H = 0$. Notes that the x-axis is the contributions *outside* H, so $H = 0$ means every scatter pairs in each quadrant. In contrast, in the wake region, the main contributor is the ejection event. This difference is also found in Wallace et al. (1972); Wallace (2016), shown in Fig. 5-12, where a higher stress contribution from the sweep event in the near-wall to buffer region is observed.

At $y/\delta_0 = 0.01$, the sweep event accounts for almost 80% of the total shear stress, while ejection event only has 50%. Also, the contribution extends to very large H criteria and even has an 8% contribution at $H > 10$. The outer interaction (Q1) and inner interaction (Q3) are relatively small and have a negative sign. In the wake region, ejection accounts for 70% of the total stress, whereas sweep takes up $\approx$ 60%. Also, the difference between $y/\delta_0 = 0.15$ and $y/\delta_0 = 0.2$ is marginal, compared to the buffer layer. Overall, the contribution in each quadrant decays as H becomes higher. This decay reflects the fact that fewer events are being collected, as H goes higher. To visualise the decay, the total event occurrence (Q1+Q2+Q3+Q4) in each H bin is shown in the asterisk scatters. The asterisks thus represents the total percentage of the data points inside H criteria. For clarity, only the smooth plate percentage data is shown. In every sampled level, it reveals that the majority of the quadrant events are mild. At $H = 2$, almost 80% of the scatter pairs lie inside H. Comparing the total occurrence with the event partitions of the total shear stress, it is found that few intense events contribute to a large amount of shear stress. Specifically, the grey lines indicate the total quadrant contributions inside H. At $H = 2$, the contribution inside H only accounts for $\approx$ 45% of the total shear stress. That means the rest 20% quadrant events contribute over half of the total shear stress. Such phenomenon is more significant in the lower layer, seen from the buffer layer, $y/\delta_0 = 0.01$, plot.

Regarding the responses under the dimple plate, it is found that most responses are in the buffer layer. The wake region also reveals small deviations from the smooth plate, but it should be considered within statistical uncertainty. At $y/\delta_0 = 0.01$, four quadrants have a larger contribution to the Reynolds shear stress. That means a more active turbulent boundary layer, and all quadrants generate more stress than the smooth plate case. Both inner and outer interactions have a significant increase in the weak events, and the influences extend to $H = 3$. The influence of dimples on the ejection event is limited to relatively weaker events: mainly $H < 1$. On the contrary, the sweep event shows significantly increased stress contributions, and the influence extends to the intense event. Since the stresses in the smooth plate and dimple plate are normalised by their own shear stress, a larger sweep event contribution means the sweep event now contribute more stress compared to the rest quadrants. At $y/\delta_0 = 0.02$, the increased contributions in inner interaction and outer interaction vanished. The sweep

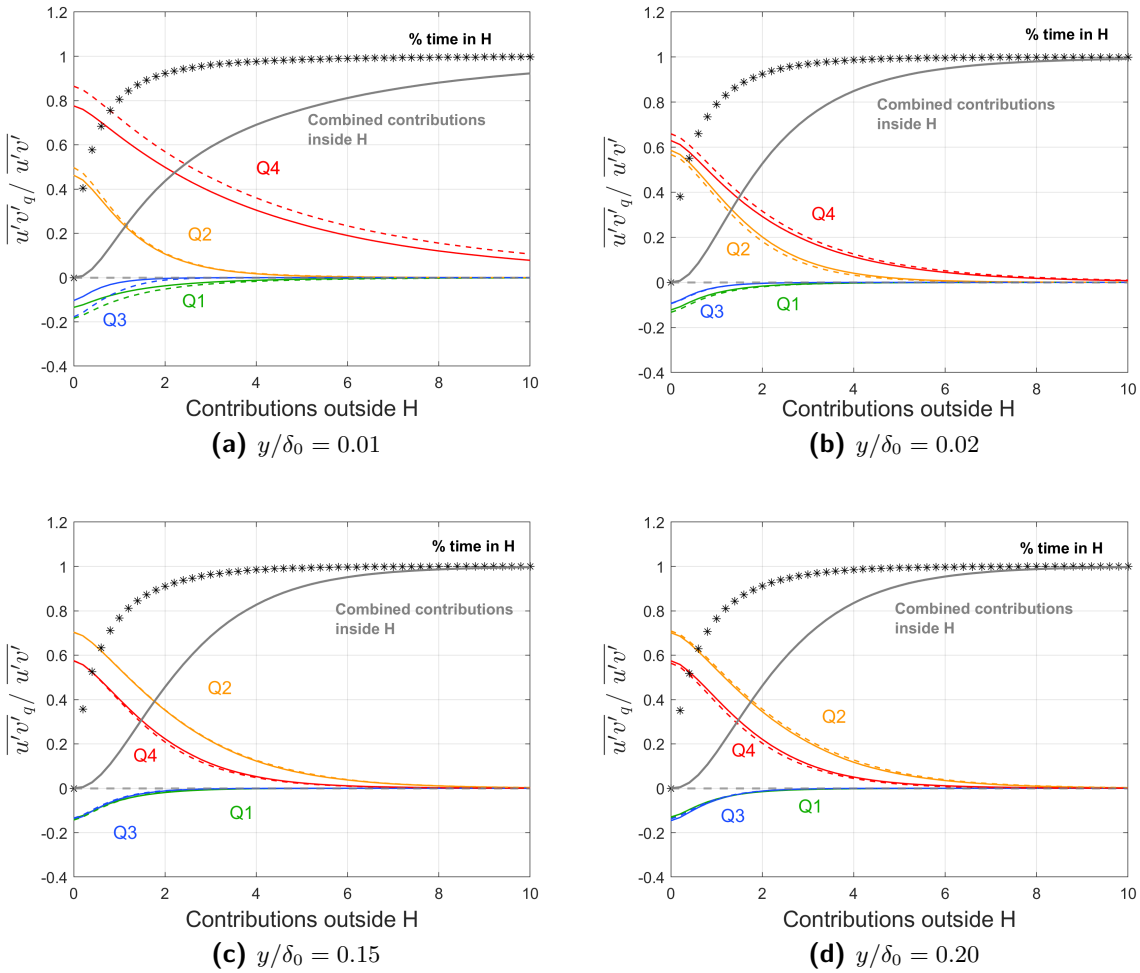

(a) $y/\delta_0 = 0.01$ **(b)** $y/\delta_0 = 0.02$

(c) $y/\delta_0 = 0.15$ **(d)** $y/\delta_0 = 0.20$

Figure 5-11: Partitions of the total Reynolds shear stress in each quadrant of a smooth plate (solid line) and a dimple plate (dashed line). The asterisk scatter represents the total percent of time inside curtain hole-filtering criteria of a smooth plate. The grey line indicates the contributions inside the hole-filtering criteria of a smooth plate.

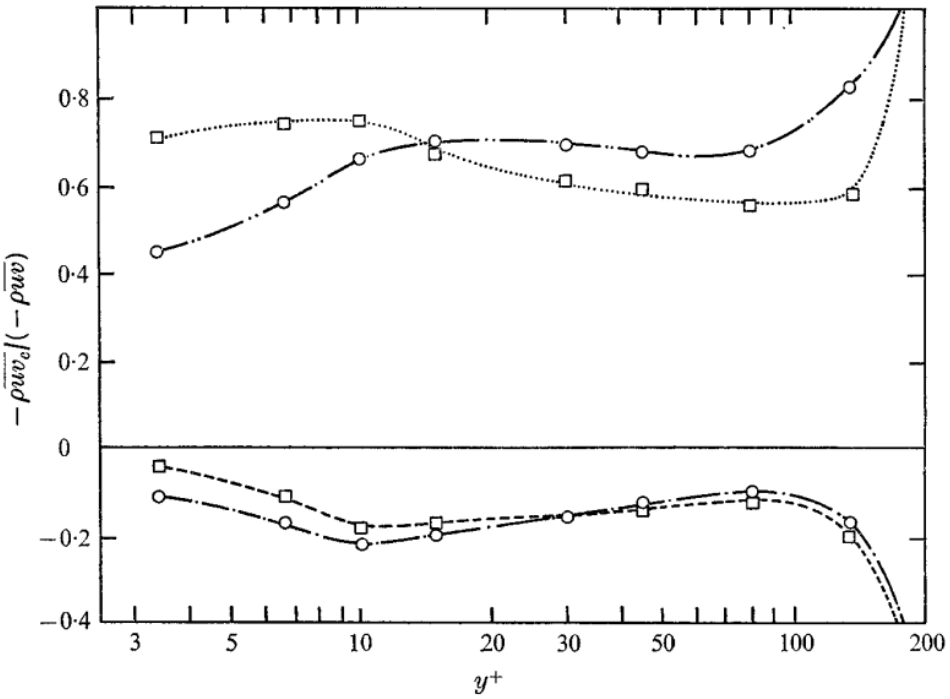

Figure 5-12: Partition to the Reynolds shear stress. Square dot line:sweep event. Square dashed line: outer interaction. Circle dashed line: ejection and inner interaction. (Wallace et al., 1972)

event still has a larger partition, but the ejection takes a smaller part. Apart from the different trend between two levels, the responses in $y/\delta_0 = 0.02$ are smaller, suggesting the influences are mainly in the lower layer.

In conclusion, dimples mainly affect the buffer layer. On the one hand, the influence is limited to the weaker event for inner interaction, outer interaction and ejection. The effect is to increase their relative contribution to the Reynolds shear stress. On the other hand, the impact on the sweep event is more profound, extending to the more intense event. Notably, the sweep event shows a significant response that increases the stress contribution in almost every event strength.

5-2-4 Responses normalised by the smooth plate

In previous sections, all scatters and stress partitions are normalised by their fluctuation levels. It is thus meant to investigate the responses in the internal structures. Therefore, we now retrieve the mean stress values from the smooth plate and then used as the normalisation factor for the dimple plate. By dividing with the same total Reynolds stress, it reveals the actual stress response under the dimple plate. Since only different normalisation factor is used, the JPDF scatter shows a minimum difference between the different normalisation. For simplicity, they are not shown here. The weighted JPDF in Fig. 5-14 suggests that the overall trend is the same for all four levels except ejection. The ejection in the buffer layer, $y/\delta_0 = 0.01$, exhibits a different response. In Fig. 5-9a, the weighted J-PDF peak moves towards positive x-axis, indicating the principal stress contributor in the ejection is now by the weaker event. On the contrary, smooth plate normalised weighted JPDF in Fig. 5-14a indicates the peak shifting toward negative x-axis, meaning the primary stress contributor by stronger events. Similar peak shifting in ejection is also found at $y/\delta_0 = 0.02$, but with a smaller difference and hence the smaller peak shifting. Such smaller difference suggests that this deviation is mainly in the lower layer. Lastly, Fig. 5-13 gives an overview of the stress partition normalised by smooth plate value. Since the partition from the wake region is identical, for simplicity only the buffer layer results are shown. Compared with Fig. 5-11, it is found that at $y/\delta_0 = 0.01$, weak ejection event now has a contribution higher than the smooth plate. This phenomenon coincides with the result of weighted J-PDF. Besides the difference in ejection, the rest quadrants also have higher contributions than the smooth plate. It means that the turbulent boundary layer under the dimple plate becomes more active. It can be inferred that the TBL now has a higher Reynolds stress generation under the dimple plate.

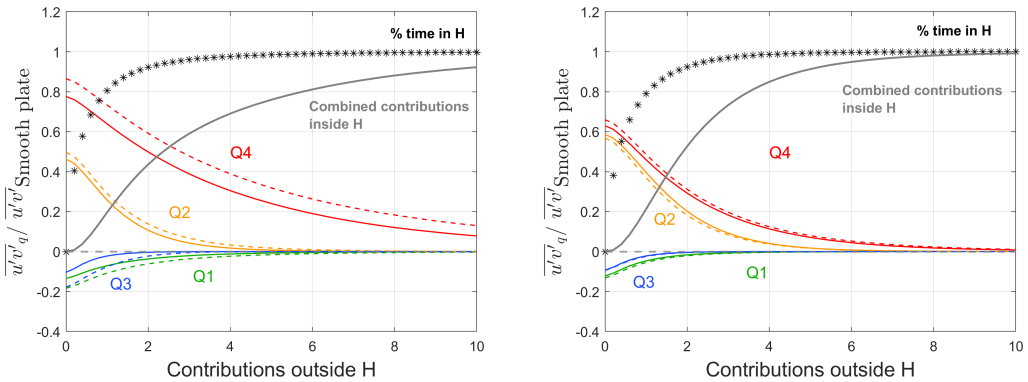

(a) $y/\delta_0 = 0.01$ **(b)** $y/\delta_0 = 0.02$

Figure 5-13: Smooth plate normalized partitions of the total Reynolds shear stress in each quadrant of a smooth plate (solid line) and a dimple plate (dashed line). The asterisk scatter represents the total percent of time inside curtain hole-filtering criteria of a smooth plate. The grey line indicates the contributions inside the hole-filtering criteria of a smooth plate.

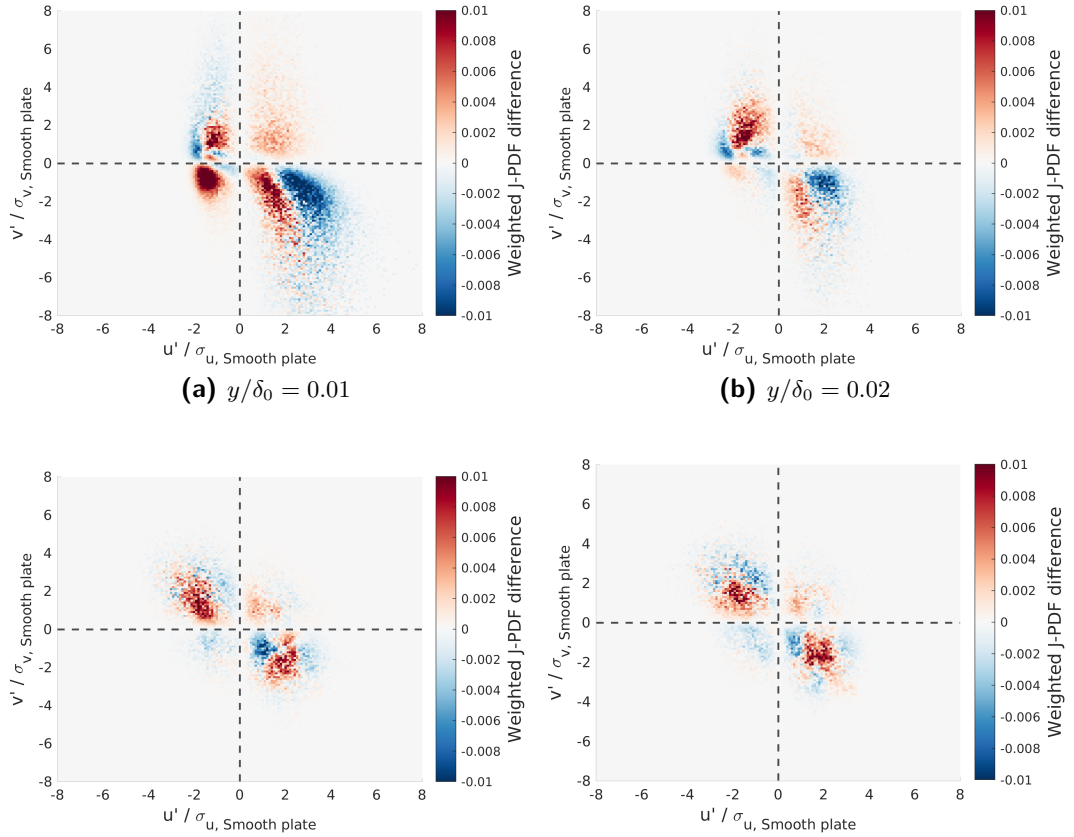

(a) $y/\delta_0 = 0.01$ **(b)** $y/\delta_0 = 0.02$

(c) $y/\delta_0 = 0.15$ **(d)** $y/\delta_0 = 0.20$

Figure 5-14: Smooth plate normalized Weighted J-PDF differences (Dimple plate - Smooth plate) at four levels over the $3rd$ dimple.

5-2-5 Responses across the dimple

In this section, comparison between the $3rd$ and the $4th$ dimple is shown. Overall, the responses are very similar to the $3rd$, yet the responses are more significant. It is due to the fact that we are sampling at a relatively lower TBL layer due to the growth of the boundary layer thickness. That being said, the TBL still shows a similar trend. The JPDF scatters indicates a stronger vertical fluctuation in the buffer layer, as shown in Fig. 5-15a. For the weighted JPDF in Fig. 5-15b, again a strong response in sweep event is found, and the weighted scatters move towards negative x-axis for the sweep and ejection. Lastly, the shear stress partition shown in Fig. 5-15d suggests a similar trend as Fig. 5-11a. Regarding the contribution to the total Reynolds stress, every quadrant has a larger contribution, as is the case in the $3rd$ dimple. It means the turbulent coherent structures under the dimple plate become more active than the smooth plate. As H goes higher, the responses of inner interaction and outer interaction decay, and the sweep event remains a higher contribution, which infers a stronger sweep contribution under the dimple plate.

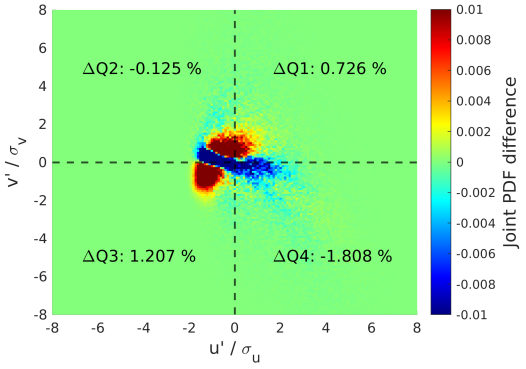

(a) J-PDF difference (Dimple plate - Smooth plate)

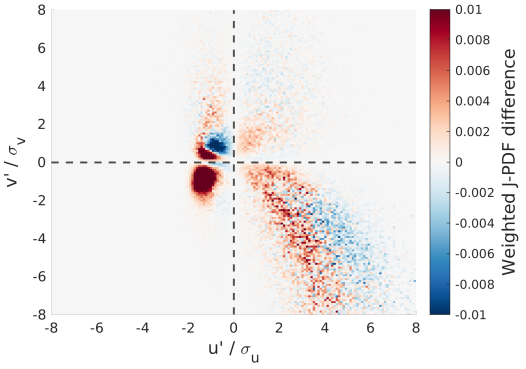

(b) Weighted J-PDF difference (Dimple plate - Smooth plate)

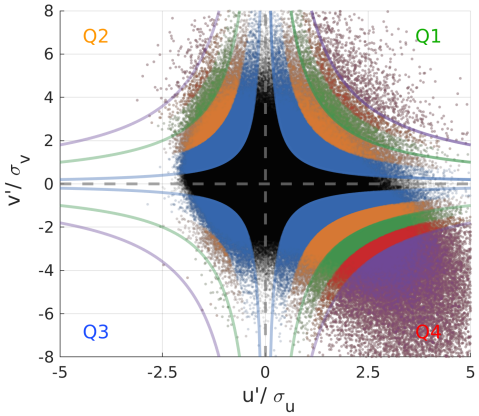

(c) Fluctuation scatter of a smooth plate and its hole-filtering criteria $\mathbb{H}$.

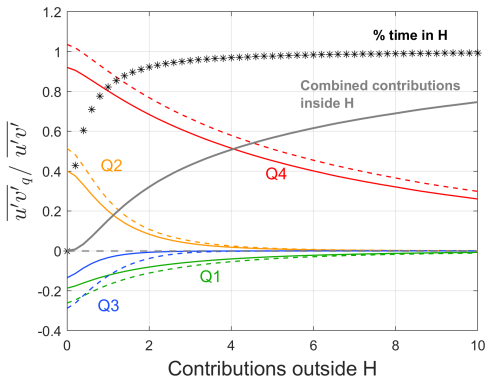

(d) Partitions of the total Reynolds shear stress.

Figure 5-15: Responses at $y/\delta_0 = 0.01$ over the $4th$ dimple.

5-3 Variable Interval Time Averaging (VITA) analysis

In the last section, it is found that dimples overall increase outer interaction and sweep event. With the hole-filtering technique, it is also concluded that the impact of dimples on the Reynolds shear stress is mainly in the buffer layer and the weaker quadrant event. However, the quadrant analysis only reveals the statistical status of the turbulent boundary layer; it does not tell how each ejection and sweep event develops. Furthermore, it is logical to suspect that a spatially varying surface will somehow affect the evolution of the turbulent coherent structures as the flow travel downstream. Therefore, Variable-Interval Time-Averaging (VITA) is carried out to investigate the development of turbulent coherent structures. The target of interest will be the intense quadrant events since few intense events summing up contribute to a large portion of the Reynolds shear stress. In signal processing practice, it is also logical to focus on the strong event to maximise the signal-to-noise ratio. In this project, a different quadrant event detection algorithm is employed. This detection method is based on the fact that a finely resolved flow data is available, and thus a rather precise fluctuation signal can be obtained. Combined with the hole-filtering method, such well-resolved data can extract the signals with a particular strength. This approach leads to an excellent and coherent framework to match the results from the quadrant analysis. The combination can then qualitatively and consistently describe how dimples affect turbulent coherent structures with different event strength.

5-3-1 Hole-filtering based VITA

In general, VITA analysis consists of three subjects: windowing, conditional sampling and averaging. The method implemented here mainly uses different conditional sampling method, and others remain the same as Blackwelder et al. (1976). Even though the algorithm is conceived independently by the author, the algorithm is similar to what Fujimatsu et al. (2010) have proposed: the so-called Q-burst detection. In this project, the author prefers to call it "Hole-filtering based VITA" to stress out the connection to the hole-filtering technique used in the quadrant analysis section. For simplicity, only the sampling procedures will be explained.

To begin with, the quadrant event mask, M_{q2} and M_{q4}, are computed from the fluctuation velocity signal u' and v':

$$M_{q2}(t) = \begin{cases} 1 & \text{, if} \quad u'(t) > 0 \ \wedge \ v'(t) < 0 \\ 0 & \text{, otherwise} \end{cases} \tag{5-1}$$

$$M_{q4}(t) = \begin{cases} 1 & \text{, if} \quad u'(t) < 0 \ \wedge \ v'(t) > 0 \\ 0 & \text{, otherwise} \end{cases} \tag{5-2}$$

then, the Reynolds shear stress and its mean value are calculated. The mean value is needed to compute the hole-filtering mask M_H. The hole-filtering mask reads:

$$M_H(t) = \begin{cases} 1 & \text{, if } \quad (u'v')/\ \overline{u'v'}\ > \ k \\ 0 & \text{, otherwise} \end{cases} \tag{5-3}$$

where k is the arbitrary hole-filtering criteria. To extract the strong event, k is set to 3. A detection function is then defined as the product of a quadrant event mask and hole-filtering mask. When sweeping over the time-series, a point of detection is first found if $D(t_0)$ equals to 1. Then a detection window is defined as $t = [t_0, t_0 + 2T_w]$. The trigger point of a particular event is determined at the minimum of $u'v'$ within each window. That is:

$$D(t) = M_q(t) \cdot M_H(t) \tag{5-4}$$

$$t_{\text{event}} = \underset{t \in [t, t+2T_w]}{\arg\min} \quad u'v'(t) \tag{5-5}$$

After identifying the occurrence, the detected signals are segmented and averaged to derive an ensemble-averaged signal $\langle u' \rangle$ and $\langle v' \rangle$. Fig. 5-16 gives an overview of the entire algorithm for both ejection and sweep events. Firstly, the mean is subtracted from the raw signal, as shown in the first subplot. Both sweep and ejection are plotted for reference. Then, a

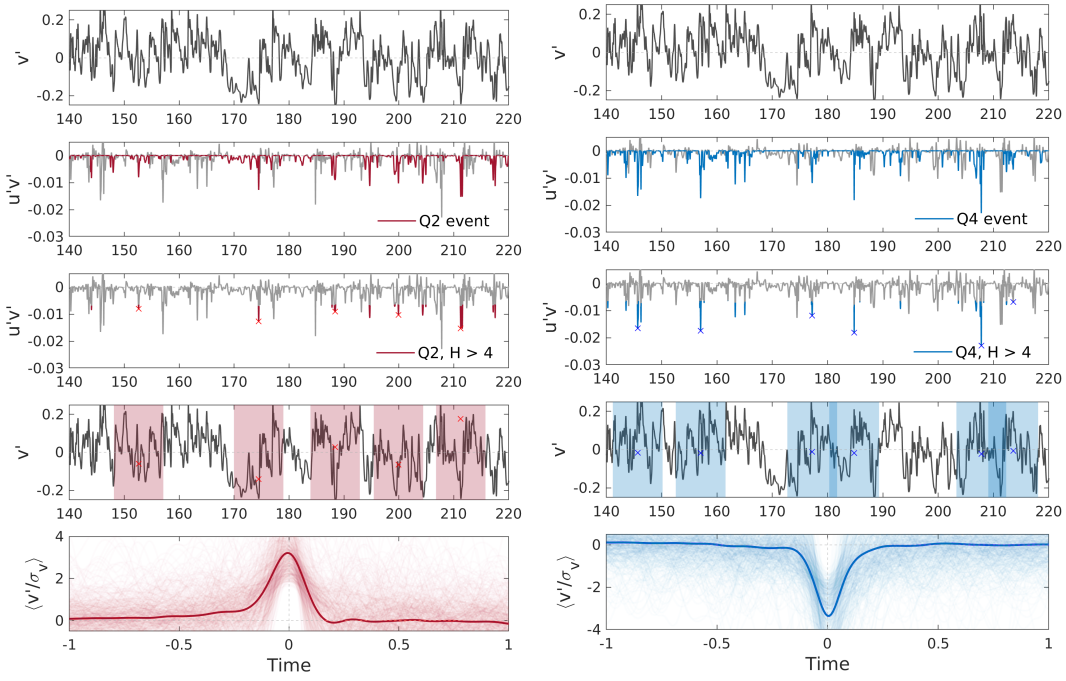

(a) Ejection event. **(b)** Sweep event.

Figure 5-16: Algorithm demonstration of the hole-filtering based VITA. The velocity signal is drawn from an arbitrary station from the smooth plate probe data.

quadrant event mask is computed, as indicated from the coloured lines in the second subplot. The quadrant mask is further multiplied with the hole-filtering mask, as shown in the third subplot in Fig. 5-16. Then, the trigger points of the event are pinpointed, shown as cross symbols in the figure. Lastly, the averaging window is defined as $[t_{\text{event}} - T_w, t_{\text{event}} + T_w]$, as illustrated as the transparent shading in the fourth subplot.

5-3-2 Ejection development

First off, the time-series data used in VITA analysis is the probe data, which contains three vertical levels with the spatial resolution that comparable to $Refx2$ grid. The sampling area is over the $3rd$ dimple, as indicated in Chap. 3-1-2. The outcome signals are from the ensemble average over the entire sampling area. Fig. 5-17 illustrates the ejection development in the buffer layer $y/\delta_0 = 0.01$ and wake region $y/\delta_0 = 0.2$. The blue line represents the ensemble signal from the smooth plate case; whereas the orange line represents the ensemble from the dimple plate. The shadings are individual detected signals. Since the results from $y/\delta_0 = 0.02$ is analogous to $y/\delta_0 = 0.01$, their plots are shown in the Appendix. B-7 for simplicity. From the overall shape of the detected signals, it is found that there are lots of variation among each detected signals. However, around the trigger point ($t = 0$), all segmented signals collapse into a coherent surge, as shown from the sharper edge of the shading around the trigger point.

In general, it is found that the evolution of individual velocity fluctuation is not symmetrical around the peak value. Interestingly, albeit the general shape looks the same, the signal evolution is quite different between the buffer layer and wake region. In the buffer layer, the lead of the u' and v' signals are longer than the lag. It thus leaves a longer tail as one seen along the negative x-axis. The lead-lag patterns mean that during the ejection event, the fluid parcel decelerates in the streamwise direction before reaching its minimum velocity and afterwards accelerates in a relatively fast pace. Similarly, fluid parcel takes a longer run in accelerating in the wall-normal direction than the decelerating thereafter. On the contrary, signals from the wake region exhibit relatively symmetrical distribution. The lead-lag evolution can still be observed, but it is relatively marginal compared to the development in the buffer layer.

Even though the individual fluctuation velocity components u' and v' show asymmetry in its development, the shear stress is less asymmetrical around the peak. The resulting velocity product grows and decays symmetrically. The shear stress development is more asymmetrical in the buffer layer, but this is mainly due to a long tail observed along the negative x-axis of u' signal. There are two possible reasons for this long lead. Firstly, it is probably due to the sampling issue. As discussed, only one sample point is collected to avoid aliasing within each sampling window. However, the above approach only takes the time-wise signal into account. Turbulent coherent structures are not point-wise structures. They occupy particular area in the space and evolve through time. It is possible that the current algorithm re-samples one single event due to the fact that every spatial point is treated as a statistically independent time-series. Secondly, the long lead might be due to the sweep event. The high-speed streaks move the decelerated region away from the wall, which results in the ejection of low-speed flow away from the wall. This low-speed updraft is the sweep event. Due to the large velocity shear, the streak becomes unstable and triggers the inrush of high-speed flow, leading to the next ejection/sweep cycle (Corino et al., 1969). With this regard, the long tail could just be the residual signal from the sweep event.

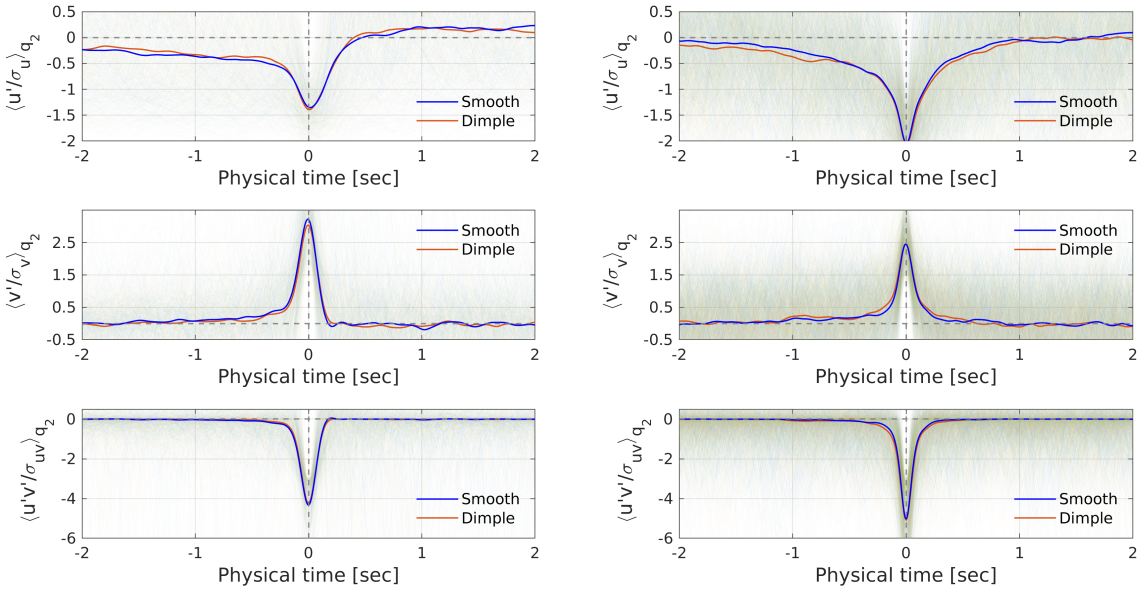

(a) Ejection event at the buffer layer, $y/\delta_0 = 0.01$.

(b) Ejection event at the wake region, $y/\delta_0 = 0.2$.

Figure 5-17: Ejection evolution at $y/\delta_0 = 0.01$ and $y/\delta_0 = 0.2$.

Inspecting the difference between the smooth plate and dimple plate, the impact of dimples on the event evolution is relatively marginal for the ejection event. Most responses are in the tails, which could be the sampling effect. In the buffer layer, a small increase in u', and a decrease in v' at the trigger point are obtained. Two responses counteract each other, leaving the resulting shear stress almost identical to the smooth plate. In the wake region, most differences are in the tails, but the differences are again very mild. Such marginal responses could be explained in two ways. One is that dimple does not affect the strong ejection. The other is that the responses are smoothed out by the large sample numbers. It is possible that dimple indeed affects ejection evolution in the strong event, but its signal is being submerged under the weaker but still detectable events. To address this issue, a parameter sweep over different hole-filtering strength is performed to investigate the event evolution. The details will be given in Chap. 5-3-4.

5-3-3 Sweep development

Fig. 5-18 shows an overview of the sweep event development at $y/\delta_0 = 0.01$ and $y/\delta_0 = 0.2$. The development is again nearly symmetrical. However, the sweep evolution exhibits opposite lead-lag pattern. In the buffer layer, the lead of the u' and v' signals are shorter than the lag, which leaves a long tail along the positive x-axis. The lead-lag patterns mean that during the sweep event, the fluid parcel accelerates in the streamwise direction faster and afterwards decelerates in a slower pace. Similarly, fluid parcel takes a shorter run in decelerating in the wall-normal direction than the accelerating afterwards. In the wake region, the asymmetry

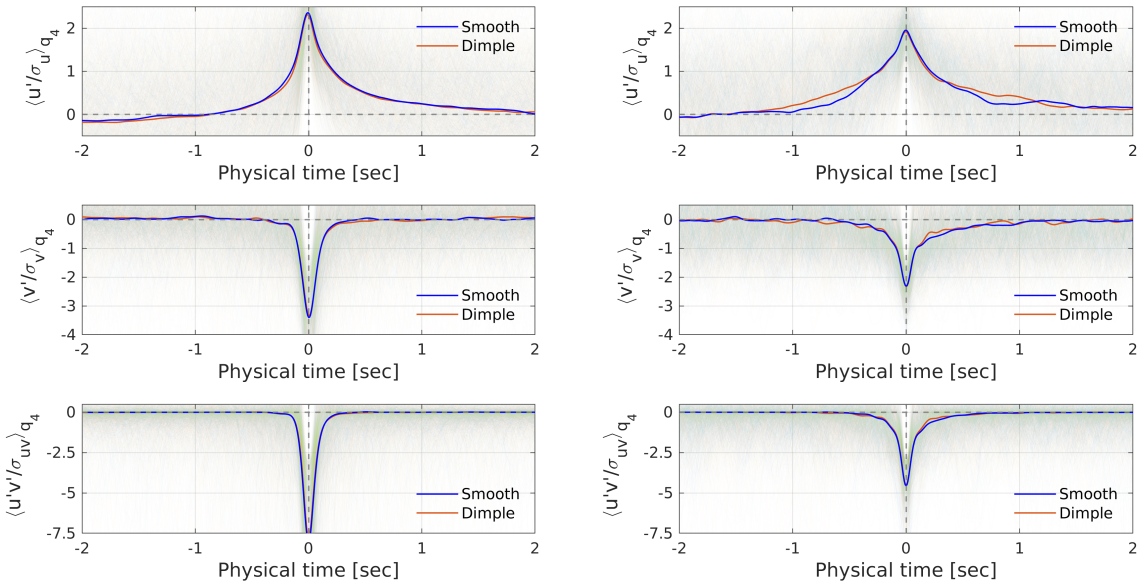

(a) Sweep event at the buffer layer, $y/\delta_0 = 0.01$.

(b) Sweep event at the wake region, $y/\delta_0 = 0.2$.

Figure 5-18: Sweep evolution at $y/\delta_0 = 0.01$ and $y/\delta_0 = 0.2$.

is milder, similar to what we have found in ejection evolution. The shear stress is again less asymmetrical around the peak.

The development is in general opposite to the ejection. However, it is found that the shear stress magnitude between the buffer layer and wake region is larger in the sweep event. The average shear stress in the trigger point in the buffer layer is stronger than in the wake region, and this is mainly due to larger vertical fluctuation. The magnitude of the streamwise fluctuation is comparable between $y/\delta_0 = 0.01$ and $y/\delta_0 = 0.2$. Also, the peak value of the velocity fluctuation u' and v' does not coincide with the event trigger time. This phenomena only occurs in the sweep event. The algorithm detects the minimum shear stress as the trigger point, and ideally, the fluctuation velocities should also be at the extrema. In the ejection event, the peaks are matched to the trigger point. That means, it is indeed coming from the sweep signals. The streamwise fluctuation peak shifts to the left; whereas the vertical fluctuation peak shifts to the right. The resulting shear stress signal is then aligned with the trigger point. That means, when the shear stress reaches the minimum, the streamwise fluctuation is already decelerating, and the wall-normal fluctuation is starting accelerating. Such peak-shifting phenomena are also observed by Hoogsteen (1990) shown in Fig. 5-19.

Aside from the asymmetry, a long tail in the u' signal is found. It is also observed previously in the ejection event. In contrast to ejection event, the tail signal in the sweep event extends over the positive x-axis. Both quadrant events observed a tail signal but extended along the opposite x-axis. Then, it becomes clear that such phenomena can be attributed to flow physics, not the sampling issue. There is a succession of both sweep and ejection events. Two events might have an overlap in time, and thus one signal around the trigger point is

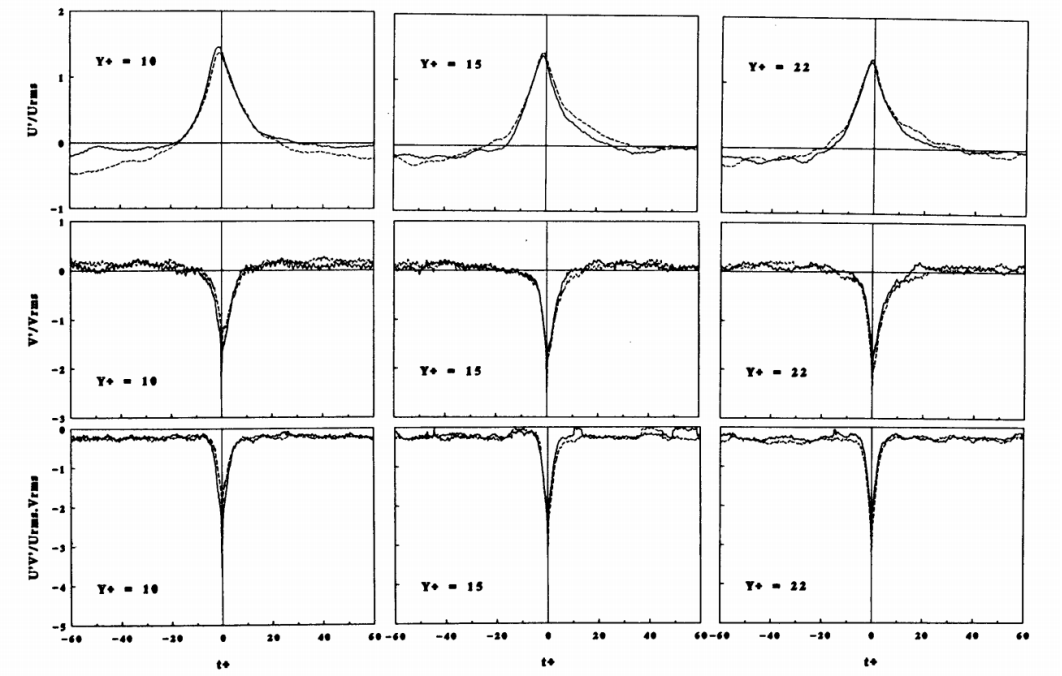

Figure 5-19: VITA conditional averaged for the u',v' and $u'v'$ component of a sweep event. Solid line: riblet wall. Dashed line: smooth wall. $y^+ = 10, 15, 22$. (Hoogsteen, 1990)

being influenced by the other. For instance, the ejection occurs before the end of a sweep, and vice versa. Physically, as one event occurs, the resulting velocity shear makes the flow so unstable that it might already trigger a sweep/ejection well before current event decays. From the present calculation, it suggests that the sweep event occurs first, followed by the ejection event. However, the author is sceptical about the sequence of the sweep/ejection event. Since VITA is a conditional sampling technique, it only conveys "statistically", these two events somehow has a sequential relation and interact with each other. At most, if sweep on average happens first, it might be because of the numerical factor, like initialisation, or influence from the B.C. that triggers the sweep event first. It is hard to certainly pinpoint the exact reason why sweep event leads the event succession.

Regarding the response of the dimple plate, a minimal difference in most of the signals is found. Compared with the sweep evolution under the spanwise oscillation, shown in Fig. 5-20, the peak and the lag of the signal in the dimple plate are identical to the controlled case. In the spanwise oscillation case, the duration and the intensity are reduced. Although the experiment from Choi et al. (2011) focuses on the plasma actuators, the results from the riblet experiment also show similar trend (Choi, 1989), suggesting that such reductions are the general characteristics for a drag-reduced flow. Despite having a nearly identical development, a discernible response in the wake region is found. The streamwise fluctuation in the dimple plate has a broader distribution. With equal peak strength, this suggests that the sweep event has similar strength, but with longer developing time. The flow accelerates slower in the streamwise direction before the trigger point; decelerates slower after the trigger point. The vertical fluctuation is almost identical, with increased variation during the evolution, yet minimal. While the development in the streamwise fluctuation is less intense, it mainly

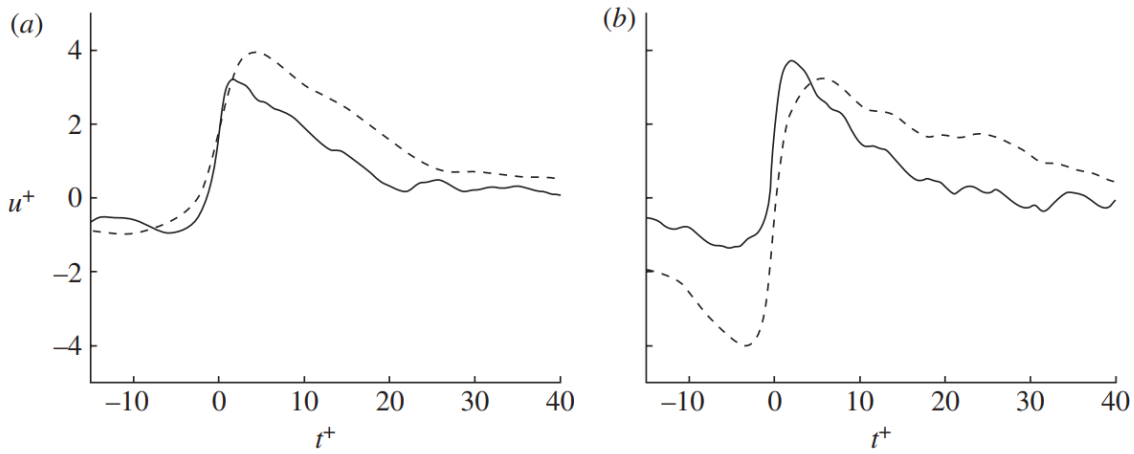

Figure 5-20: Sweep event with spanwise oscillation at (a): $y^+ = 5$ and (b): $y^+ = 20$. velocites are scaled by u_τ. Dashed line: controlled case. Solid line: spanwise oscillation. (Choi et al., 2011)

happens away from the trigger point. The resulting influence in shear stress production is still marginal.

5-3-4 VITA ensemble with varying hole-filtering strength H

Current VITA results suggest that dimple has a mild impact on the development of the strong ejection and sweep events. However, the above observation is based on the detection criteria $H > 3$. With such thresholds, it is possible that the dimple indeed affects strong events, but the signals are submerged under the weaker event. The responses might be smoothed out by a large number of weaker detected events. To rule out such possibility, VITA algorithm is applied with different detection criteria H. By sweeping over the filtering strength space $\mathbb{H}$, we could qualitatively examine how dimple affects the development of turbulent coherent structure with different strength.

Fig. 5-21 depicts the streamwise fluctuation and vertical fluctuation development of ejection events in the buffer layer and wake region. For simplicity, the results from $y/\delta_0 = 0.02$ are shown in Appendix. B-8. Each subplot represents the VITA ensembles with the corresponding filtering strength bin. The sizes of the detection bins are arbitrarily defined such that there are enough detected events to generate statistically converged results. In general, it is found that both fluctuations components in the dimple plate remain identical to the smooth plate. The peak values are scaled with detection strength, with vertical fluctuation being more sensitive to the detection strength, shown in Fig. 5-21a and Fig. 5-21b. A large variation is observed in the stronger event, and it is due to the fewer detected signals. The variation is mainly in the signal tails. In contrast, the development around the trigger point is identical. Moving forward to the wake region, again a minimal difference between the smooth plate and dimple plate is found. On the contrary to ejection events, there is a clear response in sweep event streamwise fluctuation, in the wake region. Fig. 5-22c reveals that the sweep event in the wake region has a longer development time. The flow accelerates slower in the before the trigger point and decays slower after the trigger point. The responses are mainly in strong events. In

$3 \leq H < 4$ bin, signals between the smooth plate and the dimple plate are almost identical, but the onset of the event in the dimple plate is more mild. At higher H, the trend becomes more and more apparent that the flow undergoes a slower transition during the event. This binned detection analysis confirms the results from Chap. 5-3-3. With almost all detection bins showing such responses, it is unlikely that it is originated from the sampling issue.

In summary, through VITA analysis, we are managed to extract the averaged evolution of the turbulent coherent structures with different event strength. Only the streamwise fluctuation of the strong sweep event in the wake region shows salient changes. While showing different evolution, the sweep event in the wake region still has the same peak level between two plates. This finding suggests that dimple does not affect the strength of the turbulent coherent structures, but it prolongs the development of the sweep events in the wake region. It is not clear how this difference will affect the TBL in general, but the overall impact on the skin friction must be relatively small since the event peak value and the resulting shear stress production are almost identical.

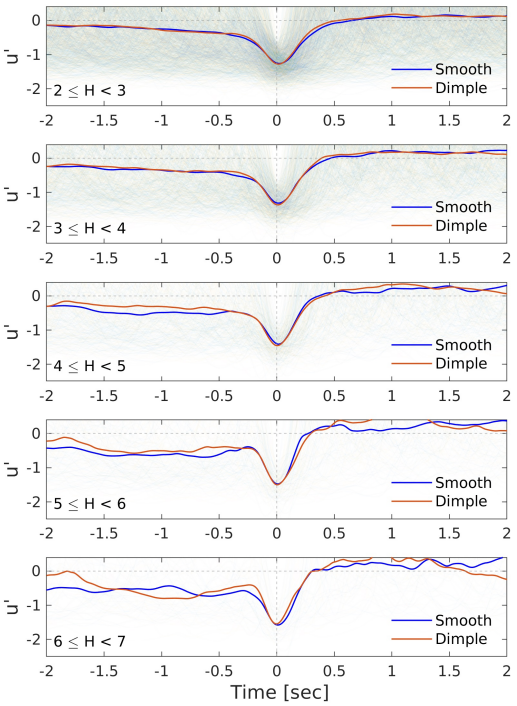

(a) Streamwise fluctuation u' at $y/\delta_0 = 0.01$.

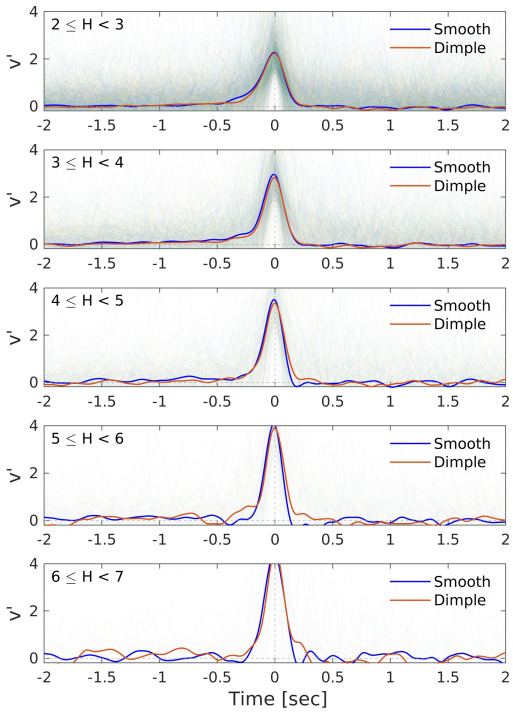

(b) Wall-normal fluctuation v' at $y/\delta_0 = 0.01$.

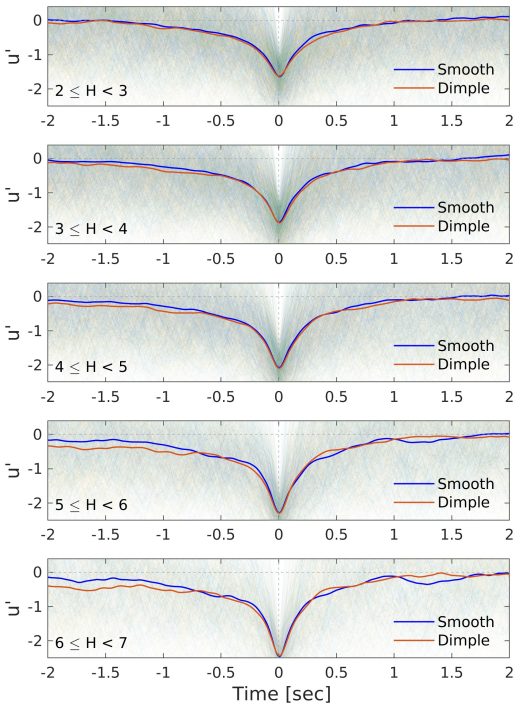

(c) Streamwise fluctuation u' at $y/\delta_0 = 0.2$.

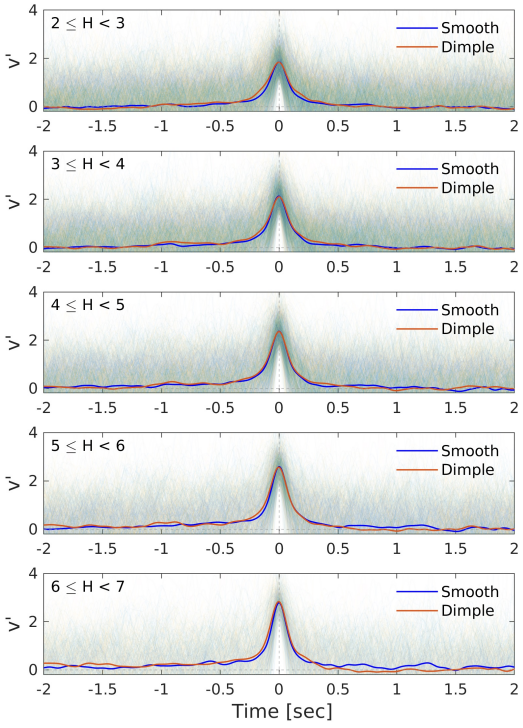

(d) Wall-normal fluctuation v' at $y/\delta_0 = 0.2$.

Figure 5-21: VITA ensemble of the ejection event with different detection criteria. Shadings are the individual detected signal.

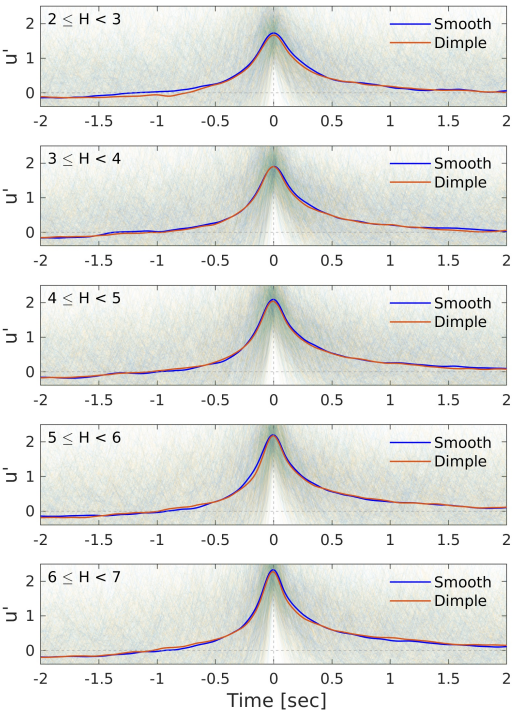

(a) Streamwise fluctuation u' in the buffer layer $y/\delta_0 = 0.01$.

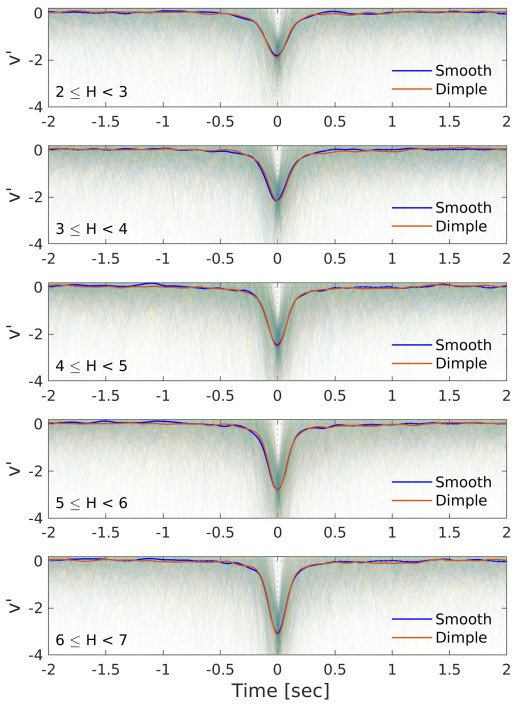

(b) Wall-normal fluctuation v' in the buffer layer $y/\delta_0 = 0.01$.

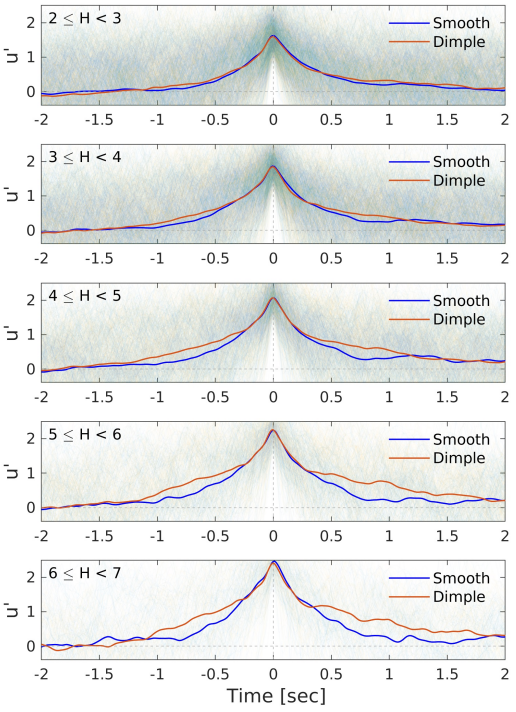

(c) Streamwise fluctuation u' in the wake region $y/\delta_0 = 0.2$.

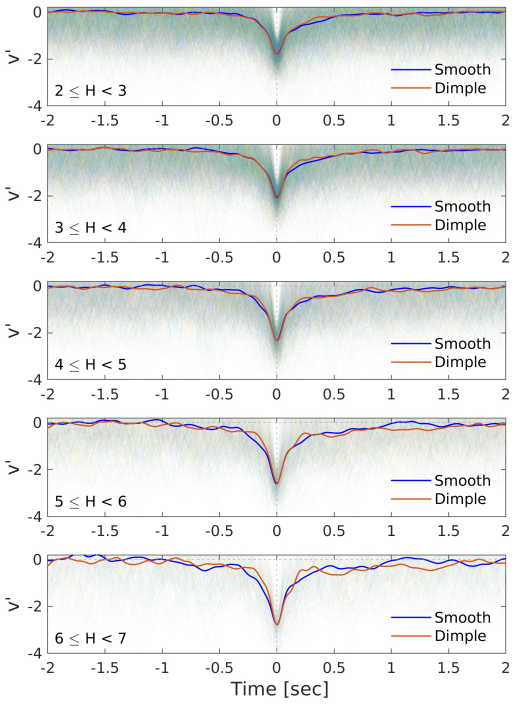

(d) Wall-normal fluctuation v' in the wake region $y/\delta_0 = 0.2$.

Figure 5-22: VITA ensemble of the sweep event with different detection criteria. Shadings are the individual detected signal.

5-4 Fukagata-Iwamoto-Kasagi identity

With quadrant analysis and VITA analysis, we are able to qualitatively assess the impact of dimples on the turbulent coherent structures. Moving one step forward, it is desirable to relate those structure responses to skin friction. Even though present simulation gives a small total drag increase, a systematic investigation of how dimple affects skin friction would still be insightful for future passive flow control research. The skin friction can be decomposed into several components by applying triple integration to the RANS equation with regard to the vertical direction. The friction-producing mechanisms can then be qualitatively isolated and have a clear physical origin. Over the years, the integration technique has been generalized to account for complex surfaces and even compressible flows (Peet et al., 2009; Bannier et al., 2015). In this study, the original FIK formulation with minor extensions will be used to account for the spanwise heterogeneity.

5-4-1 Derivation of the extended FIK identity

The original formulation from Fukagata et al. (2002) assumes a spanwise homogeneous, fully-developed turbulent channel flow. Hence, some terms are dropped off due to the simplified flow physics. With such an assumption, the inner integration can be simplified into over a single vertical profile. For a dimpled plate, to include the influence in the spanwise variation, the inner integration is performed over a finite volume V that enclose the boundary layer and across the dimple area A. Therefore, a full derivation of the extended FIK identity will be given below.

The starting point will be the unsteady incompressible RANS equation. In Einstein summation convention, it reads:

$$\overline{\frac{\partial u}{\partial t}} + \overline{\frac{\partial u u_i}{\partial x_i}} = -\overline{\frac{\partial p}{\partial x}} + \frac{1}{Re_\delta}\overline{\frac{\partial^2 u}{\partial x_i \partial x_i}} \tag{5-6}$$

Applying the Reynolds averaging and gathering terms with wall-normal derivative, the streamwise momentum equation now reads:

$$\frac{\partial \overline{u}}{\partial t} + \frac{\partial(\overline{u}\overline{u})}{\partial x} + \frac{\partial(\overline{u}\cdot\overline{v})}{\partial y} + \frac{\partial(\overline{u}\overline{w})}{\partial z} = -\frac{\partial \overline{p}}{\partial x} + \frac{1}{Re_\delta}\left[\frac{\partial^2 \overline{u}}{\partial x^2} + \frac{\partial^2 \overline{u}}{\partial z^2}\right] + \frac{\partial}{\partial y}\left[\frac{1}{Re_\delta}\frac{\partial \overline{u}}{\partial y} - \overline{u'v'}\right] \tag{5-7}$$

Notes that only the Reynolds shear stress $\overline{u'v'}$ is isolated, and the other two stress components will be merged into the so-called spatial development term. It is desirable to inspect the quadrant event $u'v'$ separately from the other shear stress events. The spatial development term can then be defined as:

$$\overline{I}_{x,z} = \frac{\partial(\overline{u}\overline{u})}{\partial x} + \frac{\partial(\overline{u}\overline{w})}{\partial z} + \frac{\partial(\overline{u}\cdot\overline{v})}{\partial y} - \frac{1}{Re_\delta}\left[\frac{\partial^2 \overline{u}}{\partial x^2} + \frac{\partial^2 \overline{u}}{\partial z^2}\right] \tag{5-8}$$

Fukagata et al. (2002) call this term "spatial development" since it contains spatial gradients. Compared the formulation from Fukagata et al. (2002), additional term arise because of the spanwise variation introduced by the dimple. Substituting Eqn. 5-8 into Eqn. 5-7 and gathering terms accordingly, the equation becomes:

$$\left(\overline{I}_{x,z} + \frac{\partial \overline{p}}{\partial x} + \frac{\partial \overline{u}}{\partial t}\right) + \left(\frac{\partial \overline{u'v'}}{\partial y}\right) - \left(\frac{1}{Re_\delta}\frac{\partial^2 \overline{u}}{\partial y^2}\right) = 0 \tag{5-9}$$

Here the pressure gradient and transient tendency are grouped with spatial development terms. The FIK identity can then be deduced through triple integration of Eqn. 5-9 over vertical direction, with the inner integration being a volume integral. In each integration, a simplified relation can be obtained for any function $\mathcal{F}$ by making use of Integration by Parts. The triple integral can then be simplified using those relations. Firstly, the double integration can be simplified as follows:

$$\begin{aligned}
\int_0^1 \iiint_V \mathcal{F}\ dxd\eta dz\ d\eta &= \int_0^1 \left(1 \cdot \iiint_V \mathcal{F} dxd\eta dz\right) d\eta \\
&= \left[\eta \int_0^\eta \iint_A \mathcal{F}\ dxdzd\eta\right]_{\eta=0}^{\eta=1} - \int_0^1 \eta \iint_A \mathcal{F}\ dxdzd\eta \\
&= \int_0^1 (1-\eta) \iint_A \mathcal{F}\ dxdzd\eta \\
&= \int_0^1 \iint_A (1-\eta)\cdot \mathcal{F}\ dxdzd\eta
\end{aligned} \tag{5-10}$$

Where η is the normalised vertical coordinate y/δ. Note that now the double integration have been simplified to single volumetric integration with a linear weighting components w.r.t normalised vertical position. Similarly, a triple integration can be simplified into a single volumetric integration by applying Integration by Parts twice:

$$
\begin{aligned}
\int_0^1 \int_0^\eta \iiint_V \mathcal{F}\ dxd\eta dz\ d\eta\ d\eta &= \int_0^1 \left(1 \cdot \int_0^\eta \iiint_V \mathcal{F}\ dxd\eta dz\ d\eta\right) d\eta \\
&= \left[\eta \int_0^\eta \iiint_V \mathcal{F}\ dxd\eta dz\ d\eta\right]_{\eta=0}^{\eta=1} - \int_0^1 \eta\ \iiint_V \mathcal{F}\ dxd\eta dz\ d\eta \\
&= \int_0^1 \iiint_V \mathcal{F} dxd\eta dz\ d\eta - \left\{\left[\frac{1}{2}\eta^2 \int_0^\eta \iint_A F dxdz\ d\eta\right]_{\eta=0}^{\eta=1} - \int_0^1 \frac{1}{2}\eta^2 \iint_A F dxdz\ d\eta\right\} \\
&= \int_0^1 (1-\eta)\ \iint_A \mathcal{F}\ dxdz\ d\eta - \int_0^1 \frac{1}{2} \iint_A F dxdz\ d\eta + \int_0^1 \frac{1}{2}\eta^2 \iint_A F dxdz\ d\eta \\
&= \int_0^1 (\frac{1}{2} - \eta + \frac{1}{2}\eta^2)\ \iint_A \mathcal{F}\ dxdz\ d\eta \\
&= \int_0^1 \frac{1}{2}(1-\eta)^2 \iint_A \mathcal{F}\ dxdzd\eta \\
&= \int_0^1 \iint_A \frac{1}{2}(1-\eta)^2 \cdot \mathcal{F}\ dxdzd\eta
\end{aligned}
\tag{5-11}
$$

Making use of Eqn. 5-10 and Eqn. 5-11, a triple integration of Eqn. 5-9 then gives a decomposition of the wall skin friction. After normalised by freestream velocity U_∞, boundary layer thickness δ and streamwise extend L_x and spanwise width L_z, finally a decomposition of the skin friction coefficients can be deduced, and it can be grouped into three categories:

$$
C_f = C_{f,\delta} + C_{f,\ \overline{u'v'}} + C_{f,\ \overline{I}_{x,z}} \tag{5-12}
$$

Here, the subscripts represent the ratio between displacement thickness and boundary layer thickness δ_d/δ, Reynolds shear stress $\overline{u'v'}$ and spatial variation $\overline{I}_{x,z}$, respectively. The first term $C_{f,\ \delta}$ is due to the thickness effect, and Fukagata et al. (2002) called it "Laminar term" since the formulation is exact in a fully-developed laminar channel flows. The author prefers to call it "thickness term" since $C_{f,\delta}$ in a plane boundary layer flow depends on the ratio between displacement thickness δ^* and boundary layer thickness δ. The complete expression for each term reads:

$$
\begin{aligned}
C_{f,\delta} &= \frac{4}{L_x L_z} \frac{1}{Re_\delta} \int_0^\delta \iint \frac{\overline{u}}{U_\infty} \frac{1}{\delta} dV \\
&= \frac{4(1-\delta^*/\delta)}{Re_\delta}
\end{aligned}
\tag{5-13}
$$

$$\begin{aligned} C_{f,\overline{u'v'}} &= \frac{4}{L_x L_z}\int_0^1 \iint (1-\eta)\frac{-\overline{u'v'}}{U_\infty^2} dxdz\ d\eta \\ &= \frac{4}{L_x L_z}\int_0^1 \iint (1-\eta)\frac{-(\overline{q_1}+\overline{q_2}+\overline{q_3}+\overline{q_4})}{U_\infty^2} dxdz\ d\eta \end{aligned} \tag{5-14}$$

$$\begin{aligned} C_{f,\ \overline{I}_{x,z}} &= \frac{-2}{L_x L_z}\int_0^1 \iint (1-\eta)^2 \left(\overline{I}_{x,z} + \frac{\partial \overline{p}}{\partial x} + \frac{\partial \overline{u}}{\partial t}\right)\frac{1}{U_\infty^2} dxdz\ d\eta \\ &= \frac{-2}{L_x L_z}\int_0^1 \iint (1-\eta)^2 \left(\overline{I}_{x,z} + \frac{\partial \overline{p}}{\partial x}\right)\frac{1}{U_\infty^2} dxdz\ d\eta \end{aligned} \tag{5-15}$$

Note that in Eqn. 5-14 the shear stress is further decomposes into four quadrant $\overline{q_i}$. The transient term is omitted, assuming the solution have reached a quasi-steady state. The last term $C_{f,\ \overline{I}_{x,z}}$ can be further expanded and gives a full description of how convection, diffusion and pressure gradient contribute to the skin friction:

$$\begin{aligned} C_{f,\ \overline{I}_{x,z}} = \frac{-2}{L_x L_z}\int_0^1 \iint (1-\eta)^2 \Bigg(& \overline{u}\frac{\partial \overline{u}}{\partial x} + \overline{v}\frac{\partial \overline{u}}{\partial y} + \overline{w}\frac{\partial \overline{u}}{\partial z} + \overline{u}\left(\frac{\partial \overline{u}}{\partial x} + \frac{\partial \overline{v}}{\partial y} + \frac{\partial \overline{w}}{\partial z}\right) \\ & - \frac{1}{Re_\delta}\left[\frac{\partial^2 \overline{u}}{\partial x^2} + \frac{\partial^2 \overline{u}}{\partial z^2}\right] + \frac{\partial \overline{p}}{\partial x} + \frac{\partial(\overline{u'u'})}{\partial x} + \frac{\partial(\overline{u'w'})}{\partial z}\Bigg)\frac{1}{U_\infty^2} dxdz\ d\eta \end{aligned} \tag{5-16}$$

Even though the formulation can be further simplified by the incompressibility assumption, those terms are retained to investigate the contribution to the skin friction. Those continuity terms can also be used to examine if the calculation is converged.

5-4-2 FIK derived skin friction

In the previous section, the extended FIK identity is deduced. Before demonstrating the impact of dimples on the skin friction, the derived formulation needs to be validated. The sampling area will be a rectangle box around the $3rd$ and the $4th$ dimple, and both statistical and snapshot data will be used to compute the mean shear stress and spatial gradients. An overview of the smooth plate skin friction decomposition in $3rd, 4th$ dimple are shown in Fig. 5-24a, 5-24b, respectively. The grey bars show the sub-total values from each friction-producing categories. The coloured bars in the $\overline{u'v'}$ quadrants represent partitioned contributions from the Q1 to Q4 quadrant events. The deduced total C_f, as shown in the figure legend, is in close agreement with the simulated C_f. In addition to total skin friction, the magnitude from each friction-producing categories also matches the values from the literature, shown in Fig. 5-23.

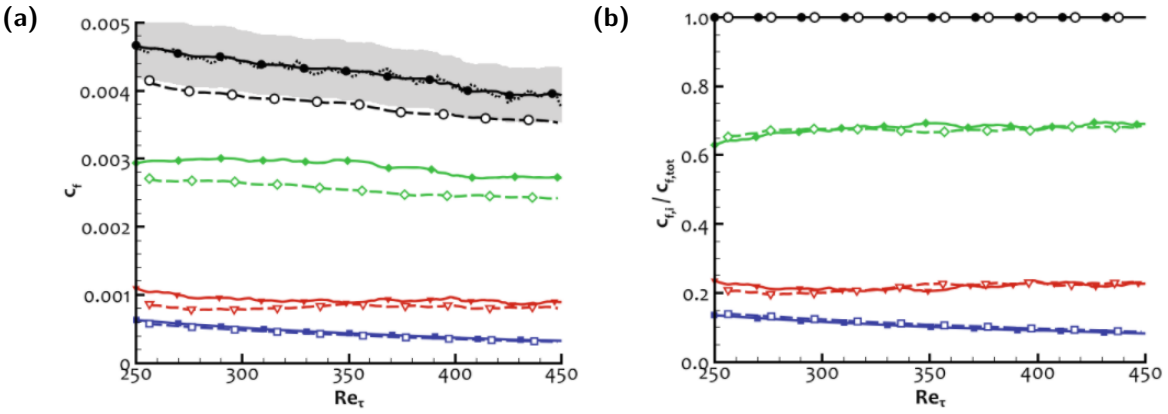

Figure 5-23: (a) skin friction C_f and its FIK decomposition as a function of Re_τ. (b) relative magnitude as a function of Re_τ. Smooth wall: *solid lines, filled symbols*. Ribbed wall: *dashed lines, opened symbols*. The grey area shows a $\pm 10\%$ variation w.r.t the total smooth wall friction. $C_{f,\delta}(\square)$;$C_{f,\ \overline{u'v'}}(\diamond)$; $C_{f,\ \overline{I}_{x,z}}(\triangledown)$. (Bannier et al., 2015)

The thickness term contributes to $\approx 4\%$ of the total skin friction, whereas the shear stress is about 65%. The smaller contribution of the thickness term is due to the Reynolds number difference. Current simulation has a higher inflow friction Reynolds number compare to Bannier et al. (2015). The thickness term has a slightly higher value than the skin friction formulation of a laminar plane boundary layer $C_{f,LBL} = 2.6/Re_\delta$. The average difference between FIK derived $C_{f,\delta}$ and $C_{f,LBL}$ is 15%. This deviation is expected since the physical meaning of thickness term in plane turbulent boundary layer flow is less straightforward than channel flow. As stated by Fukagata et al. (2002), thickness contribution in a plane turbulent boundary layer depends on the mean velocity profile via displacement thickness, and thus it is not a constant in plane TBL.

As for the shear stress contribution, Tbl. 5-3 summaries the relative contribution of quadrant events to the total skin friction. Ejection and sweep event are the main contributor to the friction. In detail, Q1 and Q3 event reduce the skin friction on the order of $\approx 20\%$, whereas Q2 and Q4 together account for 80% of the total wall friction.

Lastly for the spatial development category, a homogeneous plane TBL contains five terms: $\overline{u_{xx}}$, $\overline{u} \cdot \overline{v}_y$, $\overline{v} \cdot \overline{u}_y$, $2\overline{u} \cdot \overline{u}_x$, and $\overline{u'u'}_x$. Their contributions are shown in Fig. 5-25. Among other terms, $\overline{u} \cdot \overline{u}_x$ is the dominant term and account for almost 50% of the total skin friction. This term has an clear physical meaning: the boundary layer growth. As the plane TBL travel downstream, the boundary layer becomes thicker. At any arbitrary height, there is a net momentum source in a local infinitesimal volume element, due to the higher momentum influx (the product of streamwise velocity) and the lower momentum outflux. This is because the velocity at the same height is lower due to thicker TBL, leading to a net streamwise momentum source. This term is not what commonly deemed as the freestream entertainment, which causes the TBL growth and lowers skin friction. In the current case, the computation only includes the contribution inside the TBL. The effect of such entertainment is contained in the first term $C_{f,\delta}$. A synthesised result is summarised in Tbl. 5-1 and Tbl. 5-2. Overall, current calculation using the extended FIK formulation gives a consistent value compare to simulated C_f.

	$C_{f,simulated}$	$C_{f,FIK\ derived}$	Difference
3rd dimple	0.003519	0.003531	0.34 %
4th dimple	0.003469	0.003505	1 %

Table 5-1: Comparison between simulated and FIK derived skin friction of a smooth plate.

	$C_{f,\delta}$	$C_{f,\ \overline{u'v'}}$	$C_{f,\ \overline{I}_{x,z}}$
3rd dimple	$1.47 * 10^{-4}(4.16\%)$	$2.22 * 10^{-3}(63.14\%)$	$1.14 * 10^{-3}(32.7\%)$
4th dimple	$1.39 * 10^{-4}(3.97\%)$	$2.24 * 10^{-3}(64.03\%)$	$1.12 * 10^{-3}(32.0\%)$

Table 5-2: Decomposition of the skin friction of a smooth plate.

5-4-3 Impact of dimples on the skin friction

Fig. 5-27 shows an overview of the skin friction responses in the $3rd$ and $4th$ dimple. Among three friction-producing categories, spatial development has the largest response, and dimples hardly have any effect on the thickness contribution. Inspecting the effect on drag reduction, it is found that the drag reduction is mainly from the spatial development category. The Reynolds shear stress response is actually to increase the skin friction. Specifically, increased contributions from the ejection event (Q2, orange bar) and sweep event (Q4, red bar) in both $3rd$ and $4th$ dimples are identified. This finding is consistent with the results from quadrant analysis. On the other hand, different response strength in quadrant contribution is spotted. In the $3rd$ dimple, larger ejection and sweep contributions are observed, whereas in the $4th$ dimple the responses are weaker. This is due to two possible reasons. One is the different spanwise structures inside the $3rd$ and $4th$ sampling area. The different response might be due to different low-speed streak distribution inside the $3rd$ and $4th$ averaging area. Another possible reason is the fixed region of influence of dimple. From the flow topology result in Chap. 4-2, it is found that dimples have a fixed region of influence in the vertical direction. Most mean flow structures are limited below $y/\delta_0/D = 0.4$, regardless of the downstream position. However, TBL grows as the flow travel downstream. It is possible that at the downstream station, the boundary layer is too thick and dimple can not cast significant influence on the turbulent structures. Consider a more extreme case, in which the TBL is so thick that the dimple influence is limited below the buffer layer. In this case, the influence of dimples on the turbulent activity will be inconsequential, as the turbulence is most active in the buffer layer.

The above analysis suggests dimple increases Q2 and Q4 activity and thus generates higher skin friction. Compared to the study from Yakeno et al. (2014), where a spanwise wall oscillation technique is applied, it is found that most of their drag reductions are from the turbulent coherent structure response. As shown in Fig. 5-26, during the entire wall oscillation period, the ejection event has a higher bulk velocity, which stands for smaller skin friction in the channel flow. This trend can also be observed in a particular oscillation period for the sweep event. In other words, current simulation suggests a different skin friction reduction mechanism, which might not be the ones that summarises in Chap. 2-1-4, and is less relevant to turbulent activities.

Although a larger skin friction contribution by shear stress is obtained, a large skin friction

	$10^3 C_{f,\ \overline{u'v'}_{Q1}}$	$10^3 C_{f,\ \overline{u'v'}_{Q2}}$	$10^3 C_{f,\ \overline{u'v'}_{Q3}}$	$10^3 C_{f,\ \overline{u'v'}_{Q4}}$
3rd dimple	-0.335 (-9.48%)	1.61 (45.5%)	-0.332 (-9.4%)	1.29 (36.7%)
4th dimple	-0.309 (-8.84%)	1.64 (46.9%)	-0.328 (-9.35%)	1.23 (35.2%)

Table 5-3: Decomposition of the smooth plate wall friction from the Reynolds shear stress.

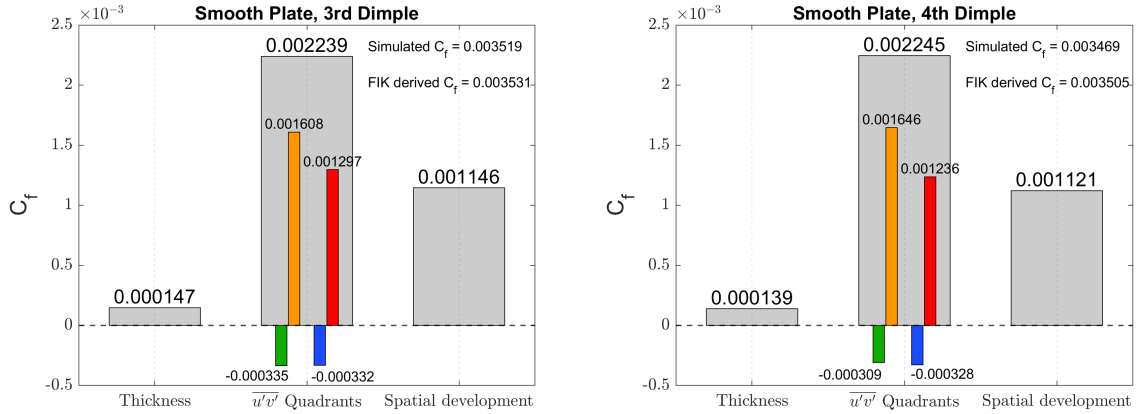

(a) Averaged over the $3rd$ dimple , $x/\delta_0 = [14.7, 16.8]$.

(b) Averaged over the $4th$ dimple, $x/\delta_0 = [20.4, 22.5]$.

Figure 5-24: Composition of the FIK derived skin friction compared with simulated value.

reduction in the spatial development category is found. The skin reduction is almost twice the value of shear stress response, and thus leads to an overall skin friction reduction. Next, the spatial contributions are expanded to investigate the responses.

5-4-4 Responses in the spatial development category $C_{f,\overline{I}_{x,z}}$

In this section, the response in each spatial term is demonstrated. Fig. 5-28 gives an overview of the skin friction response in each term for the $3rd$ and $4th$ Dimples. To begin with, it is found that the diffusion almost remains the same. It is reasonable since this term is relatively small. Although it shows a small friction reduction, with that indiscernible difference, a conservative conclusion will be "neutral". Overall, four terms exhibit skin friction reduction capabilities: $\overline{p}_x$, $\overline{u} \cdot \overline{v}_y$, $\overline{v} \cdot \overline{u}_y$, $\overline{u} \cdot \overline{w}_z$ and $\overline{u'w'}_z$; whereas other three terms have opposite effect: $\overline{u} \cdot \overline{u}_x, \overline{w} \cdot \overline{u}_z$ and $\overline{u'u'}_x$. In regards to their physical origin, it is found that most skin friction comes from the mean flow convection in the vertical and spanwise direction, while the latter has an opposite contribution from spanwise transportation. The Reynolds stress $\overline{u'w'}$ indeed has a small skin friction reduction in the $4th$ dimple but it should be considered within statistical uncertainty. Besides the general trend across the $3rd$ and $4th$ dimples, it is also found that the streamwise convection and vertical convection exhibit different sensitivity to the presence of dimple. The streamwise convection term is more sensitive and responsive to the downstream location. This is due to two possible reasons. One is the different different low-speed streak distribution inside the averaging area. Another possible cause is the fixed region of influence of dimple and the thickness of the boundary layer. Since the dimple has

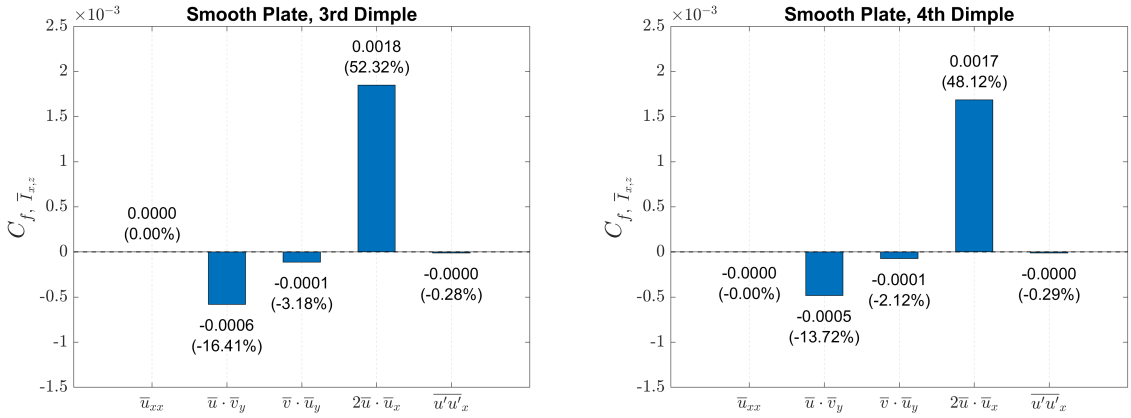

(a) Averaged over the $3rd$ dimple , $x/\delta_0 = [14.7, 16.8]$.

(b) Averaged over the $4th$ dimple, $x/\delta_0 = [20.4, 22.5]$.

Figure 5-25: Decomposition of the spatial development category of a smooth plate.

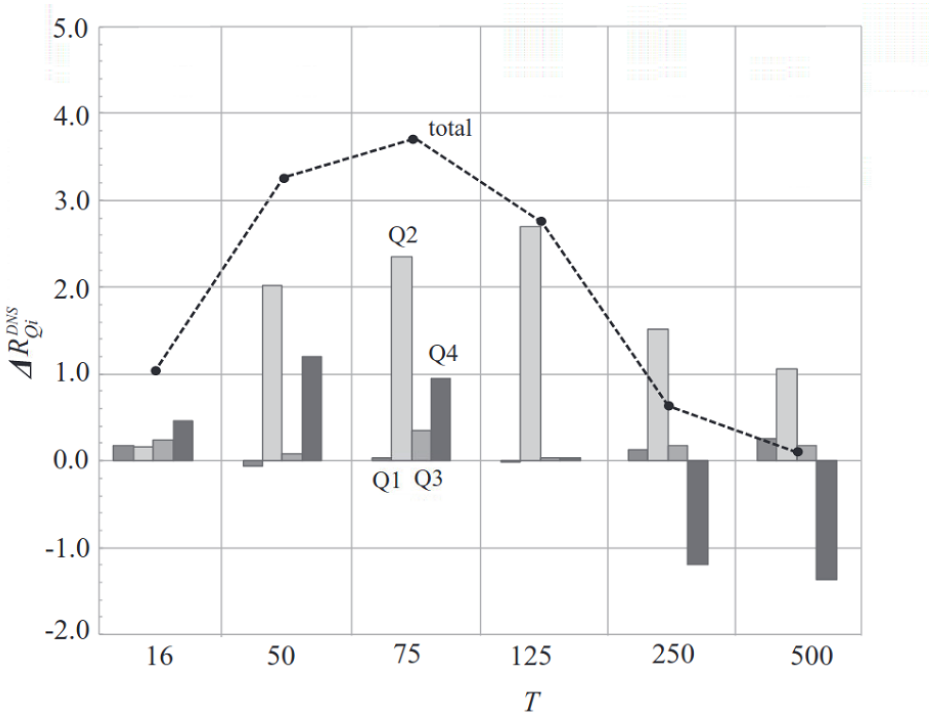

Figure 5-26: Quadrant contribution to the bulk velocity. In channel flows, higher bulk velocity represents lower skin friction. The dotted line corresponds to the sum of four quadrant contributions. X-axis is the oscillation periods. Y-axis is the normalised bulk velocity response. (Yakeno et al., 2014)

a fixed region of influence in the vertical direction, a thicker TBL means closer influence to the wall. In general, as fluid parcel moves closer to the wall, it will experience more drastic velocity gradient. This might explain why the $4th$ dimple shows a larger response in the streamwise convection.

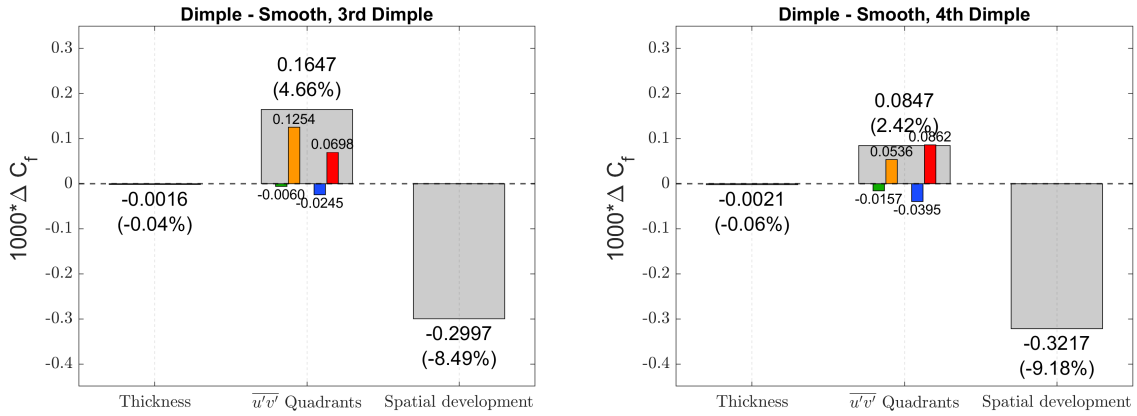

(a) Averaged over the $3rd$ dimple , $x/\delta_0 = [14.7, 16.8]$.

(b) Averaged over the $4th$ dimple, $x/\delta_0 = [20.4, 22.5]$.

Figure 5-27: Total Skin friction response and its decomposition.

The primary contributor of skin friction reduction have been identified: $\overline{p}_x$, $\overline{u}\cdot\overline{v}_y$, $\overline{v}\cdot\overline{u}_y$, $\overline{u}\cdot\overline{w}_z$ and $\overline{u'w'}_z$. However, it is a bit hard to grasp their physics due to the fact that the skin friction response from Fig. 5-28 is the sampling-box-averaged value. From the drag results in Chap. 4-4, it can be realised that the symmetry often introduces an opposite effect: the downstream half dimple counteracts the responses in the upstream half. Therefore, the gross effect across the dimple did not tell us much of its flow physics.

To better study its physical origin, the spatial responses are further considered. However, the FIK integration is performed over the entire volume, and thus the reconstructed Cf will be an average over a dimple. It would be favourable to inspect the skin friction distribution over streamwise and spanwise directions. This can be achieved by swapping the integration sequence such that the integration over vertical direction is in the inner layer. The difficulty lies in the fact that the integration orders are fixed during the simplification of the double integration and the triple integration. Luckily, the integration problems can be addressed with the Theorems of Fubini, which states that the integration order is exchangeable for any uniformly continuous functions. It is almost a guarantee for a physical system expect few exceptions when the system is in critical condition like shock waves or hydraulic jumps. It is possible that due to the limited snapshot data, the derived variables will be slightly discontinuous at the freestream interface, but the author believes such impact will be minor. Hence, the expression for $C_{f,\,\overline{I}_{x,z}}$ can be written as:

$$C_{f,\,\overline{I}_{x,z}} = \frac{-2}{L_x L_z}\iint\int_0^1 (1-y)^2\Bigg(\overline{u}\frac{\partial\overline{u}}{\partial x}+\overline{v}\frac{\partial\overline{u}}{\partial y}+\overline{w}\frac{\partial\overline{u}}{\partial z}+\overline{u}\Big(\frac{\partial\overline{u}}{\partial x}+\frac{\partial\overline{v}}{\partial y}+\frac{\partial\overline{w}}{\partial z}\Big) - \frac{1}{Re_\delta}\Big[\frac{\partial^2\overline{u}}{\partial x^2}+\frac{\partial^2\overline{u}}{\partial z^2}\Big]+\frac{\partial\overline{p}}{\partial x}+\frac{\partial(\overline{u'u'})}{\partial x}+\frac{\partial(\overline{u'w'})}{\partial z}\Bigg)\frac{1}{U_\infty^2}dy\,dxdz \quad (5\text{-}17)$$

This allows us to evaluate the spatial variation of the friction contribution in each spatial development terms! For reference, the theorems of Fubini is listed in Appendix. A-1. With

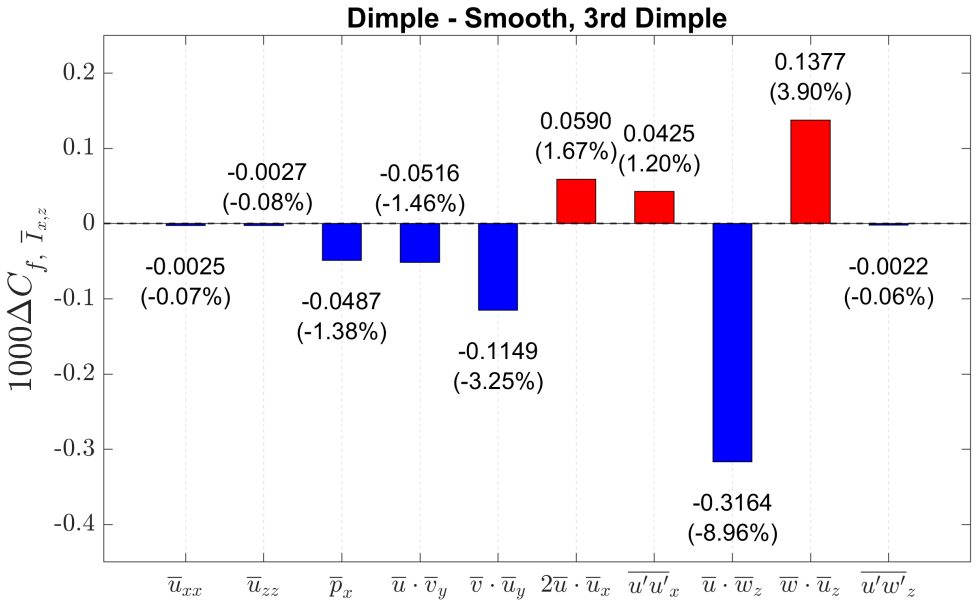

(a) Averaged over the $3rd$ dimple, $x/\delta_0 = [14.7, 16.8]$.

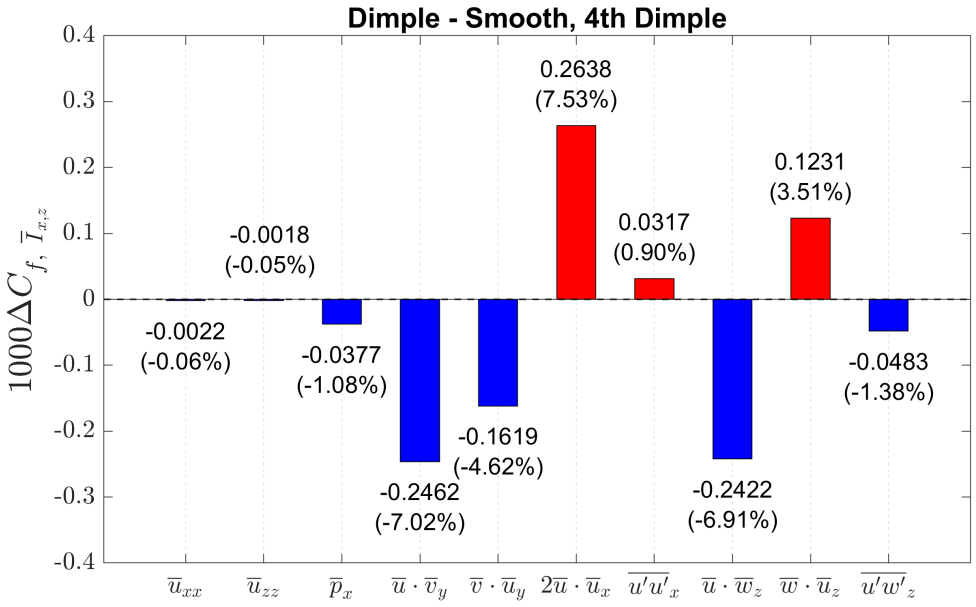

(b) Averaged over the $4th$ dimple, $x/\delta_0 = [20.4, 22.5]$.

Figure 5-28: Skin friction response in the spatial development category.

the re-arrangement of the integration, we can finally inspect the spatial impact on the skin friction.

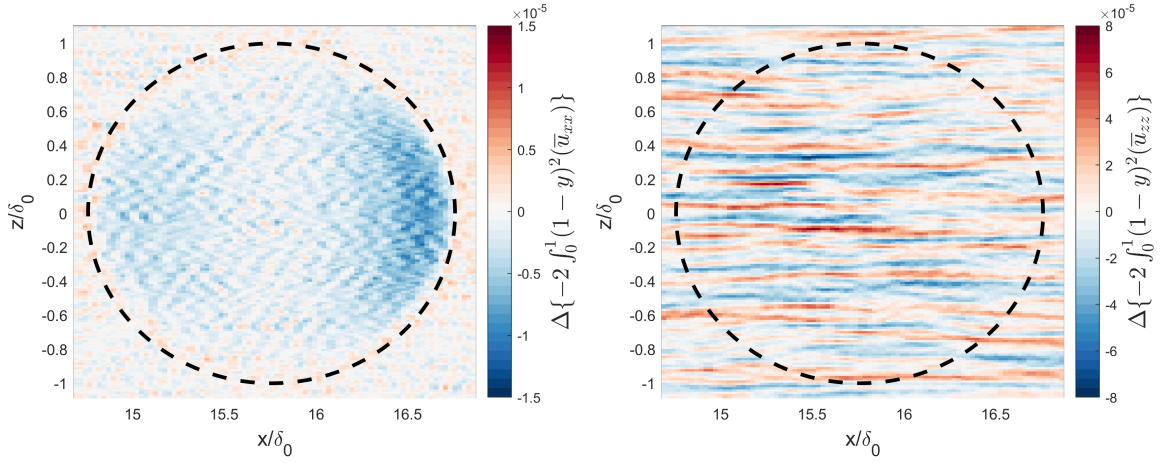

(a) Streamwise diffusion of mean streamwise velocity: $\frac{\partial^2 \overline{u}}{\partial x^2}$

(b) Spanwise diffusion of mean streamwise velocity: $\frac{\partial^2 \overline{u}}{\partial z^2}$

Figure 5-29: Skin friction response in diffusion. Averaged over the $3rd$ dimple, $x/\delta_0 = [14.7, 16.8]$.

1. **Diffusion ($\overline{u}_{xx}, \overline{u}_{zz}$)**
   The response is relatively small, as shown in Fig. 5-29. After normalised by the averaging area, the difference is of the order of $O(10^{-6})$. Streamwise diffusion shows a large response in the region where a large velocity gradient is present. For spanwise diffusion, it marks the boundary of the low-speed streak structures.

2. **Mean streamwise pressure gradient ($\overline{p}_x$)**
   The pressure gradient response is shown in Fig. 5-30a. This term, on average, gives a small skin friction reduction and is mainly from the upstream half contribution. The opposite response across the dimple can be easily realised by considering the pressure field developed by the dimple. Recall the mean flow structure in Chap. 4-4: there is a higher pressure being developed inside the dimple because of the surface curvature. As a result, flows enter the dimple experiencing a positive pressure gradient; and leave the dimple with a negative pressure gradient. Notes that the FIK formulation has a negative sign in the integration. This results in smaller skin friction in the upstream half of the dimple. Overall, a smaller averaged skin friction is retrieved.

3. **Mean streamwise velocity convection ($\overline{u} \cdot \overline{u}_x$)**
   As indicated in Fig. 5-30b. The response is mainly around the outer rim of the dimple. This is not surprising since flow near the dimple edge undergoes the most considerable streamwise velocity variations. As the flow enters the dimple, it suddenly reaches a higher boundary layer position due to the dimple depression. Specifically, it means flow at the same height has a larger streamwise velocity. As a result, the flow enters the dimple experiences a positive streamwise velocity gradient and vice versa. Overall, this term on average increase the skin friction. Noticeably, as the boundary layer become thicker, the response is more significant. The reason might be due to the higher sensitivity as one move closer to the wall.

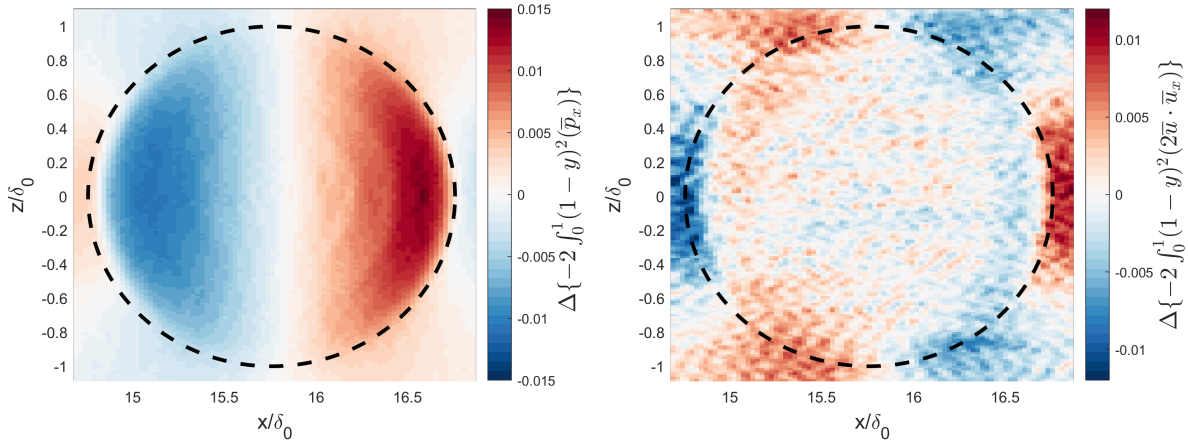

(a) Mean streamwise pressure gradient: $\frac{\partial \overline{p}}{\partial x}$

(b) Mean streamwise velocity convection: $\overline{u} \cdot \frac{\partial \overline{u}}{\partial x}$

Figure 5-30: (a) Skin friction response in mean streamwise pressure gradient. (b) Mean streamwise velocity convection. Averaged over the $3rd$ dimple, $x/\delta_0 = [14.7, 16.8]$.

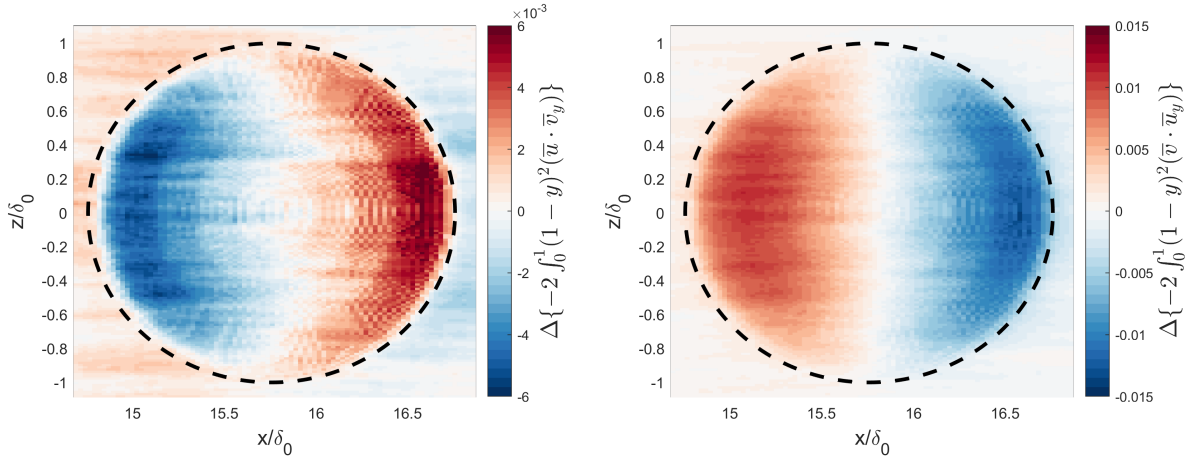

(a) Response due to varying vertical velocity: $\overline{u}\frac{\partial \overline{v}}{\partial y}$

(b) Response due to varying streamwise velocity: $\overline{v}\frac{\partial \overline{u}}{\partial y}$

Figure 5-31: Skin friction response in mean vertical velocity convection. Averaged over the $3rd$ dimple, $x/\delta_0 = [14.7, 16.8]$.

4. **Mean vertical velocity convection ($\overline{u} \cdot \overline{v}_y$ and $\overline{v} \cdot \overline{u}_y$)**
   This item contains two terms: $\overline{u} \cdot \overline{v}_y$ and $\overline{v} \cdot \overline{u}_y$. The reason why the author put them together is that it is a bit vague to grasp the physical meanings of individual term. If we rehash these two terms into flux form:

$$\overline{u} \cdot \frac{\partial \overline{v}}{\partial y} + \overline{v} \cdot \frac{\partial \overline{u}}{\partial y} = \frac{\partial (\overline{u}\ \overline{v})}{\partial y} \tag{5-18}$$

   then the physical meaning becomes very clear: momentum transport in the vertical

direction. Physically, a gradient in a infinitesimal volume is nothing but measuring the balance of any physical quantities. In the present case, the variable of interest will be the streamwise momentum carried by vertical velocity. In any arbitrary volume, the balance of the streamwise momentum is contributed by both ever-changing vertical velocity and streamwise momentum. The streamwise momentum flux can then be split into two base components: one with constant streamwise momentum but varying the vertical velocity inside the infinitesimal volume, and the other with constant vertical velocity but varying streamwise momentum. That is, $\overline{u} \cdot \overline{v}_y$ and $\overline{v} \cdot \overline{u}_y$, respectively. Fig .5-31 gives an overview of their friction contribution. Although these two terms are the main contributors of skin friction reduction, they also exhibit the opposite spatial response. For $\overline{u} \cdot \overline{v}_y$ component, the downward motion in the upstream half of the dimple leads to a positive vertical velocity gradient, and hence a negative contribution to the skin friction, and vice versa for the downstream half part. Likewise, $\overline{v} \cdot \overline{u}_y$ component has a positive friction contribution due to the downward motion in the upstream half of the dimple. Overall, these two terms, on average, contribute to skin friction reduction.

5. **Mean spanwise velocity convection ($\overline{u} \cdot \overline{w}_z$ and $\overline{w} \cdot \overline{u}_z$)**
   Similar to vertical velocity transport, the spanwise convection can be merged and re-written as:

$$\overline{u} \cdot \frac{\partial \overline{w}}{\partial z} + \overline{w} \cdot \frac{\partial \overline{u}}{\partial z} = \frac{\partial (\overline{u}\ \overline{w})}{\partial z} \tag{5-19}$$

then, these two terms represent the streamwise momentum balance due to spanwise velocity difference and due to varying streamwise momentum carried by constant spanwise velocity, respectively. For $\overline{u} \cdot \overline{w}_z$ shown in Fig. 5-32a, it is the principal contributor of the skin friction reduction and has to do with the confuser-diffuser flow topology. Considers the spanwise velocity gradient $\overline{w}_z$ as follows. Sweeping from $z/\delta_0 = -1$ to

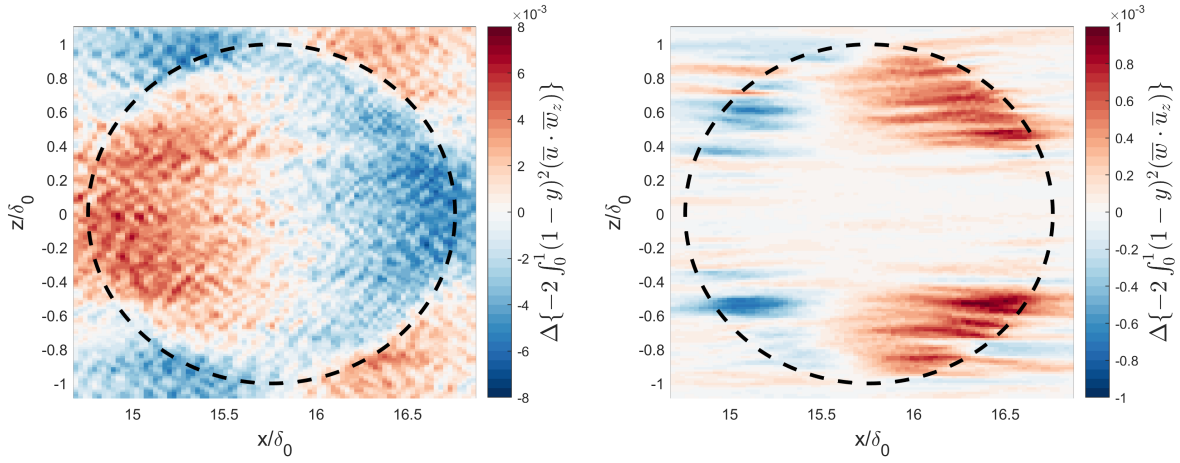

(a) Response due to varying spanwise velocity: $\overline{u}\frac{\partial \overline{w}}{\partial z}$

(b) Response due to varying streamwise velocity: $\overline{w}\frac{\partial \overline{u}}{\partial z}$

Figure 5-32: Skin friction response in spanwise velocity convection. Averaged over the $3rd$ dimple, $x/\delta_0 = [14.7, 16.8]$.

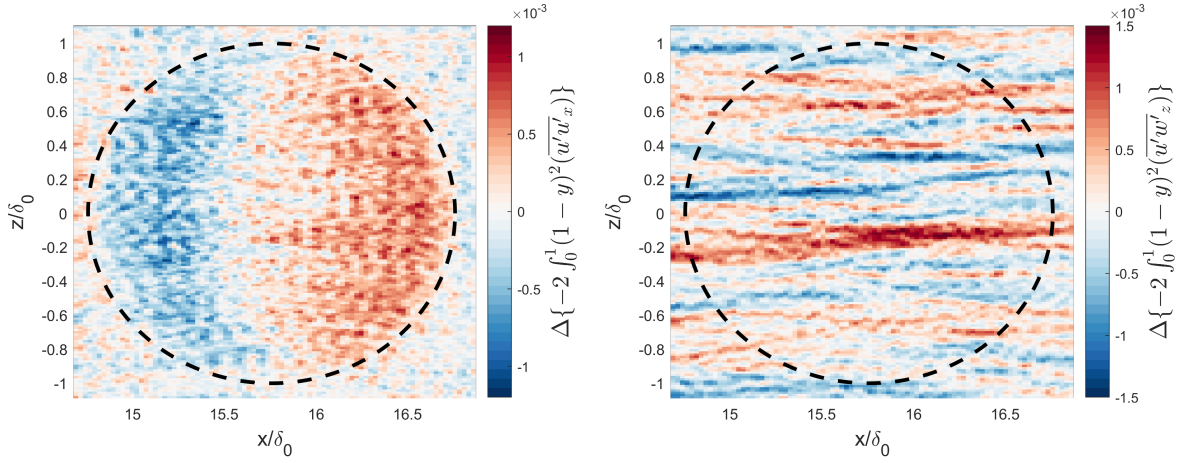

(a) $\overline{u'u'_x}$ **(b)** $\overline{u'w'_z}$

Figure 5-33: Skin friction response in Reynolds stress gradient $\overline{u'u'_x}$ and $\overline{u'w'_z}$. Averaged over the $3rd$ dimple, $x/\delta_0 = [14.7, 16.8]$.

$z/\delta_0 = 1$, the spanwise velocity starts from positive to negative across the dimple. It refers to the confuser part of the flow topology and has a negative spanwise velocity gradient. Hence, a positive contribution to the skin friction in the upstream half of the dimple. Physically, a net momentum source is generated in the upstream half dimple. A similar argument can be made for the downstream half skin friction reduction. Overall, this term generates a net skin friction reduction. The reason for this net balance is clear, and it comes from the uneven strength of the confuser-diffuser flow pattern. As discussed in Chap .5: Fig. 5-3, the vortex tube is weaker in the upstream half of the dimple, and thus a weaker upstream half flow structures. The uneven strength of the confuser-diffuser flow not only leads to a near wall spanwise velocity layer in the upstream half of the dimple, but also generates a net skin friction reduction through $\overline{u} \cdot \overline{w}_z$.

On the other hand, the $\overline{w} \cdot \overline{u}_z$ counteracts the skin friction reduction made by $\overline{u} \cdot \overline{w}_z$. This term is also built upon the confuser-diffuser flow topology, as seen in Fig. 5-32. A clear streamwise asymmetry can be seen. The positive friction contribution in the rear-end is due to the transport by spanwise velocity through the streamwise velocity gradient. Considers a finite volume with constant spanwise velocity. If the streamwise velocity at the volume faces $+z$ and $-z$, is different, a net streamwise momentum source/sink will be generated. In the downstream half, the developed diffuser flow in spanwise velocity convects the streamwise momentum. If the streamwise velocity is uniform, then there is no net balance. However, from Chap. 4-2, it has been concluded that the streamwise velocity is larger in the dimple centre. This, in turn, creates a net momentum inflow at the edge of the downstream half dimple, and vice versa for the upstream half.

6. **Reynolds stress gradient ($\overline{u'u'}_x$ and $\overline{u'w'}_z$)** The contribution from the Reynolds stress is generally smaller than the mean flow field. The streamwise gradient of $\overline{u'u'}$ has a positive contribution; whereas the spanwise gradient $\overline{u'w'}$ on average results in small skin friction reduction. Inspecting the spatial distribution, as shown in Fig. 5-

33, it can be inferred that dimples create stronger turbulent stress, which is consistent with the results from Chap .4-2. That is, flow enters the dimple undergoes a positive streamwise gradient of turbulent shear stress $\overline{u'u'}$, and thus a negative contribution to the skin friction. Similarly, flow leaves the dimple experiences weaker turbulent stress and hence a negative streamwise gradient of $\overline{u'u'}$. On the other hand, the response in $\overline{u'w'}_z$ is less comprehensible. From the colour shading, it suggests that the $\overline{u'w'}_z$ is stronger inside the dimple. However, such a large response could just because of the presence of low-speed streak. The large gradient only marks the interface of each coherent structures.

5-5 Uncertainty quantification

After applying three different techniques, the responses in turbulent coherent structures and their impact on the skin friction are revealed. However, these methods use different output data and post-processing procedure, and a discussion on their uncertainty is thus needed. To begin with, the quadrant analysis uses the mean flow statistics and snapshot data. These datasets are used to compute the fluctuation velocities and perform normalisation. The binning of JPDF and weighted JPDF are exact, so the primary source of uncertainty will be how close does the collected snapshot converge towards the mean flow. If the collected snapshots did converge, then the derived Reynolds contribution curve, as shown in Fig. 5-11, will not be reliable enough to draw any conclusion. Qualitatively speaking, current snapshots are collected over one flow-through cycle. In total, 243 snapshot files and 271 snapshots files are generated for the smooth plate and dimple plate, respectively. The quadrant analysis is then applied over a rectangle box around a dimple. Specifically, around 2.9 million sample points are collected for one vertical level. Compared to the quadrant scatters from van Campenhout et al. (2018), the author believes current dataset contains enough data points to have a statistical converged result. On the other hand, a simple test can also be done to examine the validity of present snapshots data, and that is to simply compare the mean values

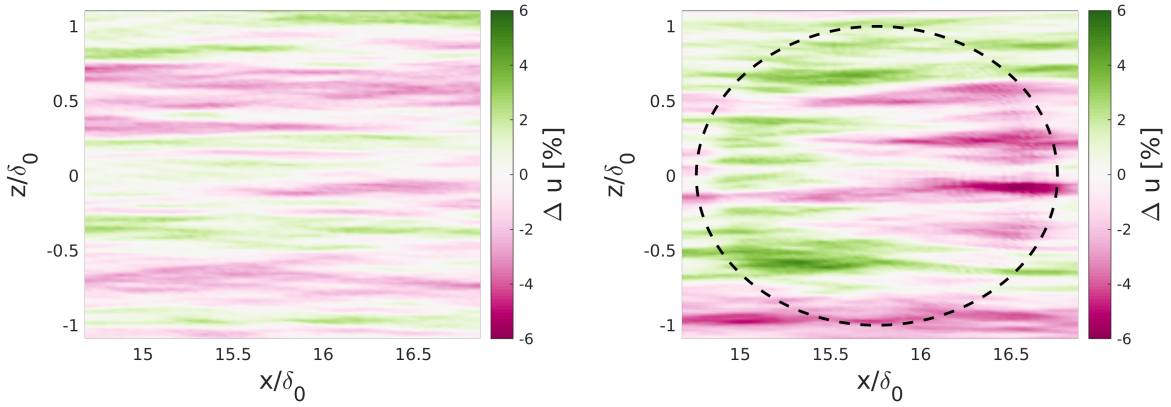

(a) Smooth plate **(b)** Dimple plate

Figure 5-34: Mean streamwise velocity difference (statistical file - snapshots averaged) at $y/\delta_0 = 0.01$ over the $3rd$ dimple.

to the solver output statistics. Fig. 5-34 shows the relative difference of the mean streamwise velocity between the solver output statistics and averaged from collected snapshots. Overall, the differences are below 5%. If we consider the domain average, which is analogues to collecting every sample in the domain, then the averaged bias is -0.38% for the dimple plate and -0.18% for the smooth plate. Ideally, one could, of course, collect snapshots for a longer time, but then the disk storage becomes the limiting factor. Specifically, present snapshots take about 8 TB disk storage for each simulation. Along with the statistics, a total of 20 TB is needed to store all data. Therefore, it is a trade-off between accuracy and data availability. The author believes current set up has collected enough data points with tolerable bias, and thus justifiable observations can be made.

Moving on to VITA analysis, the entailed uncertainty consists of three parts: the uncertainty of the probe data, a reliable algorithm that capable of capturing the desired signals and enough numbers of collected samples that a statistically converged ensemble can be made. Firstly, VITA uses probes data, which includes three vertical levels with a spatial resolution that comparable to $Ref.x2$ grid. From the Chap. 4-1, it has been shown that $Ref.x2$ has very close skin friction to the final case. Therefore, the underlying sub-sampled signal should also in agreement with the resolved flow field. The second part has to do with signal detection. Specifically, one wishes to know how sensitive is the algorithm to detect the correct signal. The author believes the present VITA method is more reliable than the original method in detecting the desired ejection/sweep event. In the original algorithm, a potential concern is the signal mixing from other quadrant events. In detail, the original algorithm sweeps the sampling window and computes window-averaged variance. If the resulting variance is larger than a particular threshold, the signal in the corresponding window is segmented. The sweep and ejection event is then determined based on $\frac{\partial u}{\partial t}$. However, such method requires careful selection of threshold value. Suppose the threshold is too low, then it is possible that some captured signals are from the outer interaction (Q1) and inner interaction (Q3). Compared to the original method, the current algorithm uses a pre-determined event mask to differentiate different quadrant event. Therefore, it is more reliable in capturing desired signals. The second part of the uncertainty comes from the issue of statistical convergence. This convergence can be assured by performing a set of VITA with varying window length. If the results from different window length are the same, then a statistical converged signal can be concluded. In detail, the present algorithm only samples one signal inside a window. By doing so, it prevents signal aliasing that distorts the ensemble. However, this also means as the window length becomes larger, the collected number of samples will be fewer. If the result from a large window is similar to a result drawn from a small window, then the ensemble signal is statistically converged. Fig. 5-35 shows the ensemble signals at $y/\delta_0 = 0.01$ for window length of $1.5, 3, 6$ seconds for $H > 3$. It can be found that present analysis is indeed statistically converged.

For the FIK identity, the snapshots and statistical files are used. The uncertainty is mainly from the underlying assumption to derive the formulation and the post-processing. Firstly, the derivation of the skin friction expression assumes that fluxes have vanished at the TBL/freestream interface. This requirement is exact in a fully developed turbulent channel flow, but not for turbulent boundary layer flows. Ideally, in a mean flow perspective, the flux should vanish at the interface, but it is quite hard for numerical simulations to have such perfect and smoothed interface. Also, in the formulation, a linear weighting function is retrieved from the simplification of the triple integration. This linear weighting function has a clear physical

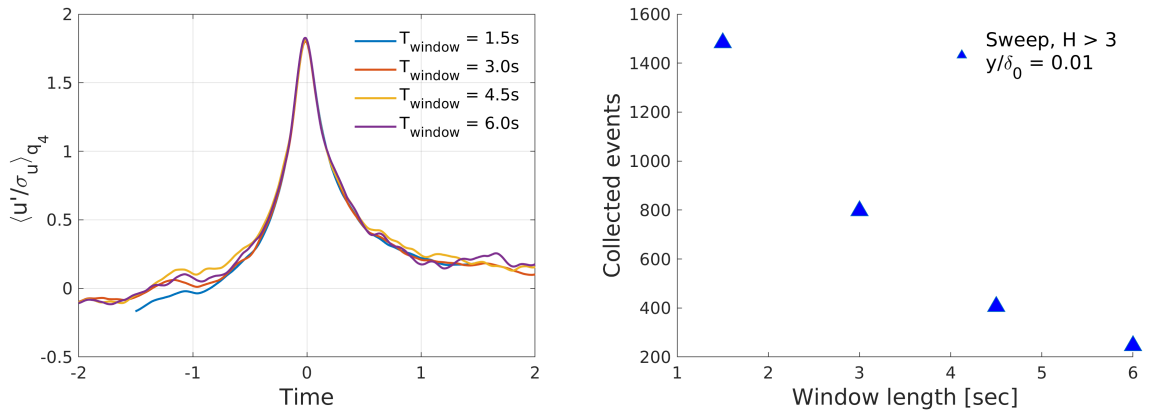

(a) Ensemble of the sweep event **(b)** Numbers of the collected samples.

Figure 5-35: Validation of the VITA analysis. The window length is from $1.5s$ to $6.0s$

meaning in a fully developed channel flow. An alternative weighting has been proposed by Peet et al. (2009), which could offer a better description for a turbulent boundary layer flow. As for the post-processing, the uncertainty comes from integration and spatial differentiation. The current approach uses Simpson' s rule for integration, which has an order of accuracy of 3. The spatial differentiation uses the central difference scheme in the centre, and upwind/-downwind scheme at the domain boundary. The larger error might be produced because of the manipulations mentioned above, along with the averaging of limited numbers of snapshot files. In the end, FIK identity has a higher uncertainty compared to the other two methods. Nevertheless, the close agreement between solver output and recovered skin friction suggests it could still be credible in revealing the skin friction contribution from the turbulent coherent structure and mean flow. The resulting Cf in Fig. 5-24a and Fig. 5-36 below supports this point.

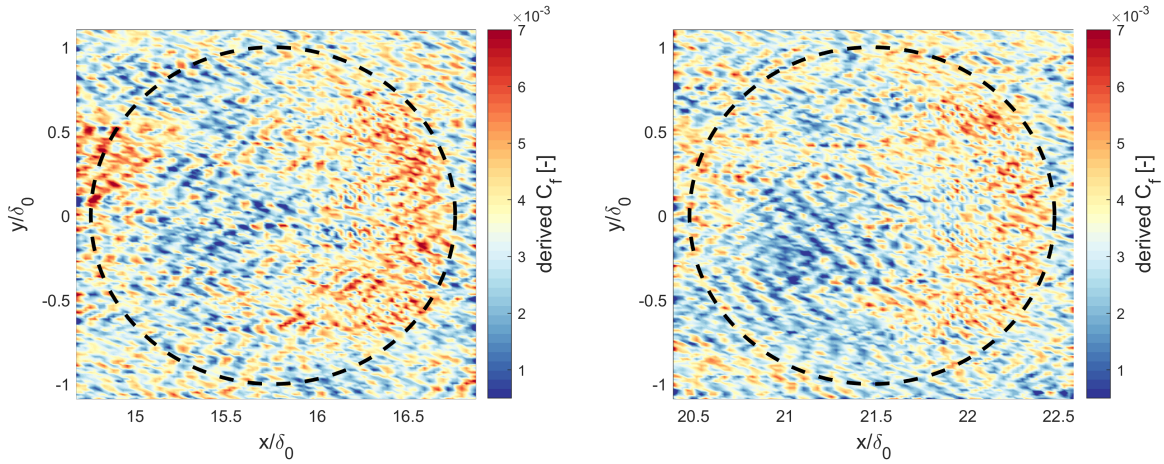

(a) Recovered over the $3rd$ dimple **(b)** Recovered over the $4th$ dimple

Figure 5-36: Skin friction recovered from the FIK identity.

Lastly, the author would like to stress out that even though the above-mentioned techniques all bear a certain level of uncertainty, the combined analysis metric, on the other hand, provides a more consistent observation of the responses in the coherent structures and skin friction. By comparing the result with other drag-reducing devices in each analysis scenario, a more reliable conclusion can be made.

5-6 Summary

Briefly speaking, in this chapter, the formation of near-wall spanwise velocity layer and statistical analysis of the turbulent coherent structure are investigated and performed. The statistical analysis starts from the general status of the turbulent coherent structures, in terms of their event occurrence and contribution to the Reynolds shear stress, to the averaged development of the intense event and eventually linking those variations to the skin friction responses. The combination of three analysis techniques gives a thorough and bottom-up examination of the responses in the turbulent coherent structures.

In detail, possible mechanisms are proposed to explain the formation of the residual layer inside the upstream half of the dimple. Utilising the Biot-Savart law, the vorticity fields suggest the streamwise vorticity in general forms a confuser-diffuser flow structures; whereas the vertical vorticity induces an opposite flow field. The formation of the near-wall spanwise velocity layer then is due to the weaker streamwise vorticity formed in the upstream half of the dimple. The flow field induced by the weaker steamwise vorticity is annulled by vertical vorticity in the upstream half of the dimple, leading to a residual spanwise velocity layer that has to do with the mass conservation. Further visualisation of the vorticity vectors supports such a hypothesis, showing a smaller L2-norm in the upstream half dimple.

Moving forward to the statistical analysis, firstly the quadrant analysis with hole-filtering sampling is considered. The raw snapshot data is first normalised by the mean statistics, and then re-sampled into 200x200 bins. Following the re-sampling, the Joint Probability Density Function can be retrieved. JPDF difference is computed, and the results suggest that dimples, in general, increase the occurrence in the outer interaction and sweep event. In the lower buffer layer, a small decrease in ejection and sweep is found. Further multiplying the JPDF with regard to its bin coordinates, the weighted JPDF can be derived, which reveals the contribution to Reynolds shear stress in each bin. The results demonstrate that the influence of dimples on the Reynolds stress generation is mainly in the buffer layer. In the wake region, the responses are relatively small in every quadrants. In the buffer layer, the extrema move towards positive x-axis. This means the principal contributor to the Reynolds tress in the ejection quadrant is the weaker ones, but the more substantial sweep events are now the primary source of the Reynolds inside the sweep quadrant. Also, a long tail in the sweep event is found, illustrating that the response in the sweep motion extends to the intense event. Besides the JPDFs, the hole-filtering technique is applied to perform conditional sampling. By sorting out different event strength, a quantitative decomposition of the stress contribution from each quadrant can be derived. The decomposition suggests that most dimple influences are again in the lower buffer layer and the weaker event. In the buffer layer, almost every quadrant has a larger contribution to the total Reynolds stress, hinting a more active turbulent coherent structures due to the presence of dimples. At the lower buffer layer, a larger contribution from the sweep event is obtained. This trend of increased contribution

extends to the strong event, which suggests dimple increases the activity of sweep event in the lower buffer layer. Besides focusing on single dimple, the downstream influence is also quantified. The responses are very similar to upstream dimples. Together with the results from mean flow topology in Chap. 4-2, it seems that dimples exert consistent influences on the plate regardless of the downstream location, and the main factor influencing the response would be Re_D.

For the Variable-Interval Time Averaging analysis, a different algorithm in event detection is applied. An algorithm demonstration is first carried out to justify the current method. Firstly the general shape of the ensemble signal is investigated. It is found that the sweep and ejection event seems to have a connection in terms of their time evolution. The long tails of the sweep/ejection event in the streamwise fluctuation reflect the residual signals from the other. However, it is not clear which of these two events starts first from the current analysis framework. Forwarding to inspect the responses under dimple plate, the ensemble time series shows that the impact of dimples on the intense quadrant event is marginal. The statistically averaged development of the quadrant event is identical between the smooth plate and dimple plate. The peak values are also identical, meaning that the Reynolds stress generation is the same for individual quadrant event. However, this could be due to the large numbers of collected signals, which inevitably overshadow responsive signals. To rule out such possibility, a sweep of different hole-filtering strength is applied. The resulting signals found a clear signal due to the presence of dimples. In the wake region, the sweep event now has a slower development, which means the flow is accelerating/decelerating at a slower pace during the event burst. However, the peak value remains the same, meaning that the magnitude of the generated Reynolds stress is still the same.

In order to relate the impact of dimples on the turbulent coherent structure to the skin friction responses, the FIK identity analysis is carried out. Different from the formulation of Fukagata et al. (2002); Yakeno et al. (2014) and Bannier et al. (2015), a volumetric averaged version of the FIK identity is derived. This gives an overall evaluation of the responses across the dimple. From the overall skin friction partition, it suggests that the Reynolds shear stress indeed leads to a small skin friction increase, which coincides with previous stronger mean turbulent boundary layer profiles and the results from quadrant analysis. On the other hand, spatial development terms are found to be the main contributor to skin friction reduction. Among all the spatial gradient contributions, the wall-normal convection $\overline{u} \cdot \overline{v}_y$ and $\overline{v} \cdot \overline{u}_y$, streamwise pressure gradient $\overline{p}_x$ and spanwise convection $\overline{u} \cdot \overline{w}_z$ are the main sources of skin friction reduction; whereas the streamwise convection plays a major opposite role. To further study the spatial distribution of each friction-producing components, a revision of the extended FIK formulation is implemented. By utilizing the Theorem of Fubini, the integration order can be swapped to obtain the skin friction contribution in each horizontal point. In general, it is found that the skin friction responses are very symmetrical, but their overall averaged values give a small skin friction reduction. Interestingly, the effect of confusser-diffuser flow topology on the skin friction is revealed. It has two opposite effect on skin friction. $\overline{u} \cdot \overline{w}_z$ leads to skin friction reduction, whereas $\overline{u} \cdot \overline{w}_z$ gives a small skin friction increase. Inspecting the spatial plots of $\overline{u} \cdot \overline{w}_z$, we found that the small increase is due to the asymmetry of the confusser-diffuser flow topology, which can be linked to the weaker flow topology in the upstream half of the dimple, as discussed in Chap. 5-1.

Lastly, the uncertainty of each analysis technique is discussed. Possible factors are considered and quantified. The uncertainty in quadrant analysis is investigated by comparing the mean

flow quantity between solver output statistics and snapshots averaged value. The resulting deviations are within 5%, indicating a good agreement in terms of the convergence. This means with such consistency of the normalisation factors and a large number of the collected sample points; the underlying quadrant analysis should be reliable enough to draw a tenable observation and conclusion. Next, the VITA analysis uses probe data, which has a spatial resolution comparable to the $Refx2$ simulation. The grid convergence from Chap. 4-1-2 suggests such set up would still retain a close flow feature to the resolved flow field. Besides the spatial sampling issue, the convergence test is also carried out by adapting different windowing time. The outcome suggests current VITA ensemble is indeed statistically converged. Lastly, the uncertainty in the FIK identity analysis is discussed. Since FIK identity adapts a few physical assumptions and lots of post-processing, higher uncertainty is anticipated. The uncertainty from the physical assumption is relatively small compared to the post-processing, in which the spatial differentiation and integration are performed. Still, a close agreement between simulated skin friction and reconstructed skin friction provides strong evidence that current FIK identity analysis is reliable.

From the above analysis, it can be concluded that dimples do not have a skin friction reduction mechanism that analogous to other drag-reducing methods, of which the underlying turbulent coherent structures are weakened. The analysis reveals that mostly dimples lead to higher turbulent activity and thus, a higher skin friction contribution. The skin friction reduction, on the other hand, seems has to do with the developed mean flow structures.

Chapter 6

Conclusion

This thesis project focuses on the numerical investigation of a turbulent boundary layer flow over dimpled surfaces. The mean flow topology and the drag performance are quantified. Also, in this project, three different statistical analysis techniques are applied: Quadrant Analysis with the hole-filtering technique, Variable-Time Interval Averaging and the Fukagata-Iwamoto-Kasagi identity analysis. This evaluation metric provides a clear, logical flow to understand the responses in the turbulent coherent structure. In Chap. 1, four research questions were identified based on proposed research objectives. The following section then concludes the thesis by answering these four questions based on the foregoing investigation.

1. **Can the drag result from Spalart et al. (2019) be reproduced?** The result from Spalart et al. (2019) is confirmed. Current LES result reveals a small drag increase on the order of 1%, which is in-line with the outcome from Spalart et al. (2019). Also, the recent tunnel experiment by van Campenhout et al. found a small drag increase on a similar order. These consistent results oppose the idea of drag reduction by dimples. On the other hand, the convergence issue in Spalart et al. (2019) can not be evaluated, due to the improper solver output settings being done. Currently, a new set of simulations is carrying out to clarify the influence of oscillated signals to the drag results.

2. **How does a dimple locally affects the mean flow of the turbulent boundary layer? What are the developed flow structures and the corresponding drag in spanwise and streamwise direction?** It is concluded that confuser-diffuser flow structures are present over the dimples, and the structures in the downstream dimples are identical. The flow topology extends to $0.15D$ to $0.2D$ above the wall for the mean spanwise velocity, and $0.35D$ to $0.4D$ for the mean vertical velocity. A spanwise oscillation sequence that connects the upstream dimple and downstream dimple is observed in the buffer layer. Also, a near-wall spanwise velocity layer is found in the upstream half of the dimple. The top-view of the total drag reveals that mostly the total drag reduction is from the upstream half of the dimple; downstream half shows a strong drag increase in the rear end. In the spanwise direction, the influence on the total drag is relatively homogeneous. The influence upstream/downstream of a dimple is also observed.

It is concluded that the influence can extend up to $1.5D$, with downstream/upstream showing a smaller/larger total drag.

3. **How does a dimple affect the turbulent coherent structures?** It is observed that dimples increase the occurrence in Q1 and Q4 quadrants. Given a small JPDF difference, the weighted JPDF shows a strong shift towards stronger Q4 event. The resulting Reynolds stress hence shows a larger contribution from the Q4 event in the buffer layer. Further inspecting the intense ejection and sweep events using VITA analysis, a marginal influence on the event development except for the sweep event is concluded. In the wake region, the sweep event shows a slower, extended development pace, yet the event strength being identical to the smooth plate. Overall, the above investigations suggest a higher turbulent activity in the dimple plate, and this higher activity is mainly originated from the occurrence distribution, not the variation in the event development.

4. **How does a dimple affects each drag-contributing term?** It is concluded from the FIK identity analysis that dimples increase the activity of turbulent coherent structures, and the increased activity, in turn, produces higher skin friction drag. The FIK identity reveals that the coherent structures under the dimple plate on average increase the skin friction drag on the order of 3%. In this regard, even though a clear spanwise oscillating flow structure is observed, it is unlikely that dimples bear similar working mechanism as the spanwise wall oscillation. The effect of dimples is to enhance the turbulent activity, which results in higher skin friction contribution. The FIK identity suggests that mostly the skin friction reduction comes from the mean flow convection.

6-1 Recommendations for Further Research

Motivated by the improved understanding of dimple flow physics, the author recommends further research of the following.

- **Perform simulations with the aligned dimples.** Due to limited computational resource, the current project only focuses on the staggered layout. In general, the aligned layout is found to be increasing larger drag compared to the staggered layout. It might be insightful to examine what causes such a larger response, and which drag-contributing terms are significantly affected by the dimple layout.

- **Study other drag-reducing surfaces that apply similar concept.** This project has provided exhaustive analysis on how dimples alter the flow topology, turbulent coherent structure, and the underlying drag. It would be beneficial to investigate other drag-reducing surfaces like wavy-walls, based on the current finding.

- **Investigate the vortex activity using lambda-2 or Q criterion.** Although the present study applies various statistical techniques to extract specific characteristics of the turbulent coherent structures, less emphasis is placed on the turbulent vortex structures. Performing conditional sampling technique using L2 or Q criterion might deliver invaluable vortex structure data into the dimple flow physics.

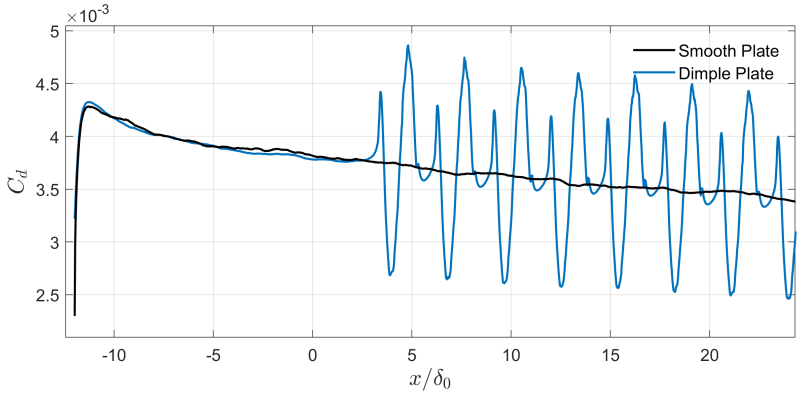

Figure 6-1: Skin friction near the inflow station $x/\delta_0 = 0$.

Besides potential research, the author would like to stress out some issues confronted in the current project for future improvement in this topic.

- **Limited geometry resolution.** As stated in Chap. 4-4, the surface variables suffered from the coarse STL resolution, and thus anomalous patterns were formed inside the dimple. Even though the wall shear plot suggests these patterns did not lead to flow separation and the effect on the mean flow is relatively mild, the impact on the coherent structures is more subtle. To address this issue, a new plate geometry has been implemented with much-refined triangulation.
- **Small C_f deviation in the upstream.**The skin friction near the inflow station is shown in Fig. 6-1. A 0.55% drag deviation at the inflow station is obtained. It can be found that the flow in the recycling module has different skin friction value, yet the difference is very small. Since the order of interest in the dimple drag reduction is very small, this deviation must be addressed to have a more convincing argument. Two possible sources are identified. Firstly, it could come from slightly different meshing. Even though the wall vertical spacing is kept the same between two plates, the dimple plate implements a $0.5mm$ uniform spacing layers to resolve the dimpled surface. This could potentially affect the resolved wall shear. However, this set up is relatively hard to modify. A more consistent approach will be using a surface conformed mesh, but it is not viable with the current numerical set-up. The second source is the inflow recycling module. Chances are due to the initialisation, the recycled profile has different adjustment and thus slightly different inflow state. The new set of the simulations could be initialised using the same random seed, and therefore a similar random perturbation is applied during the initialisation.
- **Drag reduction by the mean flow convection.** Lastly, in the FIK identity analysis, it is found that the skin friction reduction is mainly from the mean flow convection. However, the momentum balance then suggests that an overall skin friction reduction inside the current sampling box must come from the rest plate area. If it is just this momentum transfer, then it will cancel out the drag reduction when a larger domain is sampled. However, due to limited disk storage, the snapshots are post-processed and sampled only around the dimple. More study is needed to explore the ”zero-sum” problem with the skin friction reduction by the mean flow convection.

Appendix A

List of Theorem

A-1 Fubini's theorem

Theorem. If A and B are complete measure spaces. Suppose function $f(x, y)$ is $A \times B$ measurable. If:

$$\int_{A\times B} |f(x,y)| \; d(x,y) < \infty \tag{A-1}$$

Where the integral is performed over a product measure on the space $A \times B$. Then we have:

$$\int_A \Big(\int_B f(x,y)dy \Big) dx = \int_B \Big(\int_A f(x,y)dx \Big) dy = \int_{A\times B} f(x,y) \; d(x,y) \tag{A-2}$$

If the absolute value of the product integral is not finite, then the two iterated integrals might not have equal values. Furthermore, if the function $f(x, y)$ is continuous on a rectangular space $R \in A \times B : a \leq x \leq b, \; c \leq y \leq d$, then we have:

$$\int_R f(x,y) \; d(x,y) = \int_b^a \left(\int_d^c f(x,y)dy \right) \; dx = \int_d^c \left(\int_b^a f(x,y)dx \right) \; dy \tag{A-3}$$

Proof. Take arbitrary partitions $x_0 = a < x_1 < ... < x_m = b$ in a bounded interval of $[a, b]$ and $y_0 = c < y_1 < ... < y_n = d$ in a bounded interval of $[c, d]$. Let $\mathcal{P}$ be the partition of the

corresponding rectangular space $R \in A \times B : a \leq x \leq b,\ c \leq y \leq d$ into $m \times n$ sub-rectangle $R_{ij} = [x_{i-1}, x_i] \times [y_{j-1} \times y_j]$. Suppose the increments in (x, y) and the maximum f and minimum f among sub-rantangles R_{ij} can be written as:

$$\begin{aligned} \Delta x_i &= x_i - x_{i-1} \\ \Delta y_j &= y_j - y_{j-1} \end{aligned} \tag{A-4}$$

$$\begin{aligned} m_{ij} &= \inf_{R_{ij}} f \\ M_{ij} &= \sup_{R_{ij}} f \end{aligned} \tag{A-5}$$

Apparently, the function $f(x, y)$ is bounded by Infimum and Supremum:

$$m_{ij} \leq f(x, y) \leq M_{ij}, \quad \text{for } (x, y) \in R_{ij} \tag{A-6}$$

Integrate in a sub-rectangle R_{ij} over small increment $[x_{i-1}, x_i]$, we have:

$$m_{ij}\Delta x_i \ \leq \ \int_{x_{i-1}}^{x_i} f(x, y)\ dx \ \leq \ M_{ij}\Delta x_i, \quad \text{if } y \in [y_{j-1}, y_j] \tag{A-7}$$

Summing R_{ij} from $i = 1$ to $i = m$, we reach the following inequality:

$$\sum_{i=1}^{m} m_{ij}\Delta x_i \ \leq \ \int_a^b f(x, y)\ dx \ \leq \ \sum_{i=1}^{m} M_{ij}\Delta x_i, \quad \text{if } y \in [y_{j-1}, y_j] \tag{A-8}$$

Applying similar approach, Integrate Eqn. A-8 over small increment $[y_{i-1}, y_i]$ and sum from $j = 1$ to $j = n$:

$$\sum_{j=1}^{n}\sum_{i=1}^{m} m_{ij}\Delta x_i\Delta y_j \ \leq \ \int_c^d \int_a^b f(x, y)\ dxdy \ \leq \ \sum_{j=1}^{n}\sum_{i=1}^{m} M_{ij}\Delta x_i\Delta y_j \tag{A-9}$$

Therefore, for every partition $\mathcal{P}$, we have:

$$L(f, \mathcal{P}) \ \leq \ \int_c^d \int_a^b f(x, y)\ dxdy \ \leq \ U(f, \mathcal{P}) \tag{A-10}$$

On the other hand, if we assume function f is integrable on the rectangle R, the integral $\iint_R f dA$ has a unique number which satisties:

$$L(f, \mathcal{P}) \ \leq \ \iint_R f dA \ \leq \ U(f, \mathcal{P}) \tag{A-11}$$

Note that above inequality holds for every partition $\mathcal{P}$. Therefore, equation below must holds:

$$\iint_R f dA = \int_c^d \int_a^b f(x, y) dx \ dy \tag{A-12}$$

Since the order of integration and summation in Eqn. A-7 and Eqn. A-8 can be switched, above procedures can be followed with reversed (x, y) order, and eventually we have:

$$\int_c^d \int_a^b f(x, y) \ dxdy = \int_a^b \int_c^d f(x, y) \ dydx \tag{A-13}$$

Appendix B

List of figures

B-1 Results

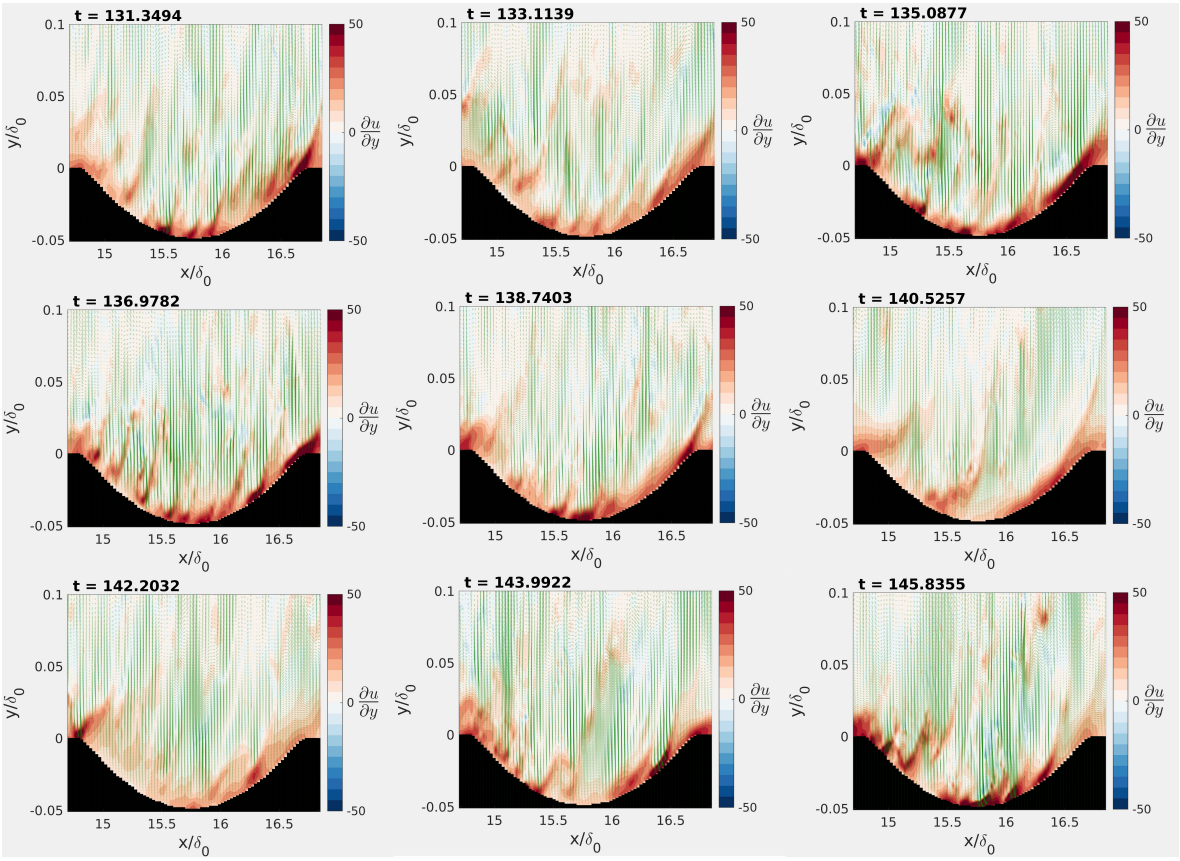

Figure B-1: Instantaneous shear $\frac{\partial u}{\partial y}$ and the (u', v') quivers.

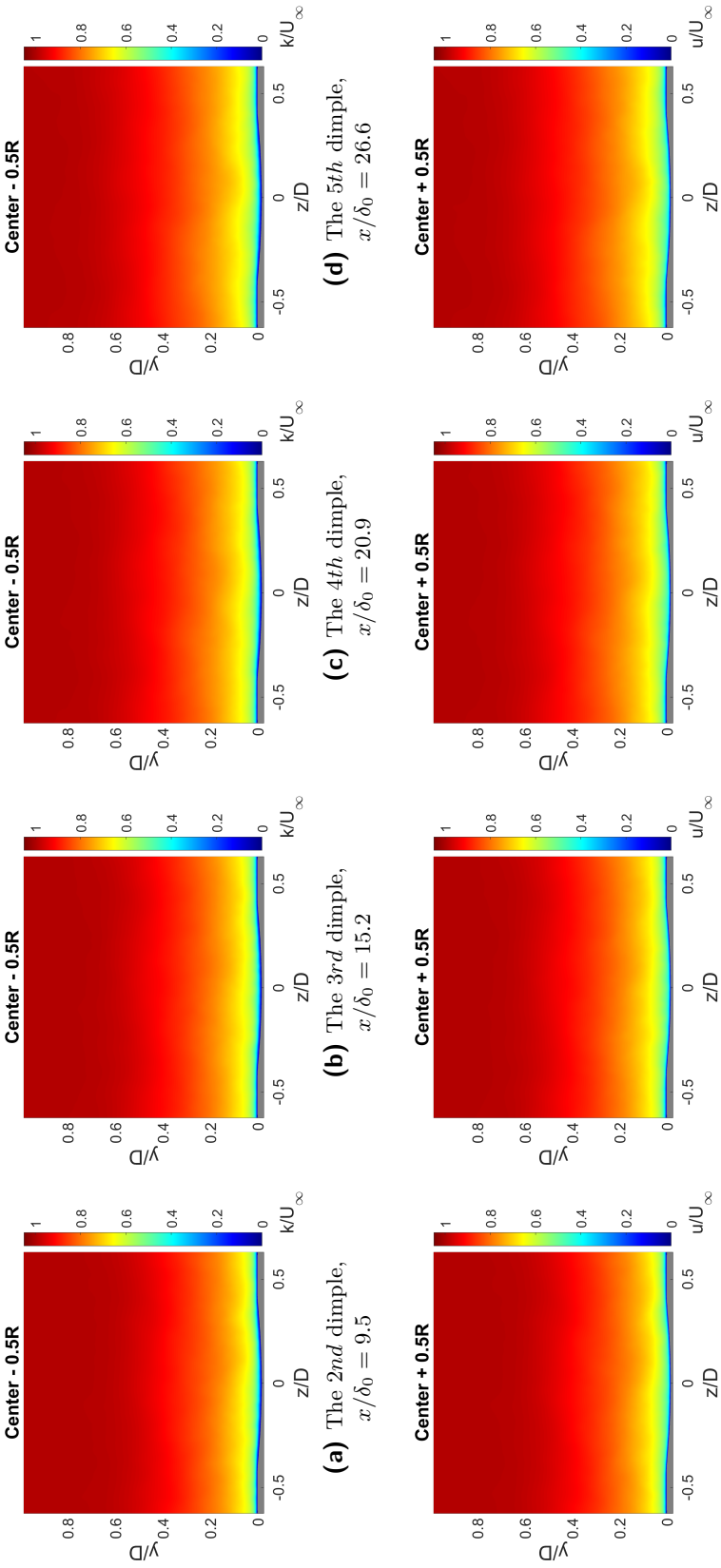

(a) The $2nd$ dimple, $x/\delta_0 = 9.5$ **(b)** The $3rd$ dimple, $x/\delta_0 = 15.2$ **(c)** The $4th$ dimple, $x/\delta_0 = 20.9$ **(d)** The $5th$ dimple, $x/\delta_0 = 26.6$

(e) The $2nd$ dimple, $x/\delta_0 = 10.5$ **(f)** The $3rd$ dimple, $x/\delta_0 = 16.2$ **(g)** The $4th$ dimple, $x/\delta_0 = 21.9$ **(h)** The $5th$ dimple, $x/\delta_0 = 27.6$

Figure B-2: Mean streamwise velocity cross section of the dimple plate at the upstream and downstream Y-Z plane, over the $2nd$ to the $5th$ downstream dimples.

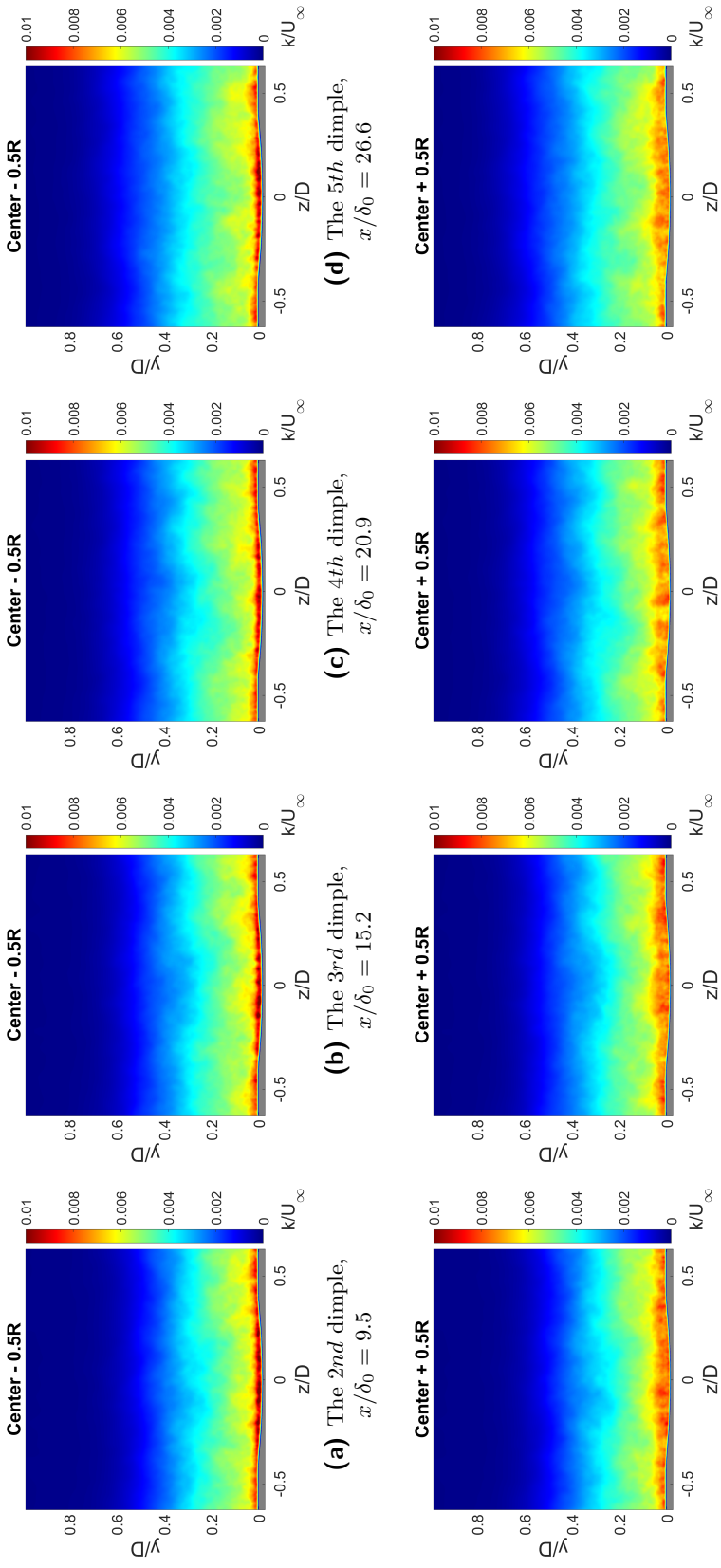

(a) The $2nd$ dimple, $x/\delta_0 = 9.5$

(b) The $3rd$ dimple, $x/\delta_0 = 15.2$

(c) The $4th$ dimple, $x/\delta_0 = 20.9$

(d) The $5th$ dimple, $x/\delta_0 = 26.6$

(e) The $2nd$ dimple, $x/\delta_0 = 10.5$

(f) The $3rd$ dimple, $x/\delta_0 = 16.2$

(g) The $4th$ dimple, $x/\delta_0 = 21.9$

(h) The $5th$ dimple, $x/\delta_0 = 27.6$

Figure B-3: Mean turbulent kinetic energy cross section of the dimple plate at the upstream and downstream plane, over downstream dimples.

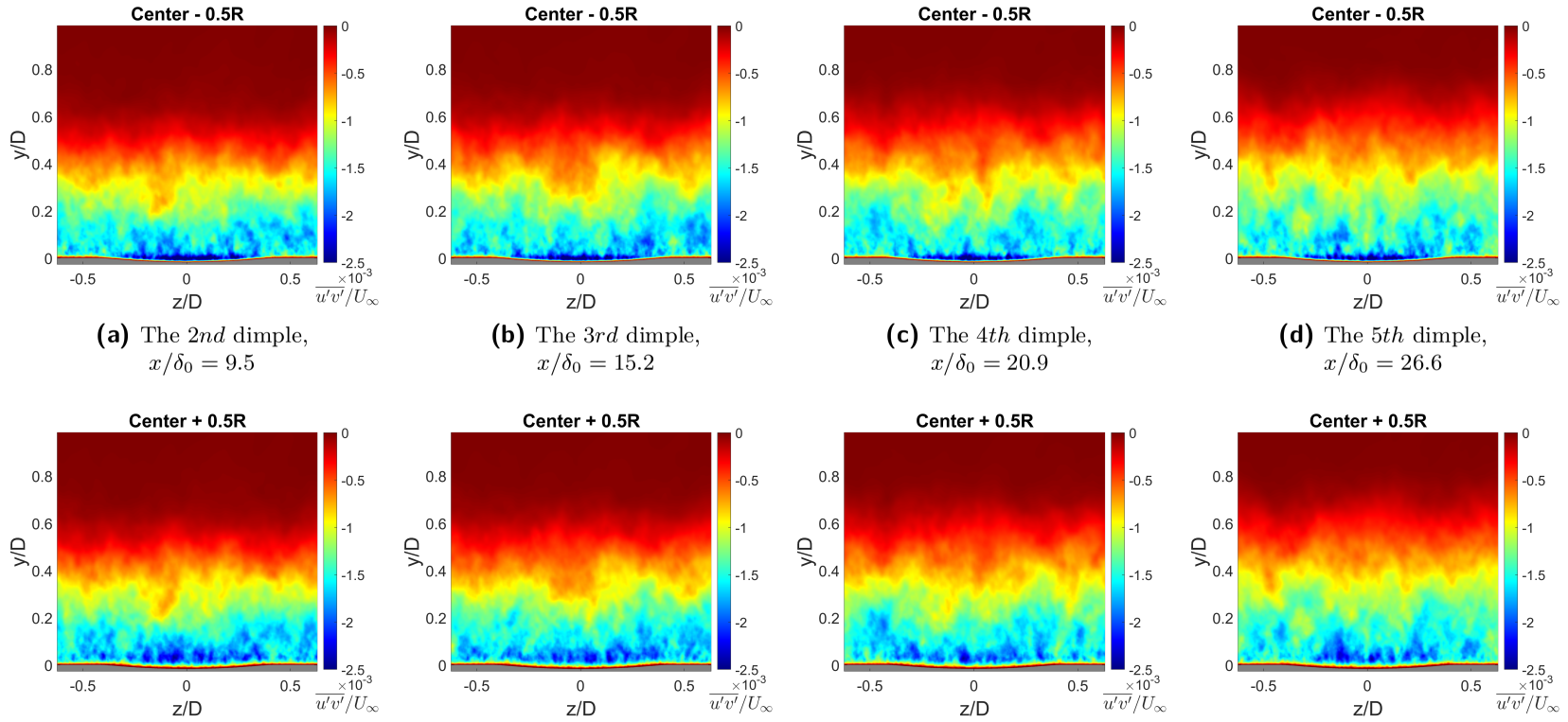

(a) The $2nd$ dimple, $x/\delta_0 = 9.5$

(b) The $3rd$ dimple, $x/\delta_0 = 15.2$

(c) The $4th$ dimple, $x/\delta_0 = 20.9$

(d) The $5th$ dimple, $x/\delta_0 = 26.6$

(e) The $2nd$ dimple, $x/\delta_0 = 10.5$

(f) The $3rd$ dimple, $x/\delta_0 = 16.2$

(g) The $4th$ dimple, $x/\delta_0 = 21.9$

(h) The $5th$ dimple, $x/\delta_0 = 27.6$

Figure B-4: Mean Reynolds shear stress cross section of the dimple plate at the upstream and downstream plane, over downstream dimples.

B-2 Quadrant Analysis

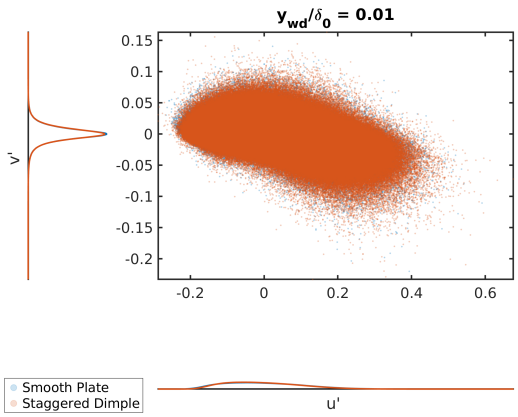

(a) Raw quadrant scatter at $y_{wd}/\delta_0 = 0.01$

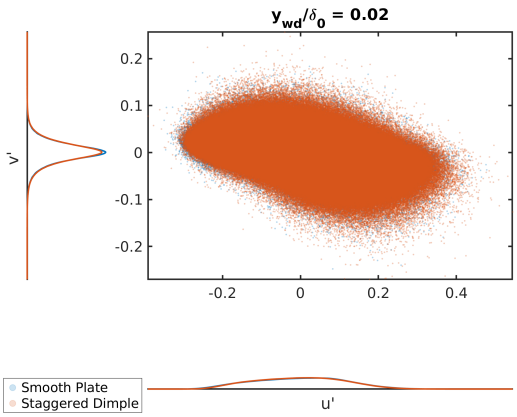

(b) Raw quadrant scatter at $y_{wd}/\delta_0 = 0.02$

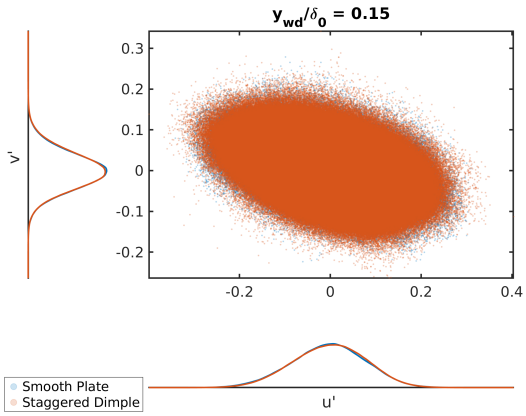

(c) Raw quadrant scatter at $y_{wd}/\delta_0 = 0.01$

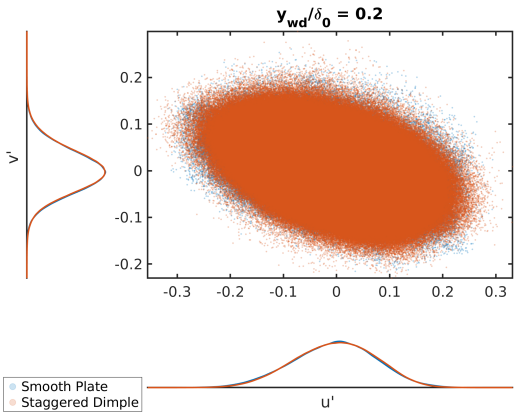

(d) Raw quadrant scatter at $y_{wd}/\delta_0 = 0.02$

Figure B-5: Raw quadrant scatters. The histogram shares the same axis limits, so lower peak suggests a more flat, uniform distribution compared to the another axis.

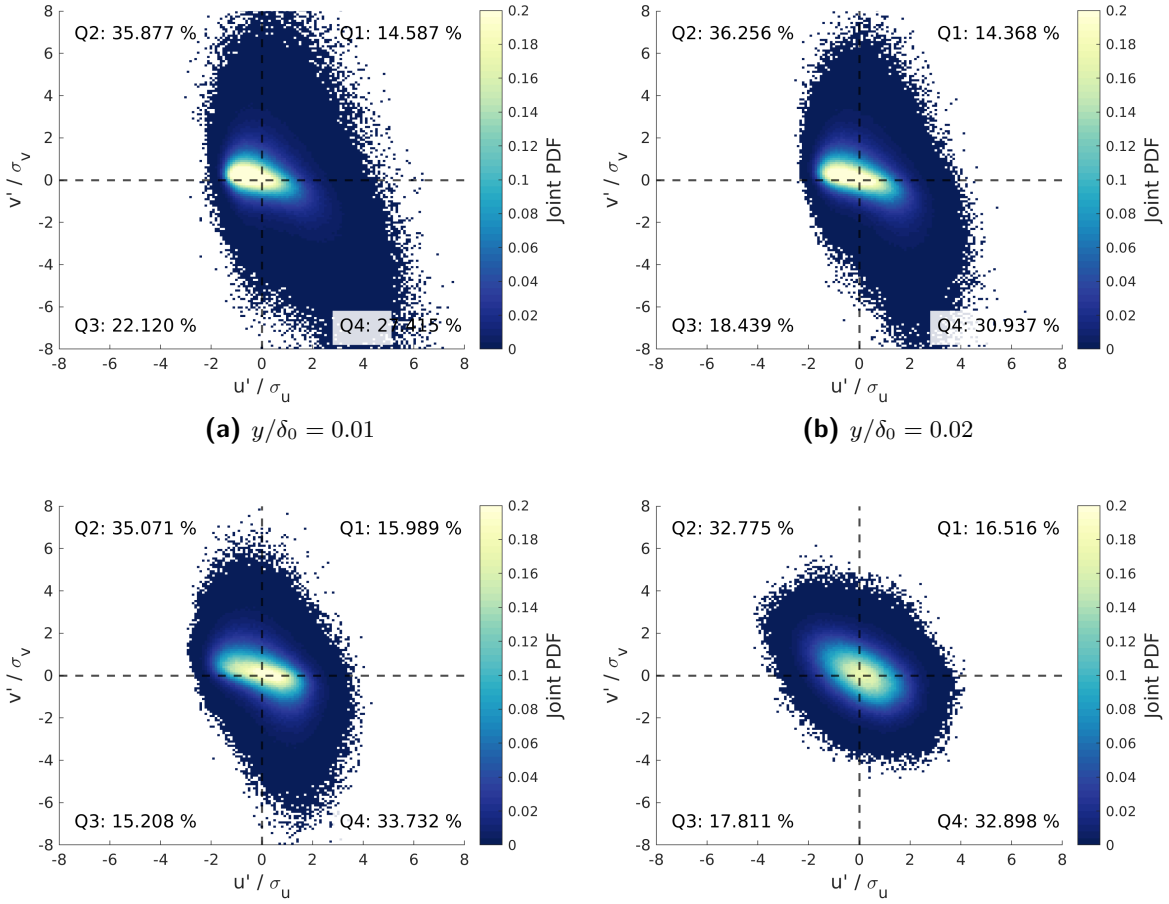

(a) $y/\delta_0 = 0.01$ **(b)** $y/\delta_0 = 0.02$

(c) $y/\delta_0 = 0.15$ **(d)** $y/\delta_0 = 0.20$

Figure B-6: Quadrant Joint Probability Density Function (J-PDF) of a smooth plate at four levels over the $4th$ dimple. The results are drawn from sampling the raw data into 200×200 bins.

B-3 VITA analysis

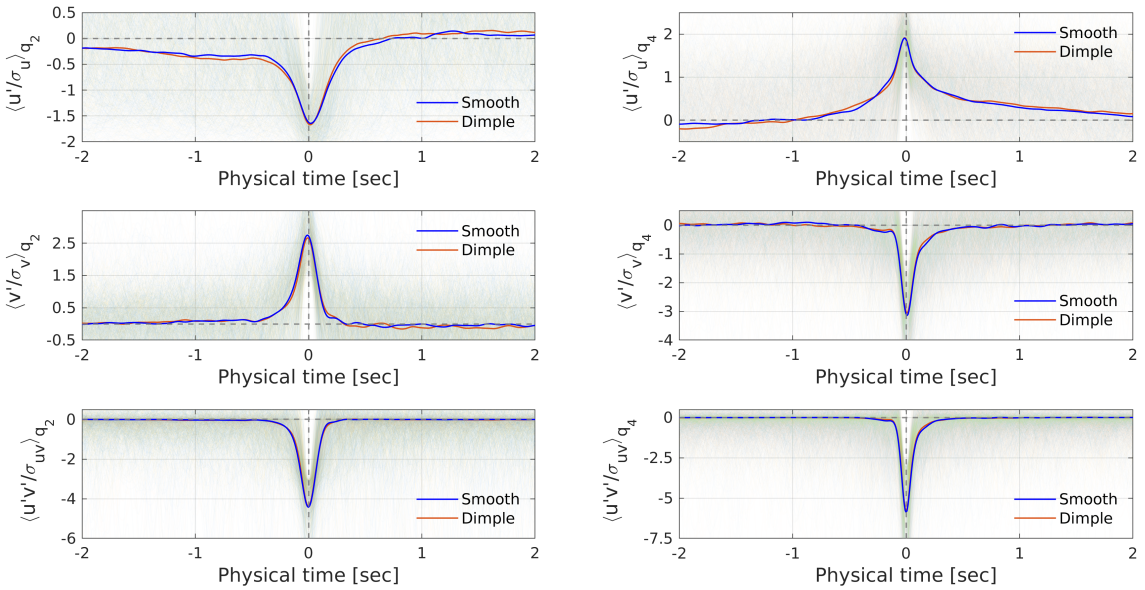

(a) Ejection event. **(b)** Sweep event.

Figure B-7: Ejection/Sweep evolution at $y/\delta_0 = 0.02$.

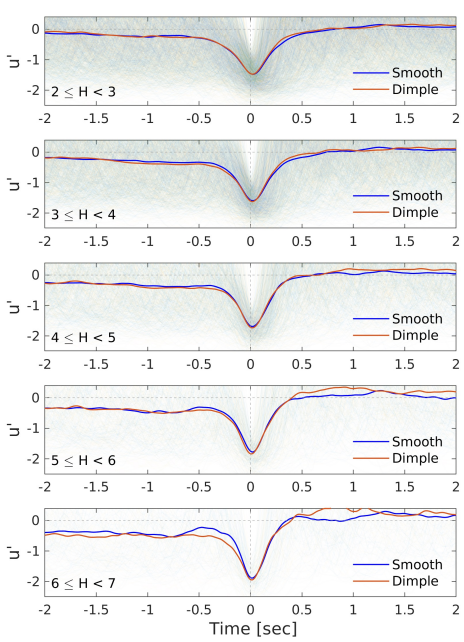

(a) Streamwise fluctuation u' of the ejection event at $y/\delta_0 = 0.02$.

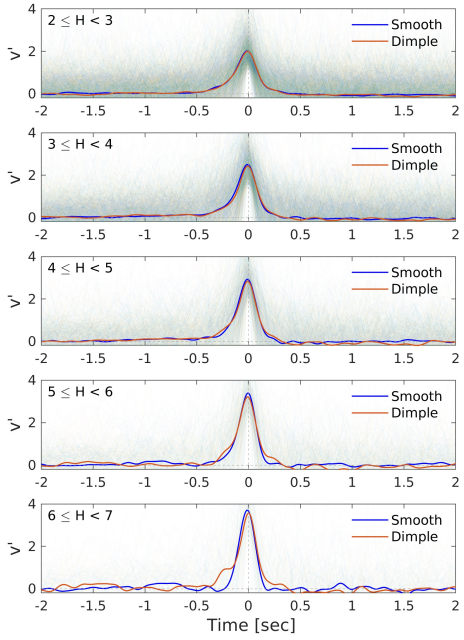

(b) Wall-normal fluctuation v' of the ejection event at $y/\delta_0 = 0.02$.

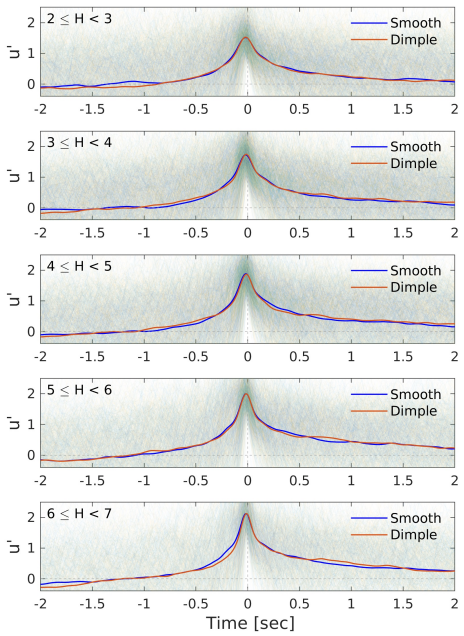

(c) Streamwise fluctuation u' of the sweep event at $y/\delta_0 = 0.02$.

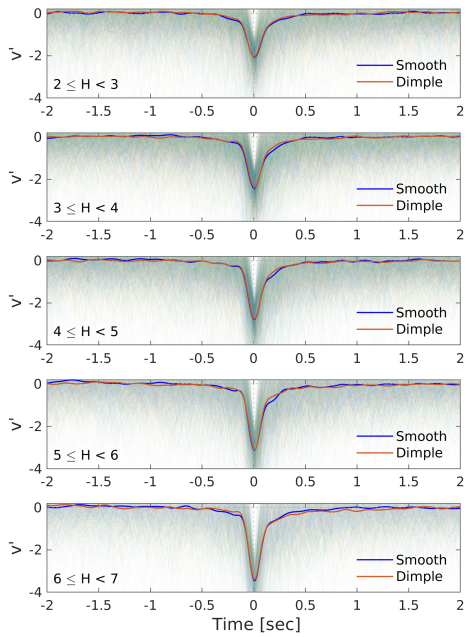

(d) Wall-normal fluctuation v' of the sweep event at $y/\delta_0 = 0.02$.

Figure B-8: VITA ensemble of the ejection/sweep event with different detection criteria. Shadings are the individual detected signal.

Bibliography

Abbas, A., de Vicente, J., and Valero, E. (2013). "Aerodynamic technologies to improve aircraft performance". In: *Aerospace Science and Technology* 28(1), pp. 100–132.

Adrian, R. J., Meinhart, C. D., and Tomkins, C. D. (2000). "Vortex organization in the outer region of the turbulent boundary layer". In: *Journal of Fluid Mechanics* 422, pp. 1–54.

Anderson, J. D. (2011). *Fundamentals of aerodynamics*. 5th. McGraw-Hill.

Bakewell, H. P. and Lumley, J. L. (1967). "Viscous sublayer and adjacent wall region in turbulent pipe flow". In: *Physics of Fluids*.

Bannier, A., Garnier, É., and Sagaut, P. (2015). "Riblet Flow Model Based on an Extended FIK Identity". In: *Flow, Turbulence and Combustion*.

Blackwelder, R. F. and Kaplan, R. E. (1976). "On the wall structure of the turbulent boundary layer". In: *Journal of Fluid Mechanics* 76, pp. 89–112.

Bogard, D. G. and Tiederman, W. G. (1986). "Burst detection with single-point velocity measurements". In: *Journal of Fluid Mechanics* 162, pp. 389–413.

Brodkey, R. S., Wallace, J. M., and Eckelmann, H. (1974). "Some properties of truncated turbulence signals in bounded shear flows". In: *Journal of Fluid Mechanics*.

Burgess, N. K. and Ligrani, P. M. (2005). "Effects of dimple depth on channel nusselt numbers and friction factors". In: *Journal of Heat Transfer*.

Cary Jr., A. M., Weinstein, L. M., and Bushnell, D. M. (1980). "Drag Reduction Characteristics of Small Amplitude Rigid Surface Waves". In: *Viscous Flow Drag Reduction*, pp. 144–167.

Choi, K. S. et al. (2011). "Turbulent boundary-layer control with plasma actuators". In: *Philosophical Transactions of the Royal Society A: Mathematical, Physical and Engineering Sciences* 369(1940), pp. 1443–1458.

Choi, K.-S. (1989). "Near-wall structure of a turbulent boundary layer with riblets". In: *Journal of Fluid Mechanics* 208, pp. 417–458.

Choi, K.-S. (2002). "Near-wall structure of turbulent boundary layer with spanwise-wall oscillation". In: *Physics of Fluids* 14(7), pp. 2530–2542.

Choi, K.-S., DeBisschop, J.-R., and Clayton, B. R. (1998). "Turbulent Boundary-Layer Control by Means of Spanwise-Wall Oscillation". In: *AIAA Journal* 36(7), pp. 1157–1163.

Corino, E. R. and Brodkey, R. S. (1969). "A visual investigation of the wall region in turbulent flow". In: *Journal of Fluid Mechanics*.

Dennis, D. J. C. (2015). "Coherent structures in wall-bounded turbulence." In: *Anais da Academia Brasileira de Ciencias* 87 2, pp. 1161–93.

Elsinga, G. et al. (2007). "Investigation of the Three-Dimensional Coherent Structures in a Turbulent Boundary Layer with Tomographic-PIV". In: *45th AIAA Aerospace Sciences Meeting and Exhibit*.

Ferreira, C. S. (2018). *Rotor/Wake Aerodynamics Lecture Notes*. URL: https://csimaoferreira.github.io/Rotor-Wake-Aerodynamics-Lifting-Line/#/Coverslide.

Fujimatsu, N. and Misu, I. (2010). "Improvement of VITA Technique and Quadrant Analysis Considering Coherent Motion in Turbulent Boundary Layer". In: 実験力学 10(1), pp. 82–88.

Fukagata, K., Iwamoto, K., and Kasagi, N. (2002). "Contribution of Reynolds stress distribution to the skin friction in wall-bounded flows". In: *Physics of Fluids*.

Gad-el-Hak, M. (2007). *Flow Control: Passive, Active, and Reactive Flow Management*. Cambridge University Press.

Hickel, S. and Adams, N. A. (2007). "Efficient Implementation of Nonlinear Deconvolution Methods for Implicit Large-Eddy Simulation". In: *High Performance Computing in Science and Engineering '06*. Ed. by W. E. Nagel, W. Jäger, and M. Resch. Springer Berlin Heidelberg: Berlin, Heidelberg.

Hickel, S., Egerer, C. P., and Larsson, J. (2014). "Subgrid-scale modeling for implicit large eddy simulation of compressible flows and shock-turbulence interaction". In: *Physics of Fluids* 26(10), p. 106101.

Hoogsteen, R. (1990). "Quadrant analysis of turbulent boundary layers over smooth and riblet surfaces". MA thesis. the Netherlands: Eindhoven University of Technology.

Howarth, L. (1938). "On the Solution of the Laminar Boundary Layer Equations". In: *Proceedings of the Royal Society of London. Series A - Mathematical and Physical Sciences*.

Hu, X. et al. (2006). "A conservative interface method for compressible flows". In: *Journal of Computational Physics* 219(2), pp. 553–578.

Hutchins, N. and MARUSIC, I. (2007). "Evidence of very long meandering features in the logarithmic region of turbulent boundary layers". In: *Journal of Fluid Mechanics* 579, pp. 1–28.

Isaev, S., Leontiev, A., et al. (2005). "Comparative Analysis of the Vortex Heat Exchange in Turbulent Flows around a Spherical Hole and a Two-Dimensional Trench on a Plane Wall". In: *Journal of Engineering Physics and Thermophysics* 78, pp. 749–761.

Isaev, S. A. et al. (2013). "Analysis of thermohydraulic efficiency increase during transformer oil flow in a minichannel with a single-row package of spherical and oval dimples at a heated wall". In: *High Temperature*.

Isaev, S. A., Kornev, N. V., et al. (2010). "Influence of the Reynolds number and the spherical dimple depth on turbulent heat transfer and hydraulic loss in a narrow channel". In: *International Journal of Heat and Mass Transfer*.

Isaev, S. A., Schelchkov, A. V., et al. (2017). "Vortex heat transfer enhancement in the narrow plane-parallel channel with the oval-trench dimple of fixed depth and spot area". In: *International Journal of Heat and Mass Transfer*.

Kasagi, N. et al. (1995). "Kinematics of the quasi-coherent vortical structure in near-wall turbulence". In: *International Journal of Heat and Fluid Flow* 16(1), pp. 2–10.

Kiknadze, G. I. (2013). “Friction reducing surface and a mass and heat transfer enhancing surface”. In:

Kiknadze, G. I., Gachechiladze, I. A., and Barnaveli, T. T. (2012). “The Mechanisms of the Phenomenon of Tornado-Like Jets Self-Organization in the Flow Along the Dimples on the Initially Flat Surface”. In: ASME International Mechanical Engineering Congress and Exposition Volume 7: Fluids and Heat Transfer, Parts A, B, C, and D, pp. 3017–3026.

Kiknadze, G. I., Krasnov, Y. K., and Chushkin, Y. V. (1984). “Investigation of the Enhancement of Heat Transfer due to Self-Organization of Ordered Dynamic Twisted Heat-Carrier Structures on a Heat Transfer Surface”. In: *I. V. Kurchatov Institute of Atomic Energy*.

Kline, S. J. et al. (1967). “The structure of turbulent boundary layers”. In: *Journal of Fluid Mechanics*.

Kovalenko, G. V., Terekhov, V. I., and Khalatov, A. A. (2010). “Flow regimes in a single dimple on the channel surface”. In: *Journal of Applied Mechanics and Technical Physics* 51(6), pp. 839–848.

Lashkov, Y. A. and Samoilova, N. V. (2002). “On the viscous drag of a plate with spherical recesses”. In: *Fluid Dynamics*.

Leontiev, A. I. et al. (2017). “Experimental investigation of heat transfer and drag on surfaces coated with dimples of different shape”. In: *International Journal of Thermal Sciences*.

Lienhart, H., Breuer, M., and Köksoy, C. (2008). “Drag reduction by dimples? - A complementary experimental/numerical investigation”. In: *International Journal of Heat and Fluid Flow*.

Lund, T. S., Wu, X., and Squires, K. D. (1998). “Generation of Turbulent Inflow Data for Spatially-Developing Boundary Layer Simulations”. In: *Journal of Computational Physics* 140(2), pp. 233–258.

Mahmood, G. I. et al. (2001). “Local heat transfer and flow structure on and above a dimpled surface in a channel”. In: *Journal of Turbomachinery*.

Meyer, M. et al. (2010). “A conservative immersed interface method for Large-Eddy Simulation of incompressible flows”. In: *Journal of Computational Physics* 229(18), pp. 6300–6317.

Mitsudharmadi, H., Tay, C. M., and Tsai, H. M. (2009). “Effect of rounded edged dimple arrays on the boundary layer development”. In: *Journal of Visualization*.

Morrison, J., Tsai, H., and Bradshaw, P. (1988). “Conditional-sampling schemes for turbulent flow, based on the variable-interval time averaging (VITA) algorithm”. In: *Experiments in Fluids* 7, pp. 173–186.

Nagib, H. M., Chauhan, K. A., and Monkewitz, P. A. (2007). “Approach to an asymptotic state for zero pressure gradient turbulent boundary layers”. In: *Philosophical Transactions of the Royal Society A: Mathematical, Physical and Engineering Sciences* 365(1852), pp. 755–770.

Nieuwstadt, F. T., Westerweel, J., and Boersma, B. J. (2016). *Turbulence–Introduction to Theory and Applications of Turbulent Flows*. Springer, Cham.

Peet, Y. and Sagaut, P. (2009). “Theoretical prediction of turbulent skin friction on geometrically complex surfaces”. In: *Physics of Fluids* 21(10), p. 105105.

Peskin, C. S. (1972). “Flow patterns around heart valves: A numerical method”. In: *Journal of Computational Physics* 10(2), pp. 252–271.

Piomelli, U. (2001). “Large-eddy and direct simulation of turbulent flows”. In:

Pope, S. (2000). *Turbulent Flows*. Cambridge University Press.

Quadrio, M. and Sibilla, S. (2000). "Numerical simulation of turbulent flow in a pipe oscillating around its axis". In: *Journal of Fluid Mechanics* 424, pp. 217–241.

Quadrio, M. and Ricco, P. (2004). "Critical assessment of turbulent drag reduction through spanwise wall oscillations". In: *Journal of Fluid Mechanics* 521, pp. 251–271.

Ricco, P. et al. (2012). "Changes in turbulent dissipation in a channel flow with oscillating walls". In: *Journal of Fluid Mechanics* 700, pp. 77–104.

Shu, C.-W. (1988). "Total-Variation-Diminishing Time Discretizations". In: *SIAM Journal on Scientific and Statistical Computing* 9(6), pp. 1073–1084.

Smith, C. R. and Metzler, S. P. (1983). "The characteristics of low-speed streaks in the near-wall region of a turbulent boundary layer". In: *Journal of Fluid Mechanics* 129, pp. 27–54.

Smith, C. R. (1984). "A Synthesized Model of the Near-Wall Behavior in Turbulent Boundary Layers." In:

Smits, A. J., Matheson, N., and Joubert, P. N. (1983). "Low-Reynolds-Number Turbulent Boundary Layers in Zero and Favorable Pressure Gradients". In: *Journal of Ship Research*.

Spalart, P. R. et al. (2019). "Experimental and numerical study of the turbulent boundary layer over shallow dimples". In: *International Journal of Heat and Fluid Flow* 78.

Spalart, P. R. (1988). "Direct simulation of a turbulent boundary layer up to R $= 1410$". In: *Journal of Fluid Mechanics* 187, pp. 61–98.

Tay, C. et al. (2014). "Development of flow structures over dimples". In: *Experimental Thermal and Fluid Science*.

Tay, C. M., Khoo, B. C., and Chew, Y. T. (2015). "Mechanics of drag reduction by shallow dimples in channel flow". In: *Physics of Fluids*.

Tay, C. M. J. (2011). "Determining the Effect of Dimples on Drag in a Turbulent Channel Flow". In:

Tay, C. M. J. and Lim, T. T. (2018). "Drag reduction with teardrop-shaped dimples". In: *2018 Flow Control Conference*.

Terekhov, V., Kalinina, S., and Mshvidobadze, Y. (1995). "Flow structure and heat transfer on a surface with a unit hole depression". In: *Russ. J. Eng. Thermophys.* 5, pp. 11–33.

Theodorsen, T. (1952). "Mechanism of turbulence". In: *in Proceedings of the Midwestern Conference on Fluid Mechanics (Ohio State University, Columbus, OH)*.

Tran, L. V. et al. (2011). "PIV study on the dimple mid-plane of a narrow rectangular channel with dimples applied to one wall". In: *Proceedings of the ASME Turbo Expo*.

Turnow, J. et al. (2011). "Vortex mechanism of heat transfer enhancement in a channel with spherical and oval dimples". In: *Heat and Mass Transfer/Waerme- und Stoffuebertragung*.

van Campenhout, O. et al. (2016). *Flow visualization over drag reducing dimpled surfaces in turbulent boundary layers using Particle Image Velocimetry*. Tech. rep., pp. 4–7.

van Campenhout, O. et al. (2018). "An experimental investigation into the flow mechanics of dimpled surfaces in turbulent boundary layers". In: *2018 AIAA Aerospace Sciences Meeting*.

van Nesselrooij, M. et al. (2016). "Drag reduction by means of dimpled surfaces in turbulent boundary layers". In: *Experiments in Fluids*.

van Nesselrooij, M. (2015). "On the drag reduction of dimpled surfaces in turbulent boundary layers: Proof of concept and identification of flow structure". MA thesis. Delft University of Technology.

Veldhuis, L. L. and Vervoort, E. (2009). "Drag effect of a dented surface in a turbulent flow". In: *Collection of Technical Papers - AIAA Applied Aerodynamics Conference*.

Vervoort, E. (2009). “Drag Effect of Dented Surfaces in Turbulent Flows.” In: *27th AIAA Applied Aerodynamics Conference*(June), pp. 1–12.

Vida, N. (2004). “Three dimensional surface structure for reduced friction resistance and improved heat exchange”. In: *European Patent Office, EP1604122*.

Vorst, H. A. van der (1992). “Bi-CGSTAB: A Fast and Smoothly Converging Variant of Bi-CG for the Solution of Nonsymmetric Linear Systems”. In: *SIAM Journal on Scientific and Statistical Computing* 13(2), pp. 631–644.

Wallace, J. M. et al. (1972). “The wall region in turbulent shear flow”. In: *Journal of Fluid Mechanics* 54(1), pp. 39–48.

Wallace, J. M. (2016). “Quadrant Analysis in Turbulence Research: History and Evolution”. In: *Annual Review of Fluid Mechanics*.

Wallace, J. M., Brodkey, R. S., and Eckelmann, H. (1977). “Pattern-recognized structures in bounded turbulent shear flows”. In: *Journal of Fluid Mechanics*.

White, F. (2006). *Viscous Fluid Flow*. McGraw-Hill international edition. McGraw-Hill.

Willmarth, W. W. and Lu, S. S. (1972). “Structure of the reynolds stress near the wall”. In: *Journal of Fluid Mechanics*.

Wu, X. H. and Moin, P. (2009). “Direct numerical simulation of turbulence in a nominally zero-pressure-gradient flat-plate boundary layer”. In: *Journal of Fluid Mechanics* 630, pp. 5–41.

Wüst, C. (2004). “Dellen im dach”. In: *Der Spiegel 14*.

Yakeno, A., Hasegawa, Y., and Kasagi, N. (2014). “Modification of quasi-streamwise vortical structure in a drag-reduced turbulent channel flow with spanwise wall oscillation”. In: *Physics of Fluids*.